

BRNO UNIVERSITY OF TECHNOLOGY

VYSOKÉ UČENÍ TECHNICKÉ V BRNĚ

CENTRAL EUROPEAN INSTITUTE OF TECHNOLOGY BUT

STŘEDOEVROPSKÝ TECHNOLOGICKÝ INSTITUT VUT

2D MOLECULAR SYSTEMS AT SURFACES

2D MOLEKULÁRNÍ SYSTÉMY NA POVRŠÍCH

DOCTORAL THESIS

DIZERTAČNÍ PRÁCE

AUTHOR

AUTOR PRÁCE

Ing. Lukáš Kormoš

SUPERVISOR

ŠKOLITEL

doc. Ing. Jan Čechal, Ph.D.

BRNO 2020

Abstrakt

Molekulárne systémy predstavujú jeden zo smerov súčasného výskumu nových nanoelektronických zariadení. Organické molekuly nachádzajú uplatnenie v rôznych aplikáciách, ako sú napríklad solárne články, displeje alebo kvantové počítače. Rast vysokokvalitných molekulárnych vrstiev s požadovanými vlastnosťami často vyžaduje využitie samousporiadavaných štruktúr, hlboké pochopenie rozhrania kovu a organických molekúl a tiež dynamiky rastu molekulárnych vrstiev. Predkladaná práca sa zaoberá predovšetkým samousporadanými štruktúrami bifenyldikarboxylovej kyseliny (BDA) na Cu(100) a Ag(100), ktoré boli skúmané v UHV s využitím STM, XPS a LEEM. V prípade BDA-Ag je podrobne opísaných niekoľko chemicky a štrukturálne odlišných molekulárnych fáz. Ďalej boli BDA a TCNQ molekuly skúmané na grafene pripravenom na Ir(111). Okrem toho sa organo-kovové systémy syntetizovali depozíciou atómov Ni a Fe s molekulami TCNQ a BDA. Záverečná časť tejto práce popisuje povrchovú syntézu grafénových nanoribonov (7-AGNR) na špecificky štrukturovanom substráte Au(161415) z prekursorových molekúl DBBA. Rekonštrukcia povrchu po raste bola analyzovaná pomocou STM a elektronickej vlastnosti 7-AGNRs pomocou ARPES.

Summary

Molecular systems represent one direction of the current research of the novel nanoelectronic devices. Organic molecules are considered in various applications such as solar cells, displays or quantum computing. Growth of high-quality molecular layers with desired properties often employs self-assembled structures and requires a deep understanding of metal-organic interface and dynamics of the molecular layer growth. Work presented in this thesis is in the beginning focused on the self-assembly of biphenyldicarboxylic acid (BDA) on Cu(100) and Ag(100) studied in a UHV utilising STM, XPS and LEEM. In the case of BDA/Ag, multiple chemically and structurally distinct molecular phases are described in detail. Next, the BDA and TCNQ self-assembly is studied on graphene grown on Ir(111). In addition, metal-organic systems were synthesised by deposition of additional Ni and Fe atoms with TCNQ and BDA molecules on graphene. The final part of this work presents on-surface synthesis of graphene nanoribbons (7-AGNR) on the kinked Au(161415) substrate from DBBA precursor molecules. Surface reconstruction after the growth is analysed by STM and electronic properties of 7-AGNRs by ARPES.

Klíčová slova

samousporiadované vrstvy, grafen, organo-kovové siete, TCNQ, BDA, molekuly

Keywords

self-assembly, graphene, metal-organic networks, TCNQ, BDA, molecules

KORMOŠ, L. *2D Molecular systems at surfaces*. Brno University of Technology, Faculty of Mechanical Engineering, 2020. 140 s. Thesis supervisor: doc. Ing. Jan Čechal, Ph.D.

DECLARATION:

I declare that I have written this work independently, under the guidance of the thesis supervisors and using the technical literature and other sources of information which are all quoted and detailed in the list of literature at the end of the work.

Ing. Lukáš Kormoš

ACKNOWLEDGMENT

First, I would like to thank doc. Ing. Jan Čechal, Ph.D. for his scientific expertise, guidance and proofreading of the text. His optimism and talent “*to find the needle in the haystack*” of measured data greatly improved quality of research presented in this work. Second, i want to thank prof. RNDr. Tomáš Šikola, CSc. for all the effort he put into establishing new CEITEC research centre. Without the new high-tech experimental facilities this work would not have been possible. Further, I want to thank and acknowledge my colleagues Pavel Procházka, Anton O. Makoveev, Veronika Stará and Štěpán Kovařík for their great cooperation and help with the endless experiments. I want to also include few of my fellow PhD students and friends who helped in big or small ways with the research, discussions or occasional foosball match, namely Marek Vaňatka, Lukáš Flajšman and Vojtěch Švarc.

I would also like to thank prof. Erique Ortega for allowing me to visit his research group at the Materials Physics Centre in San Sebastian. Additionally my gratitude also goes to several of the scientist there, that helped me to learn the fundamentals of UHV, namely Martina Corso, Jorge Lobo-Checa and Afaf El-Sayed.

Part of this work was carried out with the financial support from the Ministry of Education, Youth and Sports (MEYS) of the Czech Republic: projects CEITEC 2020 (LQ1601) under the National Sustainability Programme II, CEITEC Nano+ (CZ.02.1.01/0.0/0.0/16 – 013/0001728) under the program OPVVV, and project TC17021 under the program Inter-Excellence, and GAČR, project no. 19-01536S.

Ing. Lukáš Kormoš

CONTENTS

1. <i>Introduction</i>	1
2. <i>Molecular Self Assembly</i>	4
2.1 Molecule - Molecule interactions	4
2.1.1 van der Waals Interactions	5
2.1.2 Dispersion interaction	5
2.1.3 Hydrogen bonds	7
2.1.4 Halogen bonds	8
2.1.5 Intermolecular π - π interaction	9
2.1.6 Electrostatic interaction	10
2.2 Molecule-surface interactions	11
2.2.1 Metal-organic interface	11
2.2.2 Diffusion on surfaces	13
2.3 Metal-organic systems	14
2.4 Self-assembly on graphite and graphene	15
2.4.1 Metal-organic networks on graphene	19
2.5 Conclusion	21
3. <i>Experimental Setup</i>	22
3.1 UHV system	22
3.1.1 Sample transfer	22
3.2 Sample preparation	24
3.2.1 Sample holder	24
3.2.2 Sample cleaning	24
3.2.3 Temperature measurement in UHV	25
3.2.4 Material deposition	27
3.3 Sample Analysis	27
3.3.1 X-ray Photoelectron Spectroscopy	28
3.3.2 Scanning Tunnelling Microscopy	28
3.3.3 STM drift correction	29
4. <i>LEEM - Low energy electron microscopy</i>	31
4.1 Microscope setup	31
4.1.1 Gun and condenser system	31
4.1.2 Sample prism - Beam separator	33

4.1.3	Objective lens and Sample	33
4.1.4	Projector system and Apertures	34
4.2	Imaging with LEEM	35
4.2.1	LEEM contrast	35
4.2.2	Dark-field imaging	37
4.2.3	Diffraction imaging	38
4.3	Conclusion	39
5.	<i>Biphenyl Dicarboxylic Acid on metal surfaces</i>	40
5.1	BDA on Cu (100)	41
5.1.1	Structural defects	44
5.1.2	Growth Anomalies of BDA on Cu (100)	45
5.1.3	Step edge passivation	47
5.1.4	Conclusion of section BDA on Cu (100)	48
5.2	BDA on Ag (100)	49
5.2.1	Overview	49
5.2.2	XPS analysis	50
5.2.3	Structure of the BDA α -phase	54
5.2.4	Structure of the BDA β -phase	58
5.2.5	$\alpha \Rightarrow \beta$ phase transformation	59
5.2.6	Structure of the BDA γ -phases	62
5.2.7	$\beta \Rightarrow \gamma$ phase transformation	66
5.2.8	Structure of the BDA δ -phase	67
5.2.9	Other BDA self-assemblies	70
5.2.10	Long range-order	72
5.2.11	LEEM beam damage	73
5.3	BDA phases as a k -uniform tilings	74
5.3.1	Symmetry and regularity	75
5.3.2	k -uniform tilings	77
5.3.3	BDA phases as k -uniform tilings	77
5.4	Conclusion BDA on Ag (100)	79
6.	<i>Molecular networks on graphene</i>	81
6.1	Graphene electronic properties	81
6.2	Graphene synthesis	82
6.2.1	Chemical vapour deposited (CVD) graphene	83
6.2.2	Ultra-high vacuum syntheses	83
6.3	BDA on graphene/Ir (111)	88
6.4	Graphene Fe-BDA network	90
6.4.1	Preparation of Fe-BDA network	91
6.4.2	XPS analysis of Fe-BDA network	92
6.5	TCNQ self-assembly on graphene	94

6.6	Ni-TCNQ network on graphene	96
6.6.1	Preparation of Ni-TCNQ network	97
6.6.2	XPS analysis of Ni-TCNQ network	99
6.7	Conclusion	101
7.	<i>Graphene nanoribbons (GNR)</i>	103
7.1	Au(16 14 15)	104
7.2	On-surface synthesis of GNRs	104
7.2.1	GNR growth on Au(16 14 15)	105
7.2.2	XPS analysis	106
7.2.3	New surface reconstruction	107
7.2.4	7-AGNR band structure	107
8.	<i>Conclusions</i>	110
9.	<i>Supplementary</i>	112
10.	<i>Authors Publications</i>	113

1. INTRODUCTION

For the past decade, the breakdown of the Moor's law ¹, appears to be unavoidable. Although the downscaling of the devices continues with currently the most advanced 7 nm node technology, the silicon-based transistors are reaching their limit. One indicator of the stagnation in the development of current conventional CMOS (complementary metal-oxide-semiconductor) transistors is a plateau in the progress of device frequencies that rarely exceeds the 5 GHz. Combined with the increasing cost of downscaling in terms of fabrication and facility costs, the drive to utilise new materials grows exceedingly in both scientific and industrial research groups. [2, 3]

In order to make significant improvements, several non-traditional materials and structures are considered in so-called *beyond-CMOS technologies*. Between them, a new branch of molecular electronics is being developed and already various molecular devices have been discovered such as logic gates [4], diodes [5] or switches [6]. However, the most recognised application of organic molecules today are OLED (organic light-emitting diode) displays, now widely utilised in the construction of TVs. OLED screens provide improved contrast, power efficiency and most notably, the flexibility that allows them to bend and even partially fold.

In the field of computing research, molecular spintronics aims at using electron spins rather than charges. Absence of flowing current could improve the device efficiency and reduce heat accumulation which further removes design limitations. One of the most promising beyond-CMOS technologies is quantum computing. In this area, the utilisation of molecular quantum bits (MQBs) is extensively studied due to the easier spin coupling observed for electron spins compared to the more traditional nuclear spins. Further, the wide range of molecular adaptability may give MQBs the advantage over defect-based solid-state quantum information processing devices [7].

Several of the main prerequisites for the practical implementation of molecules as quantum bits were already fulfilled. First, the coherence time of MQBs was demonstrated in the range of hundreds of microseconds [8]. Second, dynamic control over the interaction between the individual metal centres in MQBs, for example, by employing photo-active or local electric control of a molecular linker [9]. Using chemical synthesis methods, two quantum bit gates have been implemented with atomic precision in one molecule. Additionally, the scalability of MQBs can be achieved by implementing principles of self-assembled and metal-coordinated long-range ordered molecular networks. For this and also many other applications, the understanding of the underlying princi-

¹ empirical relationship stating that the number of transistors in integrated circuits will double about every two years [1]

ples of molecular self-assembly and interaction between the molecules and surfaces is of great importance.

This thesis deals with a variety of surface-molecule systems ranging from weakly bonded self-assembled structures to metal-coordinated networks and eventually a covalently bonded system achieved by on-surface synthesis. This thesis is divided into eight chapters beginning with the introduction. Following second chapter provides theoretical overview focused on non-covalent bonds and various interactions most commonly involved in self-assembled processes of organic molecules on surfaces. Additionally, multiple experimental examples are given for each relevant bonding mechanisms. Several sections of the review also include examples of metal-coordinated systems with a last sections focused on graphene. In addition to the introduction, relevant overviews of specific topics are given at the beginning of each experimental chapter.

The third and fourth chapter describe the experimental apparatus and basics of work in ultra-high vacuum (UHV). Most of the experiments were performed in the multifunctional UHV system that includes particularly useful combination of techniques for studying molecular structures at surfaces e.i.: a mesoscale view provided by low electron energy microscope (LEEM), nanoscopic details from scanning tunnelling microscope (STM) and chemical information from X-ray photoemission spectroscopy (XPS). The third chapter describes LEEM in detail, its construction, operational details and various applications, mainly the dark-field imaging and μ -diffraction.

The experimental results are presented in the last three chapters. Chapter five presents an extensive work focused on self-assembled structures of biphenyl-dicarboxylic acid (BDA) on Cu(100) and Ag(100). This molecule is a model system due to its simple structure and the presence of carboxylic end groups that are often employed in the molecular self-assembly. In the first part of the chapter, the BDA/Cu(100) system is explored. BDA on Cu chemically reacted (deprotonated) at room temperature and formed a single phase. On the contrary, the BDA on Ag(100) remains intact at RT. The deprotonation reaction on Ag was initiated by additional annealing, which led to an abrupt change of binding mechanism of functional moieties and, consequently, to changes in the structure of the self-assembly. Variety of chemically and structurally distinct phases were observed and described in detail with the addition of main phase transitions followed in LEEM. In the last part of the chapter, the BDA on Ag(100) system is also presented as the experimental realisation of long-range ordered uniform tessellations.

Chapter five describes the growth of high-quality graphene layers prepared on Ir(111) in UHV conditions. Graphene prepared in this way was utilised to study the self-assembly of BDA and TCNQ molecules. Graphene as a substrate for self-assembly has several advantages. It is a conductor with high electron mobility and a high spin diffusion length due to its negligible spin-orbit coupling [10]. Additionally, graphene is able to efficiently decouple the molecules from the underlying metal substrates due to its chemical inertness and low density of states around the Fermi level [11]. In this way molecules adsorbed on graphene can partially preserve their intrinsic properties such as

magnetic moments or their catalytic activity [12, 13]. Further, controlled tuning of the charge carrier density in graphene devices may provide new opportunities to control the behaviour of molecular adsorbates [14]. On the other hand, molecules can be used as functionalising agents for graphene (or other 2D materials) based devices, that are also considered as one of the beyond CMOS technologies. Last sections of the chapter focus on the preparation of metal-coordinated molecular networks on graphene, mainly Fe-BDA and Ni-TCNQ.

Finally, the last short chapter describes the growth of graphene nanoribbons with a width of seven carbon atoms (7-AGNR) by means of on-surface synthesis from the dibromo-bianthracene (DBBA) molecules on kinked Au(16 14 15). On-surface chemistry in ultra-high vacuum offers complementary routes for synthesising molecular complexes that cannot be accessed through standard solution chemistry. In recent years this field rapidly grew due to closely cooperating chemists and physicists [15]. One of the main drives in this field was a synthesis of GNR, one-dimensional carbon structures. A significant advantage of GNRs over graphene is their tunable bandgap, which can be modified by the width of the ribbon [16]. Apart from the description of GNR synthesis, the last chapter also provides details about changes in the surface reconstruction, showcasing the bilateral relation between the substrate and adsorbed species. The last section of the chapter briefly describes the measurement of the 7-AGNR frontier valence band.

2. MOLECULAR SELF ASSEMBLY

The engineering of materials with atomic or molecular-level precision requires high levels of sophistication in both fabrication and characterisation methods. A promising pathway lies in self-assembly of organic or metal-organic molecules on surfaces: a spontaneous formation of spatially textured networks of defined shape. Investigations focused on on-surface self-assembly started with the observation of self-assembled monolayers (SAMs). In this case, molecules are functionalised to bound to the substrate and assemble in a self-limiting way into structures exactly one monolayer thick. Molecules used for SAMs typically consist from long chains with functional anchoring groups, for example, alkylthiolates on gold surface [17]. Selectivity of the bond between the substrate and anchoring group drives the self-assembly of SAMs. However, by exploiting non-covalent bonding between molecules it was possible to prepare a large variety of self-assembled molecular systems on well-defined atomically flat surfaces. In the last couple of decades the amount of research in this field rapidly grew, exploring systems prepared in ultrahigh vacuum (UHV) or at the liquid–solid interface with the ultimate goal of creating functional 2D systems. Molecules could be programmed to create an ordered structure tailored to a desired function. [18–20]

The study of molecular structures on surfaces was greatly enhanced by the use of non-contact atomic force microscopy (nc-AFM) at low temperatures. Today, molecules can be observed individually with a sub-molecular resolution, and chemical reactions on surfaces can be observed step by step. Such imaging provides a valuable tool to investigate the intermolecular and molecule-substrate bonding mechanisms [21]. Surface confined molecular self-assembly mostly depends on (I) the mobility of the molecules on the surface, (II) the competition between intermolecular and molecule/substrate interactions and (III) the thermal energy brought into the system. The following sections focus on non-covalent bonds and various interactions most commonly involved in self-assembled processes of organic molecules on surfaces.

2.1 *Molecule - Molecule interactions*

Most of the important non-covalent interactions between the molecules arise ultimately from different types of electrostatic interactions [22]. They can be separated into two main categories: long-range, where the energy of interaction decreases with some inverse power of distance, and short-range, where the energy decreases exponentially with distance. Molecular interactions can be expressed as a sum of repulsive and attractive forces:

$$V(R) = V_{rep.}(R) + V_{att.}(R), \quad (2.1)$$

where R is the distance between the two atoms. The strength of the resulting balance between attractive and repulsive forces defines the properties of self-assembly.

A typical intermolecular potential can be conventionally described (or approximated) by Lennard-Jones potential ($A/R^{12} - B/R^6$), and the repulsive potential can be further improved by incorporating exponential function (Born-Mayer ($A \cdot e^{(-BR)}$) potential)[23]. In most cases, the potential will have a steep repulsive region at closer range and an attractive region at long range. At very short distances the repulsive forces will dominate the interaction arising from the Coulomb's energy, an increased nuclear repulsion as the ions are brought closer to each other by the bond formation. The other repulsive contribution is an increased electron exchange energy dictated by the Pauli exclusion principle. At long range, typically some energy minima exist where interaction between molecules becomes attractive. The most dominant attractive long-range effects are classical electrostatic attraction, forces between instantaneously formed dipoles, and more complex dispersion forces [22].

In this section, the origin of the non-covalent molecular bonds and interaction will be briefly discussed together with classification of the most common types involved in self-assembly.

2.1.1 van der Waals Interactions

The van der Waals force is generally used to describe weak long-range attractive interactions between atoms or molecules. However, its unambiguous classification is not possible. Van der Waals (vdW) interactions encompass attractive and repulsive forces over various distances 2 – 10 Å. The interactions usually have multiple contributions, mainly London force describing dispersion interaction and various dipole interactions between molecules with fixed or rotating dipoles depending on the interacting species. The interaction strength has a strong distance dependence and is often described (modelled) with term $1/R^6$ [24].

In self-assembly on surfaces, the van der Waals interactions can be the main driving force (together with surface interactions) for larger and otherwise non-interacting molecules [25]. For example, self-assembly of amino-helicene on Cu (1 0 0) and Au (1 1 1) [26] and several long alkyl chains on graphite [27, 28] were identified as vdW dominated self-assemblies. Additionally, the surface structures are often formed by the combination of multiple molecule-molecule interactions, for example, vdW and hydrogen bonds [29].

2.1.2 Dispersion interaction

Part of vdW forces are dispersive interactions, which play an important role in the formation of self-assembled structures often in combination with other bonding mechanisms between the molecules or molecules and surface [30]. Dispersion interaction has

a quantum-mechanical origin and is more dominant at the long-range. This interaction between the atoms/molecules is formed due to a correlation between the motion of their electrons, and this manifests itself in such a way that lower-energy configurations are favoured and higher-energy ones disfavoured. The average effect is a energy decrease, and since the correlation effect becomes stronger as the molecules approach each other, the result is an attraction (up to a certain distance until other interactions prevail). In literature, this interaction is sometimes referred to as London forces, charge-fluctuation forces, electrodynamic forces or induced-dipole–induced-dipole forces. Dispersion interaction needs to be considered in density-functional theory (DFT) calculations of larger systems such as self-assembled layers, to provide accurate results. The general features of dispersion forces can be summarised as follows [24]:

1. They are long-range forces and can be effective from large distances ($> 100 \text{ \AA}$) down to interatomic spacings (about 2 \AA).
2. They may be repulsive or attractive, and in general, dispersion forces between two molecules or large particles do not follow a simple power law.
3. Dispersion forces not only bring molecules together but also tend to align or orient them mutually.
4. Dispersion forces are not additive; that is, the force between two bodies is affected by the presence of other bodies nearby (nonadditivity).

One of the recent computational approaches for dispersion forces (DFT-D3), will be partially described to better demonstrate their complex nature [31]. Here, the dispersion energy is added to the total energy and is comprised from two- and three-body energies, where the two body part is stronger:

$$E_{disp} = E^{(2)} + E^{(3)}. \quad (2.2)$$

$$E^{(2)} = \sum_{AB} \sum_{n \geq 6} s_n \frac{C_n}{r_n} f_{d,n}(r_{AB}). \quad (2.3)$$

The two body term is summed over all atom pairs in the systems and the C_n^{AB} is the averaged n-th order dispersion coefficient, r_{AB} is a internuclear distance of the atom pair AB and s_n is a scaling factor. The dispersion coefficients are computed *ab initio*, starting from the Casimir-Polder formula:

$$C_6^{AB} = \left(\frac{3}{\pi}\right) \int_0^\infty \alpha^A(i\omega) \alpha^B(i\omega) d\omega, \quad (2.4)$$

where α^A and α^B is the dynamic dipole polarizability at imaginary frequency ω of the atom A and B respectively. Higher-order coefficients then correspond to the polarizability of the quadrupole, octupole and so on. These parameters define how well the atoms can polarise. For freestanding atoms, the C_6 can be easily calculated; however, in molecules, the polarizability of atoms is quenched by the formation of

bonds or electron transfer, and the calculation becomes more complex. Additionally, the three-body contribution needs to be considered as they typically account for 5–15% of the total E_{disp} . Contribution of the dispersion effect to the attractive force is weak except for some nanostructured systems where total vdW interaction between two molecules becomes more significant [31].

2.1.3 Hydrogen bonds

Hydrogen bonding is the most frequently observed non-covalent bonding [32]. It can be found in various disciplines from biology (DNA base pairs bonding [33]) to crystallography [34]. Hydrogen bonds are often involved in self-assembly due to their reversibility, selectivity, directionality and relative strength. However, the exact nature of the hydrogen bond is still a matter of scientific discussion. According to the International Union of Pure and Applied Chemistry (IUPAC) recommendation from 2011, the hydrogen bond $X-H\cdots Y$ is defined as: "...an attractive interaction between a hydrogen atom (H) from a molecule or a molecular fragment X-H in which X is more electronegative than H, and an atom or a group of atoms Y in the same or a different molecule, in which there is evidence of bond formation." [35].

The electronegativity of atoms bonding to the H atom determines the strength of the bond and can be classified in three categories: (I) strong (0.5 – 1 eV) typically involves a charged hydrogen bonding acceptor, e.g., $\text{COOH}\cdots\text{COO}^-$; (II) weak, with energy slightly above van der Waals interactions (< 0.2 eV), e.g., $\text{CH}\cdots\text{O}$ and (III) moderate, with the strength in between. Hydrogen bond strength also has a significant non-linear distance dependence. Theoretically calculated bond energies and corresponding distances (taken from H nucleus to Y nucleus) for various dimers are shown in Fig. 2.1(a). Their specific calculation method results in the bonding energy/distance relation that could be fitted by a term $1/R^{3.8}$. Some of the data points in the plot that correspond to large atoms (gold, bromine), differ from the fit due to the increased nucleus size (points in the middle of the plot). This result shows that the strongest hydrogen bonds are formed at distances around 1.5 Å and bonding dissipates at distances larger than 3 Å.

The hydrogen bond on surfaces is most frequently utilised with carboxyl group terminated molecules such as carboxylic acids. In this case the hydrogen bond forms between the H atom in the hydroxyl group of one molecule and the oxygen atom in the carboxyl group of the other molecule. Typically, two molecules with carboxyl groups form a dimer, where molecules interact with each other and form two equivalent bonds as shown in Fig. 2.1(c). One of many examples of widely utilised hydrogen bonds in supramolecular self-assembly is a trimesic acid (TMA, benzene tricarboxylic acid) network [38]. Molecules of TMA can form a robust 2D porous self-assembled structure as shown in Fig. 2.1(b), that can be used as a molecular template for more complex functional systems [37].

A unique type of hydrogen bonding is a $X-H\rightarrow\pi$ hydrogen-bond-like interaction. It involves a weak hydrogen bond and a type of a π interaction [39]. This interaction

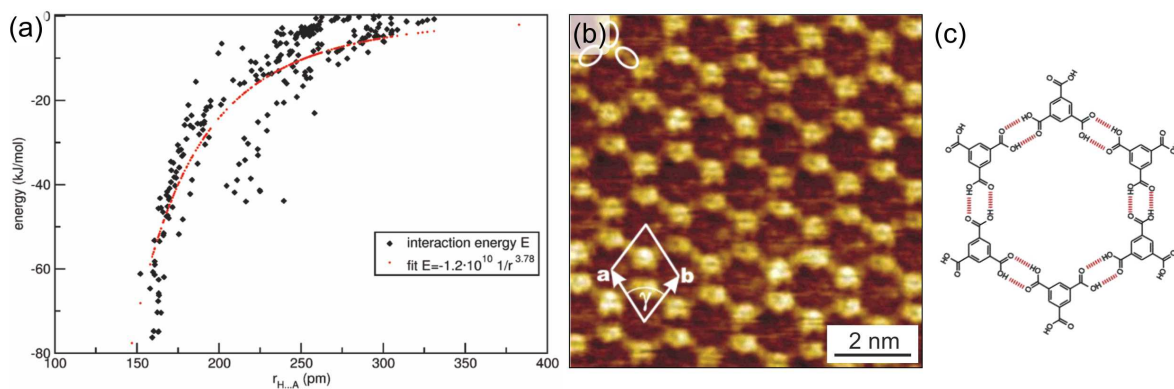


Fig. 2.1: (a) Interaction energies of hydrogen bonds dependent on a distance between H and Y atomic nuclei. (b) An STM image of a monolayer of TMA physisorbed on the interface between an organic solution of TMA in heptanoic acid and the HOPG. (c) A model of the TMA monolayer where each molecule is bound to the three adjacent molecules via hydrogen bonding of the carboxyl end groups. Dashed lines indicate the hydrogen bonds between the TMA molecules. Adapted from [36] for (a) and [37] for (b), (c).

can be classified somewhere in between conventional hydrogen bonds and weaker interactions dominated by the dispersion (vdW forces). The $\text{XH} - \pi$ bond is formed by π -electrons of an aromatic molecule that act as a proton acceptor in the hydrogen bond. The importance of this force in chemistry can be found in the conformation of different molecules and proteins, the selectivity of some organic reactions and more [40]. On surfaces, this interaction can influence the stability of one-dimensional patterns, when multiple $\text{CH} - \pi$ bonds are involved.

2.1.4 Halogen bonds

Another type of a non-covalent bond is the halogen bond formed between the electrophilic region of halogen atom (σ -hole) in a molecule and a nucleophilic region in another or the same molecule. This bond can be denoted as $\text{R} - \text{X} \rightarrow \text{Y}$, where X is the halogen atom covalently bonded to the R group and having the electrophilic region, and Y is a donor. The Y species can be an anion or a neutral group possessing at least one nucleophilic region, e.g., a lone-pair-possessing atom or π -system. However, the exact nature of the halogen bond cannot be fully explained only by the σ -hole model. The secondary region of a negative potential forms around the σ -hole and can interact with the electrophilic species. Calculation of the anisotropic electron density distribution around halogen atom is shown in Fig. 2.2(a).

Theoretical studies determining the strength and nature of the bonding involve charge-transfer, electrostatic, dispersion, polarisation interactions and the Pauli exclusion principle (see review: [41]). The strength of the halogen bond depends on the polarizability of the halogen donor atom. Generally, the atoms follow the order $\text{F} < \text{Cl} < \text{Br} < \text{I}$, where F is the smallest and least polarisable halogen atom. Fluorine halogen bonds were a matter of scientific discussions, and it was suggested that F could

act as a donor only when attached to a particularly strong acceptor group [42].

In self-assembly, the halogen bond can be viewed as an alternative to the hydrogen bond because it has similar properties. However, halogen bonds have higher directionality that can drive self-assembly process. This directionality arises as a consequence of the σ -hole localisation, i.e. opposite to the covalent bond(s) that the halogen atom is bonded to. In this respect, the halogen functionalised molecule is routinely used as a tool to control and direct self-assembly. Numerous networks were synthesised on metal surfaces and graphite. One interesting example is a polymorphic porous network of dibromo-*p*-terphenyl (DBTP) deposited on silver [43]. BBTP molecules form triangular or square motifs where the sides are terphenyl moieties, and the vertices are three or four halogen-bonded bromine atoms. In this system bromine atoms attractively interact with each other; they form a halogen bond where halogen atoms are both donors and acceptors. Porous network was also synthesized by using dibromo-*p*-quaterphenyl (DBQP) on Au(111) [44]. In this case, a square DBQP network is stabilised by four $\text{Br}\cdots\text{Br}$ halogen bonds and four $\text{H}\cdots\text{Br}$ hydrogen bonds.

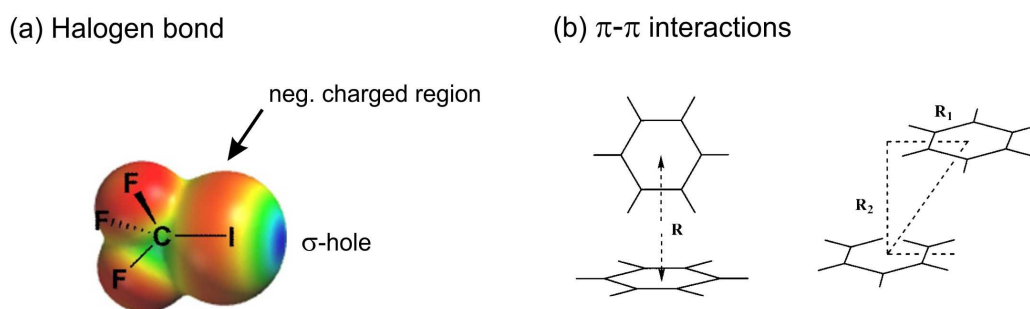


Fig. 2.2: (a) Anisotropy in electron density around the halogen atom in the CF_3I molecule. (b) Possible arrangement of two phenyl rings with an attractive π - π interaction. Adapted from [45] and [46].

2.1.5 Intermolecular π - π interaction

The interaction between two aromatic molecules can generate sufficient force to influence self-assembly between π -rich molecules. The electrostatic model can explain the origin of this interaction. However, a detailed understanding of the nature and properties of π - π is not available yet. A simple model of the charge distribution was presented by Hunter and Sanders, which accounts for many of the experimental observations [47]. The model considers the aromatic molecule as a set of three charges, one positive (+1) sandwiched between two negative ones (-0.5). In this configuration, direct stacking is disfavoured as two negative charges directly next to each other are repulsed. Optimal π - π interaction of two molecules will then favour *T* shaped structure or displaced stacking structure where the π -rings are shifted towards each other [46]. An example of the arrangement of two benzene dimers is shown in Fig. 2.2(b). Interaction between aromatic molecules plays an important role in some chemical reactions and protein recognition [48].

In self-assembled systems, the intermolecular π - π interaction drives the formation of stacked linear structures. Molecular columns parallel to the surface and perpendicular molecular filaments were observed. One example are parallel porphyrin wires assembled on the surface of KBr as shown in Fig. 2.3(c). The intermolecular distance of porphyrin can only be explained by the π - π stacking of porphyrin molecules [49].

2.1.6 Electrostatic interaction

Molecules exhibiting permanent charges, dipoles or quadrupoles, will generate electrostatic fields that will interact and can affect self-assembly process. Electrostatic interaction can be divided into multiple groups. The most straight forward one, is the ionic bond that form between two molecules or atoms of different types, one with positive (cation) and one with negative (anion) charge. A special type of molecules that appear neutral, but have both positive and negative charges at a separate positions are called zwitterions. An example of such a molecule is an amino acid *L*-methionine. Methionine can self-assemble on Ag (1 1 1) in molecular chains and form unique nanogratings of various periodicity [50]. A nanograting with periodicity 275 Å is shown in Fig. 2.3(b).

In the case of molecules with a permanent dipole, the interaction is generally weak and depends on the mutual orientation of the molecules. In the cases when dipoles can be approximated by the classical dipole, interaction strength scale with the distance approx. $1/r^3$. Several self-assembled structures have been reported to be stabilised by dipolar interactions. One example is the hexaaza-triphenylene-hexacarbonitrile (HATCN) molecule on the surface of Au (1 1 1) [51]. The report has shown that HATCN molecules form linear and hexagonal porous structures, shown in Fig. 2.3(a), stabilised by three $\text{CN}\cdots\text{CN}$ dipolar interactions per molecule.

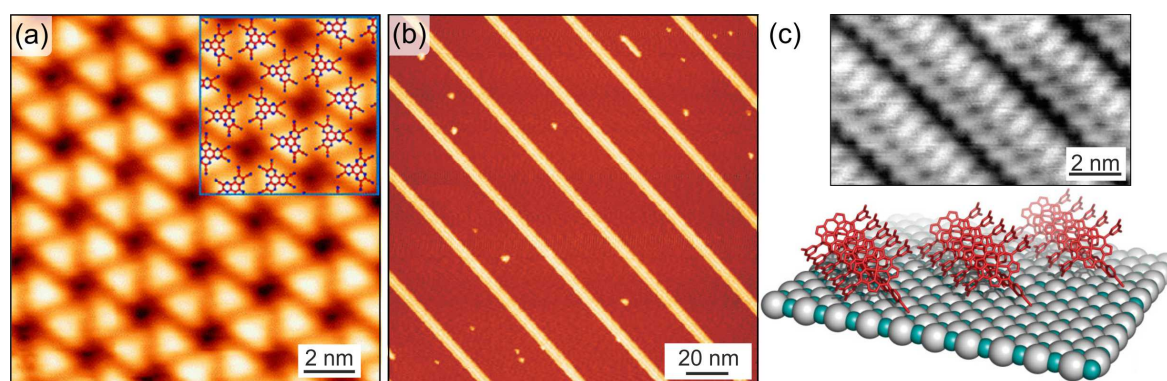


Fig. 2.3: (a) An STM image of the hexagonal porous network formed by HATCN molecules on Au (1 1 1) with molecular models partly superimposed over the image. (b) 1D Self-assembly of zwitterion molecule - *L*-methionine that forms nanogratings with periodicity 275 Å. (c) A nc-AFM image of self-assembled porphyrin monolayers as wires parallel to the surface of KBr. The intermolecular distance of the molecules was explained by the π - π stacking of the molecules as visualized by 3D model below. Adapted from [51], [50] and [49].

A unique charge transfer can also take place between strong electron donor and acceptor molecules. In such bicomponent systems, charge transfer can modify the intermolecular interactions [52]. For example, porphyrin-fullerene self-assembled architectures can be designed by controlling the peripheral functionalisation of porphyrin by the amino groups [53]. The resulting self-assembly forms different phases of striped or porous structures.

2.2 Molecule-surface interactions

The second most influential force in self-assembly is the interaction between molecules and surface. Adsorption of molecules is most commonly classified as either weaker physisorption or stronger chemisorption. The term chemisorption usually implies the presence of a bond between the surface and adsorbed molecule. In the case of physisorption, van der Waals forces are often claimed to be the only interaction causing the phenomena. However, here there is some confusion in literature because today, the van der Waals forces are not clearly defined and encompass a variety of interactions as mentioned above. To generalise, there are specific properties that differentiate the physisorption and chemisorption; however, there is no sharp distinction between them. For example, hydrogen bonding can be considered as an intermediate case because it involves various interactions and can have different strengths.

2.2.1 Metal-organic interface

The most common surfaces used for examining self-assembly of organic molecules are noble metals and graphite (HOPG; that is more often used for liquid/solid interface). Their advantage lies in the low reactivity that allows molecules to move and assemble, and their high conductivity allows a straightforward access by surface science techniques (e.g., STM, XPS). In addition to noble metals and HOPG a variety of surfaces have been tested such as oxides (e.g. In_2O_3 [54]) or even alkaline earth metals [55], however the stronger binding to the surface on these materials usually dominates the self-assembly.

Further focus in this section is given to the metal-organic interface (M/O). The electronic structure at the interface of the molecular layer and metal can involve multiple effects such as the energy level alignment, band bending, charge transfer and the formation of new interface states. Current models describe formation of a dipole layer at the interface of most M/O systems. Various theories are used to describe dipole formation in differently interacting systems.

In the category of chemisorbed molecules, charge can be transferred from the metal to the molecule, e.g. TCNQ/Au or vice-versa in case of methylphenyl-biphenyl-diamine (TDP) on Au. This charge redistribution results in the formation of an interfacial dipole [56]. Similarly, the dipole can form due to the strong bonding between the molecule and metal. Additionally, the substrate can also affect a charge transfer between dif-

ferent molecules in donor-acceptor systems. For example, a mixture of electron acceptor tetracyanonaphtho-quinodimethane (TNAP) and electron donor tetrathiafulvalene (TTF) molecules adsorbed on Au(111) forms ordered arrays of alternating rows [57]. The lowest unoccupied molecular orbital (LUMO) of the TNAP molecule when mixed with TTF, is shifted below the Fermi level of the substrate, which causes significant charge transfer compared to the almost neutral pure TNAP on Au. It was suggested that the stabilisation of charge accumulation is due to the effective screening of the underlying metal substrate [58].

In the case of physisorbed molecules, two phenomena are most prominent, the pillow effect and image charge effect. The image charge effect can be described as the formation of a weak dipole in the molecule due to quantum oscillations, followed by an image dipole formed on the metal surface. The interaction of these dipoles gives rise to van der Waals force between the molecule and metal.

The origin of the pillow effect lies in another quantum mechanical effect, the Pauli exclusion principle. When two electron systems of a molecule and metal surface start to overlap, the exclusion principle dictates that the electrons cannot be in the same state. Therefore, some of the electrons in the metal are displaced (or pushed back into the bulk) and a “*cushion*” or “*pillow*” is formed under the molecule. Rearrangement of the electrons at the surface reduces the surface dipole resulting in the reduction of the work function [59].

The least reactive metals, that are more suitable for self-assembly are usually $\text{Cu} > \text{Ag} > \text{Au}$ (where Cu is the most reactive). Early DFT studies describe the nobleness of a metal to be dependent on filling of the anti-bonding adsorbate-metal d states, which increases to the right of the transition metal series and is full for the Cu, Ag and Au. The second parameter is connected to the size of the d -band, making Au(5d) the most noble metal [60]. This behaviour is usually confirmed by experimental observations, for example the diindenoperylene (DIP) adsorption on different surfaces, Cu(111), Ag(111), and Au(111) [61]. Here the bonding distances, that indicate strength or character of the bond, were determined by X-ray standing wave (XSW) measurements. Measured distances were 2.51, 3.01, and 3.10 Å, for Cu, Ag and Au respectively. Similar results were also obtained for CuPc [62].

Often the molecules on noble metal surfaces have a different binding character or undergo some chemical reactions (e.g. deprotonation or debromination) at different temperatures. These variations will have a direct effect on self-assembly. For example, cyano-functionalised triarylamine molecules have different intermolecular interactions: H-bonding on Ag, dipolar coupling or hydrogen bonding on Au, and metal coordination on Cu [63]. The bonding differences result in distinct structures observed on these metals as shown in Fig. 2.4: (a) on Ag(111) a hexagonally close-packed phase; (b) on Au(111) two well-ordered phases, hexagonal and closed packed structures; (c) on Cu(111) only small patches of ordered molecules together with a disordered phase.

Interestingly, adsorption of a molecule can be modified by the presence of other molecules in its vicinity. Tetraphenyladamantane (TPD) formed around C_{60} was able

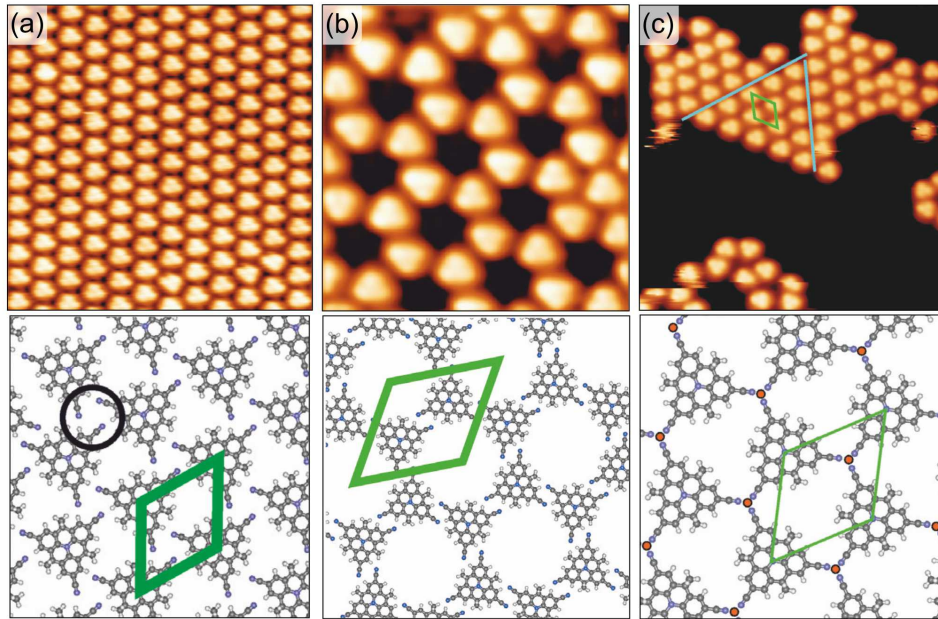


Fig. 2.4: STM images and molecular model of cyano-functionalized triarylamine molecules on (a) Ag(111); (b) Au(111) and (c) Cu(111). Adapted from [63].

to reorient and lift the C_{60} up from the surface. The lifting force was caused by the interaction between opposite charges induced on both molecules. Essentially, the TPD acts as a spacer layer capable of partially overcoming the direct C_{60} surface bonding and restoring freestanding electronic and structural properties of the C_{60} .

2.2.2 Diffusion on surfaces

In order to properly assemble, molecules have to be able to move on surfaces. This ability is quantified by the activation energy (or diffusion barrier) of an adsorbate (molecules, atoms), which characterise its ability to move in direction parallel to a surface. At any given surface, adsorption (or binding) energy has lateral variations with local minima, which are the preferred adsorption site for the molecule. To clarify, the activation energy differs from the adsorption energy; it corresponds to the energy needed for the adsorbate to move from one adsorption site to another. When the surface is complex, energy barriers can have anisotropic distribution resulting in the preferred diffusion direction (usually along principal crystal axes). The energy maximum between adjacent sites is the diffusion barrier E_D . Diffusion barriers are usually significantly lower than the energy needed for desorption.

The movement of the molecule on the surface can be realised predominantly due to thermal motion (mediated by substrate phonons) or in some special cases by quantum mechanical tunnelling. In principle, two situations can be considered:

(I) $k_B T \sim E_D$: When the diffusion energy is comparable with kT , an adsorbate moves freely on the surface and can be considered as moving in the 2D gas phase. Additionally, when the thermal energy approaches the adsorption energy (or exceeds it), the thermal desorption will become a prominent factor. Thermal equilibrium will

be established between the solid phase (self-assembled structure) 2D gas phase on the surface and the 3D gas phase.

(II) $k_B T \ll E_D$: In the second case, when the thermal energy is low, the adsorbate is confined to an adsorption site and appears immobile. If temperature reaches a specific point, surface migration starts, driven by the continuous energy exchange between the adsorbate and substrate. Movement results in random jumps from one binding energy minimum to another (i.e. the hopping mechanism).

Diffusion of large molecular species is more complex than in the case of simple molecules (e.g. CO) or atoms. Additional degrees of freedom exist because molecules can span over multiple adsorption positions, rotate, reorient or deform during the diffusion [64]. In most experimental cases, when the diffusion energy is lower than the desorption energy, short sample annealing is sufficient to allow the formation of self-assembled layers. For more comprehensive review see Ref. [65].

Surfaces can also rearrange to accommodate different molecular species. This was observed for single molecules of C_{60} [66] on Pd(110). After a thermal activation, the adsorption of the fullerene was accommodated by a vacancy that formed by 8 Pd atoms, that moved from two top substrate layers. The vacancy was observed as changes in the molecule-adsorption height. The substrate modifications can also be directly observed by STM. Molecules can be manipulated aside at low temperatures and substrate previously hidden under the molecule is imaged before it can reconstruct. For example, functionalised decacyclene molecules anchored to Cu(110) forced the removal of the Cu atoms, forming a characteristic trench base between two neighbouring close-packed rows [67].

2.3 Metal-organic systems

The deposition of reactive metals on a non-reactive substrate can direct the formation of new assemblies. The bonding between organic molecules and metals is typically stronger than the substrate-molecule interaction. Two bonding mechanisms are usually utilized in growth of metal-organic networks, electrostatic (ionic) bond and metal-coordination (dative) bond. Metal coordination networks sometimes incorporate atoms that are provided by the substrate itself.

In the case of electrostatic interactions, the simplest binding scheme is the interaction between molecules carrying charged end groups and atoms with the ability to be ionised. One example is self-assembly of aromatic carboxylic acids and caesium adatoms on a Cu(100) surface [68]. Deposited atoms can also acquire the charge through the interaction with the substrate. This is the case for perylene tetracarboxylic diimide (PTCDI), an organic semiconductor, that forms a metal-organic network with Ni on Au(111). The Ni atom acquires a partial negative charge and the Ni-PTCDI interaction is entirely electrostatic [69].

Coordination networks on surfaces are named after their 3D analogue in solution chemistry. Coordination bonding is a type of covalent bonding formed by two atoms

sharing a pair of electrons, where both electrons are provided by one of the atoms. This electron pair is then attracted to both atomic nuclei and holds the atoms together. Coordination compounds can form a large variety of regular porous structures with tailor made size and chemical properties, which made them an exciting research topic. Structures at surfaces can offer similar adaptability. For example, the length of an organic ligand can determine the size of the pores in a 2D network. 2D metal-organic coordination networks (MOCNs) are sometimes also referred to as metal-organic frameworks (MOFs), surface-confined metal-organic networks (SMONs) or metal-organic materials (MOMs). One example of MOCN is the honeycomb network assembled from simple diatopic dicyanitrile-polyphenyl molecular linkers with various lengths (number of phenyls incorporated in the molecule) and Co atoms on Ag(111) [70]. Coordination networks on surfaces have been synthesised by a variety of metal adatoms (Co, Cu, Fe, Cr, Mn, Ni) and molecular binding groups (hydroxyls, carboxyls, cyano or pyridine groups) [20, 71]. It is also possible to create networks incorporating multiple metal atoms or atomic clusters (poly-nuclear complexes). For example, terpyridine molecules bonded to tri-iron and creating an 1D coordination complex on Ag(111). Poly-nuclear complexes are attractive due to electronic and magnetic interactions occurring between the metal atoms and also their utilization in novel catalytic processes [72].

The surface is not only a tool to create structure with a planar geometry. In solution, a coordination bonding is usually formed by metal cations with known oxidation state (positive or zero). However, metallic surfaces provide a reservoir of electrons for coordination atoms allowing them to donate (or possibly accept) charge without becoming charged themselves [73]. Therefore, the nature of the bond can differ from the well understood liquid phase counterpart. Often, any metal-organic network is automatically named as a coordination network implying the formation of coordination bonds. One example of mislabeling of the bonding mechanism is the study of bonding between the phenazine and Cu adatoms on Cu(111). Typically, the bonding between the cyano group N and metal atom is described as a coordination bond where N provides a pair of electrons. However, an in-depth study by AFM and DFT simulations revealed bonding to Cu adatoms can be explained by a complex interplay between Pauli repulsion and covalent bonding which involves frontier molecular π -like orbitals and *sp*-like metallic states [74].

In summary, the interaction between metals and molecules on metallic substrates is not fully understood. The problem is that the exact charge of the interacting species is elusive because the metal substrate effectively screens the charged adsorbates. A better understanding of coordination chemistry at surfaces can help to transfer the knowledge from the solution-phase and fast-track applications of metal-organic networks.

2.4 Self-assembly on graphite and graphene

The use of highly oriented pyrolytic graphite (HOPG) as a substrate has multiple advantages. First, it has a very flat surface that can be easily prepared for an experiment,

Tab. 2.1: Overview of the strength of different interactions and processes, with associated energy. Typical distances noted when available. Adapted from multiple sources [19, 75].

Interaction	Strength [eV]	Distance	Character
van der Waals	0.01-0.1	< 10 Å	Selective, non-directional
Hydrogen bonding	0.05-1	1.5-3.5 Å	Directional
Electrostatic ionic	0.05-3	Long range	Nonselective
Ion-dipole (Metal - ligand)	0.5-2	1.5-2.5 Å	Selective, directional
CH - π	0.05-0.2		directional
X - bond	0.1-1.5		directional
π - π	0.01-0.5		partially directional
Dipole - dipole	0.05-0.5		directional
Cation - π	0.05-0.8		directional
Image charge	0.01-0.1		-
Covalent bond	1-4		directional
Metal complex	0.5-3		-
Diffusion barrier	0.05-3	2.5-4 Å	-

e.g. by cleaving the topmost layer with sticky tape, due to the weak interlayer bonding. Further, the graphite is chemically inert, and most of the molecule-substrate interactions are mediated through π - π interactions. In this respect, the majority of observed molecular assemblies on HOPG are formed by aromatic molecules (e.g. [76, 77]).

Graphene can be viewed as a single layer of HOPG and offers similar advantages. However, molecular self-assembly on graphene can be influenced by slight corrugations that are usually present on graphene grown on metals or transferred on other substrates. These structural and electronic variations can act as preferential adsorption sites. In general, self-assembly on graphene is structurally similar to the one observed on graphite [78].

Graphene is exceptionally thin and can act as an interlayer between the molecules and the metal substrate, on the one hand decoupling the molecules from the metal and on the other hand allowing partial transmission of other interactions. One example is the mediation of a superexchange interaction in phthalocyanines (Pc). It has been shown that a graphene layer can preserve the magnetic state of FePc and CuPc molecules [79]. Unmodified Pcs were then able to participate in superexchange interaction between the Co layer underneath the graphene, which resulted in antiferromagnetic and ferromagnetic couplings for FePc and CuPc respectively.

From the opposite view, the deposition of molecules on graphene can completely change graphene physical and electronic properties. Effectively this could provide controllable molecular doping of graphene by charge transfer between the graphene and

molecular orbitals [80]. Graphene also attracted considerable interest in the optoelectronics due to its low light absorption of $\sim 2.3\%$ from infrared-to-visible light [81, 82]. The high transparency, combined with graphenes high conductivity, makes it a promising candidate for a transparent electrode in touch screens [83], organic light-emitting diodes (OLEDs) [84] or solar cells [85]. Here the graphene interaction with organic molecules is of great interest for the study of charge transfer to and from the graphene electrode into the organic film.

Some of the self-assemblies on graphene could be sensitive to the interaction between the graphene and its substrate, especially for the weakly interacting molecules. On moiré-forming Gr/metal substrates, such as graphene on Ru, the molecular assembly is governed by the surface electronic corrugations. Due to the lattice mismatch between graphene and Ru surface, topographic and electronic modulation is emerging as a moiré pattern as shown in Fig 2.5(a). Real-space corrugation was calculated to be approx. 1.3 \AA [86]. The separation between the graphene and the metal also strongly varies across the unit cell with a minimum C–Ru distance of 2.1 \AA up to 3.6 \AA , identified with LEED [87]. The resulting graphene layer is highly doped (n-type), losing its semi-metallic character and its characteristic linear dispersion relation via the electronic coupling of graphene π -states with metal d-states near the Fermi energy [88].

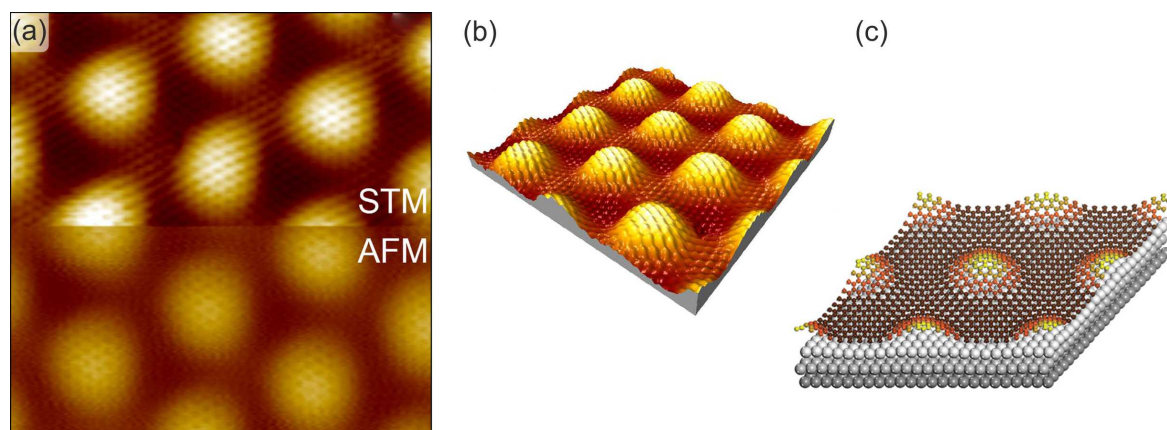


Fig. 2.5: Graphene grown on Ru(0001): (a) $9 \times 9 \text{ nm}^2$ STM and AFM image with visible moiré pattern. (b) 3D representation of the STM image detail of graphene corrugation. Adapted from [86]. (c) 3D structure model of the unit cell with exaggerated vertical displacement of graphene. Adapted from [87].

The effect of graphene corrugations on Ru can be observed, for example, for iron phthalocyanine (FePc) assembly shown in Fig. 2.6(b). FePc forms regular Kagome lattices that replicate the lattice of the underlying moiré pattern [89]. It is assumed that lateral dipoles drive the molecular adsorption and assembly on Gr/Ru(0001) [90]. Dipoles originate from the inhomogeneous distribution of charge due to the strain from the corrugation of graphene on a Ru surface. For weakly coupled substrates such as graphene on Ir(111), flat surface topography and electronic structure of graphene are mostly preserved. This system can, therefore, act as an excellent model surface for studying molecule–molecule and molecule–graphene interactions. Comparison between

graphene grown on Ir and Ru is shown in the Fig. 2.6. Cobalt phthalocyanine (CoPc) on Graphene/Ir (1 1 1) forms tightly packed self-assembly at room temperature [91], contrary to the Kagome lattice of FePc on Ru.

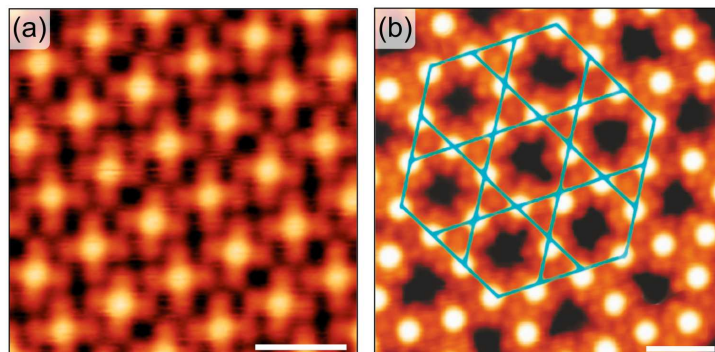


Fig. 2.6: (a) STM image of CoPc closed packed self assembly on Graphene/Ir (1 1 1). Adapted from [92]. (b) STM image of FePc on Graphene/Ru (0 0 0 1) surface. Kagome lattice is marked with blue lines. Adapted from [89]. Scale bars are 3 nm.

Phthalocyanines are not the only molecular structures that can be assembled on the graphene layer (see review [93] or [94]). However, they are important from the point of view of their applications. Metal phthalocyanines (MPc) are a family of highly stable molecules with a single metal ion in the central position surrounded by an organic macrocycle (CoPc is illustrated in the Fig. 2.7(c)). MPcs are used, for example, as semiconductors in the organic-electronic devices (review [95]). They combine the properties of the transition metals and the π -bonding present on the benzene rings and have a good match of electronic structure with the transparent conductive electrodes. Depending on the central metal ion, MPc molecules have various spin configurations, so they can also be viewed as tunable single-molecule magnets [96, 97]. Their electronic structure and interactions with the substrate can be further tuned with modifications to the macrocycle by substituting hydrogen atoms (e.g. with fluorine [98, 99]). This makes MPc versatile molecules relevant in many potential applications. Phthalocyanines can also be synthesised directly on the surfaces. FePc was recently prepared in two steps, were initially the precursor molecules and Fe atoms form coordination complexes on a clean Au (1 1 1) surface. In the second step, the molecules undergo cyclic tetramerisation during thermal annealing and forming individual FePc molecules [100].

For potential organic-electronics applications, it is crucial to see if self-assembly also holds for the graphene transferred to other relevant substrates. Cobalt phthalocyanine assembly was studied on chemical vapour deposited (CVD) graphene transferred onto silicon dioxide (SiO_2) and hexagonal boron nitride (hBN) [101]. CoPc molecules formed a tight-packed square lattice on both substrates. However, on graphene on SiO_2 shown in Fig. 2.7(b), domain size is limited by surface corrugations. Smaller disorders of the molecular arrangement were also observed inside of molecular domains. Self-assembly of CoPc on graphene transferred on hBN, shown in Fig. 2.7(c), is perfectly regular with the large scale order comparable to graphene on metals. The molecular domain size

is only limited by the size of the terraces of the hBN. Observations of the large-scale order on decoupled graphene hold a promise for effective functionalisation of graphene that can be utilised in future applications.

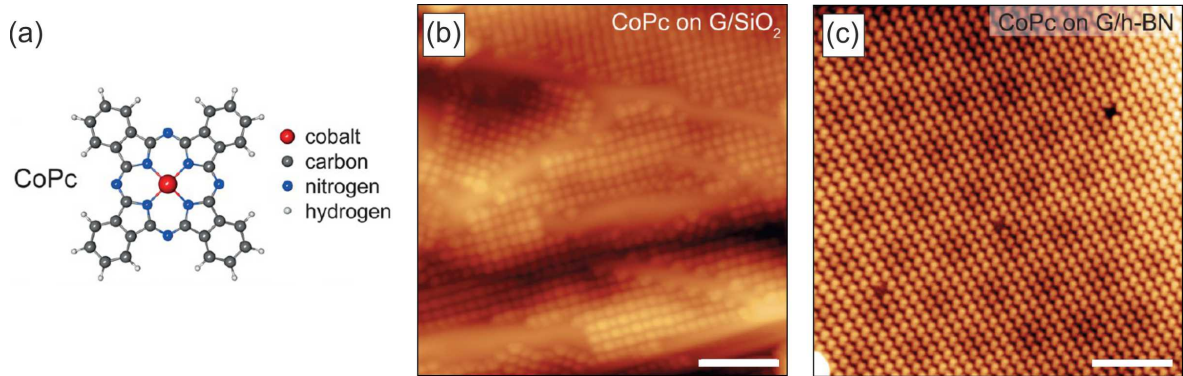


Fig. 2.7: (a) Structure of cobalt phthalocyanine molecule. (b) Self assembled CoPc molecular layer on graphene transferred on a SiO_2 substrate. Molecular assembly is limited by the surface corrugations. (c) Large scale molecular ordering of CoPc on graphene transferred on a hBN substrate. Adapted from [101].

2.4.1 Metal-organic networks on graphene

There is a very limited number of experimentally realised metal-organic networks or any on-surface synthesised materials on weakly interacting, noncatalytic substrates. In fact, there are only a handful of studies demonstrating the controlled synthesis of high-quality 2D structures on graphene, despite the numerous examples of molecular self-assembly on graphene [93]. The advantage of using the graphene substrate, as mentioned above, is the graphene non-interacting nature. For example, graphene has been suggested as a possible substrate for realising 2D organic topological insulators [102]. Additionally, theoretical studies have shown the possibility of forming graphene-molecular bilayer where graphene and molecules would mutually influence each other electronic and magnetic properties to the point of forming a new two-dimensional (2D) heterobilayered materials [103].

One of the metal-organic coordinated structures on graphene was prepared from para-hexaphenyl-dicarbonitrile (NC-Ph₆-CN) molecules and Cu atoms on graphene epitaxially grown on Ir (111) [104]. Here, the metal-ligand bonding formed at room temperature between the cyano groups and deposited Cu atoms. Various structures formed on graphene depending on the metal-molecule ratio including a basketweave-like pattern, a hexagonal porous network and 1D molecular chains as shown in Fig. 2.8(a), (b) and (e) respectively. These structures utilised either three-fold or two-fold metal coordination.

Similarly, molecules functionalised with cyano groups, the dicyanobiphenyl (DCBP) and dicyanoanthracene (DCA), were used with cobalt metal atoms to synthesise high-quality 2D honeycomb metal-organic networks on graphene [105]. Molecules were sequentially deposited with cobalt atoms and subsequently annealed (to approx. 90 °C).

Experiment resulted in honeycomb networks of DCBP_3Co_2 and DCA_3Co_2 , shown in Fig. 2.8(c) and (d). STS and DFT further showed that DCBP_3Co_2 system has only a weak coupling, while DCA_3Co_2 network shows significant in-plane hybridisation. As a result, the DCA_3Co_2 metal-coordinated structure has new 2D electronic states.

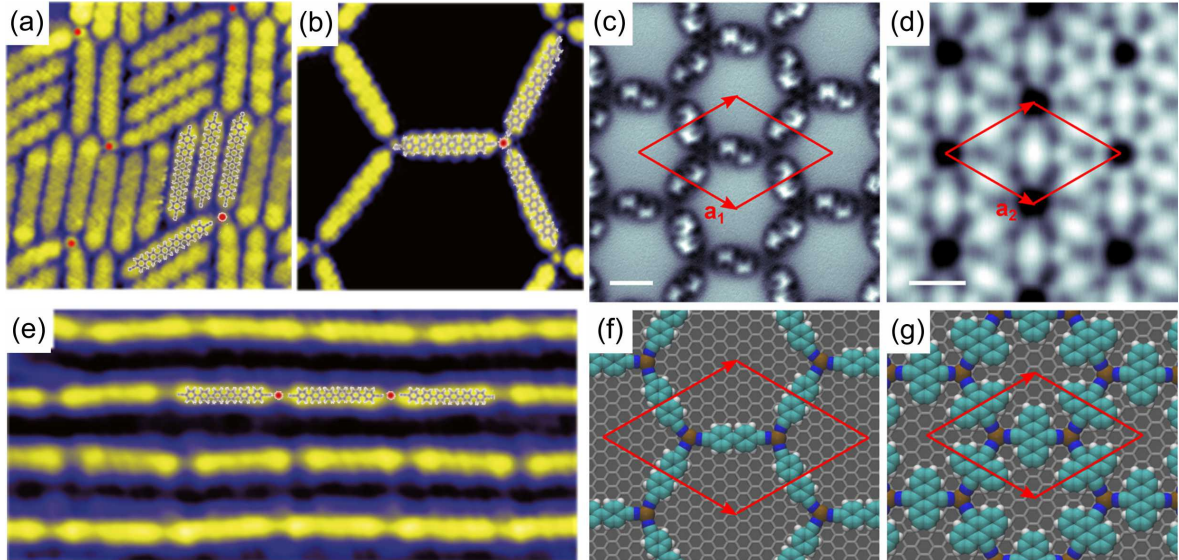


Fig. 2.8: The STM images of self-assembled molecular structures on Gr/Ir(111). The NC-Ph6-CN molecules and co-deposited Cu atoms at the different molecule-atom ratios formed: (a) the basketweave-like pattern; (b) hexagonal porous network and (e) molecular chains. Molecular models are overlaid with red dots representing the Cu atoms. (c) The nc-AFM image of a honeycomb DCBP_3Co_2 and (d) STM topography image of DCA_3Co_2 metal-organic structures. The scale bars are 1 nm. Corresponding DFT simulated images are shown below in (f) and (g). Adapted from [104] and [105].

The inert nature of the graphene substrate was also exploited for the synthesis of organo-metallic sandwich molecular nanowires [106]. Nanowires were formed by ionic metal-organic bonding between europium (Eu) atoms and cyclooctatetraene molecule (EuCot structure). Similarly to the above mention examples, the authors used single-crystalline film of graphene grown on Ir(111). Molecules were observed to stand upright, compared to their typical flat adsorption suggesting strong internal bonding in EuCot. Synthesis on graphene yields an extended domain of closed packed nanowires, compared to the gas-phase synthesis, that is limited to approx. 30 metal atoms in a chain for EuCot [107]. Additionally, the authors successfully tested the synthesis of EuCot on an h-BN monolayer. However, the typical size of a nanowire crystallite was around 10-20 nm compared to 50-100 nm for graphene. Use of the graphene also allowed to examine the magnetic and electronic properties EuCot nanowires utilizing X-ray magnetic circular dichroism (XMCD), STM and STS and discover that EuCot is a ferromagnetic insulator [108].

2.5 Conclusion

Molecular ordering on surfaces is controlled by a delicate balance between intermolecular forces and molecule/substrate interactions. In this chapter, various non-covalent bonding mechanisms and interactions between molecules have been explored, most importantly, hydrogen, halogen bonds, and π - π interactions. A weak intermolecular interaction drives a system to a closed packed molecular layer, and stronger interactions generate more directional self-assembly and their interplay results in a myriad of observed structures on surfaces.

A further focus in this chapter has been given to the metal-organic interface between the substrate and molecules, and diffusion of molecules on surfaces. Additionally, substrate atoms can be pulled out from the surface, or a new element can be deposited to form 2D metal-organic networks. The last section introduced self-assembly and metal-organic structures on graphene, which will be explored in the experimental chapter 6 of this work.

3. EXPERIMENTAL SETUP

Majority of experiments in this work were performed in a multi-instrumental UHV system, henceforth referred to as UHV cluster. This system is available for use in a cleanrooms of the CEITEC Nano Research facility in Brno [109]. UHV cluster currently incorporates ten UHV modules for sample preparation and in-situ analysis by several complementary methods. Individual chambers are connected by a linear transfer system that allows for fast sample transfer while maintaining the UHV conditions. In this chapter, some of the experimental techniques and methodology will be described.

3.1 UHV system

The complex UHV cluster system is schematically drawn in the Fig. 3.1 (top view). Each module or UHV chamber is separated from the central linear transfer chamber by a gate valve and can be vented separately. In the case of the LEEM and STM chambers, special damping elements were used to prevent the transfer of mechanical vibration from other systems. Additionally, the whole UHV cluster is installed on a concrete mono-block and thus isolated from vibrations of the building. Ultra-high vacuum conditions ($\sim 1 \times 10^{-10}$ mbar) are maintained in majority of the sub-systems. Each chamber is equipped with turbomolecular pumps (mostly Pfeiffer HiPace) with its size depending on the chamber volume. With exception of the load-lock and preparation chamber, all chambers are also equipped with an ion getter pump combined with a titanium sublimation pump.

3.1.1 Sample transfer

The central part of the UHV cluster is a linear transfer chamber that enables fast and reasonably easy sample transfer between the chambers. Samples are moved in the magnetically coupled trolley, capable to store 5 sample holder carriers. Each carrier can hold up to 3 individual sample holders. During the trolley movement, the pressure slowly increases up to 8×10^{-8} mbar and quickly restores to base level of 4×10^{-10} mbar when the movement ceases. Transfer between the chambers takes approx. 2 – 3 min. The main load-lock allows to insert whole sample carriers into the trolley and additionally individual sample can be loaded trough load-lock chambers in LEEM or PLD systems.

UHV cluster - top view

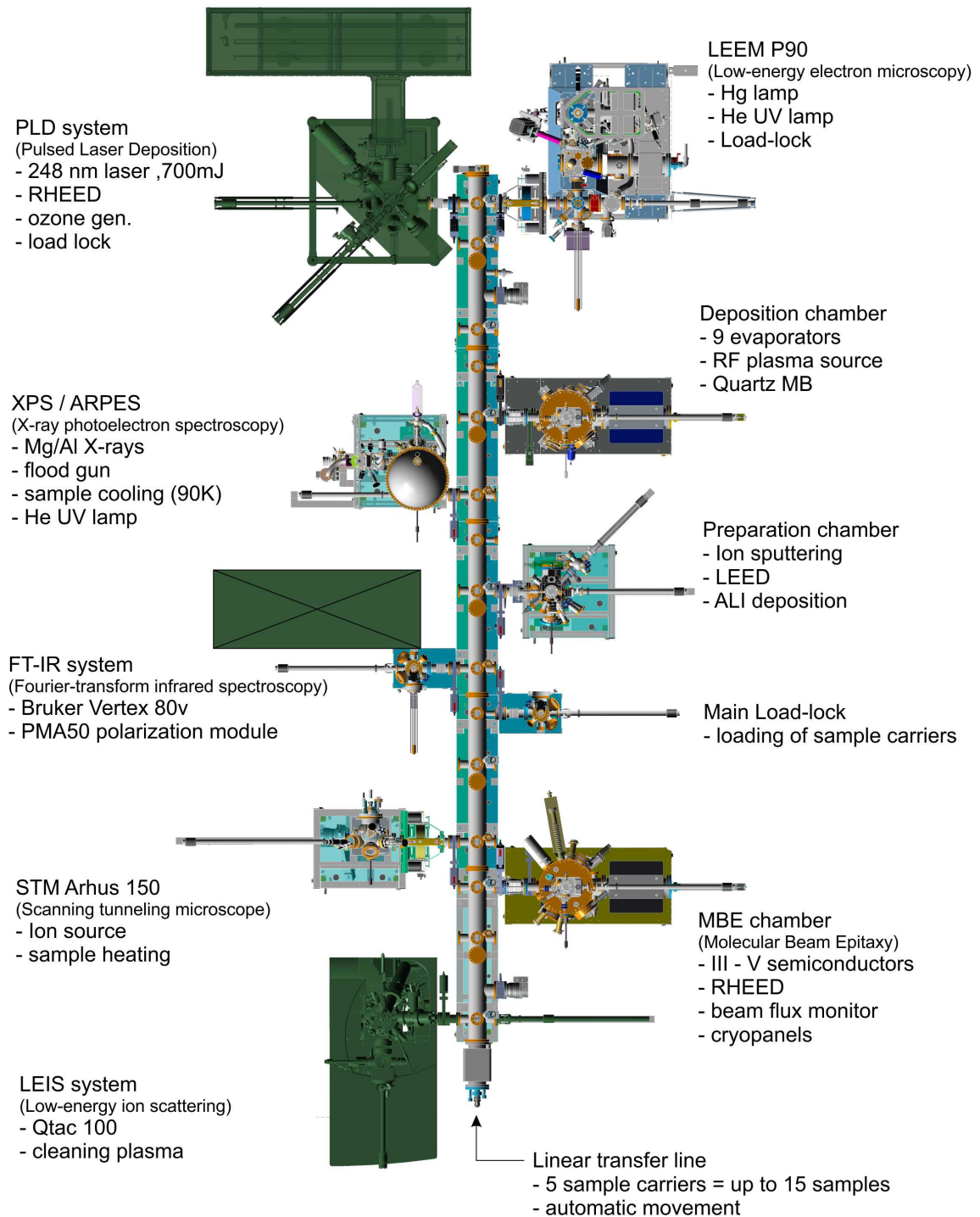


Fig. 3.1: Schematic drawing of the UHV cluster system formed by ten vacuum chambers, viewed from the top. Samples can be transferred under UHV conditions through a linear transfer chamber. Each system is isolated by gate valves and can be vented separately. Additionally, STM and LEEM instruments are mechanically decoupled by connecting dumping element, from the linear transfer to prevent the transmission of vibrations during measurement.

3.2 Sample preparation

3.2.1 Sample holder

Most of the experiments presented in this work were performed on the single crystal metal samples. The hat-shaped crystals are secured in the sandwich-type molybdenum holders shown in the Fig 3.2(a-b). This design is necessary to meet the requirements for LEEM manipulator i.e.: crystal surface should be at the same level as the sample plate to create the uniform electric field for LEEM imaging (see chapter LEEM: 4.1.3). Additionally, the bottom part of the holder is open to allow efficient direct e-beam heating. Crystals have to be mounted in the way that pressure is applied to the bottom part of the crystal. If the top part of the crystal is touching the sides of the top sample plate, stress can accumulate during annealing, which results undesired surface reconstructions and over time in significant surface morphology changes. It's recommended to use only a small amount of force on the screws to prevent crystal damage. For example, gold crystal can be pressed into the sample holder over time and become trapped. This will make impossible to remount the sample and hence repolishing of the crystal surface in the future. It was found that it is also necessary to use different metals for sample holder and screw since the materials can bond during annealing cycles (e.g.: tantalum screws for molybdenum holder).

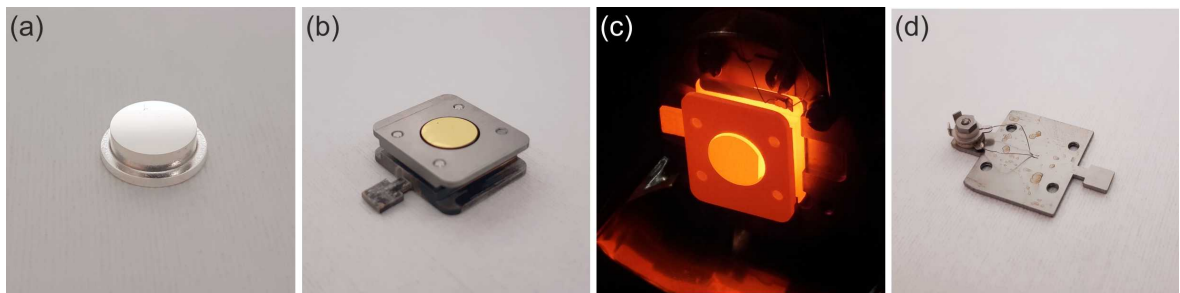


Fig. 3.2: (a) Hat shaped single crystal (silver) with a diameter of 8 mm. (b) Sandwich style sample plate with a gold single crystal. (c) Iridium crystal heated to 1500 °C inside of the manipulator in the preparation chamber. (d) Sample plate with two electrical connections and attached thermocouple for temperature calibration.

3.2.2 Sample cleaning

Samples were cleaned in the preparation chamber equipped with broad beam extractor type ion source. Sputtering was performed with various ion energies between 1 – 3 keV. Typically, three Ar⁺ sputtering cycles of 10 – 15 min with annealing after each sputtering were used. The sputtering source is not equipped with the focusing lens, therefore the beam size will change with sputtering energy. It is important to set the correct sample position to sputter the entire crystal surface and check the beam shape over time. Improper cleaning may take several cycles to discover and accumulated crystal damage may be irreversible. Fig. 3.3(a) shows Ag(100) crystal surface cleaned multi-

ple times without the proper sputtering. Crystal had to be mechanically repolished to recover the surface.

Heating cycles were applied after each sputtering. The sample is heated by electron beam extracted from the thorium coated wolfram filament and accelerated by 1 keV. The manipulator construction allows long term annealing at temperature up to 800 °C or reaching 1500 °C for short periods (Fig. 3.2(c)). The sample annealing temperature was set at approx. 50 % of the metal melting point. In the case of iridium crystal, additional cleaning cycles were used to remove the carbon residues by annealing in an oxygen atmosphere. Multiple carbon structures are shown in the STM image Fig. 3.3(b), most likely accumulated on the surface from the graphene growth and molecular depositions. Exact cleaning conditions are described in the table Tab. 3.1 for each metal.

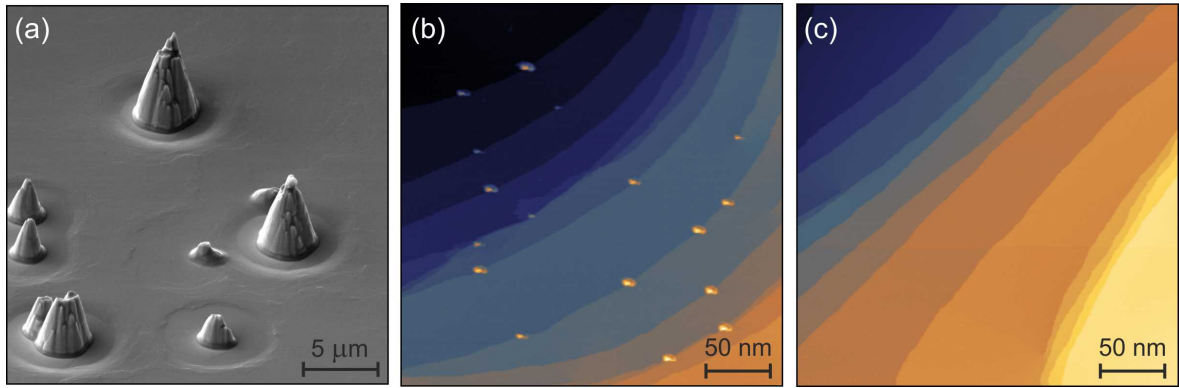


Fig. 3.3: (a) Scanning electron microscope (SEM) image (tilted by 40°) of Ag(100) surface after improper cleaning procedures. Conic structures are formed by silver. No contamination were detected by XPS or by localized EDX measurement on the structures. (b) STM image of Ir(111) surface with carbon residues. (c) Iridium surface after applying additional annealing in oxygen atmosphere during the cleaning procedure.

3.2.3 Temperature measurement in UHV

The temperature in UHV can be measured by K-type thermocouple (chromel-alumel) attached somewhere close to the sample. For our systems thermocouples are attached to the spring which pushes down the sample holder against the manipulator. This often provides misleading information, because the sample side is significantly cooler than the metal crystal which is directly heated by the e-beam. Additionally, spring contact strength can change over time, which will modify the thermal contact to the sample and result in discrepancies in temperature readout.

Remote temperature measurement can be performed by infrared (IR) optical pyrometers. They calculate the sample temperature from the intensity of the IR light emitted by the sample. The measured temperature depends on the: (I) temperature of the sample, (II) sample radiation properties (emissivity constant), (III) IR transmission of the materials in the optical path of the pyrometer, in our case mainly the chamber

Tab. 3.1: Cleaning parameters of single crystal metal samples. Temperature was monitored with IR pyrometer with emissivity set to 0.1. First sputtering cycles was usually performed at the higher sputtering energy as noted and the Ar⁺ pressure $\sim 9 \times 10^{-6}$ mbar. Iridium crystal required to use of additional annealing in oxygen atmosphere. Typically, the crystal was heated for 6 min at 800 °C at the oxygen pressure of 1×10^{-6} mbar

Material	No. of cycles	Sputt. energy [keV]	Sputt. time [min]	Annealing temp. [°C]
Cu (100)	3	2, 1	20 – 15	550
Ag (100)	3	2, 1	10 – 15	520 – 550
Au (100)	3	2, 1	10 – 15	500
Ir (111)	3 (+1 O ₂)	2.5, 1.5	10 – 15	1450 – 1550
Au (16 14 15)	3	0.8 – 1.2*	15 – 20	450 – 480

*sputtered at high incidence angle for better step reconstruction

windows. The emissivity constant ϵ is the relationship between the emission of a real object and the emission of a black body radiation source (an object which absorbs all incoming rays, $\epsilon = 1$). It is the property of each material and additionally, strongly depends on the surface properties e.g.: roughness, oxidation and the spectral range utilized by the specific pyrometer. For polished metals the emissivity is generally very low ($\epsilon < 0.1$). Annealing cycles in this work were monitored with LumaSense IMPAC IGA 140 pyrometer. It operates in range of 350 – 1800 °C and 1.45 – 1.8 μm wavelength. The minimum emissivity setting allowed by the device is 0.1 and was used for all the experiments with metals. The uncertainty of the device provided by the manufacturer is 0.3 %, with even better repeatability. However, given the uncertainty in the material emissivity constant and the small transmission losses, the precise sample temperature will be slightly different. Annealing temperature can also be set experimentally by observing the terrace formation in LEEM. It was also observed that a small amount of metal can be sputtered over time from the samples onto the chamber windows. This thin metallic layer will absorb part of the IR radiation and change the temperature measured by the pyrometer.

Second pyrometer, Micro Epsilon 3ML-SF, was used for lower temperature measurements, for example for growth of metal-organic systems. It has a range of 80 – 400 °C in the spectral range 2.3 μm . For lower temperature measurements it was observed that any heated materials in the chamber, such as deposition cells, will significantly increase the measured temperature. This is most likely caused by reflected IR light from the chamber walls. The temperature was usually set before the experiment or assumed to be comparable for the same heating parameters of the manipulator. Additionally, temperature calibration was performed with a special sample holder shown in the Fig. 3.2(d) with the mounted thermocouple.

Tab. 3.2: Deposition temperatures of used molecules.(ML = mono-layer)

Molecule	Temperature [°C]	Approximate depos. rate
TCNQ	113	0.1 ML/min
TPA	170	0.05 ML/min
BDA	185	0.04 ML/min
DBBA	170	0.35 ML/min

3.2.4 Material deposition

Material depositions were performed in the Deposition chamber that has a base pressure lower than 8×10^{-11} mbar. Organic molecules were deposited from thermal evaporators of two types. BDA (biphenyl dicarboxylic acid) and TPA (terephthalic acid) molecules were deposited by the near-ambient effusion cell (Createc) from an oil-heated crucible. The TCNQ (tetracyanoquinodimethane) molecules were deposited from organic material effusion cell (MBE-Komponenten). Typically, the molecules were degassed for several hours (4 – 8 h) after refilling or chamber venting. Unless stated otherwise, the molecules were deposited on to the sample held at room temperature. Deposition temperatures and rates are noted in Table: 3.2. Here, the monolayer coverage (ML) is estimated as fully covered surface by the molecules in the intact state in the respective self-assemblies formed at room temperature. The coverage of the surface was usually estimated from the LEEM observation.

Deposition of Ni and Fe were performed by Single Pocket Electron Beam Evaporator (SPECS) from the metal rod and crucible respectively. Here, a part of the heated metal atoms is ionized and detected on the separate electrode. Detected ion current or Flux of these atoms can be used to estimate the deposition rate. All evaporators are pointing to the sample position at an 20° angle of incidence, measured from sample normal. Chamber is further equipped with retractable quartz crystal microbalance (QCM) allowing deposition rate calibration and control of deposition layer thickness. Typically information from QCM is combined with flux and X-ray Photoelectron Spectroscopy (XPS) measurement to accurately determine the deposition rates of metals.

3.3 Sample Analysis

The following section provides a brief description and technical specifications of used XPS and Scanning Tunneling Microscopy (STM) techniques. Description of the operation principle is not part of this work since both techniques are widely used in surface science. On the other hand, Low Electron Energy Microscopy (LEEM) is a significantly less common technique. Therefore, a more detailed description is provided in the next chapter (chapter 4).

3.3.1 X-ray Photoelectron Spectroscopy

The photoelectron spectroscopy was employed for chemical analysis and valence band mapping of samples prepared in the UHV cluster. The spectroscopic system comprises 150 mm mean radius hemispherical energy analyzer (SPECS PHOIBOS 150) equipped with microchannel plate detector and 2D CCD camera, non-monochromatic Mg/Al X-ray source (SPECS XR 50), He I/He II UV source (SPECS UVS 300), and flood gun. Samples can be mounted in the 5-axis fully automated manipulator capable of annealing to temperature up to 800 °C and cooling down by the flow of liquid He or N₂ to temperatures below -250 °C and below -170 °C, respectively. Apart from the standard K-type thermocouple, low temperatures can be monitored by the silicon diode.

3.3.2 Scanning Tunnelling Microscopy

The UHV cluster is further equipped with SPECS Aarhus 150 SPM with a Nanonis controller providing atomically resolved images in a temperature range of 90 – 400 K. Aarhus SPM has miniaturized design shown in the Fig. 3.4(a). This design ensures a very small mechanical loop between the tip and the surface which results in very good measurement stability. To limit the vibration transfer during the measurement, the central cradle is suspended in space by multiple springs and additional damping is provided by rubber Viton bands. Thermal contact for cooling experiments is provided by copper braids. To allow the insertion of the sample the cradle is locked in place and sample is inserted and locked by two clamps, shown in Fig. 3.4(b).

The data in this work were obtained with standard etched tungsten tips or a special Kolibri sensor. The Kolibri is a force sensor based on a quartz length extension resonator and is capable of simultaneous STM and AFM measurement. The sensor consists of an oscillating piezoelectric rod supported by two arms. Sinusoidal voltage is then applied to one of the arms to excite the rod oscillations. When the rod is extended or contracted, induced electric charge is collected by the other arm. This allows detecting changes in the resonant frequency of the rod caused by the tip-surface interactions. The tip itself is attached to the oscillating rod and it is electrically insulated from the resonator to separate the tunneling and oscillating current.

Both types of the tips are made from tungsten, therefore no qualitative difference is expected in STM data. For the Kolibri sensor, improved long-term stability of the STM measurement was observed during the measurement of mobile organic molecules on the surface. The oscillator was turned on without the activation of the atomic force microscopy feedback providing additional high-frequency oscillation of the tip. Both types of tips can be sputtered by a parallel ion beam, while still mounted in the STM. Every new tip was sputtered for approximately 45 min at 2.5 keV at an Ar⁺ pressure of 9×10^{-6} mbar and occasionally for 5 – 10 min before the experiments.

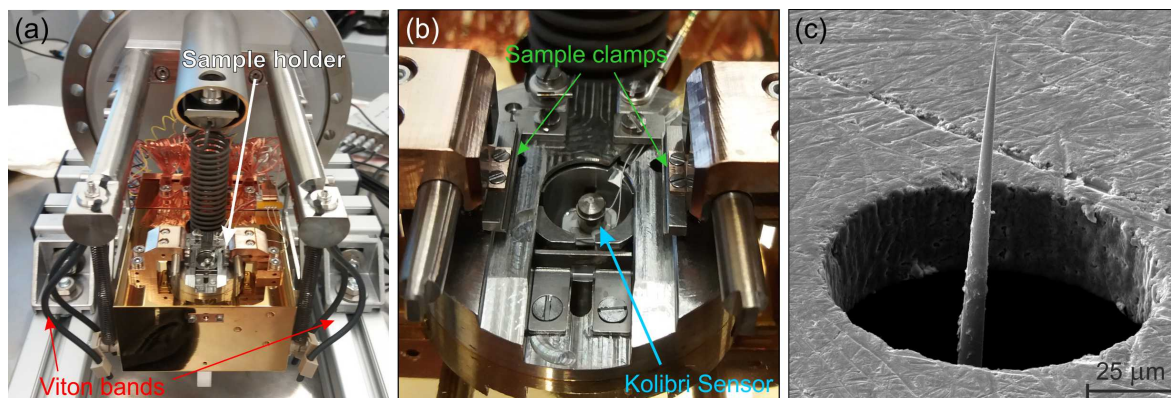


Fig. 3.4: (a) The image of Aarhus 150 SPM. During the measurement, the central part (golden cradle) is suspended by multiple metallic springs and rubber Viton bands to dampen the vibrations. (b) A close-up image of the sample stage of the SPM. The sample is inserted upside down and clamped. STM tip or Kolibri sensor is approached from the bottom. (c) SEM image of a W tip of the Kolibri sensor protruding from the metallic shield that protects the quartz oscillator. The tip is only a couple of hundred micrometers high.

3.3.3 STM drift correction

Majority of STM images in this work were obtained at room temperature. In general imaging at these conditions will suffer from distortions caused predominantly by the thermal drift of the sample and creep of the scanning piezo. This means that precise determination of distances and angles of the measured structures can be challenging. When measuring organic molecules it is often impossible to obtain atomic-resolution images of the substrate together with the molecular structures in the same scan. Therefore, the image distortion can not be corrected simply by looking at the crystal lattice of the substrate.

Piezo creep is an inherent hysteretic behaviour of the piezo material and result in non-linear distortion of the images. Creep effect becomes significant after large voltage changes on the x, y, z piezo and can be minimized by waiting after more significant shifts of STM scanning area and by choosing the proper scanning parameters. On the other hand, the thermal drift of the sample is a perpetual behaviour (at least in our laboratory). It originates from differences in the thermal expansion coefficient and in the thermal diffusivity of the different parts of the STM, sample holder and the sample itself. Even in the controlled experimental environment that is the air conditioned clean rooms, constant thermal drift was observed for multiple days.

In approximation, the thermal drift was assumed to be linear linear for images measured during the usual short scan time (5 – 15 min). In linear approximation, the sample drifts in the arbitrary direction with constant drift velocity, therefore it may be necessary to correct both vertical and lateral drift. However, in the performed experiments the vertical drift (out of plane, z - axis) was very small compared to the image size and therefore its effect on the size and shape of the measured structures was negligible.

A drift correction procedure was derived from the Ref. [110]. In two or more consecutive images, a specific feature was tracked (usually defect in the molecular island) to determine the drift velocity. The position of a tracked feature should be measured either in consecutive up or down images to minimize possible addition of the creep distortion. Following the procedure detailed in the article, polynomial equations were used to correct for the image distortion directly in the open-source software GWYDDION [111]. Example of the effect of the image distortion caused by linear thermal drift during the STM scanning is shown in the Fig. 3.5(a)-(b). The image deformation is not completely straightforward, because the STM has fast and slow scanning directions. Therefore, the constant drift velocity will deform the x and y image axis differently. Example of the measured and corrected image is shown in the Fig. 3.5(c)-(d).

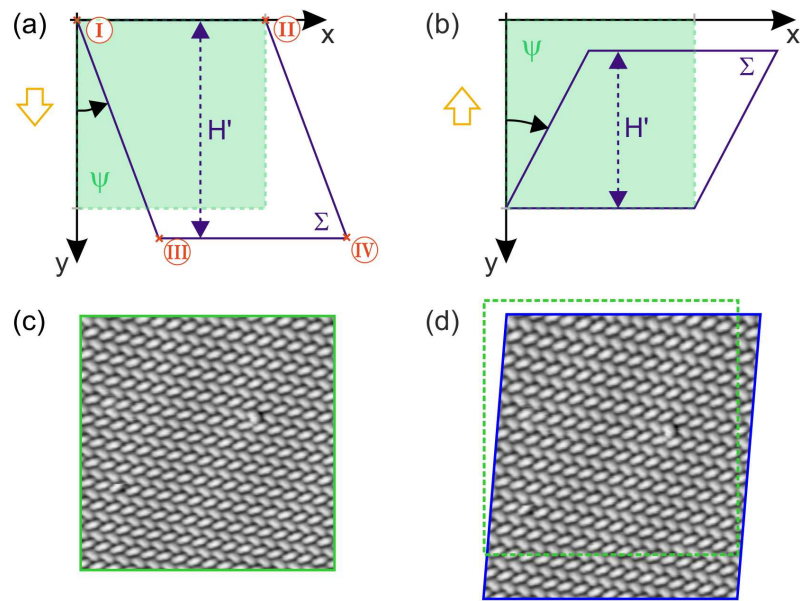


Fig. 3.5: Scheme of changes in the STM images after applying drift correction for positive drift velocities in x and y direction. Original image (Ψ) is marked in light green and corrected image (Σ) is outline in blue. Image correction of the down (a) and up (b) scanning directions. Adapted from [110]. (c) Original measured STM image and (d) drift corrected image where green dashed line marks the position of the original image (c).

4. LEEM - LOW ENERGY ELECTRON MICROSCOPY

Low Energy Electron Microscopy allows to image low energy electrons reflected, emitted or scattered from the sample. Due to the use of low primary electron energy (0 – 100 eV) high surface sensitivity is achieved. One of the most attractive advantage of this instrument is the ability to combine the nano-meter spatial resolution in real-time images of the surface with structural information provided by micro-diffraction and to trace changes on the surface in real-time. This chapter will be focused on a brief description of the principle of operation and available techniques but mainly on the FE-LEEM P90 instrument manufactured by SPECS, based on the design of Dr. Tromp [112]. The author aims to briefly introduce the reader to the basics of the LEEM setup and experimental techniques. Data obtained from this instrument will be often used in the experimental section.

4.1 *Microscope setup*

Development of the LEEM instruments began in the 1960s by Prof. Ernst Bauer, however the first functional instrument with good quality images appeared decades later [113]. LEEM development entered a new era in the 20th century with modern devices and commercial instruments from German companies SPECS and Elmitec. LEEM instruments can, at first glance, remind one of the transmission electron microscope (TEM). LEEM usually consists of the electron source, illumination system, objective lens, imaging column and a special component: magnetic beam separator or sample prism as shown in Fig. 4.1.

4.1.1 *Gun and condenser system*

Electron beam is extracted from a cold field emitter to achieve good energy dispersion ($\sim 0.3\text{eV}$) and the beam is accelerated by -15kV voltage. Electric potentials are in case of the P90 instruments arranged such, that the source and the sample are held at high potentials and the electron column is held close to the electric ground. This allows decelerating the electrons before they reach the sample surface. The opposite configuration with the sample and source grounded, is not technically compatible with the use of magnetic lenses which have, in principle, lower optical aberrations. The illumination system of the P90 instrument utilizes two magnetic lenses to create a magnified image of the source in the entrance plane of the prism. Additionally, there are special elements here to adjust astigmatism (two quadrupoles) and position of the

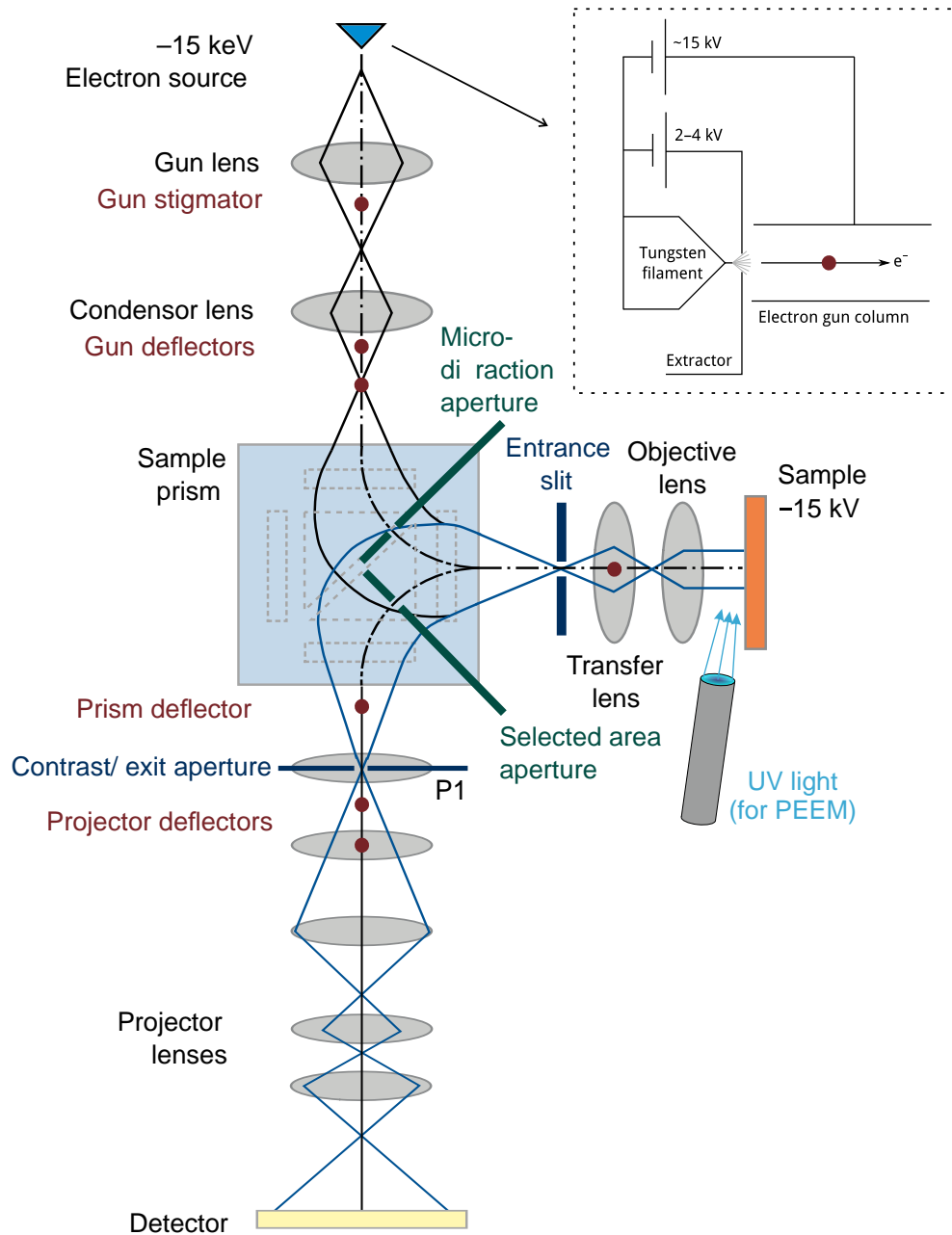


Fig. 4.1: Simplified schematics of the FE-LEEM P90 instrument manufactured by SPECS. The right inset graph shows electron extraction from the cold cathode. The beam of electrons is accelerated to an energy of -15 keV and travels through the electron optics system similar to the TEM to form a homogeneous beam. The beam of electrons is then deflected towards the sample by a 90° in a magnetic prism. Afterwards, the beam is focused at the sample by objective lens and decelerated to a low energy ($0 - 100\text{ eV}$) using a strong electric field formed between the lens and the sample (sample is held at -15 kV). After the interaction with the sample, electrons are accelerated back towards the objective lens and travel through the magnetic prism to projector lenses and finally to a detector consisting from the microchannel plate (MCP) with a CCD camera [114].

beam on the sample (electrostatic deflectors).

4.1.2 Sample prism - Beam separator

At the center of the LEEM instrument lies the magnetic prism which has a dual role. First, the prism deflects the illuminating electron beam by 90° toward the objective lens and second, it turns the electrons reflected from the sample towards the projection column. Both beams are therefore separated in the prism and do not interact with each other. In the easiest way the prism can be realized as a magnetic dipole which creates a homogeneous magnetic field. Electron moving in this magnetic field will be influenced by the Lorentz force, we need to simply adjust the strength of the magnetic field to adjust their path through the prism. In reality, more complex multipole designs of the prism are required to compensate for the additional focusing effect of the magnetic field and astigmatism.

Prism can be also utilized as a simple energy filter. The inelastically scattered electrons travelling from the sample with different energies (velocities) will be dispersed in the magnetic field of the prism. These electrons carry information, for example, about the band structure. The entrance slit (positioned between the objective lens and prism) allows to cut the beam in a way that creates narrow 2D slice of reciprocal space. This function can also be utilized with secondary illumination, for example, Helium UV lamp to perform angular resolved photoemission experiments although with lower resolution, than offered by proper ARPES setup with hemispherical analyzer (see Ref. [115]).

4.1.3 Objective lens and Sample

The objective lens has a dual function, it is a magnetic focusing lens but also forms a strong electrostatic field for electron deceleration. The field strength can reach $10 - 20 \text{ kV/mm}$ and its inhomogeneity can negatively impact image resolution. The quality of the electric field is enhanced by the shape of the objective (special tip), however, it will be also affected by the sample quality e.g.: planarity, conductivity. This puts a requirements on the sample and sample holders that can be used in the LEEM. Moreover, sparking can occur if the sample distance from the objective is too small or due to the increased pressure between the sample and objective (e.g. caused by a rapid degassing from the sample). Sparks can destroy the sample or damage the instrument.

To better understand the image formation, the basic information on the electron optics will be provided next. Electromagnetic lenses are, to a reasonable approximation, comparable to the glass lenses used in a standard light microscope. The main difference is that we can adjust the focal length of the lens, which determines where the electrons intersect: lenses with a higher magnetic field will have a shorter focal length. The LEEM objective can be drawn as a thin convex lens, a familiar diagram from geometrical optics is shown in Fig. 4.2. The paths of the light rays (electrons in our case) are drawn as they will transfer through the lens. The rays emerging from a

point in the object plane are focused in the back focal plane (at distance f_i) and converge to a point in the image plane. Rays that are parallel to each other, dashed yellow and blue rays in Fig. 4.2(a), will meet at the same point in the back focal plane. This means that also electrons from the sample that travel at the same angle will converge in the same point. Therefore, the diffraction pattern exists at the back focal plane of the objective. Either the image plane or the diffraction pattern from the back focal plane can be further magnified and transfer trough additional lenses.

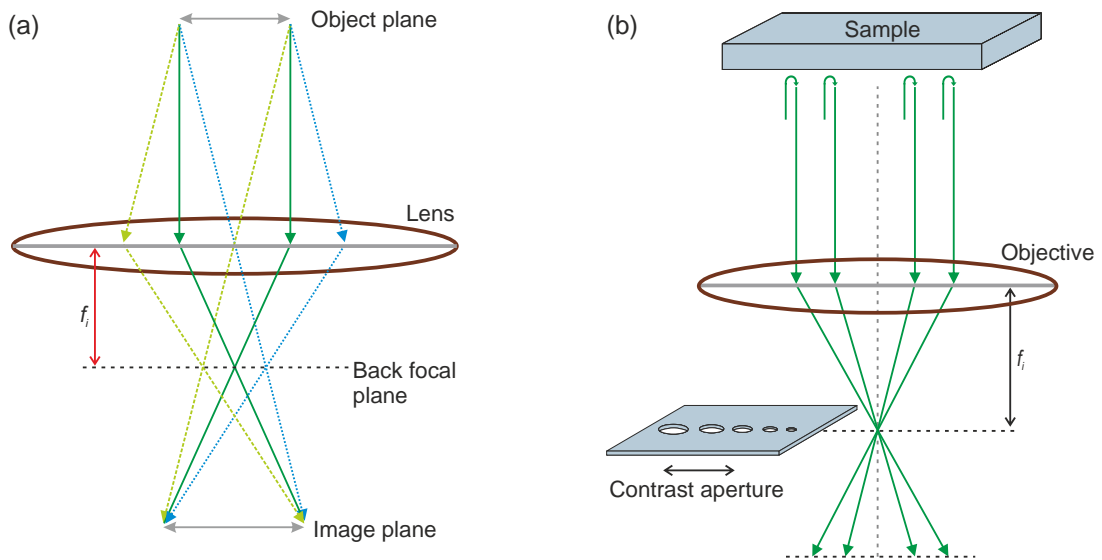


Fig. 4.2: (a) Optical path of a light ray for a thin convex lens. (b) Schematic illustration of electrons focused through the objective. A contrast aperture can be inserted to the back focal plane of the objective.

4.1.4 Projector system and Apertures

After the electrons interact with the sample they are accelerated back to the objective lens and continue through the prism to the projection system. Since we image the surface with a parallel beam, the majority of the reflected electrons will be also parallel (or close to it) and pass through the focal point of the objective lens. The contrast aperture can be inserted into this point as shown in Fig. 4.2(b) to improve the resolution¹. Aperture limits the acceptance angle for the objective, therefore, reduces the spherical aberration in the image.

Different aperture sizes can be selected depending on the beam intensity or application. However, smaller apertures also add diffraction effects and reduce contrast which ultimately degrades the image. The optimal aperture size can be found and for the P90 LEEM it is $40\ \mu\text{m}$ for an resolution increase. The contrast aperture is additionally used for dark-field imaging, where one of the diffraction spots can be deflected so it passes through the aperture. This will be explained in a more detail later.

¹ Technically, the exit aperture is located in the exit plane of the prism as shown in Fig. 6.7, not behind the objective lens, but it performs the same function.

Several other apertures are utilized in the P90 LEEM. One of the most used is the μ -diffraction aperture. It is placed parallel to the path of the illuminating electron beam in the prism. This aperture limits the viewing area of the microscope down to a circle with the 185 nm diameter. During the experiment, it allows collecting the diffraction pattern from individual structures on the surface.

The final part in the path of the electrons in LEEM is the projector column. It is a system of four projector lenses and several deflectors. Its function is to transfer and magnify either the real space image or diffraction pattern onto the detector. The detector itself contains a micro-channel plate (MCP), which is formed by millions of very thin conductive glass capillaries fused together. Each capillary acts as a secondary electron multiplier and depending on the applied voltage will amplify imaging electrons from the sample. Secondary electrons will then hit the phosphor screen and produce visible light collected by a CCD camera.

4.2 Imaging with LEEM

Several examples of LEEM imaging possibilities and fundamental sources of contrast will be reviewed in this section. Modern LEEMs can perform a large variety of experiments. The basic requirement is a conductive sample, but not necessarily with high conductivity since even oxide samples, or mica with a thin layer of metal evaporated on top can be imaged. LEEM provides the best results on relatively flat surfaces whose facets lie mainly within the surface plane. Samples are usually prepared in-situ or carefully cleaned if prepared elsewhere. A powerful advantage of LEEM is real-time tracking of the material's evolution. Depending on the construction design, it is possible to observe changes during annealing, exposure to gases or during the deposition of materials. This is achieved by separate pumping of the sample chamber, prism and electrons source (which requires best vacuum conditions). Additionally, the instrument can be connected to a synchrotron light source or laboratory UV lamp to perform PEEM (Photo Emission Electron Microscopy). This enables a wide range of spectroscopies that can be performed with nm-range spatial resolution. For state of the art aberration-corrected microscope 2 nm resolution was demonstrated [116]. Given the scope of LEEM applications, we will only focus on a few examples.

4.2.1 LEEM contrast

In standard LEEM images, the contrast of different materials can be understood as a difference in their electron reflectivity. The reflectivity usually depends on the surface work function and strongly changes with electron energy. In approximation it can be related to the band structure of the material (or rather the surface of the material). Electrons are absorbed if their landing energy coincides with the energy of unoccupied states in the material. Exact mechanism always depends on a particular system.

LEEM image of Ag(1 0 0) surface with molecular islands of BDA (biphenyl-dicarboxylic

acid) is shown in Fig. 4.3(a). Separately, the normalized intensity from marked areas was plotted for Ag and BDA. Highest contrast was formed for the electron energy of 3.6 eV, where the intensity difference between Ag and BDA is largest. Electron intensity dependence on the electron energy is called the IV curve. Additionally, other electron energies with lower contrast can also be utilized for imaging. For example, mirror electron microscopy (MEM) mode is used at very low electron energy, close to zero or even slightly more negative (relative to the sample). During the MEM, most of the electrons are reflected above the sample surface. Advantage of this technique is its sensitivity to the electric fields and reduction of the beam damage to the sample [117].

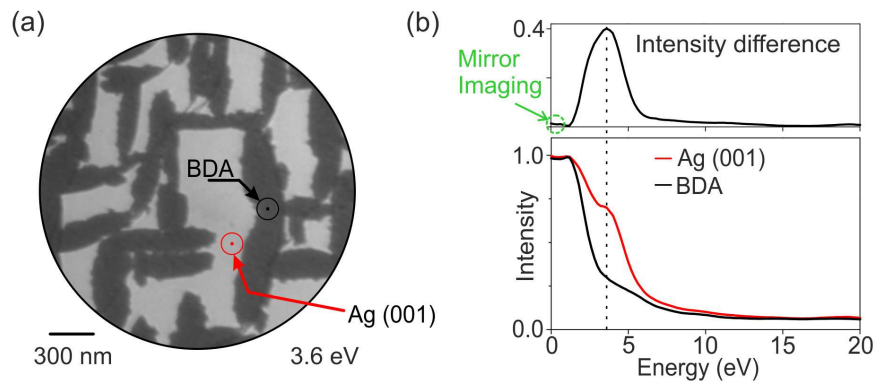


Fig. 4.3: (a) LEEM image at optimal contrast condition for BDA on Ag surface at 3.6 eV. Red and black points mark the measured position of IV curves for Ag and BDA respectively. (b) measured intensity dependence on electron energy (normalized I-V curves) of Ag(100) surface and BDA molecular islands. The top graph shows contrast plotted as a difference between Ag and BDA intensity, highest contrast is marked with a dashed line.

Atomic steps

Most of the surface scientists start their experiments by cleaning the surface of their substrates. When we observe clean surfaces in LEEM, very strong contrast at the atomic step edges is observed as shown in Fig. 4.4(a). Origin of this is Fresnel diffraction of electrons reflected at the lower and upper terrace. Steps typically appear as a single line, however, in aberration-corrected microscopes more typical oscillatory pattern can be visible. Besides the scientific possibilities, highly practical advantage of this is also calibrating the preparation parameters of the sample. For example, the proper annealing temperature of substrates can be found, since the terrace formation is clearly visible. It is important to notice the evolution of the size of the structures in LEEM, when objective focus changes, also shown in Fig. 4.4(b-d). Sometimes, the actual focus is hard to determine and combine with the beam astigmatism it can complicate the precise quantification of structure size. Slight defocus is usually used to enhance image contrast and structures visibility.

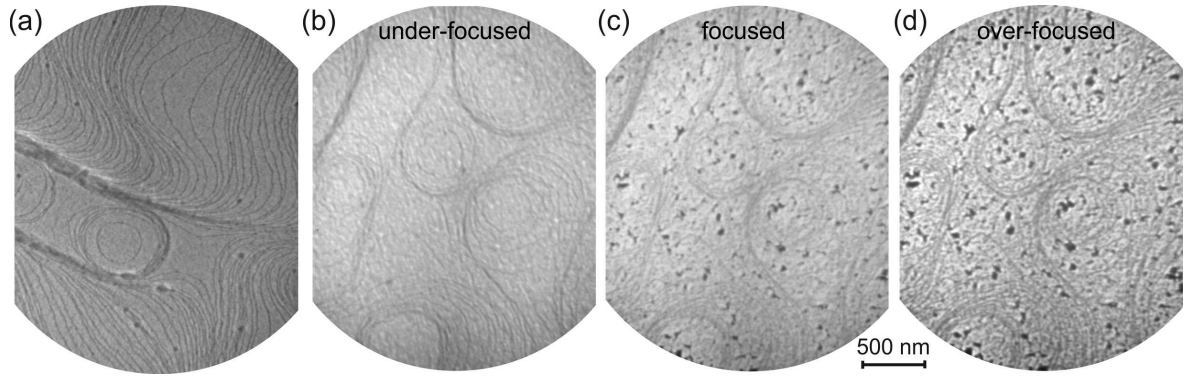


Fig. 4.4: LEEM image of Ir(111): (a) clean surface with strong step contrast formed by Fresnel diffraction. (b) and (d) Surface with carbon residues after growth of graphene monolayer. These images show evolution of structural details during focusing of the electron beam.

Contrast in thin atomic layers

LEEM is often used to observe deposition dynamics of thin layers, because of the strong sensitivity to different materials and can even be used to determine a specific number of deposited layers. For thin metallic layers, we can observe drops in electron reflectivity called the quantum size effects (QSE) [118–120]. They can occur as a result of the electron confinement by the surface and interface with the substrate or electron adsorption in quantum-well type standing waves in the films. Combined with the theoretical calculations the measurement of QSE can be used to accurately determine the number of layers on the surface. Example of coexisting 2ML and 3ML film of silver on the W(110) is shown in Fig. 4.5(a)-(b). It is possible to think of this effect as interference between electrons reflected from the film/substrate interface and from the film surface. In literature, it is also called phase contrast or quantum interference contrast.

An analogous effect was observed for 2-D van der Waals structures, for example, graphene grown on silicon carbide (SiC) shown in Fig. 4.5(c)-(d). Here the reflectivity changes because of electron scattering states localized between the graphene layers [121]. These unoccupied states derive from the interlayer band of graphite. For I-V curves of graphene on SiC, several intensity minima are observed in the spectra, depending on the number of graphene layers. Contrast changes of SiC/graphene images between energies 1.5 – 8.8 eV, can be observed in the Supplementary video file no. 1 (*1-SiC-IV.avi*).

4.2.2 Dark-field imaging

During the real space bright-field LEEM imaging, only the central electron beam (the specular beam or (0,0) beam spot) can be considered. On the other hand during the dark-field imaging, only one non-specular beam is selected by the contrast aperture inserted to the back focal plane. After the contrast aperture is inserted into the center of the diffraction image, entire image is shifted by the deflectors in the prism. In

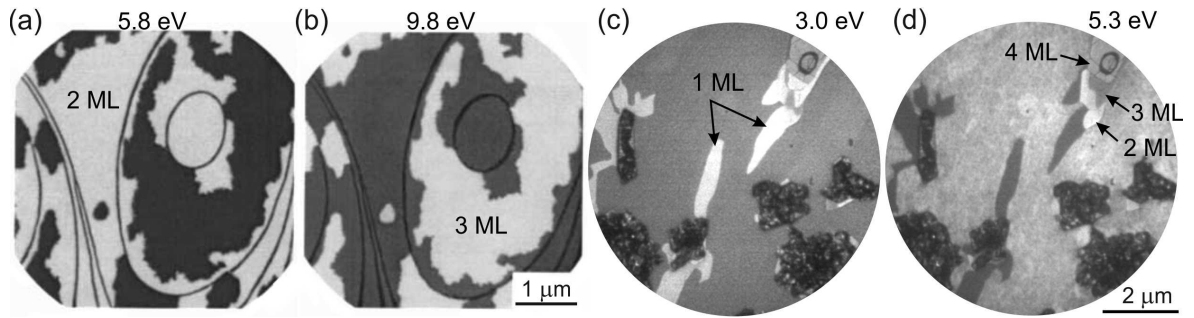


Fig. 4.5: (a) - (b) LEEM images of silver layer on the W(1 1 0) surface with different thickness (2 and 3 ML). Strong contrast for thin metal films is a result of interference effect between electrons reflected from the interface and from the film surface. Adapted from [119]. (c) - (d) Graphene flakes of various thickness on SiC substrate. Contrast in the image is formed by minima in electron reflectivity caused by the presence of unoccupied states between adjacent graphene layers.

this way, the specific non-specular diffraction spot can be chosen to pass through the aperture instead of the central spot. Imaging optics is then switched to the real space and only structures that diffract the electrons to the selected spot will appear bright in the image. This also allows distinguishing multiple structures or rotational domains on the surface.

Let's exemplify this on the simple self-assembly structure of terephthalic acid (TPA) on Ag(1 0 0) surface. This molecule consists of a phenyl ring with two carboxylic acids in para positions. The TPA is stabilized on the surface via complementary hydrogen bonding between carbonyl groups, building up a chain-like structure (stronger interaction) and it maintains a flat adsorption geometry [122]. In LEEM we can distinguish two equivalent long-range molecular domains of TPA rotated toward each other by 90° . Each domain can be separately imaged by choosing the appropriate diffraction spot for dark field imaging as shown in the Fig. 4.6. The molecular islands of TPA can be observed growing in narrow strips terminated on the step edges.

4.2.3 Diffraction imaging

Compared to the standard LEED (Low Energy Electron Diffraction) setup diffraction imaging in LEEM has several advantages. Central spot and areas around it can be imaged as shown in the in Fig. 4.6(a). Imaging energy can be very low in the range of several eV compared to the approx. 30 eV for standard LEED. This allows users to observe sensitive materials such as the organic molecules. Additionally, the diffraction spot positions are not moving with increased energy, since the change in the size of the Ewald sphere size is compensated by the electron optics. Diffraction images can be also collected from very small areas, depending on the available μ -diffraction aperture size (185 nm for P90 LEEM). Combining the structural information from μ -diffraction with spatial information from-dark field imaging gives LEEM great advantage over other surface techniques.

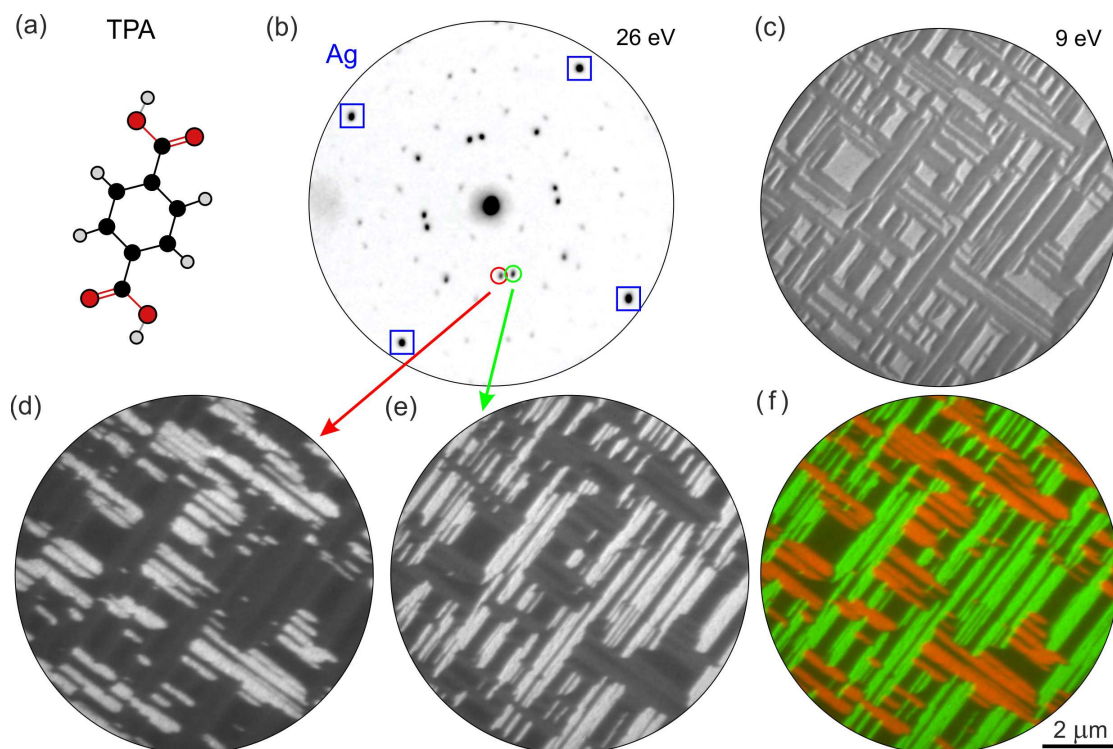


Fig. 4.6: (a) Illustration of the chemical structure of the 1,4-benzenedicarboxylic acid (TPA). (b) LEEM diffraction image at 26 eV of TPA molecular domains formed on the surface of Ag (100). (c) LEEM bright-field image acquired at 9 eV. (d) and (e) LEEM dark-field images of molecular domains acquired by selecting the specific diffraction spots noted in diffraction pattern. (f) Combined LEEM images showing the complementarity of the molecular arrangements on the surface.

4.3 Conclusion

Construction and primary operation of LEEM microscope was described with a focus on specifics of the SPECS P90 instrument used in this thesis. Basic operational modes were described to familiarize the reader with possibilities of LEEM in general. Mainly the dark-field imaging and μ -diffraction were presented on the experimental examples. Several sources of contrast in LEEM images were also described with the example of their usefulness in surface science. The real-time evolution of structures in LEEM was not presented but will be partially included in a later chapter on molecular island growth. Additional videos captured in LEEM (from experiments described later in this work) are provided in supplementary files that better showcase LEEM imaging capabilities (description here: [9](#)).

5. BIPHENYL DICARBOXYLIC ACID ON METAL SURFACES

The biphenyl-dicarboxylic acid (BDA) networks were used as a model system to study supramolecular chemistry and self-assembly. The BDA molecule, as shown in Fig. 5.1(a), is formed by two phenyl rings that are symmetrically functionalised by carboxylic end groups. Molecules with carboxylic groups have been extensively studied with a focus on their surface self-assembly. Especially the di- and tri-carboxylic acids were researched on a variety of metal surfaces including Cu [123–134], Ag [132, 133, 135–138], Au [135, 139], and Pd [140]. The intact DBA molecule usually maintains a flat adsorption geometry on metals, and it is stabilised on the surface via complementary hydrogen bonding between carboxyl groups and additionally by the van der Waals interactions bringing BDA sides closer together [122]. In this way, carboxylic acids build up a variety of structures often formed by long molecular chains both separate or adjacent to each other [124–128, 132, 134, 135, 137, 138, 140, 141].

Removal of a hydrogen atom (proton) from carboxylic group (deprotonation or carboxylation) leads to an abrupt change of binding mechanism of functional moieties and, consequently, changes the structure of the self-assembly on surfaces [124, 125, 133]. The temperature range in which deprotonation occurs strongly depends on the employed substrate. Whereas on Cu deprotonation occurs below room temperature [124–126, 133], on Ag, temperatures over 390 K are required [127, 133, 135]. On a less reactive substrates like Au (1 1 1) and graphene on Ir (1 1 1) no reaction was observed in our experiments up to temperatures at which BDA desorption takes place; this is consistent with reports for Au (1 1 1) [141], graphene/Ni (1 1 1) [142] and graphene/Cu (1 1 1) [128]. Such trend was explained in terms of the strength of bonding towards the surface, decreasing from Cu to Au [143]. In contrast, on a more reactive Pd (1 1 1) substrate, an equilibrium between carboxyl and carboxylate groups was established as hydrogen remained on the surface [140].

Structurally, the deprotonated molecules undergo rearrangement that can be understood in the simplest way as mutual repulsion of molecules that occurs due to partial negative charging of the carboxylates. New molecular self-assembly is formed that usually involves binding motif of carboxylate and hydrogen atom at phenyl ring. Additional phases can be formed when only a part of the carboxylic groups is deprotonated, either at one molecule or on average in the molecular arrangement [125, 127, 136, 138]. In such cases main binding motif is carboxylate-carboxyl bonding. Another possibility in these systems is a coexistence of several segregated “pure” phases with distinct bonding configuration [125, 128, 137].

Exploring the BDA interactions with surfaces can improve our general understand-

ing of the carboxylic group's role during the self-assembly process and surface reactions. That, in turn, will allow to design and fabricate improved supramolecular nanostructures with well-defined properties.

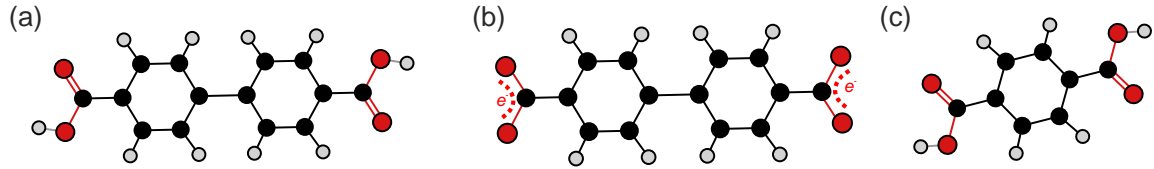


Fig. 5.1: (a) Chemical Structure of 4,4-Biphenyl Dicarboxylic Acid (BDA), (b) deprotonated BDA and (c) Terephthalic acid (TPA).

5.1 BDA on Cu (100)

Following section is based on the author's publication in Ref.[144]. It will describe the bonding mechanism of BDA on Cu (100) and the resulting model of the self-assembled structure. Further, it explains the unusual growth behaviour of molecular islands on the Cu, where no preference of nucleation at the step edges was observed. The author performed the sample preparation, molecular depositions, STM measurements, data analysis and part of the LEEM measurements. Jan Čechal and Pavel Procházka contributed in all aspects of the experimental work, data analysis and writing of the original manuscript.

On the surface of copper, the BDA deprotonates: hydrogen is removed, and resulting carboxylate groups bind to the copper surface. The exact mechanism of BDA-Cu interaction was the object of some discussion in the literature. Original studies of similar terephthalic acid (TPA) on Cu (100) suggested that molecular assembly is a result of the interplay between molecule-substrate interaction and intermolecular hydrogen bonding [124, 130, 145]. However, later studies reported that molecular deprotonation takes place near room temperature, and strong oxygen copper bonds will dominate the molecular self-assembly.

The BDA molecule observed in the STM at different chemical states during the gradual deprotonation is shown in Fig. 5.2. Here we can observe temperature dependence of chemical state and STM appearance of BDA on Cu (111) [125]. A carboxylate bound to the copper surface appears as a depression in STM (independent of bias voltage). For temperatures below $-30\text{ }^{\circ}\text{C}$ only protonated (intact) molecules can be found on the surface while at temperatures above $150\text{ }^{\circ}\text{C}$ only dicarboxylates remain. Between these temperatures, a partially ordered phase of fully protonated molecular phase coexists with a well-ordered phase made up of a combination of intact and partially deprotonated molecules. This multi phase was explained to form due to presence of atomic hydrogen from initial deprotonation, that remained on the surface. Thermal desorption spectroscopy showed, that on the clean Cu (111) surface, atomic hydrogen

is continually desorbing up to 90 °C [146, 147]. Schmitt et al. [125] further noted that additional phase of fully deprotonated molecules could be observed at step edges, however, without any further discussion.

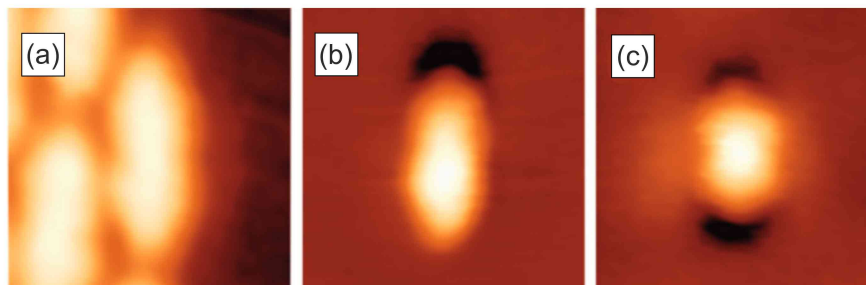


Fig. 5.2: STM images of BDA molecule on Cu(111) surface with (a) intact (b) one and (c) both carboxylic groups deprotonated. Scan size is $2 \times 2 \text{ nm}^2$, adapted from [125].

On the surface of Cu(100) at the room temperature, only a single BDA phase was observed consisting of fully deprotonated molecules. Different behaviour, compared to the Cu(111), is likely caused by lower desorption temperature of atomic hydrogen [146]. The structure of this phase is shown in Fig. 5.3, together with the proposed model consistent from both LEED and STM data. The LEED pattern taken over a large number of BDA islands shown in Fig. 5.3(a) can be associated with $(4\sqrt{2} \times 4\sqrt{2})R45^\circ$, or equivalently, $c(8 \times 8)$ molecular superstructure. Similarly to the STM measurement on the Cu(111) in Fig. 5.2, single BDA molecule appears as symmetric rod-like protrusion with the apparent length of $1.08 \pm 0.03 \text{ nm}$ (measured at 10% of the maximum height). This length is comparable with a theoretical length of 1.14 nm obtained by gas-phase geometry calculation using Arguslab and considered in recent studies [130, 148]. Consistently with the BDA structure, measured protrusion displays a slight narrowing in its centre.

In the high-resolution STM image in Fig. 5.3(b), a long-range ordered structure of the self-assembled BDA can be observed. Islands typically extend in range of 30-100 nm depending on the terrace size, at the submonolayer BDA coverage of approx. 0.4 – 0.6 ML. Within the molecular domain, the adjacent BDA molecules are oriented perpendicular to each other; the carboxylate moiety of each pointing to the centre of the neighbouring BDA. X-ray photoelectron spectroscopy shown in Fig. 5.4 confirms that the BDA carboxyl groups are deprotonated. Oxygen peak at the position 530.9 eV and secondary carbon peak at the 287.9 eV can be associated with the carboxylate group [149]. These observations are consistent with earlier studies on the carboxylic acids, TPA and BDA on the Cu(001) [150, 129, 151].

Based on the available data structural model shown in Fig. 5.3(c) was created. It presents binding motif where two carboxylate oxygen atoms point to two distinct substrate atoms and phenyl rings are localised near substrate hollow sites. Relative positions of BDA on Cu(100) were determined following recent studies [130, 152]. The model suggests that substrate mediated molecular interaction will be the dominating

factor in the self-assembly.

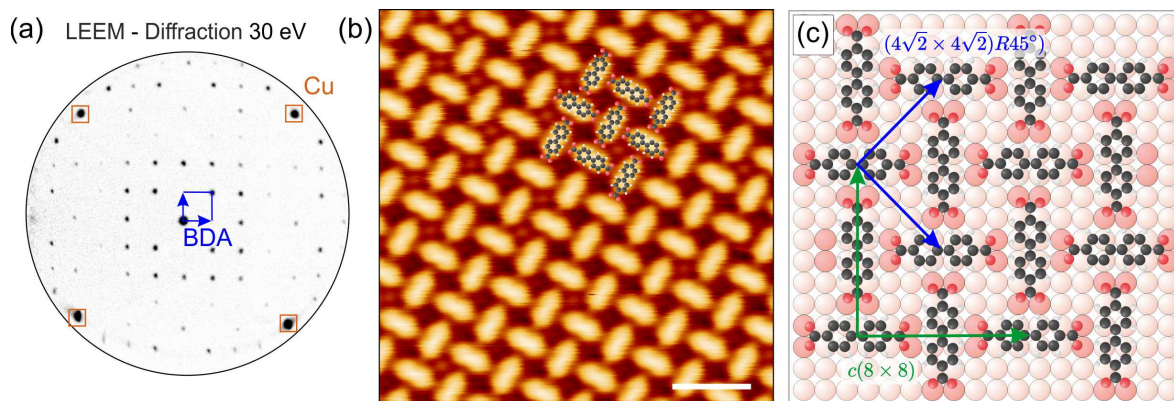


Fig. 5.3: (a) LEEM image measured at 30 eV. Cu (100) diffraction spots are marked in orange and BDA molecular superstructure in blue. Missing spots are the result of extinction due to the glide symmetry of molecular superstructure along directions $\langle 110 \rangle$. (b) STM image of BDA molecular self assembled structure on Cu (100) surface with superimposed molecular model. Scale bar is 2 nm. (c) Model of the proposed BDA phase, where atoms are marked as follow C = black, O = red, H = white, Cu = orange. Each oxygen of BDA is bonding to individual Cu surface atom. Primitive vectors of $(4\sqrt{2} \times 4\sqrt{2})R45^\circ$ superstructure are marked as blue arrows, and unit vectors of equivalent $c(8 \times 8)$ superstructure by green arrows.

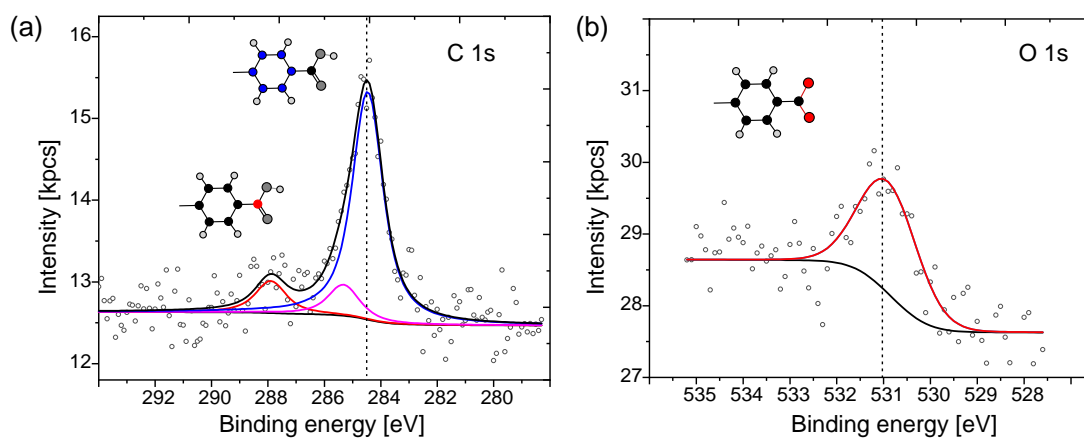


Fig. 5.4: Detailed spectra of (a) C 1s and (b) O 1s measured on the ~ 0.4 ML of BDA on Cu(100).

Parallel studies employing tetra-cyanoquinodimethane (TCNQ) on Cu(001) observed substantial structural rearrangements of both the organic and metallic elements [153]. The cyano groups act as a strong electron acceptor and thus will create strong bonds to the substrate. Subsequently, the TCNQ molecule bends toward the substrate, which is followed by rearrangement of the substrate atoms. Copper surface atoms are lifted from their equilibrium positions by about 0.3 \AA . A similar surface reconstruction has been theoretically obtained for the adsorption of the analogue strong organic acceptor tetracyanoethylene (TCNE) also on Cu(100) [154].

A significant charge transfer from the BDA carboxylate group to the substrate was also observed previously [155]. Additionally, strong bonding between the O atoms in carboxylates in TPA and the Cu atoms caused buckling of the first Cu layer [129], similarly to the above-mentioned case of TCNQ. Carboxylates in this case displayed strong carboxylate oxygen binding to substrate, charge transfer, and lifting of substrate atoms. On this basis, it can be assumed that a single substrate atom cannot accommodate the binding of two and more carboxylate oxygen atoms. However, it is still possible that there are other interactions also involved, for example, the mutual repulsion of partially negatively charged carboxylates. In any case, the proposed model dictates that two carboxylate oxygen atoms point to two distinct substrate atoms (site exclusion model).

5.1.1 Structural defects

It was possible to predict, considering the proposed bonding mechanism, that only distinct defects in the self-assembled BDA phase can occur. Indeed, in the measured STM images, specific defects could be identified, as shown in Fig. 5.5. Simplest point defect is modelled in Fig. 5.5(d) where single-molecule switches position. During the STM measurement, such structures could be observed, as shown in Fig. 5.5(a). The BDA molecule in the point defect was observed to transition back to its original position in the several consecutive images after a few intermediate jumps.

The second most commonly observed feature was dislocation line (or line defect), where the molecular assembly moves by one or two Cu surface atoms, this motif is modelled in Fig. 5.5(e-f). The part of the BDA molecular assembly shown in Fig. 5.5(b), involves both line defects types, marked with a green and blue arrow. The line defects are dividing two long-range ordered domains, and during the measurement, attachment or detachment of the whole BDA islands was observed between the consecutive STM scans. Next, Fig. 5.5(c) shows a cumulation of multiple defects in the BDA assembly and various additional cumulative defects could be observed. However, molecular arrangement within all types of defects is consistent with the site exclusion model where, as described above, a single Cu atom cannot provide more than one bond with carboxylate oxygen. Therefore, substrate positions cannot overlap.

An additional consequence of the site exclusion is the limited diffusion of BDA molecules along the side of the molecular islands. Movement of the molecule along the edge would require the bonding to the restricted position where the carboxylate oxygen atoms would be bound to the same substrate atom. In the STM single molecule was observed to detach and reattach to the sides of the molecular islands between the individual scans and sometimes only between several line scans. Such behaviour suggests that molecule movement involves detachment, diffusion in the vicinity of the edge, and reattachment at an appropriate position (previously suggested by Schwarz et al. [152]). Supplementary video file no. 2 (*2-BDA-Cu.avi*) is included in order to better exemplify the molecular movements. The video shows attachment and detachment of

BDA molecules in consecutive STM images taken on the edge of BDA self-assembled phase.

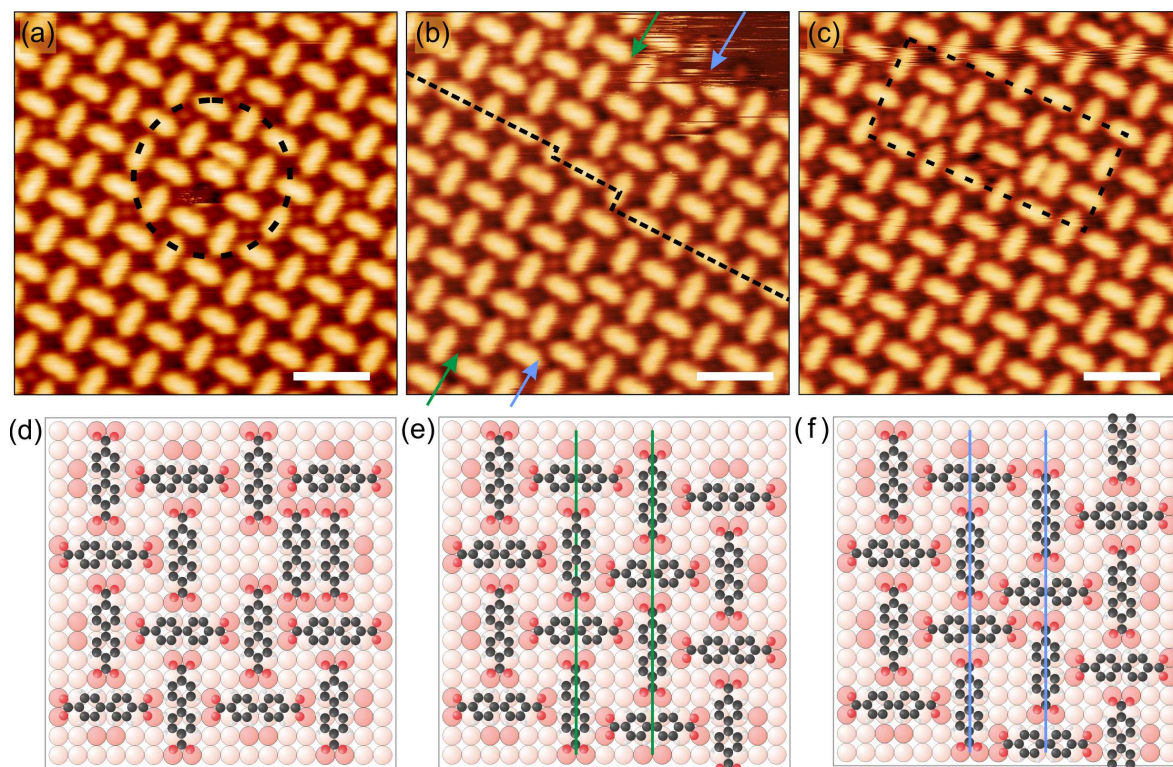


Fig. 5.5: Defects in the self-assembled BDA phase: (a) STM image of the point defect and (b) two distinct line defects. (c) STM image of additional structure created by a combination of multiple defects. (d) Corresponding model of the point defect and (e-f) line defects that show dislocation formed by a shift of the BDA phase by one (green line) or two Cu surface atoms (blue line). Blue and green arrows mark the dislocation lines in the (b) STM image. Smaller dots visible in the STM images between the BDA molecules and on the bare Cu surface are adsorbed CO molecules. Scale bars are 2 nm.

5.1.2 Growth Anomalies of BDA on Cu(100)

Modelling and quantitative understanding of thin films growth in the traditional semiconductor industry are crucial in the development of new technologies and processes. Modelling can reduce the cost of an experiment by trial and error, which is essential from an industrial viewpoint. Theoretical models are widely studied for homoepitaxial and further for heteroepitaxial systems [156, 157]. These models are now being extended in order to extrapolate for the molecular layers [75, 158–161]. Typically the materials on surfaces nucleate at the step edges as they exhibit strong chemisorption and catalytic properties, therefore, act as natural defects for nucleation [162].

Extended decoration of the step edges was observed for the vast majority of inorganic systems where monomers are single atoms displaying isotropic behaviour [163]. Additionally, many organic systems also nucleate on the step edges [70, 148, 164]. How-

ever, despite many similarities, some molecular systems show a new range of phenomena [160]. The organic molecules are one-, two-, or three- dimensional objects that can display anisotropy with respect to the shape of the molecule, surface-interlayer diffusion, interaction with other molecules or substrate, and various functionality. For example, growth regime can display transition from diffusion-limited to attachment limited aggregation due to the new activation barrier for the attachment of molecules caused by additional energy needed for a reorientation of the molecule [165, 161]. Moreover, interlayer diffusion and the associated Ehrlich-Schwoebel or step edge barriers [166] can influence the island morphology and introduce new growth phenomena such as mound formation and rapid roughening, which are frequently observed [167]. In order to predict and control the assembly of a wide variety of molecular networks, it is crucial to understand the relevant physical processes of molecules on particular surfaces.

Growth of BDA islands on the Cu(100) is one example where molecular island growth differs from typical systems. Observations in LEEM found no preference for nucleation at atomic step edges consistent with the previous work [150, 152]. This behaviour makes the presented system important from both a fundamental and application point of view. In the real space LEEM image in Fig. 5.6(a), one can observe that BDA molecule form separated islands. The BDA molecular islands appear as dark contrast areas, and the Cu substrate appears bright and upon closer inspection lines representing step edges and narrow terraces can be observed. Further, large area STM image in Fig. 5.6(b) confirmed that molecular islands are distributed over the terraces and touching the step edges only in few points. The origin of strong non-wetting of the step edge was not previously identified despite multiple studies of systems comprising BDA [125, 130], or similar TPA[129, 151], and other related dicarboxylic acids [133] on Cu substrates. This originally promoted further studies into this system.

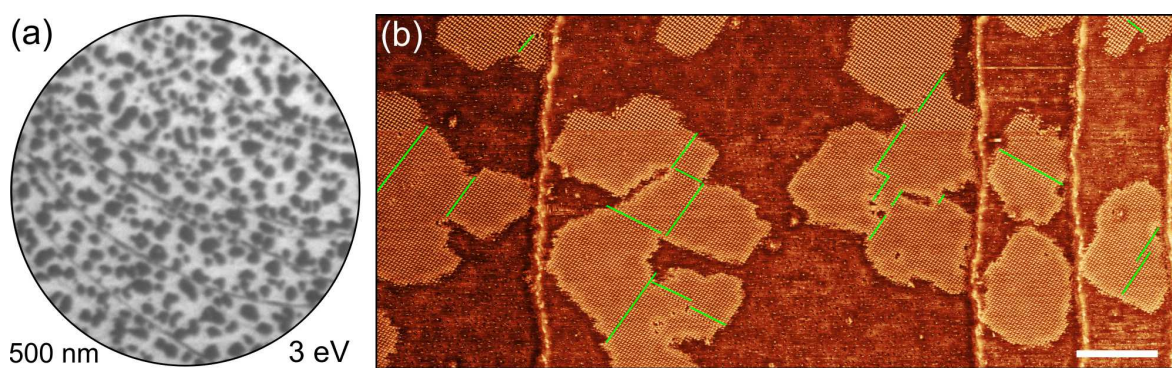


Fig. 5.6: Self-assembled islands of BDA on the Cu(100) surface: (a) LEEM image measured at 3 eV. Dark areas correspond to the molecular island and light gray to the substrate. (b) Overview STM image on the same sample. Green lines mark line defects in the molecular assembly, separating different molecular islands. STM image contrast was enhanced by adaptive filtering. Scale bar is 25 nm.

5.1.3 Step edge passivation

Previous sections argued strong molecule-atom interaction between the BDA and Cu, and, therefore, one can expect even stronger step edge interaction, which appear incompatible with the idea of BDA non-wetting the atomic step edges. In fact, closer look on the step edges of Cu(100) revealed a dense decoration by BDA molecules as shown in the STM images Fig. 5.7(d-e). Molecules at the steps are preferentially oriented in the same direction $\langle 100 \rangle$ or rotated by 45° with the respect to the BDA orientation in the islands $\langle 110 \rangle$. Given the high step-edge reactivity, some additional structures could be observed that are ascribed to the molecular fragment or other contaminants on the surface. These structures provide anchoring sites for molecular domain attachment as previously shown in the STM image in Fig. 5.6(b). However, the majority of the molecules attached to the steps retain features consistent with the appearance of intact BDA molecules.

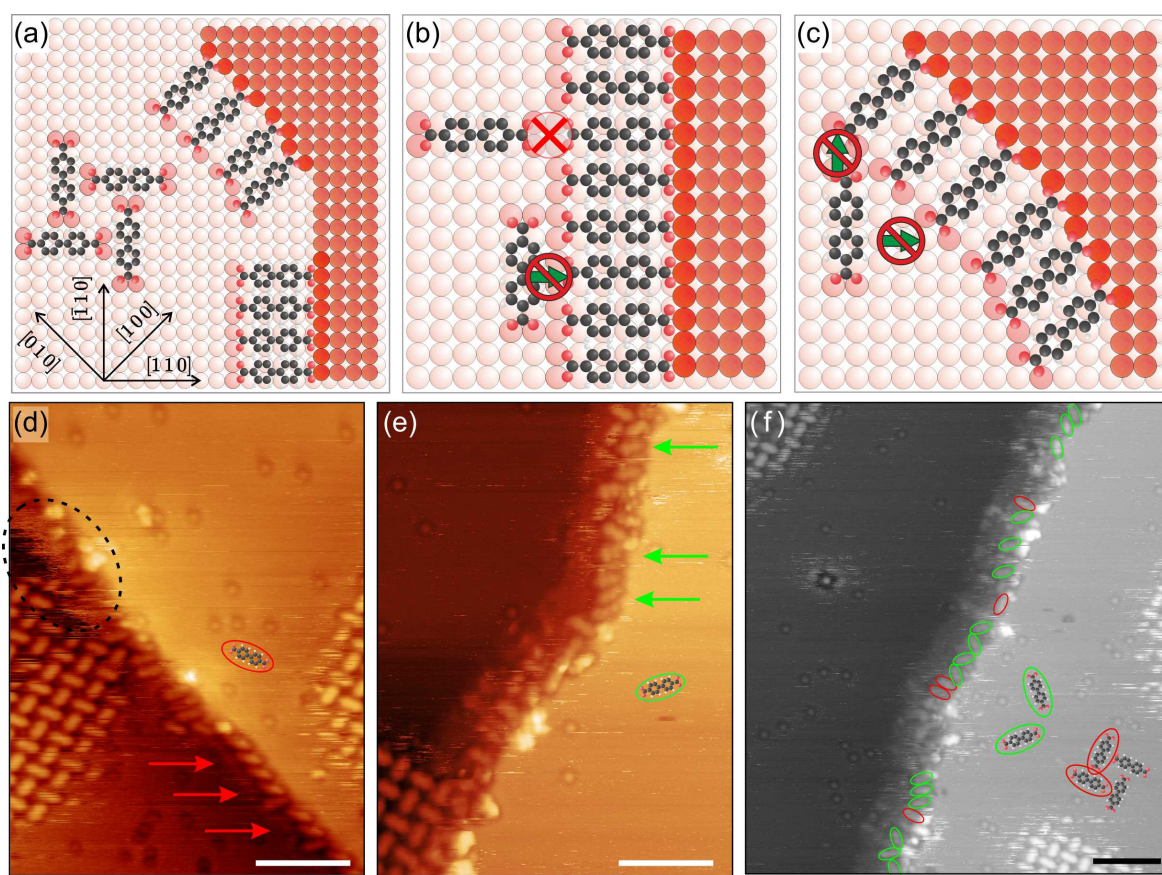


Fig. 5.7: (a-c) Models of the BDA molecules bonding to the Cu(100) atomic steps edges. Majority of the molecules at the steps are rotated by 45° with respect to the BDA orientation in the islands. Diffusion of molecules along and over the step edge is limited. (d-f) Detailed STM images of BDA step edge decoration. Molecules in the direction of the islands are marked in red and rotated molecules in green. (d) Increased noise in the STM encircled in black suggests trapped molecules between the island and the step edge since they cannot attach or diffuse to the next terrace. Scale bar is 4 nm.

By careful examination, several high-resolution STM images from multiple experiments were selected for statistical analysis. As shown in one of the selected images in Fig. 5.7(f), the orientation of the BDA was determined from the self-assembled phase. Molecules at the step edges were identified and were assigned the orientation. Only the molecules that can be unambiguously identified were included. Over 200 molecules were counted for which the $\langle 100 \rangle$ direction (molecules rotated in respect to the self-assembled phase) was slightly favoured over the $\langle 110 \rangle$ one, with the ratio of 1.6 : 1. These orientations are in accordance with the previously presented tentative model, as shown in Fig. 5.7(a-c). However, the $\langle 110 \rangle$ molecules (Fig. 5.7(b)) do not fit perfectly and the molecules can be distorted in order to comply with the site exclusion model (one oxygen binding to one Cu atom). In fact, such distortions were observed in some of the STM images (noted with red arrows in Fig. 5.7(d)). Based on this observations it is possible to hypothesise that the preferential orientation is $\langle 100 \rangle$. Nevertheless, precise molecular positions cannot be identified from our STM data, and further investigations are needed in order to determine the exact molecule position with regards to the atoms of the step edges.

The dense molecular packing of BDA at the step edges prevents the attachment of additional BDA molecules and hinders the formation of extended molecular islands. Some molecular islands were attached in areas without the decoration by intact BDA. The area between the BDA islands and the step edges often exhibited high noise levels in the STM, even when the other features appeared in high resolution. This implies high mobility of the BDA molecules in these areas and suggests another possible aspect of the BDA passivated step edge: the formation of a barrier against the diffusion of BDA molecules across the step edges (a type of Ehrlich-Schwoebel barrier). The molecules trapped between the BDA islands and step can neither attach to the passivated steps nor diffuse to the next atomic terrace.

5.1.4 Conclusion of section BDA on Cu (100)

This section was focused on the BDA/Cu (100) system. The author made a supportive argument to the previously proposed structural model and added a more complete explanation of the observed defects and growth anomalies in the BDA self-assembly structure. Proposed model explains the unusual growth behaviour of BDA molecular phase on the Cu(100). Extensive step edge decoration resulting from the strong bonding of the BDA to the atoms in the next atomic plane prevents growth of the molecular phase. Substrate step edges then become effectively passivated and form a diffusion barrier for the molecules. Study of structural and chemical distinctiveness of molecular systems is an important step toward improving theoretical growth models of atomic layers. Increased understanding of the involved intricacies is needed in order to make worthwhile predictions for similar systems.

5.2 BDA on Ag(100)

The following section describes the step by step deprotonation of BDA on the Ag(100) surface. Multiple structural assemblies (phases) of BDA are presented, corresponding to fully- and partially protonated molecules as well as deprotonated molecules. Additionally, at specific conditions a mixture of fully-, partially- and non-deprotonated BDA coexists on a substrate. Hence, we can view this system as the multi-component assembly of structurally close but chemically distinct molecular building blocks.

Parts of the following sections are based on the author's publications: Kormos et al. [168] and Procházka et al. [169]. The author performed the sample preparation, molecular depositions, XPS, STM and some of the LEEM transformations measurements and data analysis. Pavel Procházka performed significant part of the LEEM measurements, data analysis and creation of the structural models mainly the LEEDPat simulations. Jan Čechal supervised the experiments and data analysis. Anton Makoveev contributed to some of the experimental work. Additionally, low-temperature nc-AFM measurements were performed at the RCPTM centre at the Palacky University in Olomouc, in cooperation with Bruno de la Torre and Taras Chutora. In addition, the DFT modelling was performed to support the nc-AFM data in the group of doc. Pavel Jelínek at the Institute of Physics of the Czech Academy of Sciences. DFT data are not directly included in this work.

5.2.1 Overview

Combination of the mesoscale viewing area of LEEM, nanoscopic details from STM and chemical information from the XPS revealed multi-step deprotonation process of BDA on the Ag(100). During the continuous annealing of BDA/Ag(100), several phases consisting of BDA molecules with a distinct level of deprotonation were identified: fully protonated (2H-BDA), semi-deprotonated (1H-BDA), and fully deprotonated (0H-BDA). Main molecular phases shown in Fig. 5.8 are denoted as α -phase: a fully protonated molecules (as deposited); β -phase: formed by partially deprotonated BDA; γ -phase: a mixture of partially and fully deprotonated molecules and δ -phase: fully deprotonated phase of BDA. Each phase will be described in detail in the following section. In addition, multiple intermediate phases and phase transformations observed in LEEM will be shown.

The BDA molecules were deposited onto an Ag(100) crystal held at the room temperature. After the transfer to the LEEM chamber, the sample was analyzed and slowly heated by the filament (IR-heating only). The increased temperature initiated the deprotonation process and associated phase transformation. Changes of the molecular island were carefully observed in the LEEM, and the transformation was stopped at specific points. The sample was then cooled down to the room temperature and analyzed. By utilizing μ -diffraction aperture every structural domain of the BDA was identified. Each phase consisted of multiple equivalent molecular domains, and experiments sometimes yielded mixtures of different phases. After the transformation and

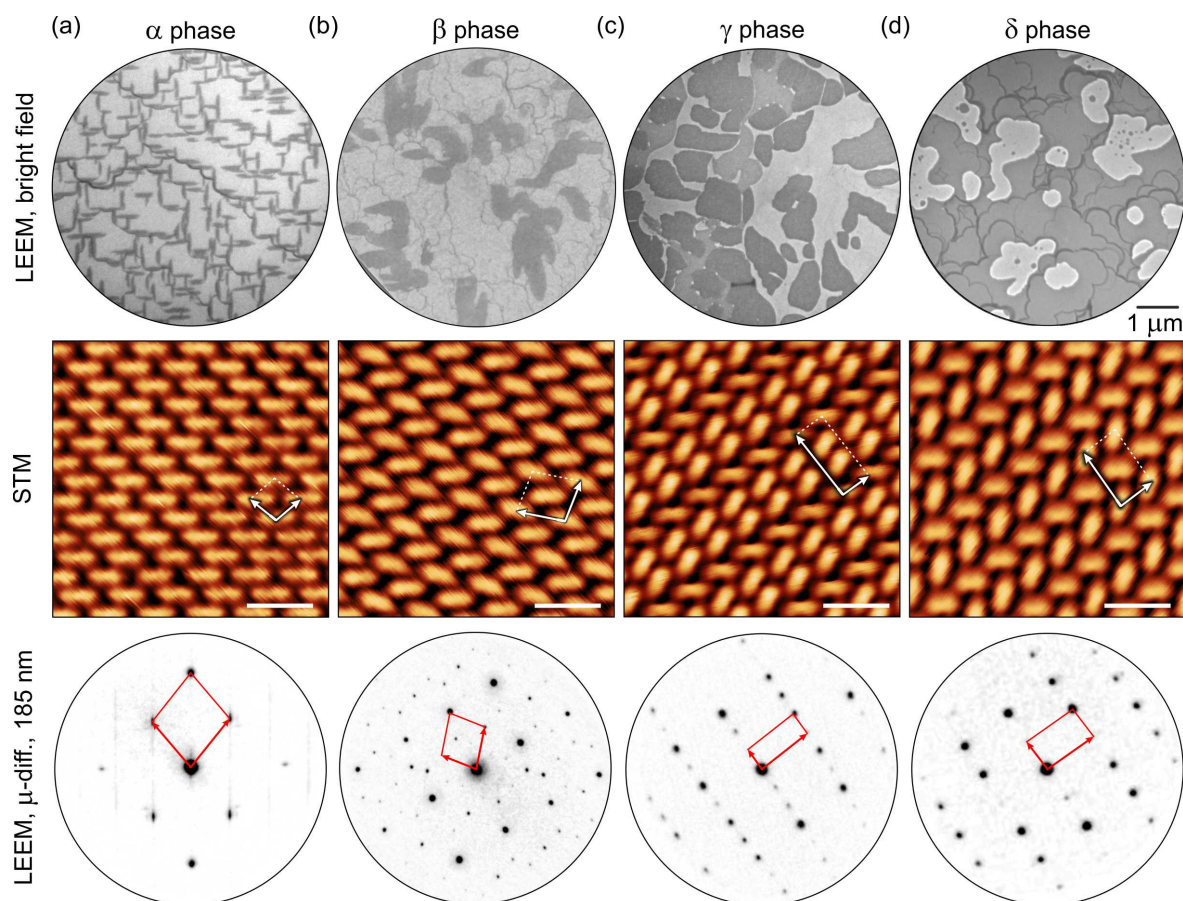


Fig. 5.8: Change of BDA molecular phases on the surface of Ag (100) with increased temperature. (a-d) Each phase represent the different chemical composition of BDA and is stable after the cooldown of the sample to the room temperature. LEEM images represent the typical appearance of molecular islands of different phases. Images were acquired at 10 eV with inserted contrast aperture. Corresponding STM images are in the second row. Diffraction patterns in the last row represent a single molecular island (domain) on the surface and were acquired by inserting μ -diffraction aperture (diameter of 185 nm). The unit cells of molecular superstructures are marked by a red in diffraction patterns and white in the STM images. Scale bars in STM images are 2 nm.

LEEM analysis in the LEEM were finished, the sample was transferred to the STM or XPS chamber for further measurements. Numerous experiments were performed with several silver crystals and yielded consistently the same molecular phases. Molecular layers were also transformed in several vacuum chambers and also in another laboratory (for nc-AFM measurement).

5.2.2 XPS analysis

Distinct chemical composition of each BDA phase was identified in-situ, by X-ray photoemission spectroscopy. Conventional non-monochromatic X-ray source that utilized Mg K α radiation with 300 W emission power and 12.5 kV cathode-anode voltage was used for all measurements. The C 1s and O 1s detailed spectra were acquired in high

magnification mode using pass energy 20 eV integrating up to 180 sweeps with 0.1 s dwell time and 0.05 eV energy step. Normal emission geometry (emission angle 0°) was employed. The prolonged measurement time was necessary due to the weaker oxygen signal for sub-monolayer BDA coverage. To prevent any changes during the spectra acquisition (up to 6 hours), some samples (where chemical change was observed during measurement at RT), were cooled down to 100 K in the liquid-nitrogen cooled manipulator. The Ag 3d peak was measured both before and after the measurement of O 1s and C 1s peaks to ensure correct binding energy reference. No charge compensation or energy scale correction was employed. The Ag 3d $5/2$ peak position was calculated as $(368.21 \pm 0.01 \text{ eV})$ as an average for all the samples with the confidence level of 95%. Calculated value is in agreement with the reference energy $(368.22 \pm 0.01 \text{ eV})$ for unmonochromated Mg K α radiation [170]. Small energy shift of the O 1s and C 1s peaks were observed during the initial sweeps in the range of 0.1 – 0.2 eV. Cause of this effect is unknown. However, because this was a consistent and reproducible behaviour, the initial 15 sweeps (from hundreds) were excluded from the data analysis.

First, the reference spectra of BDA was measured from a multilayer, shown in the first row of the Fig. 5.9. Here, it was assumed that any surface effect of the Ag substrate would be negligible in overall data. The detailed spectra of C 1s were fitted by three components and simultaneously adjusted Shirley background. The largest component of the multilayer BDA carbon can be associated with the carbon atoms of phenyl ring (C1, blue) at the binding energy of 285.4 eV and the second component with the carbon bound to a carboxyl group (C2, red). The third component (C3, green) was attributed to the shake-up satellite due to $\pi - \pi^*$ transition in the aromatic ring. Fitting procedure for all the XPS data was performed in the program *Unifit 2013* and all the fitting parameters are summarized in the tables below (Tab.: 5.1 and 5.2).

Spectra of submonolayer coverage of intact BDA (α -phase) exhibited two main differences compared to the multilayer. First, an additional fourth carbon component (C4, magenta) was added to properly fit the C 1s spectra. This component was shifted by 1 eV towards higher binding energies and could be associated with the carbon atoms that are detached from the surface. Such effect may occur for either a BDA molecule moving in the molecular gas or part of the BDA that is lifted from the surface due to the compression in the self-assembled structure. Some high variation was observed in the nc-AFM data, and this will be introduced appropriately later (Fig. 5.13). Alternatively, this peak could be explained as a signal from adsorbed CO molecules or by an asymmetry in the C1 carbon component. The second difference is that the main C1 component is shifted by $\sim 0.5 \text{ eV}$ toward lower binding energy. The corresponding shift can be observed for O 1s peak. Similar shifts are often explained for adsorbed molecules as a screening of the core levels by metal substrate, i.e.: effect of the charge transfer from the substrate to the adsorbate [171]. The peak positions are in agreement with the previous studies of carboxylic compounds [136, 149]. The intensity ratio of peaks associated with carboxylic and phenyl carbon atoms is 0.16, that is in agreement with the expected ratio of 2:12 (0.167) for BDA molecule.

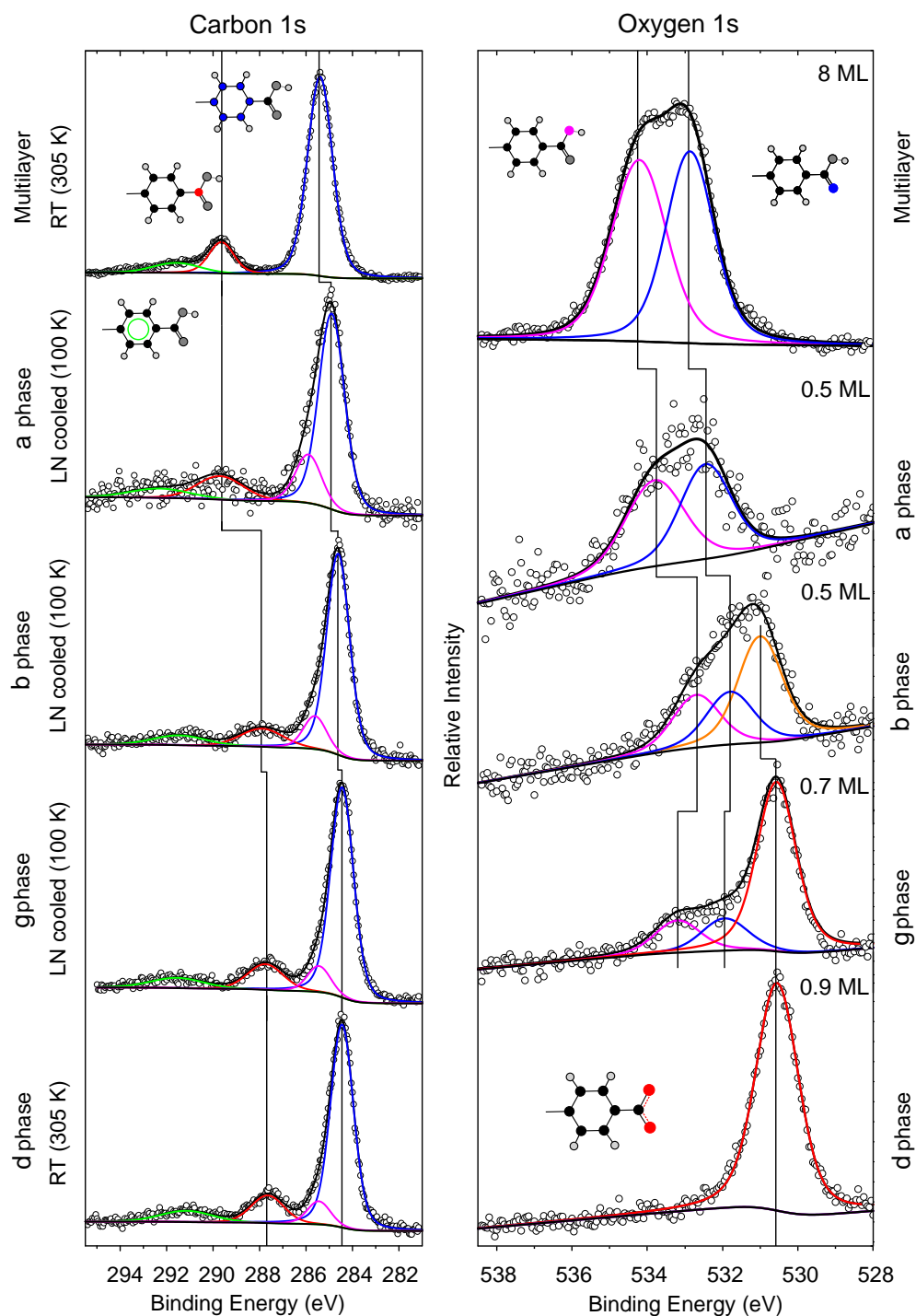


Fig. 5.9: Detailed photoemission spectra of C 1s (left) and O 1s (right) peaks measured for all main BDA phases on Ag (100). Additionally, reference spectrum from BDA multilayer (~ 8 ML) is included in the first row. The thickness of the BDA layer and temperature of measurement is marked in the respective graphs. Coloured atoms in the molecular schematic indicate the corresponding peak in the spectra.

The O 1s peak of multilayer BDA was fitted by two components corresponding to the two distinct oxygen atoms in the carboxylic group. The background was changed to a combined Shirley-linear model. The linear component was included to compensate for a decreasing background intensity at the high binding energy side of Ag 3d peak. The intensity of oxygen components is close to 1:1, which is in agreement with the presence of intact carboxylic groups. The spectrum of the α -phase is qualitatively consistent with the multilayer except for the rigid shift, also observed for the C 1s peak and described above.

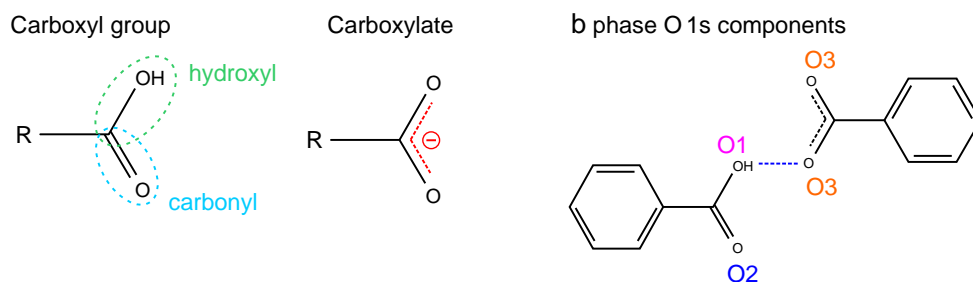


Fig. 5.10: Chemical scheme of the carboxyl and carboxylate groups. Binding configuration of β -phase (right), intact carboxyl group forms hydrogen bond with carboxylate. The spectral components of O 1s peak are marked as O1, O2, and O3 next to the associated hydroxyl, carbonyl and carboxylate oxygen atoms, respectively.

Understanding the XPS spectrum for the intermediate β - and γ -phases presented a substantial challenge. Original hypothesis follows the idea of typical chemical reaction: by annealing, the BDA molecule will undergo deprotonation process. The experiment should yield either protonated or deprotonated BDA molecules with the possibility of a mixed compound of both if the chemical transformation was not completed. The oxygen XPS spectrum was expected to be composed of 3 components, the hydroxyl oxygen (O1) and carbonyl oxygen (O2) of the carbonyl group and carboxylate oxygen atoms (O3) of deprotonated BDA (a reminder of the nomenclature is in Fig. 5.10). This follows the previous studies of the terephthalic acid on Cu(001) [129, 134] and Ag [124].

Indeed, the new oxygen component is present in the β - and γ -phases spectra as was expected due to the presence of new deprotonated molecules on the surface. Additionally, the carbon C4 component was shifted to lower binding energy by ~ 1.8 eV confirming the expected chemical change. However, the oxygen spectrum is significantly shifted compared to the α -phase. Further, the position of the new oxygen component is also shifted compared to the fully deprotonated phase of the BDA. Quiroga et al. [134] explored in detail the similar changes in case of the terephthalic acid on Cu(001). Substantiated by DFT theoretical calculations, they explained that the shifts are a result of the hydrogen bonding environment between partially and fully deprotonated molecules.

Proposed bonding scheme for the BDA β -phase is shown in Fig. 5.10. Deprotonated carboxylate oxygen was assigned to the O3 fitting component at the energy of 531 eV, in agreement with the reported peak component for TPA/Cu [134]. Component O1

Tab. 5.1: Fitting parameters of C 1s spectra components. Noted FWHM value corresponds to Gaussian component. Lorentzian peak width was fixed as 0.1 eV.

	C1		C2		C3		C4	
	(phenyl ring)		(phenyl ring)		(carboxyl)		$(\pi - \pi^*)$	
	BE	FWHM	BE	FWHM	BE	FWHM	BE	FWHM
	eV	eV	eV	eV	eV	eV	eV	eV
BDA	285.4	1.1	-	-	289.65	1.2	291.6	2.2
α	284.9	1.2	285.9	1.2	289.7	2.2	292.3	2.5
β	284.6	1	285.6	1	287.9	2	291.5	2.5
γ	284.45	1	285.45	1	287.75	1.6	291.55	2.5
δ	284.45	1	285.45	1	287.65	1.5	291.15	2

was assigned to hydroxyl oxygen) bonded through hydrogen bond to carboxylate oxygen. Its energy position 532.7 eV is close to reported 532.5 eV [129, 134] and the energy shift from the alpha phase -1.1 eV is comparable with reported value -0.9 eV. Position of the O2 component 531.8 eV is higher than 531.1 eV reported for TPA/Cu. However, the energy shift of the C2 component of 0.7 eV is much closer to the reported value of 1.0 eV. The discrepancy in the peak shifts is possibly caused by different charge transfer between carboxylate and Ag surface compared to the Cu. The ratio of the O1:O2:O3 peak area of the components is 1:1:2, which means the ratio of protonated and deprotonated carboxylic groups is 1:1. This ratio can be explained by either an 1:1 mixture of fully deprotonated and protonated molecules or only partially deprotonated BDA molecules.

In next spectrum of the partially deprotonated BDA γ -phase the O1 and O2 components of the oxygen peak associated with hydroxyl and carbonyl peaks shift back to the higher binding energy. Importantly, the energy separation of these components returned to the value of 1.25 eV (from 0.9 eV in β -phase). This energy is close to 1.35 eV that was observed for the α -phase. Finally, the interpretation of the spectrum of the fully deprotonated δ -phase of BDA was straightforward. The O 1s can be fitted with the single component, associated with carboxylate oxygen, at 530.7 eV, which is in agreement with similar systems [149]. No energy shift compared to the γ -phase was observed. A single component is consistent with the symmetric binding environment of both carboxylate oxygen atoms. Fitting parameters are summarized in the tables: Tab.:5.1 for C 1s and Tab.:5.2 for O 1s.

5.2.3 Structure of the BDA α -phase

The intact BDA α -phase deposited on the Ag surface at room temperature grows in small islands in almost a needle-like fashion. The molecular islands appear to be

Tab. 5.2: Fitting parameters of O 1s peak components. Noted FWHM value corresponds to Gaussian component. Lorentzian component width was fixed as 0.1 eV.

	O1 (hydroxyl oxygen)		O2 (carbonyl oxygen)		O3 (carboxylate)	
	BE eV	FWHM eV	BE eV	FWHM eV	BE eV	FWHM eV
BDA	534.2	1.45	532.85	1.25	-	-
α	533.8	1.6	532.45	1.3	-	-
β	532.7	1.2	531.8	1.2	531	1.1
γ	533.2	1.2	531.95	1.2	530.55	0.95
δ	-	-	-	-	530.55	1.05

preferentially growing out of the substrate steps edges indicating that the step edges present preferential nucleation sites and are not passivated by BDA, contrary to the Cu(001) described in the previous section. Elongated BDA islands preferentially grow in the substrate high symmetry orientations $\langle 110 \rangle$. The μ -diffraction images in Fig. 5.11(b), taken from individual islands, show that there are two rotational domains of the self-assembled BDA. Further, the dark field LEEM images were acquired for both molecular domains, and their superposition over the bright field image confirmed that they include all of the molecular islands on the surface as shown in Fig. 5.11(d).

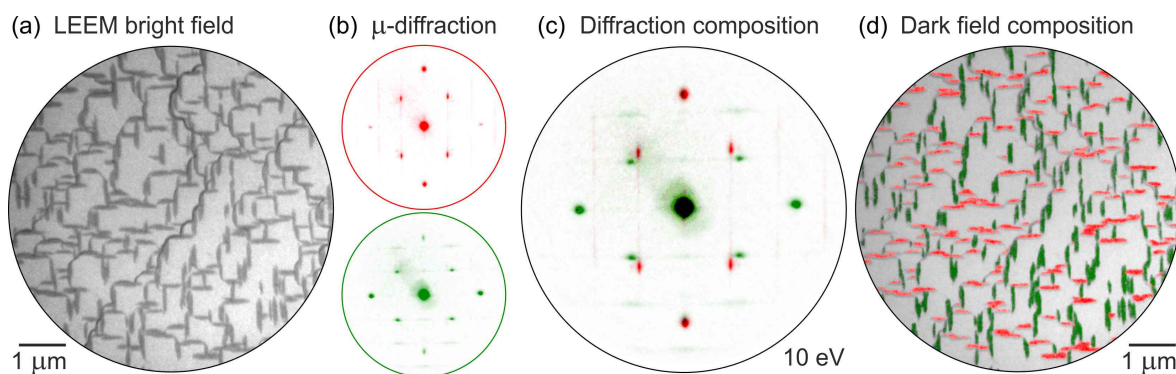


Fig. 5.11: LEEM data of α -phase: (a) Bright field LEEM image where molecular islands appear as a dark features. (b) The μ -diffraction acquired from individual BDA islands. (c) Large area diffraction image overlay with the μ -diffraction images. (d) Dark field images acquired from individual BDA structural domains superimposed on top of the bright field image (a).

The STM measurement revealed a well ordered self-assembled structure of the BDA shown in the overview Fig. 5.8(a) and in more detail in Fig. 5.12. Here, the STM image was aligned based on the previously measured atomic resolution images of clean Ag(100) surfaces. This was reasonable approximation because the position of the crystal in the sample holder was fixed over time. The BDA molecules appear as rod-like pro-

trusions with an apparent height $6.1 \pm 0.6 \text{ \AA}$, length $10.2 \pm 0.5 \text{ \AA}$ and width $3.8 \pm 0.5 \text{ \AA}$. Molecules formed a closely packed structure of straight molecular chains with an inter-chain distance of $5.5 \pm 0.3 \text{ \AA}$. Chains packing exhibits regular periodicity that can also be observed as prominent spots in the μ -diffraction images in Fig. 5.11(b). On the contrary, in the direction of the chains, the spacing of the molecules was variable. This can be observed in the STM image overlaid by a periodic lattice in Fig. 5.12.

Considering the shape of the BDA molecules and XPS chemical information that confirmed their intact chemical state, the BDA molecules were assumed to be arranged in head to head fashion. This assembly is stabilized by electrostatic hydrogen bonding between opposing carboxylic groups in agreements with multiple studies were the hydrogen bond was suggested as a driving force of the BDA self-assembly. The variation in the molecular distances corresponded to alternating intermolecular bonds that are in the range of $2.4 - 3.3 \text{ \AA}$. The bond length was calculated from theoretical BDA length of 11.4 \AA (length from O to O along the molecule) subtracted from measured molecule-molecule distances in STM images. Alternating molecular distances suggests that substrate-molecule interaction will play a significant role in the BDA self-assembly on Ag(100). The $\text{C}=\text{O} \cdots \text{HO}$ hydrogen bond usually maintain a distance of 2.7 \AA in organic crystals [172], however hydrogen bonds on surfaces with length over 3 \AA were identified as weak [36, 173].

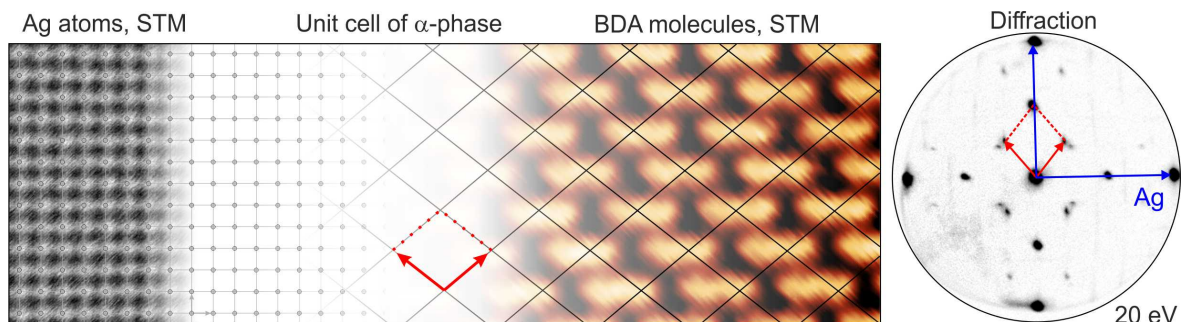


Fig. 5.12: STM data: composition of the atomic scale images of Ag(100) surface with the deposited BDA α -phase and large area ($\sim 300 \mu\text{m}^2$) diffraction pattern acquired at 20 eV.

A low temperature STM/AFM measurement shown in Fig. 5.13, was performed on the BDA α -phase. The measurement utilized a qPlus sensor functionalized by a CO molecule in a commercial CreaTec UHV system [21]. Detail of the self-assembly from STM shows prominent features that appear to be connecting the molecular chains. However, the nc-AFM measurement that reflects the actual height profile of the molecules revealed that these features are formed by non-planar adsorption of the BDA. The two phenyl rings of the molecule are mutually twisted, as shown in Fig. 5.13(b). Additionally, the bright spots are observable between the BDA carboxylic oxygen sites that are a signature of complementary hydrogen intermolecular bonding [174].

Based on the available data: STM, nc-AFM, diffraction pattern and simulating the diffraction spots in the *LEEDpat* [175], the following model was created. Each chain

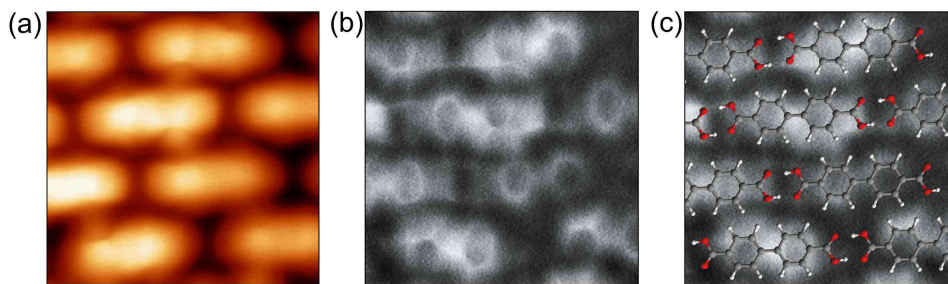


Fig. 5.13: Low temperature measurement: (a) Detail of the BDA α -phase in STM measured at 5 K. (b) nc-AFM image of the same area measured with qPlus sensor functionalized by CO molecule. (c) nc-AFM with model of the BDA molecules.

of the BDA molecules lays over two Ag atoms in the $\langle 100 \rangle$ directions of the Ag (001) surface. Both oxygen atoms are located near the on-top sites at similar heights, and the lateral repulsion of the molecular arrangement twists the phenyl rings of the BDA molecules differently as seen in the AFM data. The α -phase unit cell most closely approaches $\left(\frac{2}{2} \frac{-2}{14/5}\right)$, modelled in Fig. 5.14(b). Hydrogen bond length corresponding to this unit cell can be calculated 0.245 \AA , which corresponds to the measured minimal lengths from STM images (strongest hydrogen bond). However, hydrogen-bonded pair of BDA at the optimal position is incommensurate with the substrate periodicity.

The mutual distance between two BDA molecules is governed by BDA-BDA optimal hydrogen bonding length, but the BDA-substrate interaction is maximal for the optimal position of BDA in respect to substrate atoms. Hence, with every new BDA in a chain, the BDA-substrate shift is increased. Once it surpasses the hydrogen bond energy, it will become more energetically favourable to break the hydrogen bond and align the BDA position with respect to the substrate. The resulting irregular intermolecular spacing caused by competing BDA-BDA and BDA-substrate interactions can be observed as tear in the self-assembly. It is most prominently visible in the LT-STM image shown in Fig. 5.14(a). These tearing is also visible in the room temperature images, but in this case STM measures the time-averaged image of dynamically reordering molec-

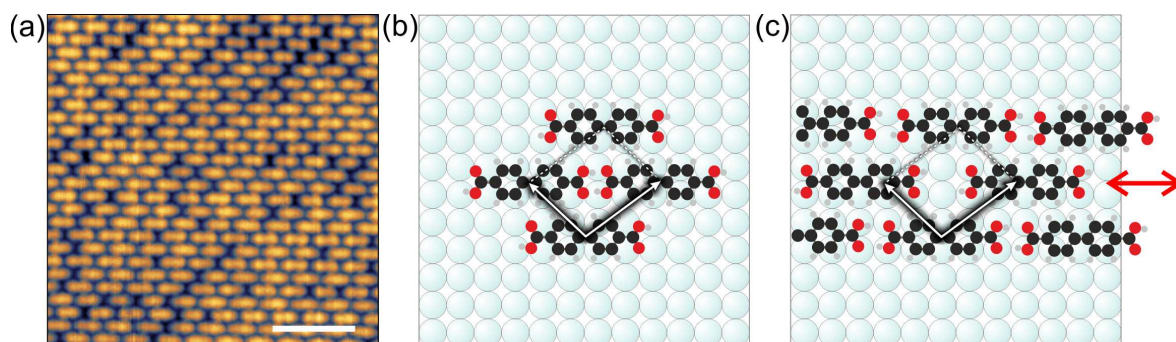


Fig. 5.14: (a) LT-STM image of the BDA α -phase with visible tearing of the self-assembly. Scale bar is 4 nm. (b) Model of the BDA α -phase unit cell and (c) model with the shifted molecules resulting in an observable space between the molecules and shift of chain arrangement.

ular positions within the molecular rows. These observations are in agreement with the recent work on TPA/Cu (111) system [126]. Variable intermolecular arrangement of BDA results in one additional phenomenon, prominent lines features (called also streaks) in the BDA α -phase diffraction patterns. These are a consequence of multiple available arrangements of the neighbouring molecular chains.

5.2.4 Structure of the BDA β -phase

The formation of the BDA β -phase was thermally induced by annealing to approx. 70 °C. The new phase consist of larger molecular islands, compared to the α -phase, as shown in Fig. 5.15(d). The diffraction image taken from the displayed area is formed by a combination of four rotational domains of the β -phase. Each domain is shown in Fig. 5.15(c) and was measured from individual islands acquired by μ -diffraction aperture in the LEEM. Observation of four rotational orientations is consistent with unit cell rotation in respect to principal substrate directions and the fourfold substrate symmetry. Additionally, individual islands of corresponding rotations were visualized with dark-field imaging, and the coloured composition image is displayed in Fig. 5.15(e). All of the domains were homogeneously distributed on the Ag surface. The unit cell of β -phase contains four BDA molecules and exhibits the interlocked row structure as can be observed in the STM Fig. 5.15(a). The molecules appear to be tilted toward each other by approx. 20°.

Detailed LT-STM/nc-AFM measurement revealed that β -phase distinct row structure is caused by bent BDA molecules as showed in Fig. 5.16(b-d) where higher molecules appear brighter. Additionally, only one bright spot on average can be observed between the BDA molecules suggesting that BDA molecules are creating carboxylate-carboxyl hydrogen bonds as can be observed in the detailed nc-AFM images. Here, only the higher positioned oxygen atoms of BDA, that are engaged in the hydrogen bonds, are visible. Additionally, bending of the molecules can be explained as a stronger interaction with the substrate by the carbonyl oxygens. The bonding mechanism is supported by the XPS data, which showed that, chemically, the β -phase consists of an equal ratio of protonated and deprotonated carboxylic groups. Unexpectedly, the nc-AFM data showed the presence of all molecular types i.e. intact, partially- and fully- deprotonated molecules as showed in Fig. 5.16(d). This suggests that the deprotonation process is random, and both carboxylic groups of the BDA can deprotonate independently. Therefore, statistically, the ratio of BDA molecules: 2H-BDA:1H-BDA:0H-BDA should be 1:2:1. However, a small area of measurement restricted by the capabilities of the nc-AFM does not provide sufficient evidence for this hypothesis.

The schematic model describing the β -phase in Fig. 5.16(e) shows that one row of BDA molecules is oriented in the substrate $\langle 110 \rangle$ directions and similarly to the α -phase molecules adsorb over 2×5 Ag atoms. In the second row, the molecules are rotated with respect to the substrate, and here the molecules occupy three rows of Ag atoms. However, there is slight modulation in the position of BDA molecules over the

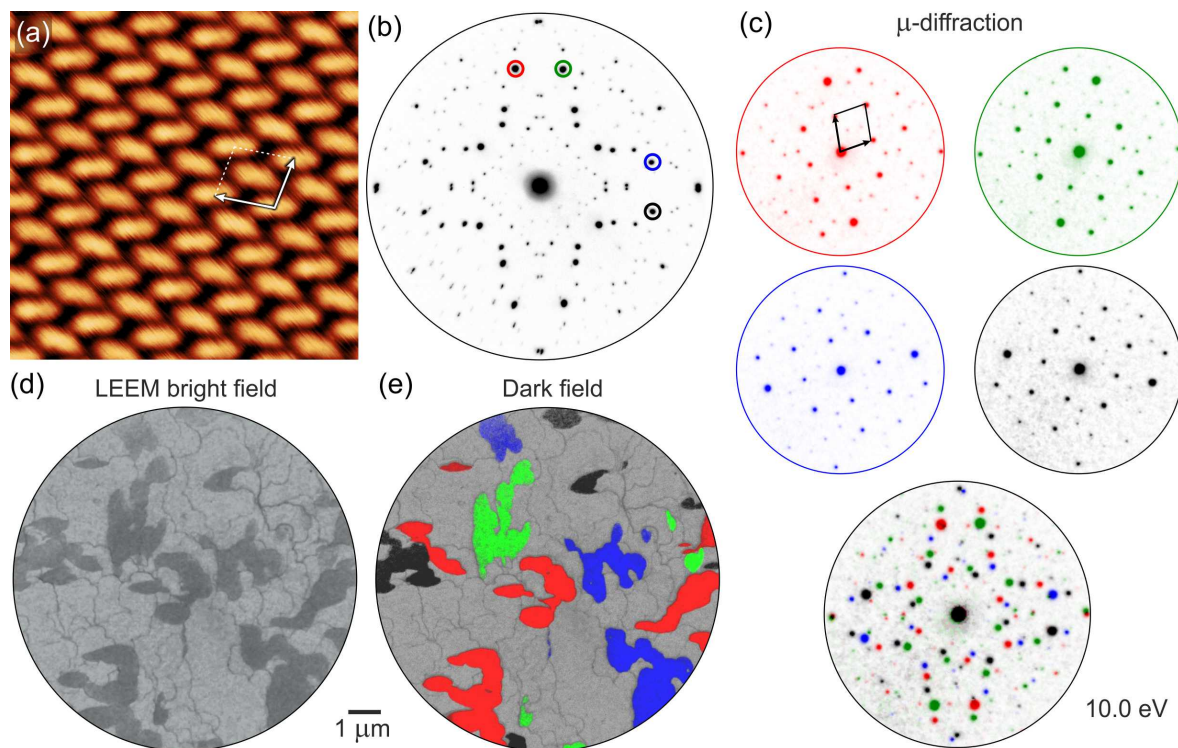


Fig. 5.15: (a) STM and (d) LEEM image of the β -phase. (b) Wide area diffraction captured at 10 eV. (c) Diffraction pattern taken from individual molecular islands and their composition with the wide area diffraction below. (e) Composition of 4 dark field images taken from diffraction spots marked in the (b).

substrate atoms resulting in height variation of the BDA. This gives rise to the weak moiré pattern shown in Fig. 5.17(a).

Further, the β -phase μ -diffraction pattern acquired at 20 eV can be de-constructed into three components: substrate spots, β -phase and the moiré pattern. The moiré has significantly larger unit cell; however, only two diffraction spots can be observed per BDA unit cell. The STM data in Fig. 5.17(b) support the presence of the moiré pattern, which can be observed in the small height variations of BDA molecules only after enhancing the STM z-axis colour scale. The moiré periodicity can be described in matrix notation as $\begin{pmatrix} 3 & -2 \\ 3 & 5 \end{pmatrix}$ in respect to the β -phase unit cell. The overall complex diffraction pattern of the β -phase can be reproduced by simulations with BDA superlattice matrix $\begin{pmatrix} 4 & -32/21 \\ 1 & 33/7 \end{pmatrix}$ in respect to the Ag(100) unit cell.

5.2.5 $\alpha \Rightarrow \beta$ phase transformation

The real-time observation of the structural transition between the BDA phases was possible thanks to the fast image acquisition in the LEEM. The sample was heated at a rate of approx. 1 – 3 °C/minute. During the transformation, the bright-field images were recorded every 1 s and the thermal drift of the sample was corrected later in the data processing. In the initial moments of heating the α -phase islands undergo significant morphological changes without change of the self-assembly structure. Some

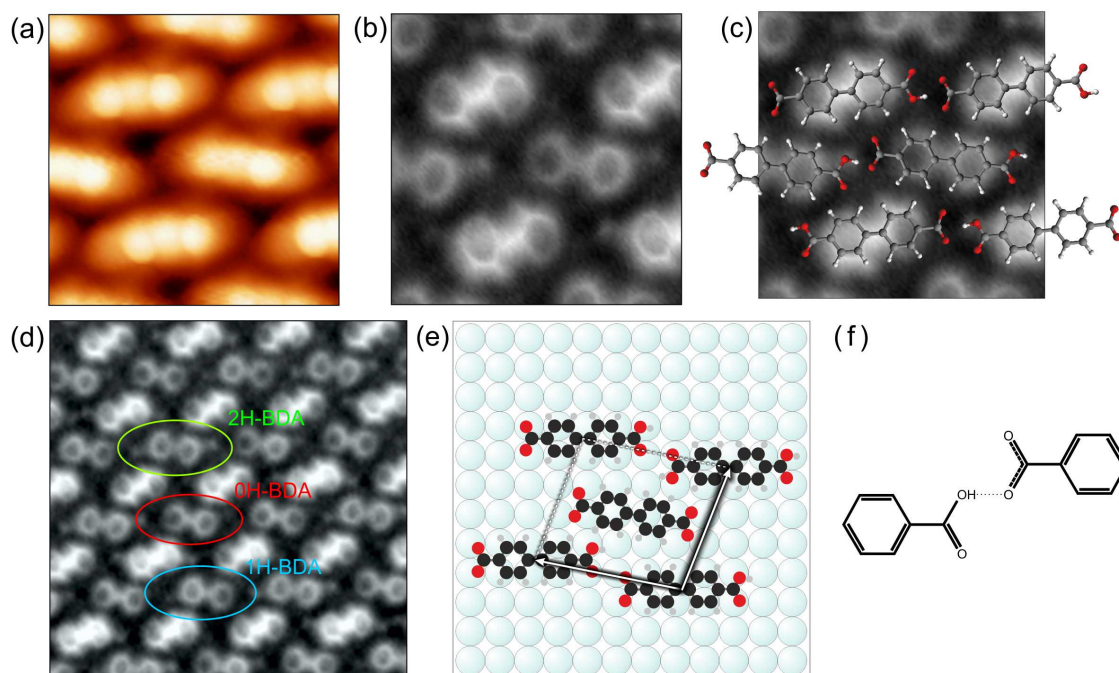


Fig. 5.16: (a) LT-STM detail of the BDA β -phase and (b) corresponding nc-AFM image acquired with the CO functionalised tip. (c) The molecular models of partially deprotonated BDA positioned on the nc-AFM image. (d) Large area nc-AFM image of the β -phase showing random placement of the 2H-, 1H- and 0H-BDA molecules in the self assembly. (e) Model of the β -phase arrangement on the Ag(100) surface and (f) illustration of the bonding mechanism.

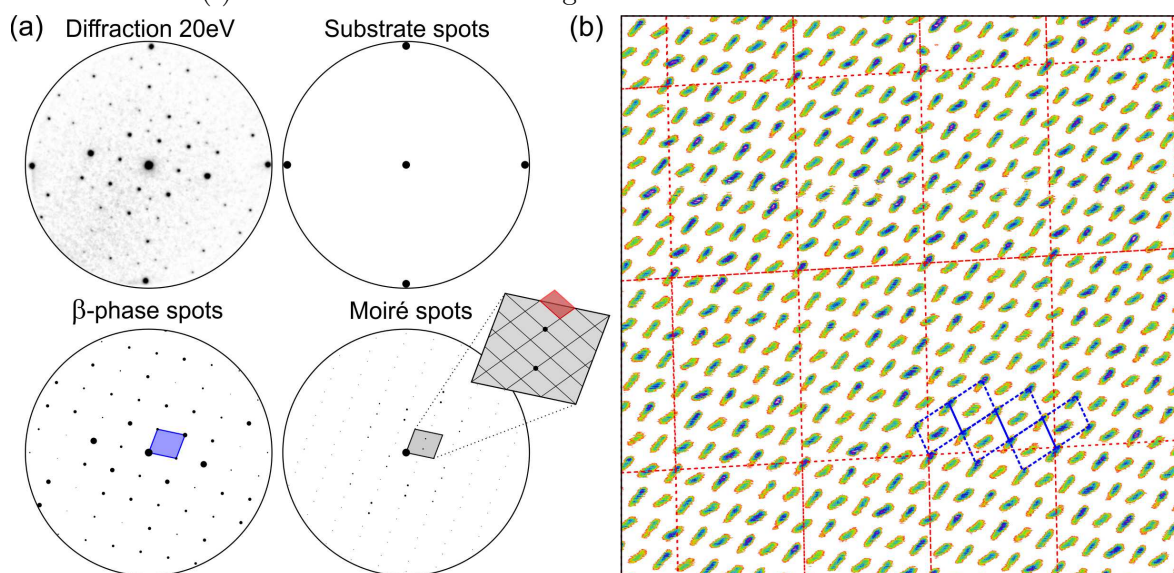


Fig. 5.17: (a) Decomposition of the β -phase μ -diffraction pattern acquired at 20 eV. The unit cell of the β -phase is marked by blue and same area in the moiré pattern that encompasses the two visible moiré spots is marked is enlarged on the right. (b) STM image with enhanced colour scale focusing on the highest features of BDA molecules. Corresponding unit cells are drawn by dashed lines.

of the smaller BDA islands decrease in size, and simultaneously other islands grow. This phenomenon is known as Ostwald ripening. Change of the size of the molecular islands during a 40 s period at 70 °C can be observed in Fig. 5.18(a-b). Additionally, the BDA islands were masked (green areas), and the island boundary from the initial image was drawn in the second image to enhance the visibility of small size changes of the islands.

The BDA molecules are moving between the island in the state of 2D gas, available on the surface. In fact, each molecular phase coexists in thermal equilibrium on the surface with corresponding 2D molecular gas. This can be observed as noise shown in Fig. 5.18(c) or rapid changes at the edges of the molecular islands in the STM images [176, 177]. In the case of 2D molecular gas, each molecule passing under the tip temporarily increases the tunnelling current and appears as an increased height (in the constant current mode).

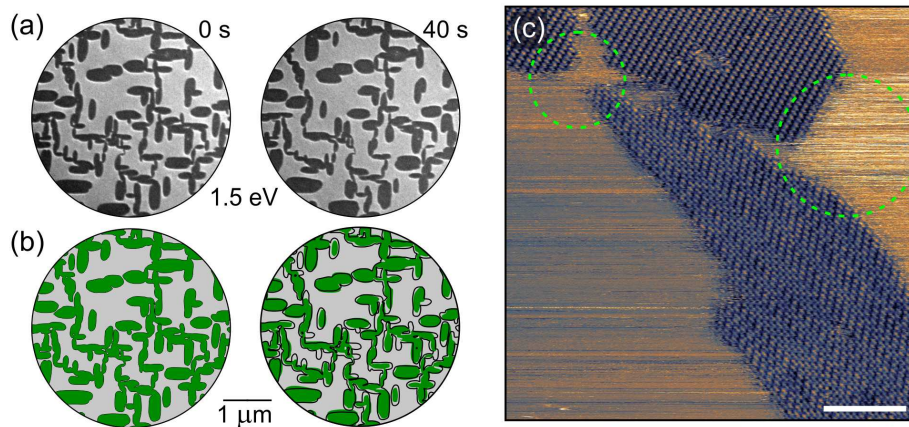


Fig. 5.18: (a) Two bright field LEEM images of $\alpha \Rightarrow \beta$ phase transformation of the same area after 40s, taken at temperature 341 K. (b) BDA islands masked by green areas with boundary lines of initial islands shape inserted in the image after 40s. (c) Unprocessed STM image of BDA phases with z-scale focused on the noise observed on Ag substrate. Green circles mark the increased noise between the molecular islands where, presumably, the 2D molecular gas density increases.

Progress of $\alpha \Rightarrow \beta$ transformation in 10 s intervals is shown in Fig. 5.19. The LEEM bright-field images were acquired at the energy of 1.5 eV where both phases have good contrast with respect to the Ag surface and each other. After reaching sufficient temperature, the nucleation of the β -phase starts simultaneously over the sample surface without any preferential nucleation sites. Transformation progresses rapidly compared to the heating rate. Islands of the β -phase grow larger at the expense of the α -phase in their close proximity. They appear to create a capture zone in which the α -phase islands quickly dissolve, however the α -phase islands outside of the zone remain intact. This process is significantly affected by the surface atomic steps which are hindering the diffusion of the molecules in the 2D gas. Therefore, at the more stepped surface, as shown in Fig. 5.19(b), the β -phase grows in smaller islands. Here, the nucleation is forced on atomic terraces after reaching sufficient saturation of transformed molecules. Typical

phase transition can be viewed in supplementary video file no. 3 (*3-AlphaToBeta.avi*)

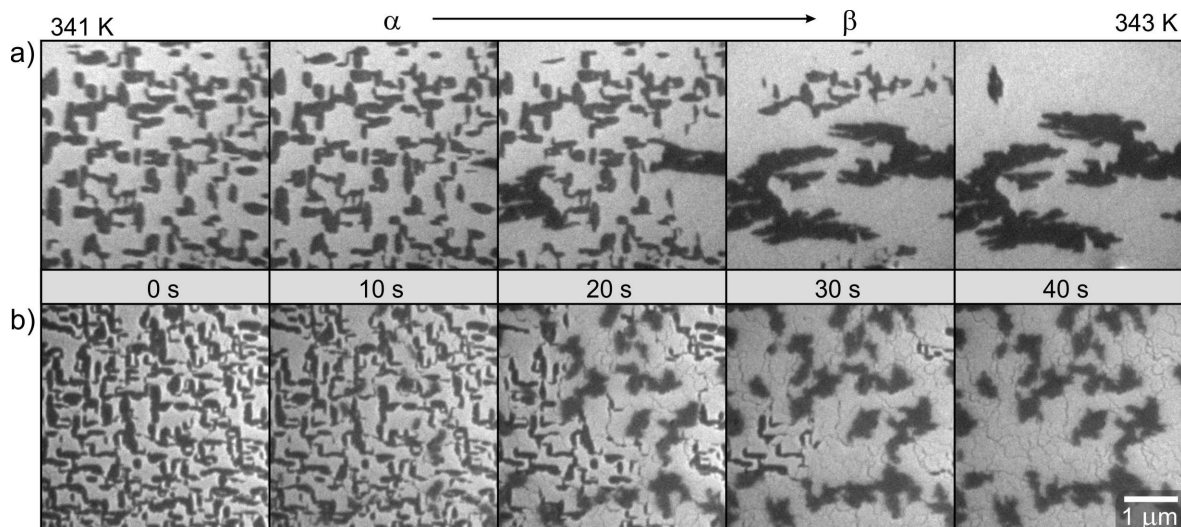


Fig. 5.19: Bright field LEEM images of $\alpha \Rightarrow \beta$ phase transformation progress in 10 s intervals. Surface of Ag(100) with small (a) and high (b) atomic step density (different experiments). Images acquired at 1.5 eV.

The structural transformation of the α to β -phase also occurs at room temperature (RT), after approx. 12 hours. An XPS measurement confirmed gradual deprotonation of the BDA at RT. However, contrary to the thermally induced transformation, the RT β -phase grows in smaller islands on the edges of the α -phase islands.

5.2.6 Structure of the BDA γ -phases

The next step in the BDA self-assembly within the deprotonation process is the γ -phase. Chemical and structural transformation starts at approx. 120 °C and leads to a sequence of γ -phases with different ratio of protonated, semi- and fully- deprotonated molecules. Originally only one γ -phase has been observed (γ_2) consisting of a sequence of alternating lines (2 and 1 rows) of distinct BDA molecules as shown in Fig. 5.20. This phase appears to be chemically and structurally most stable. However, with careful annealing and appropriately chosen LEEM observation energy, it was possible to distinguish more complex transformation progress from β -phase.

Initially, new γ_3 -phase has been formed. It is chemically similar to the β -phase as shown in Fig. 5.21(a). The (hydroxyl + carbonyl):carboxylate ratio of O 1s components is (0.26+0.27):0.47, which is close to the ratio observed for the β -phase. Structurally, it consists of alternating rows of 3 and 1 BDA molecules as shown in the STM image in the first row of Fig. 5.20. This phase was first to exhibit morphologically different types of BDA molecules in STM. This suggests heterogeneous binding motifs of two types. (I) binding between a single row and multi-row and (II) binding inside the multi-row. It can be assumed, considering the chemical composition of the γ_3 -phase, that a 0H-BDA molecule forms the single row line in the structure and, from a side, bond to the phenyl rings of a 1H-BDA molecule, while the protonated end-groups of the 1H-BDA molecules

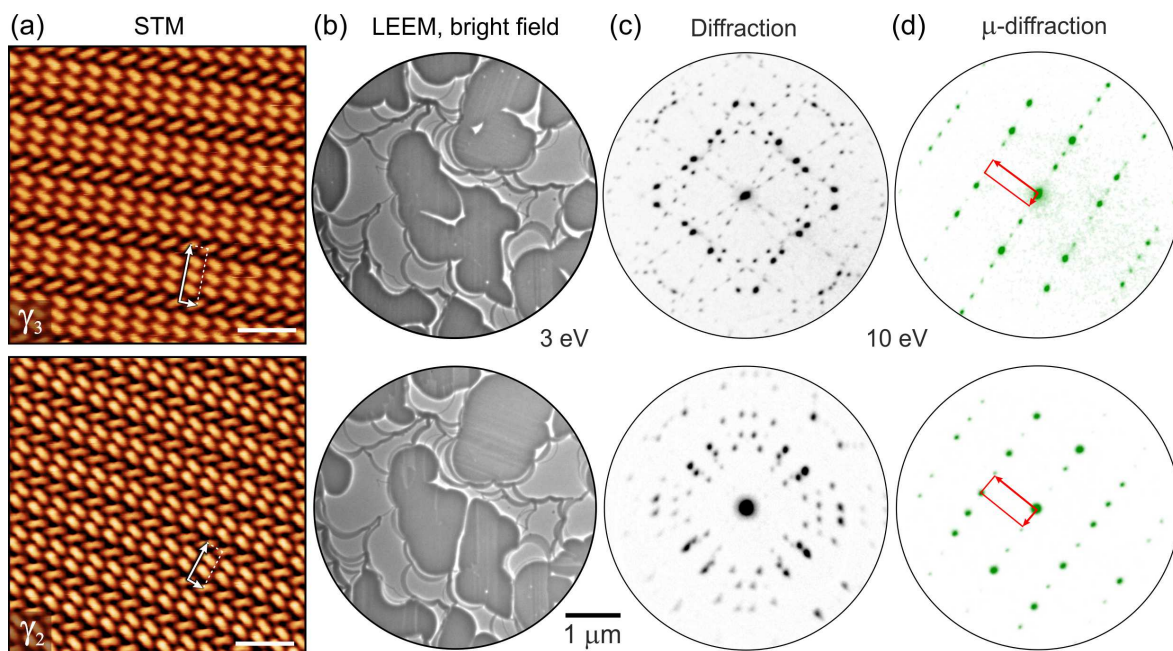


Fig. 5.20: Two most stable observed γ -phases: (a) STM images with scale bar 3 nm; (b) bright field LEEM images taken from the initial and final moments of the BDA β to γ_2 transformation, acquired at 3 eV; (c) Diffraction images measured at 20 eV and (d) single domain μ -diffraction patterns.

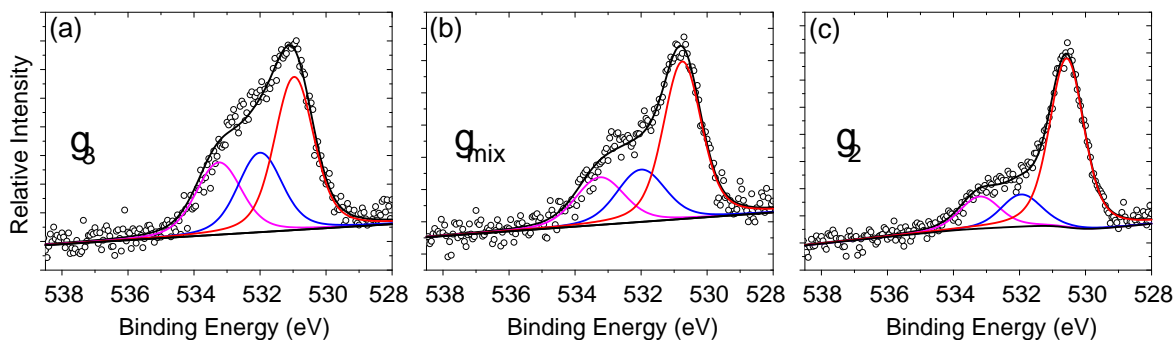


Fig. 5.21: Detailed XPS spectra of O 1s peak of structurally distinct γ -phases with increasing level of deprotonation.

bind to 2H-BDA molecule inserted between them in the multi-row arrangement of γ_3 -phase. Additionally, XPS spectra show the hydroxyl and carbonyl components of O 1s peak shifted to higher binding energies, confirming a change in the binding motif (from carboxyl-carboxylate to carboxylate-phenyl and carboxyl-carboxyl, Fig. 5.21).

Evolving deprotonation process further induced new structural transformation. Gradual changes in the chemical composition are shown in Fig. 5.21. The hydroxyl and carbonyl components of the O 1s peak decrease while the carboxylate component increases. Structurally, the transformation ended with the stable γ_2 -phase, where the ratio of the protonated to deprotonated oxygen groups is $(0.15+0.15):0.7$. Considering the two:one row structure observed in STM, it can be reasonably assumed that the γ_2 -phase is formed by one row of deprotonated 0H-BDA and two rows of 1H-BDA as

shown in Fig. 5.22. In this configuration, the ratio of different oxygen groups would be (1+1):4, which is close to the ratio measured by XPS (0.15+0.15):0.7. The self-assembly in this case will be governed by bi-functional 1H-BDA molecules that (I) bind to each other with carboxylic groups and (II) bind to the side of the phenyl ring of the 0H-BDA row with the carboxylate end-groups.

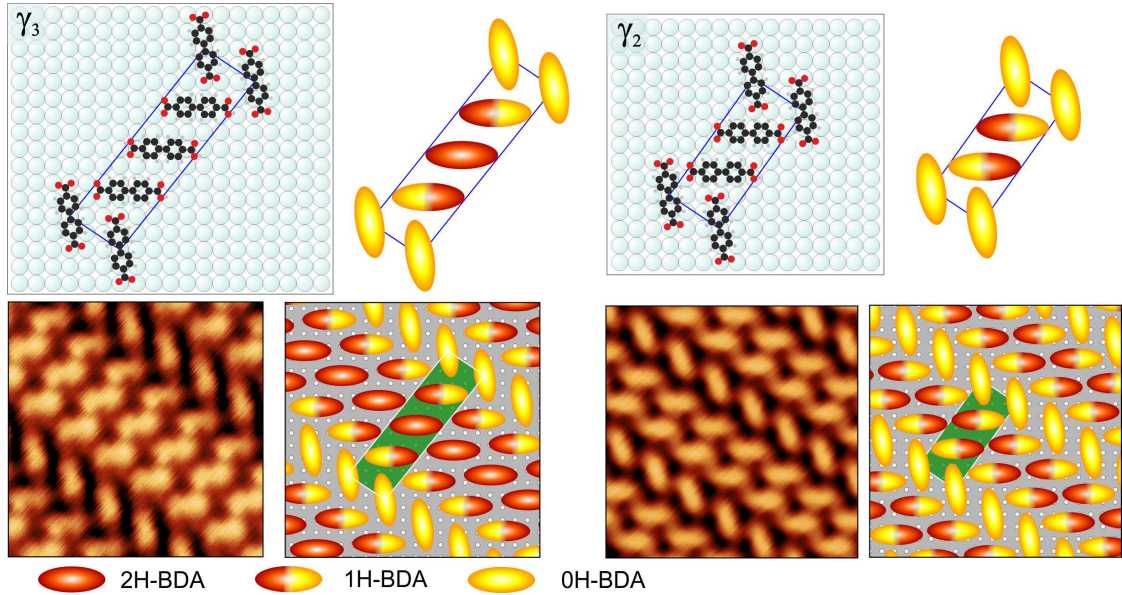


Fig. 5.22: Model of the γ_2 and γ_3 phases. 2H- and 1H-BDA molecules are oriented in the direction of the Ag atomic rows analogous to the α and β -phase. Fully deprotonated 0H-BDA molecules are tilted by approx. 10° with respect to the Ag atomic rows.

Both γ_2 and γ_3 phases form larger molecular islands compared to the β -phase. At the same time, their structure has similar four symmetry equivalent rotational domains. The μ -diffraction images from each domain of the γ_3 -phase are shown in Fig. 5.23. Due to the sensitive transformation conditions, it has not been possible to acquire nc-AFM data for the γ -phases (measured in the system without LEEM). Instead, the construction of molecular model relied entirely on the STM and LEEM diffraction data.

The unit cell of the structure cannot be measured directly from the LEEM diffraction pattern due to the distortions arising in the LEEM imaging system. In order to find the correct model of the structure, multiple diffraction patterns have been simulated in the *LEEDpat* software. Based on the mutual position of the individual spots, it is possible to confirm the validity of the proposed model precisely. Additionally, combining simulated μ -diffraction images of four equivalent domains and comparing resulting composition image to the large area diffraction it is possible to focus on specific details between similar models and chose the best match as shown in the enlarged detail in Fig. 5.23.

The unit cell of the γ_3 -phase best matches $\begin{pmatrix} 8 & 10 \\ -3 & 2 \end{pmatrix}$ parameters and that of the γ_2 -phase $\begin{pmatrix} 5 & 7 \\ -3 & 2 \end{pmatrix}$ in matrix notation. The precise molecular positions were obtained by combining the LEEM and STM data. The RT-STM (room temperature STM) images

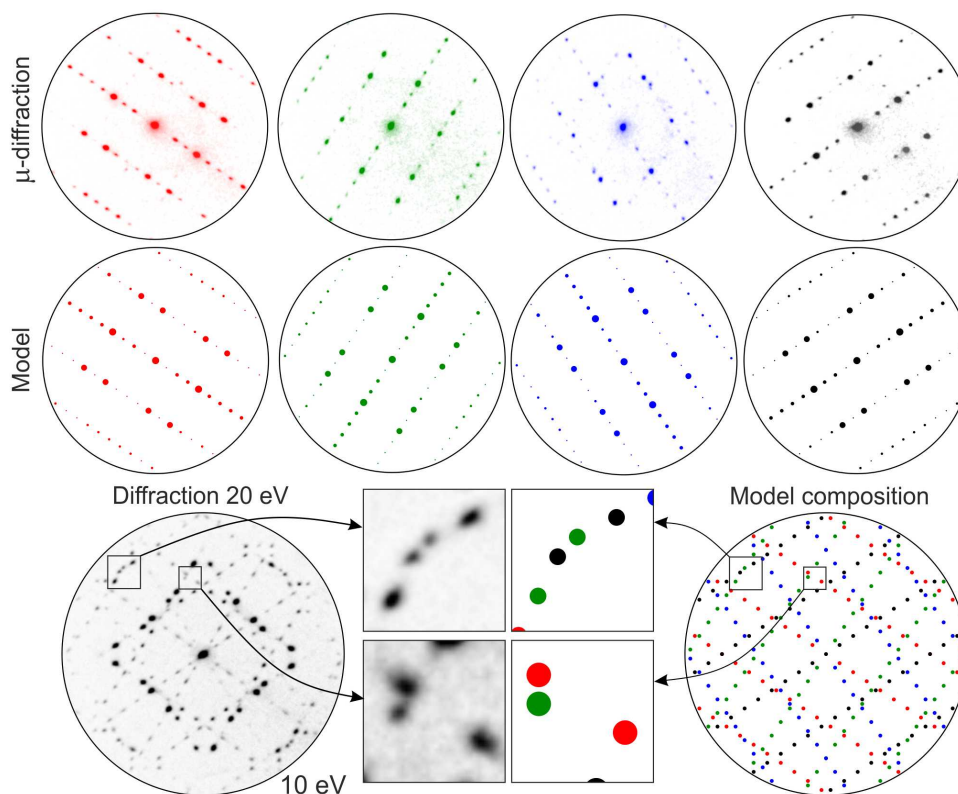


Fig. 5.23: Diffraction model of the γ_3 -phase: μ -diffraction images of four individual structural domains (top) and corresponding simulated patterns below presented in a different color for each domain. Measured large area diffraction (bottom), a composite image from the simulated patterns and enlarged details for comparison.

were superposed on the atomic resolution images of the Ag(100) surface of the same crystal. In this way, it was possible to obtain approximate rotation of the molecules towards the substrates. Although the STM images were corrected for a linear drift, additional non-linear distortions, the tilt of the sample towards the piezo or other factors usually prevented the precise determination of the unit cell solely from the RT-STM data. Moreover, when measuring with tunnelling conditions for atomic resolution (high current, low voltage), the relatively weak molecule-substrate binding resulted in the destabilization of the self-assembled structure. This prevents the simultaneous imaging of the substrate and self-assembled BDA structures at RT.

Corrected RT-STM images from multiple measurements were overlaid with the unit cell from simulated diffraction patterns to find the correct BDA positions. Additionally, the binding motifs of the α -, β - and δ -phase (introduced in the next section) and the chemical composition from the XPS were considered during the constitution of the self-assembly model shown in Fig. 5.22. Here, the fully- and semi-protonated BDA molecules lie parallel to the $\langle 100 \rangle$ directions of the Ag(001) surface similarly to the α -phase. In the case of the γ_3 -phase, these positions of the molecule over the Ag atomic rows are slightly shifted to fill the area between the fully deprotonated molecules optimally. The bonding of the OH-BDA to the Ag substrate is expected to

be the strongest and therefore being the dominating force of the self-assembly. Indeed, the position of the deprotonated molecules with respect to the substrate appears to be the same in both the γ_2 and γ_3 -phase.

5.2.7 $\beta \Rightarrow \gamma$ phase transformation

Initial relatively small changes in the β phase islands can be observed after annealing to approx. 130 °C. The BDA islands first evolved into the γ_3 phase, which then develops into an intermediate phase or mixed phase and finally transforms into the γ_2 -phase. First, the γ_3 -phase starts to nucleate inside of the β islands. These structures are homogeneously distributed and can be observed as darker spots in the LEEM bright-field images, as shown in Fig. 5.24(a). The dots continuously grow in time, both in number and size, and once the islands are fully transformed they continue to grow and coalesce with the surrounding γ_3 islands. Additionally, dissolution of β -islands without the formation of the new islands have been observed in case of lower BDA coverages or when the β islands are isolated from other islands by a certain distance. Only the internally transformed γ_3 then serves as a nucleation point, and when the new phase reaches β -phase island boundary (from within), the transformation quickly progresses as shown in Fig. 5.24(b). These observations suggest that a significant energy barrier exists for γ_3 nucleation outside of the β -phase.

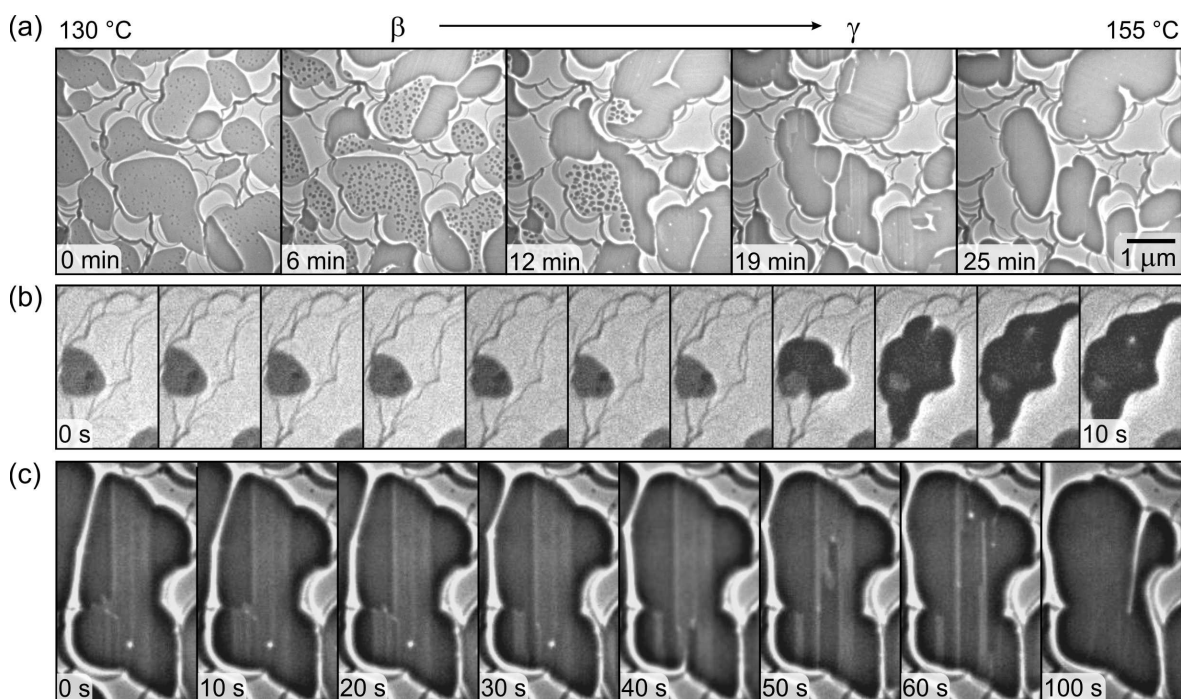


Fig. 5.24: Bright field LEEM images of thermally induced β to γ BDA phase transition. Initially small islands of γ_3 form inside of the β -phase.(b) Dissolution of the β island followed by quick growth of the γ phase island. Short time period of the transformation, 1 s per window. (c) Internal transformation of the mixed phase to the γ_2 -phase.

In the second stage, the transformation continues as an inner conversion of γ phases. The γ_2 -phase first forms on the island periphery and later inside of the islands as shown in Fig. 5.24(c). Internal transformation is slower compared to the initial transformation; however, it is still relatively fast, approx. 2 min., and experiment with lower annealing rate ($< 1 \text{ }^\circ\text{C}/\text{min}^{-1}$) was required to properly capture it in LEEM. Two main observations can be drawn from the sequence of images: (I) the transformation is propagating along with narrow stripes and (II) brighter spots appear at the forefront of the transformation. Entire phase transformation of β to γ_2 -phase can be viewed in supplementary video file no. 4 (*4-BetaToGamma.avi*).

To explain the (II) observation, we consider the differences in packing of molecules in the γ structures. Surface area per one BDA molecule in each phase of the BDA on the Ag(100) surface is plotted in Fig. 5.25(a). The data points were calculated from the unit cells of presented BDA models (blue), and additional data from the STM images are included (red) for reference (sanity check). The STM data points were calculated from the unit cells obtained by FFT (Fast Fourier Transform) of the surface scans with the exception for the γ_3 data point marked as a star. A sufficiently large image of the γ_3 BDA phase could not be acquired to reliably perform the FFT analysis.

The molecular density of γ_2 -phase calculated from the unit cell vectors, is higher than the density of γ_3 -phase. Therefore, it can be hypothesized that the observed bright spot represents a propagating cavity within the self-assembly. The cavity enhances the rate of transformation as the molecules can rearrange into the new structure while remaining in contact with Ag surface.

High directionality of the transformation (observation I) can be explained by the cavity defect propagating along the rows of the γ_3 -phase. Some structural defects of similar nature can be found in the STM images of the mixed γ -phase shown in Fig. 5.25(c) marked by green circles. Here, both γ -phases coexist on the Ag surface. The mixed-phase is usually observed as the γ_3 -phase slowly transforms during the sample transfer and prolonged data acquisitions. The γ_3 and γ_2 -phase can seamlessly interconnect as the position and orientation of the deprotonated BDA molecule in the self-assembly is the same for both phases (i.e. both phases have the same unit cell vector along one side) as shown in Fig. 5.25(b). The seamless connection of the two phases may be the key in enabling the internal transformation mechanism with a sharp directional propagation.

5.2.8 Structure of the BDA δ -phase

The last of the self-assembled structures of BDA on the Ag(100) surface, the δ -phase, was formed by the fully deprotonated molecules. The STM image, shown in Fig. 5.26(a), reveals that the BDA is arranged in an alternating row structure with the front of the molecule touching the side of the next row of molecules. The formation of the δ -phase was thermally induced by annealing above the $150 \text{ }^\circ\text{C}$. The new phase consists of molecular islands which have similar size compared to the γ -phase, as shown

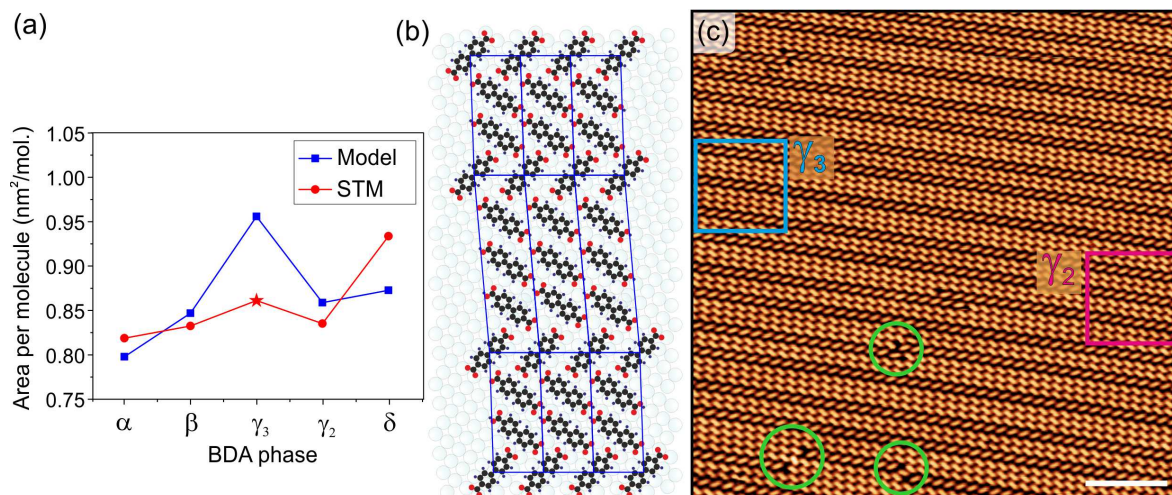


Fig. 5.25: (a) Surface area per one BDA molecule (or inverse molecular density) of each phase of the BDA on the Ag(100). (b) Model of the extended molecular structure for a mixed phase joining the γ_3 and γ_2 -phase on the the Ag(100) surface. Unit cells are marked by blue lines. (c) STM image of the mixed γ -phase. Defect where the γ_3 rearrange into the γ_2 -phase are marked by green circles. Scale bar is 5 nm.

in the LEEM image in Fig. 5.26(d). Here, the contrast of the molecular island is reversed, and they appear bright because the image was acquired at higher energy 6 eV. The diffraction pattern taken from the displayed area is formed by a combination of four rotational domains of the δ -phase similarly to the previous γ and β phases. The individual domains were visualized by dark-field imaging from the selected diffraction spots, and their coloured composition image is displayed in Fig. 5.26(e). The unit cell of the δ -phase is marked in the STM image Fig. 5.27(a), and in the μ -diffraction patterns measured from the individual island, Fig. 5.26(c).

Low-temperature nc-AFM data revealed that molecules in one of the rows are flat and slightly buckled in second one, where BDA molecules protrude outward as shown in Fig. 5.27(a-c). Absence of the bright feature between the molecules suggests that molecules are fully deprotonated as previously determined by the chemical analysis from XPS. As a result, BDA molecules are stabilized by a strong interaction between the carboxylate oxygen atoms and the substrate. In the self-assembled structure, BDA molecules are tilted toward each other by approx. 75° and the carboxylate end groups point to the phenyl rings of the molecules in the next row.

A detailed analysis of the diffraction patterns and STM images revealed, that the unit cell of the δ -phase is $\begin{pmatrix} 3 & 5 \\ -3 & 2 \end{pmatrix}$, in matrix notation. Model of the δ -phase is shown in Fig. 5.27(d). Here, it can be observed that molecules in one of the rows are adsorbed in the direction of the Ag surface atoms and occupy 2×5 Ag atoms. Comparison of atomic resolution STM images of the Ag surface and the δ -phase self-assembly identified that the slightly deformed BDA molecules that appear brighter in the STM images are tilted by approx. 15° with respect to the principal Ag direction $\langle 110 \rangle$. In this configuration, there is a subtle difference in the positions of the carboxylate oxygens between the two differently positioned molecules that lead to their different adsorption heights, as

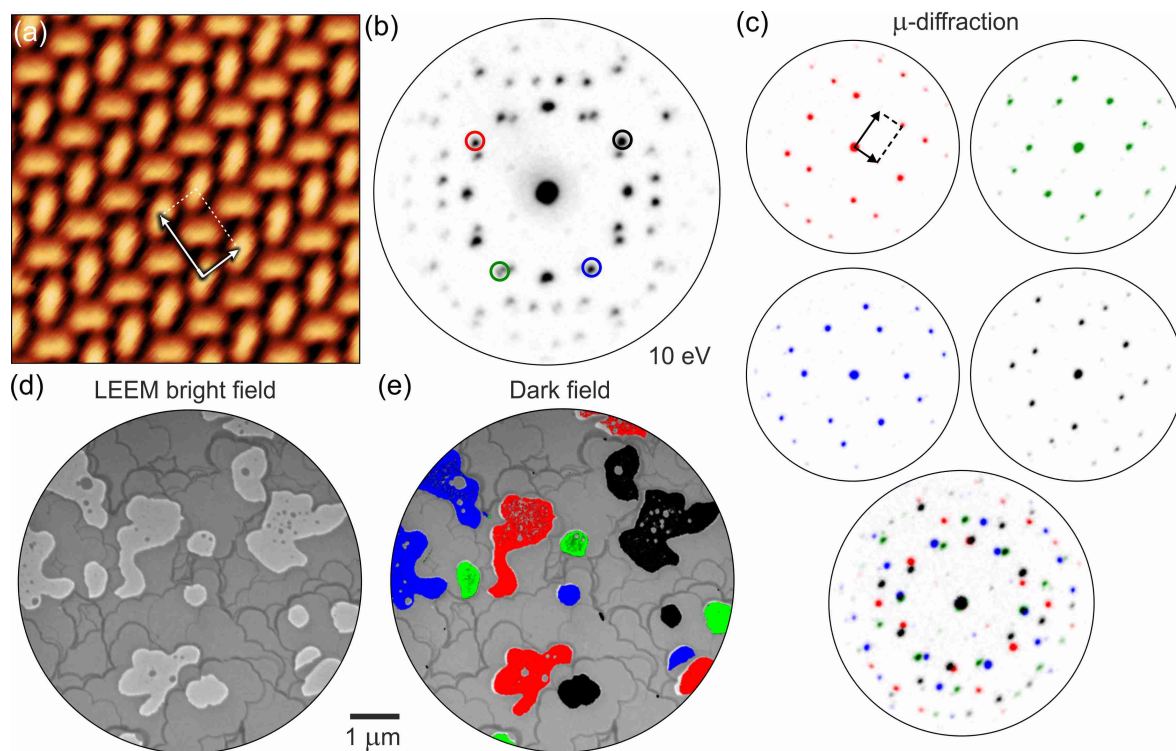


Fig. 5.26: (a) STM and (d) LEEM image of the δ -phase. (b) Wide area diffraction captured at 10 eV. (c) Diffraction pattern taken from individual molecular islands and their composition with the wide area diffraction below. (e) Composition of 4 dark field images taken from diffraction spots marked in the (b) with respective color.

captured in the nc-AFM images.

δ -phase transformation

The transformation of the γ_2 to δ -phase is shown in Fig. 5.28. Some of the molecular islands nucleate on the periphery of the γ_2 -phase islands and continue to grow. However, majority of the new phase formation takes place internally, similarly to the γ_3 to γ_2 transformation. Again, it can be observed that the growth is partially propagated through bright spot (presumable cavities in the self-assembly). However, the difference in γ_2 and δ molecular surface density is negligible (shown previously in Fig. 5.25) and the mechanism of the cavity formation, if in fact present, must be different from the β to γ transformation. Full video of the transformation can be viewed in the supplementary file no. 5 (*5-GammaToDelta.avi*).

The higher temperature, for example, compared to the γ transformation may allow for easier desorption of the BDA molecules from Ag surface inside of the transformation front. Additionally, the transformation also continues to propagate in all directions and is not limited to the narrow stripes as in the case of γ_2 .

The role of the Ag adatoms in the overall BDA deprotonation process has also been tested. The Ag thermal evaporator was installed directly into the LEEM chamber. Evaporation of Ag atoms during the annealing experiments did not enhance the

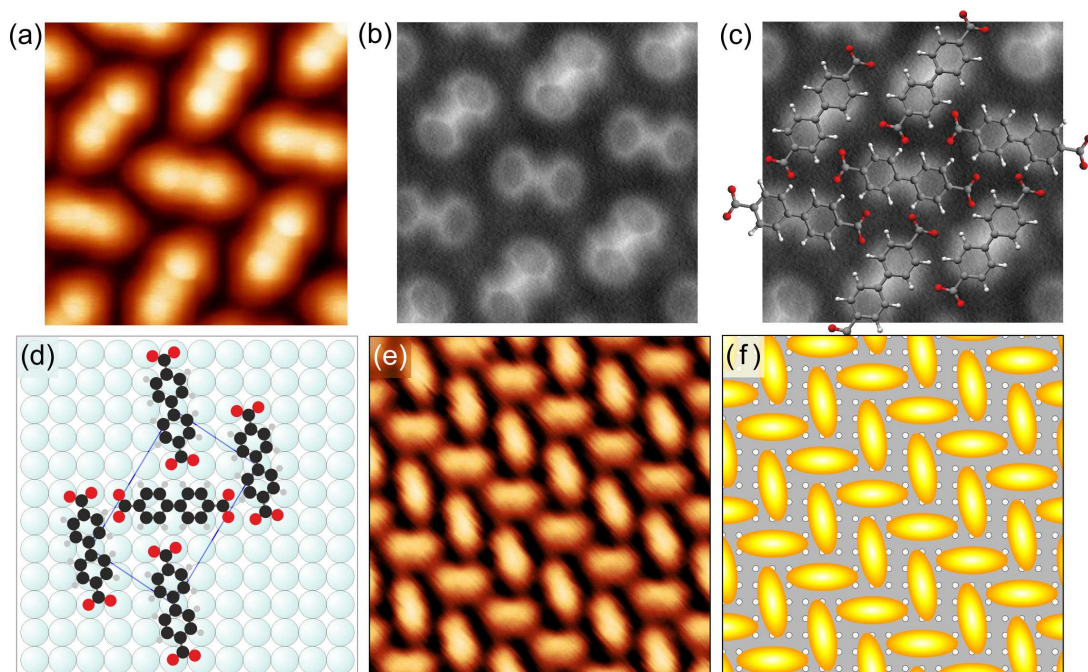


Fig. 5.27: Low temperature measurement: (a) STM detail of the BDA δ -phase and (b) nc-AFM image of the same area measured with qPlus sensor functionalized by CO molecule at 5 K. (c) Model of the BDA molecules overlaid on the nc-AFM image. (d) Model of the δ -phase unit cell on the Ag(100) surface. (e) Extended molecular arrangement model with Ag atoms illustrated under the molecules (with reduced size) and corresponding RT-STM image (e).

transformation process. No observable effect was found other than the growth of Ag islands.

5.2.9 Other BDA self-assemblies

Additional deprotonated phases have been occasionally observed on the Ag(100) surface. First, the new phase, denoted as δ_ϵ -phase shown in Fig. 5.29(a), was observed to form with the γ_2 and δ -phase at room temperature. Contrary to δ -phase, the carboxylate oxygen atoms of the new phase appear to bind to two phenyl rings in two distinct neighbouring molecules. The resulting pattern is similar to the molecular ar-

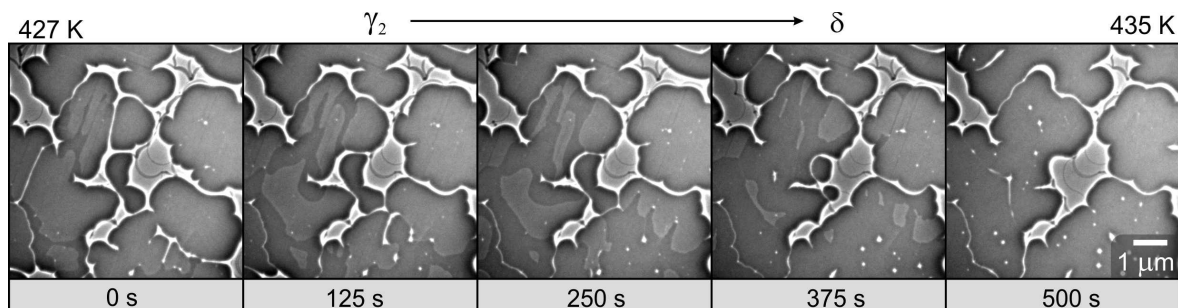


Fig. 5.28: Transformation of the γ to δ -phase observed in the LEEM. Measured at 1.1 eV

arrangement of TPA on Cu (001) and Ag (001) [124, 178]. In this configuration, a more open structure is formed at much lower molecular density compared to the δ -phase.

The formation of this phase was observed on a large scale, and the diffraction images were obtained in the LEEM, as shown in Fig. 5.30(a-b). Additionally, the chemical composition of this new phase was confirmed by an XPS measurement to be identical to δ -phase. From the μ -diffraction pattern and the STM data, the simple model was proposed as shown in Fig. 5.30(d). Here, each BDA molecule lies symmetrically on the 2×4 Ag atoms. Annealing of the δ_ϵ -phase slightly above the room temperature ($\sim 60^\circ\text{C}$), immediately leads to the formation of the δ -phase whereas typical thermally induced transformation of the δ -phase occurs at a much higher temperature of 160°C . Therefore, it can be assumed, that δ_ϵ -phase is a metastable assembly of deprotonated BDA molecules formed due to the limited diffusion at room temperature.

The second example is the phase which was observed coexisting with the δ -phase and tentatively named the BDA “windmill” phase as shown in Fig. 5.29(b). This self-assembly is similar to the molecular arrangement of BDA on Cu(100) as discussed in the previous section (e.g. Fig. 5.3). Here, the BDA carboxylic groups appear to be bonding to the sides of the phenyl ring of neighbouring BDA molecule forming a windmill like chiral structures. Additionally, the “windmill” structure and δ_ϵ -phase formed extensive assemblies integrating protonated molecules similarly to the γ_3 -phase, shown in Fig. 5.29(c). This phase was found to grow at the step edges; therefore, it can be assumed that some contaminants may be involved in its formation. One possibility could be a foreign metal atoms (Cu, Co) forming metal coordinated complexes. Unfortunately due to the sparse amount of this phase, no further analysis could be performed.

Beyond the δ -phase

Annealing of the δ -phase above 170°C resulted in the evaporation of the most of molecular islands. No diffraction patterns were observed in the LEEM. Examination of

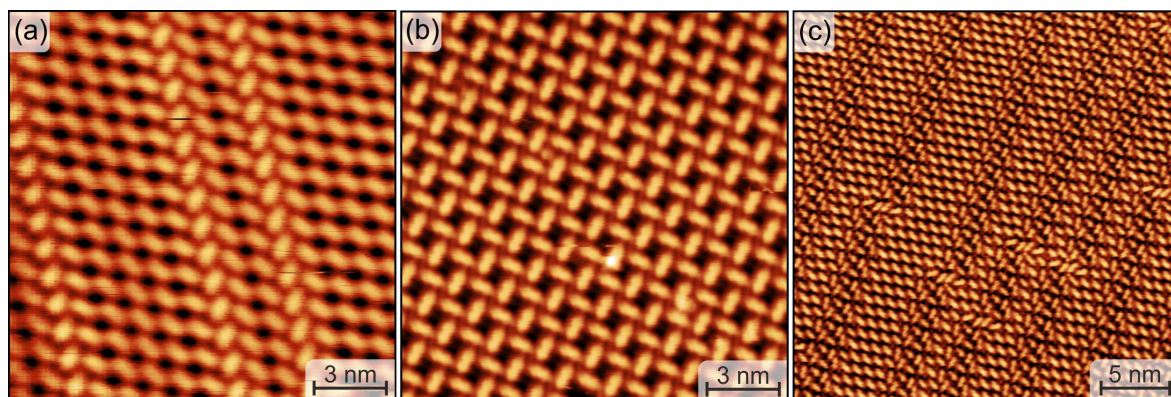


Fig. 5.29: Minor phases of deprotonated BDA: (a) Areas of δ_ϵ -phase; (b) BDA “windmill” phase. (c) Mixture of the “windmill” phase with protonated BDA molecules forming structure similar to the γ_3 -phase

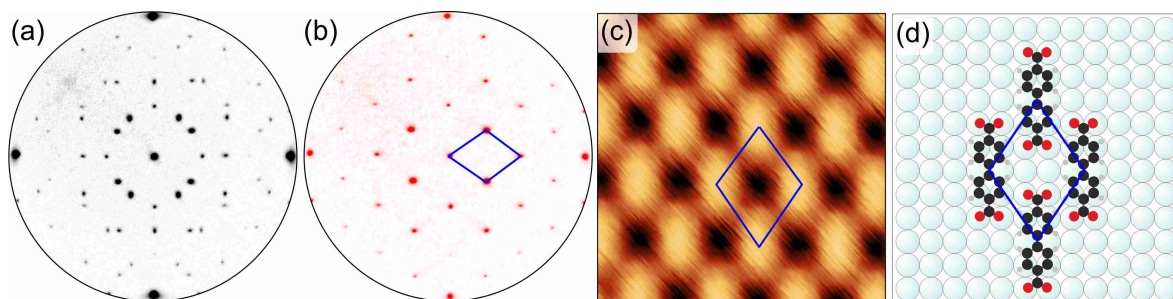


Fig. 5.30: (a) Diffraction and (b) μ -diffraction image of the δ_ϵ -phase. (c) STM image $4 \times 4 \text{ nm}^2$ and (d) model of the δ_ϵ unit cell.

the Ag(100) surface in the STM, after the sample was cooled down, discovered small molecular islands with unorganized structures, as shown in Fig. 5.31(a). The dominant features here are the long chains of the molecules and the areas with “tripod” structures where individual molecules additionally fill the area between them.

It has been previously reported that decarboxylative polymerization of dicarboxylic acids occurs on the metal surfaces at elevated temperatures [179]. In that report, annealing naphthalenedicarboxylic acid on the Cu surface first leads to the formation of organometallic polymers and later to poly-naphthalenes structures. In parallel, it can be assumed that the observed BDA structure on the Ag surface may be poly-BDA chains or more likely Ag mediated metallic polymers given the lower Ag reactivity compared to the Cu. Due to the very low coverage of these structures after annealing, no XPS data were obtained in our system.

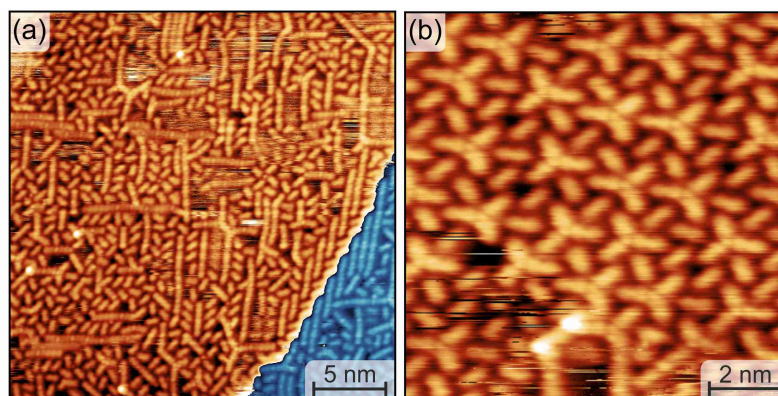


Fig. 5.31: (a) BDA chains and (b) tripod structures formed after annealing BDA above 440 K. The blue area in (a) is colored to enhance contrast and represents next atomic terrace.

5.2.10 Long range-order

The long-range order is sometimes misleading on the nano-scale. In this work, most of the described BDA phases, areas larger than $45 \times 45 \text{ nm}^2$ were observed in the STM as shown in the 5.32(a) - (d). Exception was the α -phase where large area STM measurements are problematic due to the weak molecule-substrate interactions. However, the

presence of long-range order in all phases is supported by the clear diffraction patterns. As previously mentioned, the diffraction images in LEEM are acquired over relatively large areas of approx. $150 \mu\text{m}^2$ and μ -diffraction from circular areas with a diameter down to 185 nm ($\sim 0.1 \mu\text{m}^2$). Diffraction patterns were always recorded at multiple sample positions. Furthermore, in all our experiments each of the molecular islands has grown from a single nucleus, and thus each of them is a single crystal as evidenced in the presented dark field images for every major BDA phase.

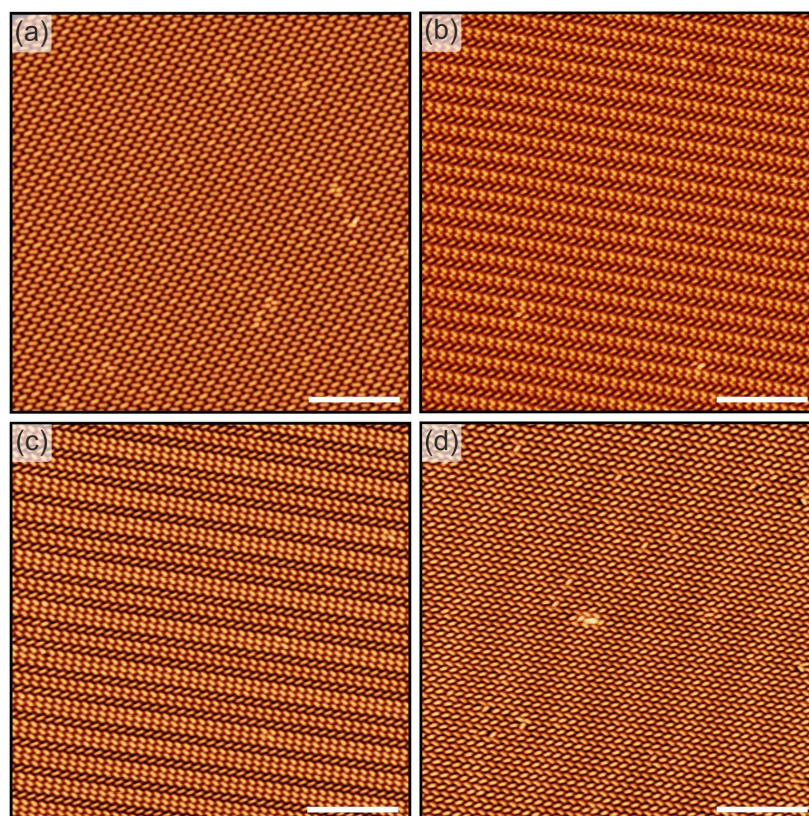


Fig. 5.32: Large scale $45 \times 45 \text{ nm}^2$ STM images of (a) β - , (b) γ_2 - , (c) γ_3 - and (d) δ -phase. Scale bar is 10 nm

5.2.11 LEEM beam damage

It should be noted that the electron beam in the LEEM is not an inert observation tool. Depending on the energy of the electron beam, it can damage the molecular structures or induce the deprotonation of the BDA. Low energy electrons can initiate a variety of reactions. Electron inelastic collisions can induce ionization, excitation of the molecule or assortment of other chemical/physical processes. Controlling and understanding chemical reactions involving the electron irradiation is of some interest in the chemistry field (see reviews: [80, 180]).

The electron energy for observation was chosen as small as possible to mitigate the beam damage during the observation while maintaining good contrast between the

molecular islands and substrate (1 – 3 eV). Examples of the e-beam induced transformation at the typical observation energies are shown in Fig. 5.33(a-b). After several minutes of measurement in LEEM (electron irradiation), the β -phase islands started to grow from the sides of the α -phase domains. Prolonged observation can lead to a full transformation of the α -phase without the annealing. Therefore, during the annealing experiments, the observed area was shifted to ensure that the molecular transformation occurs everywhere on the surface in the same fashion and it is not the result of the e-beam induced effects.

High electron beam energies (10 – 30 eV) utilized during the acquisitions of diffraction patterns also results in the gradual deprotonation of the BDA. For example the observation of the α -phase at 12 eV results in the formation of the β -phase and δ_ϵ -phase after approx. 3 – 5 min. To visualize this effect the large μ -aperture was utilized to locally irradiate the α -phase as shown in Fig. 5.33(c). Here, the fully transformed darker islands formed in the central circle. One can note that due to limited thermal diffusion, the β -phase and δ_ϵ -phase islands have a similar shape to the α -phase. To limit the e-beam induced effects during the diffraction imaging it was necessary to occasionally shift the observed area and acquire the diffraction pattern from the “fresh” structures.

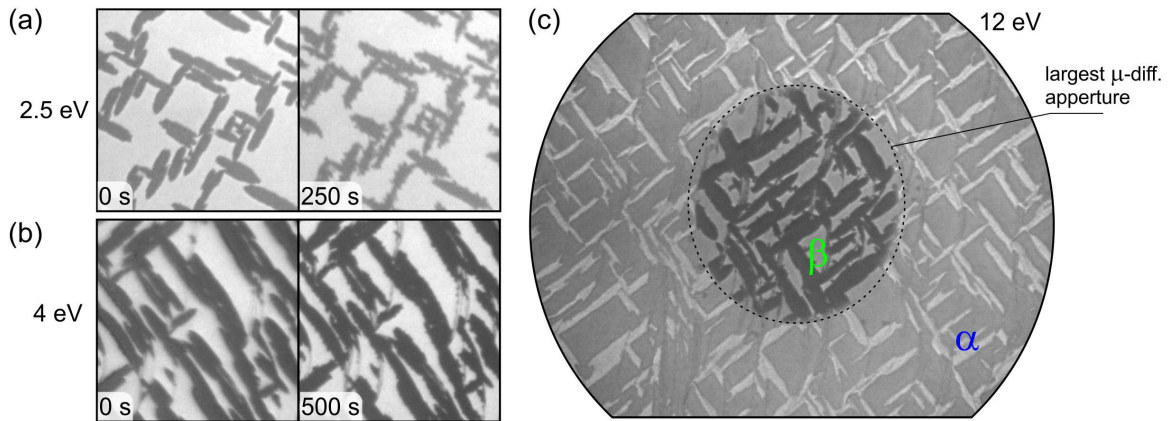


Fig. 5.33: Electron beam induced transformation of the BDA α -phase. (a) Irradiation at the 2.5 eV: Small islands of β -phase start to grow over time from the sides of the α -phase islands. (b) Irradiation at the 4 eV: β -phase forms after approx. 500 s. (c) β -phase and δ_ϵ -phase formed after 300 s in the central area of the view-field irradiated by 12 eV electrons.

5.3 BDA phases as a k -uniform tilings

The described BDA phases are attractive from a geometrical point of view as they present the experimental realizations of long-range ordered systems of uniform tilings. Generally, any partition of the plane can be considered as tiling. Tiling can be broadly defined as a division of the plane into regular regions (tiles). Regular patterns have been found throughout the history of human society in art and architecture and division between regular patterns and tilings was blurred. To find tiling patterns, one can simply

look around in homes or pay attention to the pavements, floors, walls or ceilings, on the way to work. Besides a visual appeal, the practical relevance of regular tilings can be found in fields of mathematics, aesthetics, engineering and crystallography [181].

5.3.1 Symmetry and regularity

First, some essential terms and definitions will be explained in the following section. However, the library of knowledge about regular patterns is extensive. First, the **tiling** of the plane can be defined as a repeating 2D pattern which covers the plane without gaps or overlaps, and the **tessellation** is a tiling created by one or more regular polygons. **Vertex** can be simplified as an intersection of the set of tiles. In a polygon type tilings (tessellation), usually only the **edge to edge** tilings are considered which means, that the corners and sides of the polygon correspond to vertices and edges of the tiling, respectively. To further narrow down the scope of the study, only regular and uniform tilings will be considered in the following part.

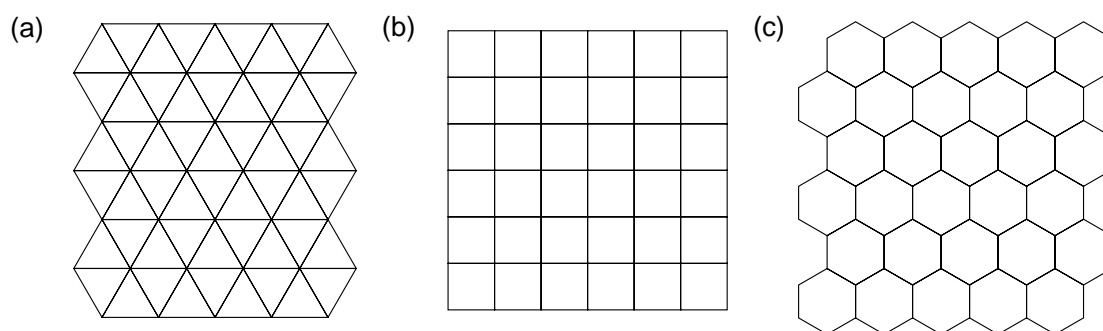


Fig. 5.34: Three types of regular tilings: (a) triangular - $[3^6]$, (b) square - $[4^4]$, (c) hexagonal - $[6^3]$.

Tiles of a regular tiling are necessarily regular polygons (but not vice versa). This comes from the condition that a regular tiling has a symmetry group transitive on the flags of the tiling. Here, the term **flag** encompasses a group consisting of a vertex, an edge and a tile. The symmetry of an object is an isometry that maps the object onto itself. There are four types of plane isometry: a) rotation, b) translation, c) reflection, d) glide-reflection. Most of them are self-explanatory with the possible exception of glide-reflection, which is reflection combined with translation through a given distance parallel to the plane of reflection.

There are only three regular tilings, shown in Fig. 5.34, hexagonal, square, and triangular. In simplified terms, in a regular tiling, a flag must have the capability to be copied into any other position in the tiling (another tile/flag), through one of the plane isometry operations as shown in Fig. 5.35. Further, if the *flag* transitivity condition is reduced to the vertex transitivity, there exists an additional eight edge to edge tilings formed by regular polygons. These are called Archimedean ¹, uniform or demiregular

¹ Their name was given as a reference to the supposed description of regular solid polyhedra by Archimedes later rediscovered by Kepler.

tilings, some authors also consider the previously shown three regular polygons to be included in the Archimedean tilings. Same group of tiles can construct only a single tiling pattern (monomorphic type), but also multiple tiling patterns (polymorphic tiles, k-morphism).

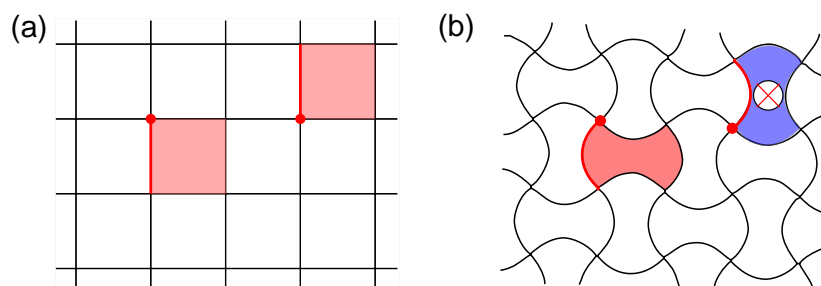


Fig. 5.35: Examples of the regular tiling (a) and (b) one that is isotoxal, isogonal and isohedral, but not regular. The flag is marked in red. Adapted from [181].

The first theoretical description of tilings was formulated in the pioneering work of Johannes Kepler in 1619 [182]. There, 11 edge-to-edge tessellations of a Euclidean plane were introduced. Three of them are regular tilings shown in Figure above (Fig. 5.34) and the remaining eight are tilings formed by a combination of two or more different polygons (semi-regular and other tessellations).

Tilings formed by regular polygons appear to be an extremal solution to various problems, and the treatment of more general problems can be often reduced to ones involving regular polygons ([183] and Chapter 4: [181]). Tilings are often used as a method of rationalizing and classifying complex lattice structures. In crystallography, the tiling patterns can be found in the more complex arrangements of atoms such as quasi-crystals [184]. In fact, many crystallographic ideas such as fault lines, planes of cleavage have their analogues in the theory of tilings.

Edges and vertices of abstract tiling assemblies can be reimaged as atoms and molecules to construct a particular network. The links between the network components have to follow specific criteria that mirror some of the known favourable coordination of real elements (e.g. preferred bonding positions). This may lead to new materials with properties not previously observed [185]. In this respect, Archimedean tiling patterns have been used to model a photonic crystals and simulate their properties [186–188] or in biology to clarify the nature of self-assembled virus capsids made from pentamers [189]. Examples of tiling utilization in other fields include 2D non-coarsening fluid foams [190], modelling a random diffusive motion of classical particles over the edges of Archimedean lattices [191], the study of cellular structures [192], artificially created electronic quantum fractals [193] or design of new topologies for geometrically frustrated magnets [194].

In surface science, tilings represent a way to design and study the novel molecular networks and enable control of the surface properties. Significant progress has been made in the development of spontaneous self-assemblies of supramolecular systems. Chemistry can now provide complex molecular species that create surface systems

of increasing complexity. For example, terphenyl tetracarboxylic acid, adsorbed on graphite, which is stabilized by hexagonal junctions can be mapped onto a rhombus tiling [195]. Quasi-degenerate locally stable states of these molecules can rearrange through defect migration and molecules exhibited changing behaviour varied with subtle chemical changes in the system [196]. Many other supramolecular tessellations have been successfully synthesized on surfaces by self-assembly including regular [197–199], semiregular [200–205], fractal [206–209], quasicrystalline [210–214] and random tilings [185, 195, 196, 215]. However, investigations of more complex k -uniform tilings formed by multiple types of vertices are sparse.

5.3.2 k -uniform tilings

A tiling is described as **k -uniform** if it is k -isogonal and its tiles are regular polygons ($k \geq 1$ is an integer). A tiling is **k -isogonal** if its vertices form k transitivity classes. Vertex transitivity requires the possibility to map every vertex of the tiling into any other vertex through one of the symmetry operations. In other words, the tiling will have k -number of vertex types that are not equivalent. Correspondingly, the k -hedral and k -tozal tilings have k -number of tile types and tile edges. The tiling type can be described by the set of integers $[n_1^{\alpha_1} \cdot n_1^{\alpha_2} \cdot \dots \cdot n_n^{\alpha_n}]$ that correspond to the numbers of sides of the polygons n_i that meet at each vertex. For example, the hexagonal tiling is shown in Fig. 5.34(c) can be denoted as $[6^3]$ since its hexagonal tile has six sides and three polygons meet at each vertex. The sequence of polygons is usually listed in a clockwise direction [181]. If two or more identical polygons are neighbouring their count is given by superscript α_i .

5.3.3 BDA phases as k -uniform tilings

Previously described Archimedean tilings were 1-uniform. These tilings can be experimentally realized from a single molecule with two separate functional centres that formed a single binding motif [201] or by mixing two molecular phases to form a new vertex type not present in the pure phases [202]. Another strategy can be to utilize rare earth directed metal-organic assembly, where the central ion enables the adaptability of opening angles between two neighbouring ligands [200] or a distinct number of coordinated ligands at each of the central ions [210].

In our case, the δ - , γ_2 - and γ_3 - phases represent complex tessellation as shown in Fig. 5.36. In the previous section, the BDA phases were described chemically from the intact to the fully deprotonated phase. On the other hand, from the geometrical point of view, the simplest structure is the δ -phase, that can be expressed as six triangular tiles meeting at a single vertex. The assembly is composed of a single polygon tile type, and it is a regular tiling that can be denoted as $[3^6]$.

Triangular tiles of the δ -phase can be divided into two types portrayed in yellow and orange in the detailed STM image in Fig. 5.36(a), however, they still have identical geometry. The molecular structures associated with these triangles display a distinct

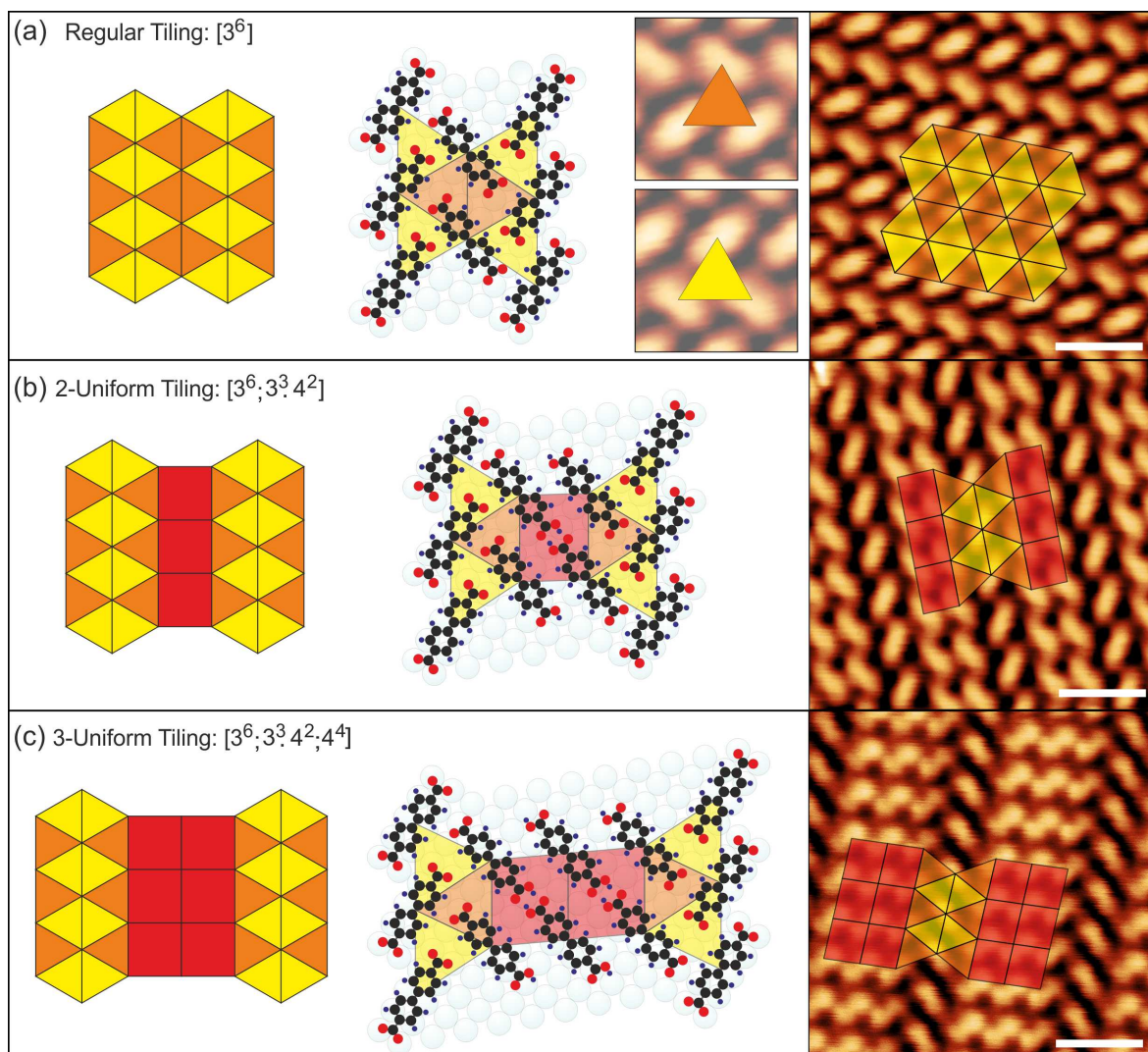


Fig. 5.36: BDA tiling structures illustrated as triangles and squares and overlaid on the BDA phases models and STM images. An additional STM detailed view in the first row shows two chiral types of triangular tiles, representing different intermolecular binding motif. Scale bar 2 nm.

chirality of the BDA arrangement. Measured lengths of the triangle's sides (10.4 Å; 10.1 Å; 9.7 Å) and inner angles (60.3°; 56.3°; 63.4°) are close to those of the equilateral triangle, and therefore they represent a good approximation of Archimedean and k-uniform tilings [201, 206, 216–218].

Presented complex tessellations were enabled by the bifunctional 1H-BDA molecule that was integrated into the γ_2 - and γ_3 - phases. The 1H-BDA allows homogeneous transition between δ and γ binding motifs. The new binding motifs added another rectangular tile type, as shown in Fig. 5.36(b) and (c). The tessellation of γ_2 molecular structure now incorporated two distinct types of vertices, which are characteristic for the 2-uniform tiling $[3^6, 3^3 \cdot 4^2]$. The new notation includes the second vertex type marked as $[3^3 \cdot 4^2]$ since it connects three triangular tiles $[3^3]$ and two square ones $[3^4]$. The new rectangular tile is a parallelogram with sides 10.4 Å and 8.3 Å and inner

angles 88.2° and 91.8° . The shape of the triangular tiles is slightly changed compared to the δ -phase because, as described in the previous sections, the γ_2 -phase unit cell is commensurate with the substrate and therefore binding motif has to adapt to the substrate. Sides are 10.4 \AA ; 9.6 \AA ; 9.9 \AA and inner angles are 56.5° ; 59.2° ; 64.3° . The slight changes in the geometry between these tessellations are enabled by the structural adaptability of BDA binding on Ag(100). Similar adaptability may be important in facilitating the formation of other molecular systems comprising two or more distinct binding motifs.

In the γ_3 -phase, the addition of 2H-BDA molecules results in the second row of rectangles and also a new vertex type [4⁴] in the structure. Therefore the resulting tessellation is 3-uniform tiling noted as [3⁶, 3³ · 4², 4⁴]. Compared to the γ_2 -phase the sizes of the rectangular tiles became more uniform (10.4 \AA ; and 9.2 \AA) and slightly distorted (inner angles 85.0° and 95.0°). The triangular tile again adjusted (10.4 \AA ; 10.2 \AA ; 11.0 \AA , 56.9° ; 64.4° ; 58.7°) to allow matching the molecular structure with the substrate.

The use of carboxylation of terminal hydroxyl groups of simple molecules, to steer the evolution of supramolecular tessellations is not unique to BDA systems. A recent study on the Ag(111), showed that stepwise deprotonation of similar 4,4 dihydroxy biphenyl leads to a wide variety of tessellations [203]. The BDA-Ag(100) system is distinct from other multi-component systems because the bifunctional 1H-BDA allows the seamless expression of complex tessellations formed by two binding motifs. For the majority of multi-component systems [75] and systems featuring carboxylic acids and carboxylates in particular [137, 128] the individual components segregate into sub-phases forming separate islands or domains.

A multi-component BDA phase coexisting with other phases has been observed for BDA on a Cu(111) substrate [125]. Here, the intact and partially deprotonated BDA molecules formed 2-uniform tiling [4⁶, 3³ · 4²]. However, the fully deprotonated BDA molecules form separate islands and the third [3⁶] vertex was not formed. This suggests that the unique matching of substrate geometry and molecular assemblies has an important role in obtaining higher-order uniform tilings, additionally, in contrast to Archimedean tilings formed by metal-organic networks [200, 201, 210], the BDA tilings on Ag(100) display long-range order.

5.4 Conclusion BDA on Ag(100)

Initially it was expected that the deprotonation of the BDA molecule will be a simple chemical reaction. However, it was discovered that the reaction involves multiple steps of chemically and structurally distinct molecular self-assemblies. This chapter described in detail, the arrangements of BDA molecules analyzed by STM, AFM, LEEM and XPS. Atomic models were presented for each self-assembled phase. Additionally, a description of the molecular islands morphology and real-time transformation of the molecular islands in LEEM were presented. A better understanding of surface chemi-

cal reactions can be extended to other molecules functionalized by carboxylic groups. Furthermore, investigated dynamical evolution of the phase transformations can lead to improved models of organic layer depositions.

In the last section of the chapter, the BDA self-assembled phases were presented as k -uniform tessellations with 1, 2 and 3 distinct vertex types. The BDA/Ag(100) system has a unique structure, where the partially deprotonated BDA mediates connection of two distinct binding motifs in a single long-range ordered molecular phase. This system can help to form new design rules for the utilization of complex supramolecular tilings with novel physical and chemical properties.

6. MOLECULAR NETWORKS ON GRAPHENE

The goal of the experimental work presented in this chapter is the preparation of Ni-TCNQ metal-organic layer on graphene. On metal surfaces, the Ni-TCNQ (7,7,8,8-tetra-cyano-quinodimethane) molecular network exhibit weak ferromagnetic coupling [219]. The coupling was explained in terms of indirect coupling mediated by the conduction electrons, i.e., Ruderman-Kittel-Kasuya-Yosida (RKKY) interactions [220], or in terms of superexchange via the negatively charged ligand [221]. The tunability of the Fermi level position in graphene and consequently the electronic states in Ni-TCNQ system in its vicinity could theoretically enable external control of the magnetic coupling for application in spintronics and quantum processing [222, 223].

This chapter describes graphene, its properties and examples of molecular self-assembly experimentally realised on graphene. High quality graphene layers were prepared on Ir(111) in UHV conditions. The growth procedure is described in more detail in order to provide a practical guide. Rest of the chapter describes self-assembly of BDA and TCNQ molecules on the graphene as well as attempts to synthesise 2D metal-organic networks on graphene with Fe and Ni atoms.

Part of the work in this chapter, specifically graphene with BDA molecules and Fe-BDA network was done in cooperation with masters student Ing. Štěpán Kovařík and results are part of his master's thesis [224].

6.1 Graphene electronic properties

Carbon atoms in the graphene layer are hybridised in sp^2 configuration and form covalent σ -bonds with each other. Strong σ -bonds in the horizontal plane are responsible for its extraordinary mechanical properties. The $2p_z$ electrons form a delocalised π -bond and give rise to many of the graphene unusual electronic properties. The graphene band structure in the first Brillouin zone is depicted in the Fig. 6.1(a). The valence band and conduction band are connected at the \mathbf{K} and \mathbf{K}' points also called charge neutrality or Dirac points¹. This makes graphene a unique combination of semiconductor and metal (no bandgap). Semiconducting behaviour means that the conductivity will depend on the graphene doping level. If the Fermi level of graphene is moved around the K point, the density of the occupied states is increasing/decreasing, and the conductivity will significantly change. This is often exploited for graphene-based

¹ Other meeting points, visible in Fig. 6.1, are equivalent through translation by a reciprocal lattice vector. There are three \mathbf{K} and three \mathbf{K}' points due to two inequivalent carbon atoms in the graphene unit cell.

sensors. Additionally, linear dispersion around the Dirac point (Fig. 6.1(b)) means, that electrons in graphene can be described as relativistic massless charged particles moving with the Fermi velocity ($\sim 10^6 \text{ m} \cdot \text{s}^{-1}$) [225]. The charge carriers can therefore be effectively described with the Dirac equation for fermions. Consequently the \mathbf{K} and \mathbf{K}' points in the reciprocal space are denoted as the Dirac points. As the description of the charge carrier properties relies on quantum theory, many unusual phenomena may be observed in graphene, e.g. the symmetry-broken quantum Hall effect, the integer quantum Hall effect (IQHE) or the Klein tunnelling.

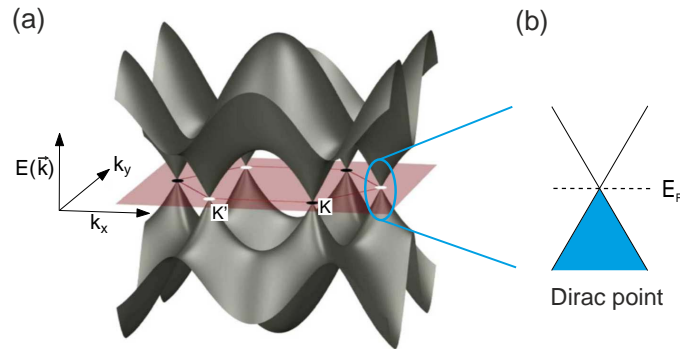


Fig. 6.1: (a) 3D illustration of the graphene band structure, the conduction and valence band, connected at the Dirac points (\mathbf{K} and \mathbf{K}'). (b) The band structure of graphene near the Dirac points. The linear dispersion relation is similar with massless relativistic particles. Adapted from [226].

6.2 Graphene synthesis

The first method used for the graphene fabrication was a micro-mechanical cleavage (often called scotch tape method or exfoliation) of HOPG (highly oriented pyrolytic graphite) utilized by A. Geim and K. Novoselov in 2004 [227], when the graphene was discovered. This method yields single- or multi-layer graphene flakes of micrometre size. It is a time-consuming process which needs additional techniques such as atomic force microscope (AFM) or Raman spectroscopy to verify the thickness and quality of the graphene flakes. The advantage of the exfoliation is a simple production of high-quality graphene [225]. In the following years, many other methods were developed e.g.: thermal decomposition of SiC [228], liquid-phase exfoliation [229] and molecular beam epitaxy [230]. However, one of the most promising methods for future industrial production of graphene layer are based on the graphene growth on metal substrate.

Graphene growth on metals can be divided into two approaches. One is based on segregation of carbon atoms from the bulk of the metals such as Ru(0001)[231] or Pt(111)[232], during thermal annealing in vacuum. The main problem of the segregation approach lies in achieving exactly one layer due to additional segregated carbon, which often results in thicker, few-layer graphene stacks.

The second approach is based on the thermal decomposition of hydrocarbons catalysed via its adsorption on the surface. Many transition metals are catalytically active

and can decompose hydrocarbons at elevated temperatures. Several types of precursors can be used to synthesize graphene such as ethylene [233], PMMA layer [234] or even liquid precursors, e.g. hexane [235].

6.2.1 Chemical vapour deposited (CVD) graphene

Currently, the most promising method for commercial applications is CVD growth utilising thin polycrystalline copper foil. This method allows the preparation of graphene layers on the large scale (30-inch foils [83]). Compared to graphene exfoliation, the CVD process usually results in growth of polycrystalline graphene layer, as shown in Fig. 6.2(a). During the typical CVD process, a metal foil is heated in the growth chamber with the presence of a short-chained hydrocarbon gas molecules (e.g. methane, benzene). At a high enough temperature, the gas will thermally decompose on the metal surface, which acts as a catalyst that reduces the temperature of decomposition (~ 1000 °C for Cu). One of the advantageous properties of copper substrate is low solubility of carbon, even at high temperatures. Therefore, the growth process is restricted to the surface, where decomposed carbon atoms start to nucleate and form the graphene mono-layer [236].

On the other hand, graphene is strongly influenced by substrate quality and growth properties. Crystal defects in the substrate structure and chemical residues from the fabrication process can aggravate the electronic properties of the subsequently grown graphene layer. A substantial number of research publications today is devoted to improving the quality of CVD graphene. For example, by reducing the number of nucleation sites utilising ultrasMOOTH copper foil, it is possible to decrease the density of substrate defects and grain boundaries which improves mobility of charge carriers in graphene [237].

Studies of CVD growth led to the development of growth techniques for large area single crystal graphene, which have comparable quality to that of exfoliated graphene. Electrochemical polishing of copper prior to the CVD growth and high-pressure annealing was used to achieve graphene crystal size over 2 mm in diameter [238]. It was recently discovered that besides the standard surface-limited growth mechanism, the diffusion of carbon atoms through the Cu bulk occurs in the presence of oxygen in the bulk [239]. Oxygen atoms enhance the dehydrogenation of hydrocarbons, and for a carbon atom, it becomes energetically favourable to diffuse under the first copper layer. This led to a large single crystal growth achieved with oxygen-rich foil capsule and controlled growth of bilayer graphene [240]. Results from utilising this method in our laboratory are shown in Fig. 6.2(b). These crystals are planned as a possible substrate for future graphene-molecular devices.

6.2.2 Ultra-high vacuum syntheses

Studies of graphene growth and properties on the well-defined metallic surfaces in ultra-high vacuum are beneficial for understanding the nucleation, growth processes

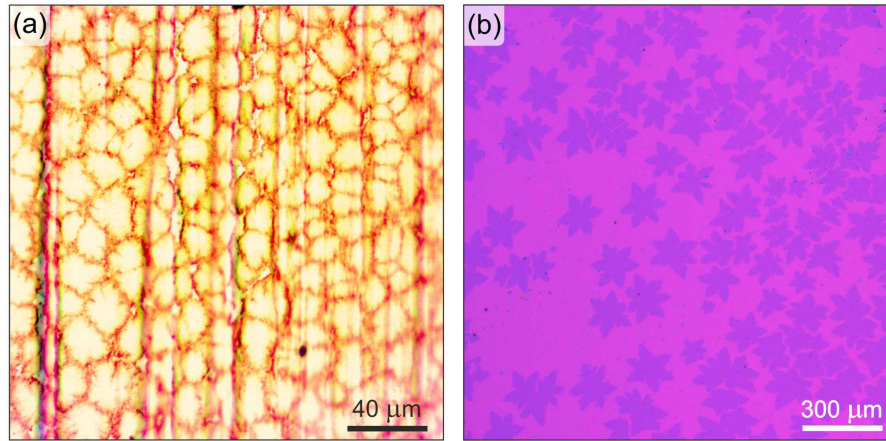


Fig. 6.2: Optical images of CVD grown graphene: (a) graphene layer on the Cu foil. Graphene growth was terminated before the crystals formed uniform layer. Cu foil was oxidized by annealing on air at $\sim 200^\circ\text{C}$ for increased contrast. (b) Large single crystals ($100 - 200\ \mu\text{m}$) of graphene transferred on $280\ \text{nm}\ \text{SiO}_2$ substrate. Note the difference between the scales.

and interactions of graphene with metals. Number of transition metals have been previously used to synthesize high quality graphene including platinum [241], nickel [242], copper [243] and others (see review [244]). A special technique was also developed for the growth of graphene on the noble metals, where ethylene was ionised by electron bombardment in ion gun [245]. Subsequently, the ionised products mostly C_2H_4^+ , were accelerated at low energy ($500\ \text{eV}$) and aimed toward the surface. Irradiating the hot surface ($\sim 800^\circ\text{C}$) with low energy ethylene ions enhances its decomposition and resulted in graphene grown on $\text{Au}(111)$. This process was also exploited to grow large single-domain graphene on Cu [246], where the standard CVD process yields two domain graphene layer [243] and is generally problematic due to temperatures close to the melting point of Cu.

Use of a clean single crystal as opposed to the polycrystalline foils reduces the number of defects and grain boundaries which interfere with the growth process and damage the graphene crystal structure. In this work, graphene was prepared by combination of temperature-programmed growth (TPG) and CVD. During the TPG growth, hydrocarbon molecules are adsorbed at a room temperature followed by pyrolysis and graphene growth at a fixed elevated temperature. Single TPG cycle usually yields approx. $0.2\ \text{ML}$ graphene. It wasn't utilised in this work, but it is possible to continue the TPG by repeating the cycles several times to increase the graphene coverage and eventually form almost full layer [247].

Graphene / Ir(111)

The low solubility of carbon atoms in the Ir [248], which inhibits the growth of multi-layer graphene and a weak interaction of Ir with graphene, made it a substrate of choice for the graphene growth in UHV. Graphene was observed to grow continuously

across Ir atomic step edges, thus acting as a perfect layer with a very low density of defects [247]. The ARPES (angle-resolved photoemission spectroscopy) measurement also showed that the electronic structure of the π -orbital (Dirac cone) is intact, with slightly induced p-type doping of the graphene [249].

For the purposes of this work, graphene layer was grown in the LEEM chamber, which allowed direct observation of the growth process. Once the growth parameters were optimized, the subsequent depositions were checked only after the growth. The first step in the graphene growth procedure on Ir(111) is proper cleaning of the Ir crystal as noted in the chapter about experimental setup (Sec.:3.2.2). Ir crystal required an additional annealing step in an oxygen atmosphere to remove the carbon residues from the surface. Clean surface, as observed in LEEM, is shown in Fig. 6.3(a), with corresponding diffraction pattern in Fig. 6.3(b).

In the next step, ethylene is adsorbed on the surface. In order to ensure the full coverage, ethylene pressure was raised to $3 - 5 \times 10^{-6}$ mbar for 3 - 5 min, measured with the ionisation vacuum gauge (Barion). According to the thermal desorption study, the ethylene stays on the surface during the annealing and decompose as evidenced by the measured hydrogen pressure spike [250]. Interestingly, in this study from 1976, the authors noted the formation of “ordered carbonaceous residue” upon annealing to temperatures over 800 °C and stable up to 1500 °C (maximum for their setup). They also noted that it is a well-ordered surface structure due to observed LEED pattern (typical for graphene as we know today).

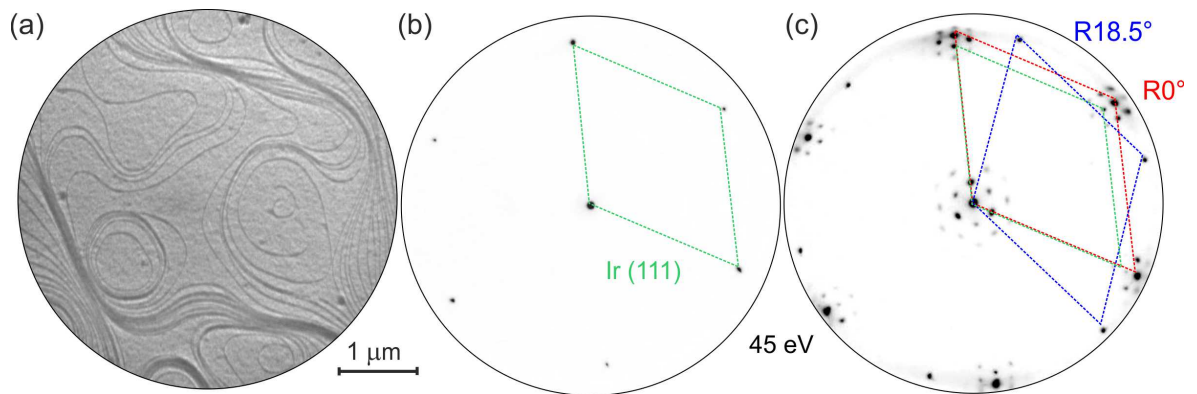


Fig. 6.3: (a) Clean Ir(111) surface with large atomic terraces observed in LEEM at 4 eV. (b) Diffraction pattern corresponding to (a) acquired at 45 eV, Ir reciprocal unit cell marked in green. (c) Diffraction image after the growth of graphene shows typical moiré structure of $R0^\circ$ domain marked red and the $R18.5^\circ$ domain marked in blue.

Graphene grows on Ir(111) preferentially in a way, that densely packed graphene rows are aligned with the densely packed substrate rows (referred to as $R0^\circ$ domain). However, several other graphene islands with a variety of rotational angles in respect to the Ir are also formed [251]. Initial TPG step during the growth leads to the formation of a high density of small aligned $R0^\circ$ graphene islands. During the second step of the growth, the CVD, any new graphene domains that impinge on existing nuclei are effectively forced to grow in $R0^\circ$ [252] (observed for $T_{\text{CVD}} \sim 1150^\circ\text{C}$). However,

occasionally, the more than one rotational domain of graphene was observed to grow in some areas during our experiments. This can be observed from the appearance of additional diffraction spots, as shown in Fig. 6.3(c). Uniform high-quality graphene growth is essential because the graphene corrugation and graphene-metal interaction varies for each the rotational domain [253].

After the adsorption of ethylene, the chamber pressure is reduced to $(3 - 4) \times 10^{-8}$ mbar, which should correspond to approx. 1×10^{-7} mbar of ethylene pressure (after correcting for the gauge sensitivity). The second step, the CVD growth then continues by annealing of Ir(111) crystal to 1150 °C for approx. 12 min. Graphene growth speed decreased with increasing coverage. Therefore, sufficient duration of CVD growth was calibrated by STM measurements, as shown in Fig. 6.4. After 8 min, there are still considerable gaps in the graphene layer; however, after 10 min the layer is almost complete. Once the whole metal surface is covered with graphene, the ethylene can no longer decompose, and the growth is terminated.

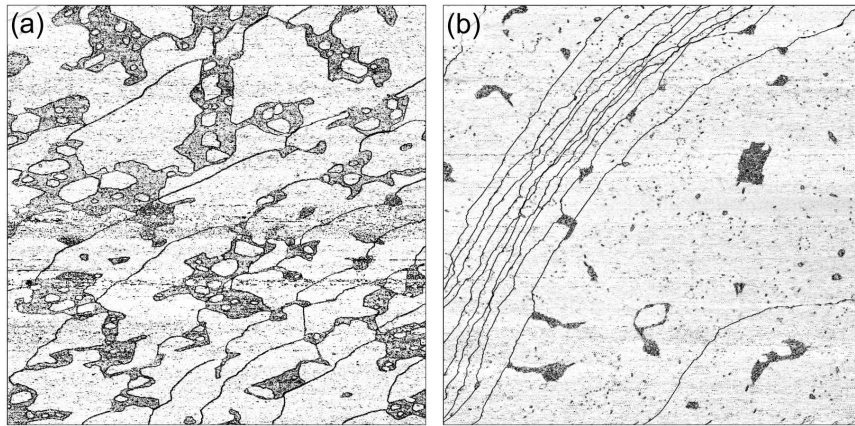


Fig. 6.4: Derivative of the STM topography image of graphene grown on Ir(111) after (a) 8 min and (b) 10 min of CVD growth. Dark area correspond to rough surface without the graphene layer. Scan size is $400 \times 400 \text{ nm}^2$.

Alternatively, the graphene on Ir can be grown purely by the CVD method. Hattab et al. [254] achieved single domain graphene for high pressure growth (5×10^{-6} mbar) after 60 s annealing at 1250 °C. In the report, the author observed continuous improvement of CVD graphene quality with increased temperature. They concluded that above 1250 °C graphene grows in the single domain $R0^\circ$. However, initial results following this procedure in our laboratory resulted in inadequate graphene quality. Higher pressure also prevents the use of LEEM imaging due to the need to maintain the high voltage at the sample. Further experiments were therefore performed in lower pressures, as mentioned above.

Combined TPG+CVD growth yields predominantly $R0^\circ$ graphene. However, the resulting quality varies from experiment to experiment. Two different results from growth performed at 1150 °C are shown in Fig. 6.5(a) and (b). Typically, a broad distribution of rotational domains would show up as Debye-Scherrer rings surrounding the (00)-spot. In our case, the spots often appear broader suggesting variations in

graphene orientations around the $R0^\circ$. Recently, this broader spots were explained as strain minimisation between the graphene layer and the Ir(111) substrate [255]. Graphene lattice parameter remains almost constant at various temperatures [256], meanwhile, the Ir lattice parameter changes. This difference puts compressive stress on the graphene layer, and the resulting strain is relieved by rotations of the graphene lattice.

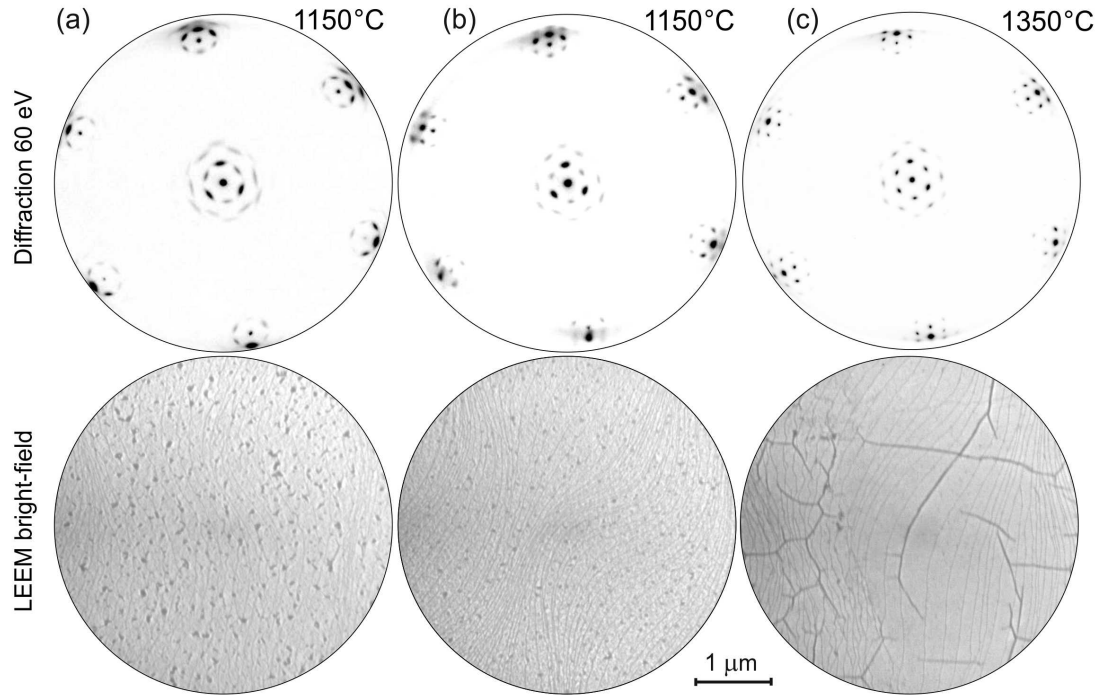


Fig. 6.5: LEEM diffraction patterns acquired at 60 eV and real-space images of graphene grown on Ir(111): (a) and (b) show different result of TPG+CVD growth at 1150 °C; (c) shows an improved graphene crystallinity upon annealing of sample (b) to 1350 °C. Diffraction spots appear sharper and graphene wrinkles are observed as thick black lines in real-space image.

In order to improve the graphene quality and yield uniform results across the experiments, an additional annealing step was added to the growth procedure. Immediately after termination of the ethylene flow, the sample temperature was raised above 1300 °C for approx. 1 min. The temperature was chosen to be above the optimal temperature mentioned in previous studies [254, 255]. Above this temperature, the strain in the graphene layer is released. During the cool-down, when Ir lattice shrinks again, newly induced stress in graphene is relaxed through the formation of wrinkles [257] as shown in Fig. 6.5(c). Wrinkles are 1-dimensional defects usually several micrometres long and can be described as folds of the delaminated graphene layer. Summary of the optimised growth procedure steps is shown in Tab. 6.1.

Atomic structure of graphene on Ir(111) was observed in STM as shown in Fig. 6.6(a) and (b). The distinct superstructure can be observed with unit cell vector of approx. 25 Å. Ir(111) surface has a hexagonal lattice with cell parameter of 2.715 Å [254]. Commonly accepted lattice parameter of unstrained graphene is 2.465 Å [233, 255].

Tab. 6.1: Parameters of graphene growth procedure.

Time [min]	Ethylene pressure [mbar]	Temperature [°C]	Note
3-5	$1 - 5 \times 10^{-6}$	25	Adsorption
11-12	$3 - 4 \times 10^{-8}$	1150-1200	CVD growth
1	-	1350	Relaxation
2-3	-	1000	Cool-down

Mismatch between these lattice parameters of approx. 10% results in the typical moiré structure observed in the STM and LEED/LEEM diffraction. Distinct moiré satellite spots formed around (0,0) spot and can be observed in detailed diffraction image shown in the Fig. 6.6(c). In case of relaxed graphene $R0^\circ$, its layer is not rotated with respect to the Ir substrate, and the satellite spots also appear around Ir substrate spots. As mentioned in previous paragraphs the position of the moiré spots strongly dependent on any small variations of the graphene lattice parameter [254] or rotations [255, 258]. In this way, moiré spots act as a good identifier of graphene quality.

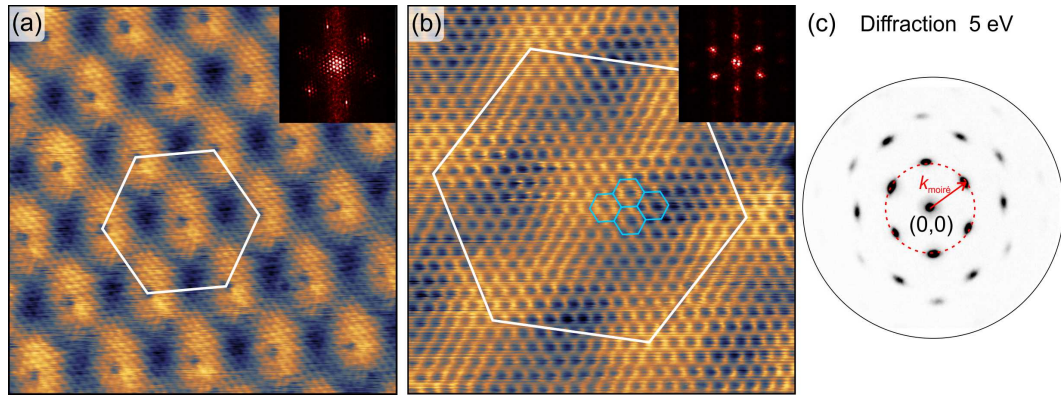


Fig. 6.6: STM topography of graphene grown on Ir(111): (a) large scale image with moiré structure marked by white hexagon; (b) atomic resolution image showing one moiré unit cell. FFT images are inserted in top right corner.

6.3 BDA on graphene/Ir(111)

Initially, the self-assembly of molecules on graphene was tested with BDA molecule. This molecule was previously extensively studied in experiments on Cu(100) and Ag(100) as described in Chapter 5. Approximately 0.5 ML of BDA was deposited on the graphene surface. BDA molecules formed needle-like islands, as shown in LEEM images in Fig. 6.7(a) and (d). The islands appear at 5 eV as darker areas, shaped similarly to the BDA on Ag(100). However, diffraction pattern from these structures typically had a distinct ring structure, with several brighter spots, as shown in Fig. 6.7(b), suggesting a large number of rotational domains of BDA.

Area of the diffraction acquisition was then reduced by μ -diffraction aperture. However, even with the smallest 185 nm aperture, no single rotational domain could be

observed. Often, the spots appeared in pairs as shown in Fig. 6.7(f), most likely corresponding to mirrored domains. When the image contrast of large area diffraction was enhanced as shown in Fig. 6.7(e), twenty-four brighter spots could be counted inside of the ring.

Graphene structure belongs to the $p6mm$ wallpaper group, generated by the point group C_{6v} and in-plane translations. The point group C_{6v} is comprised of 12 symmetry elements: one identity, five rotations and six reflections [259]. Together with the observed diffraction spots, it can be concluded that there are six preferential island directions and six additional mirrored domains. However, the μ -diffraction observations also suggest, that there are always multiple directions around the preferential one.

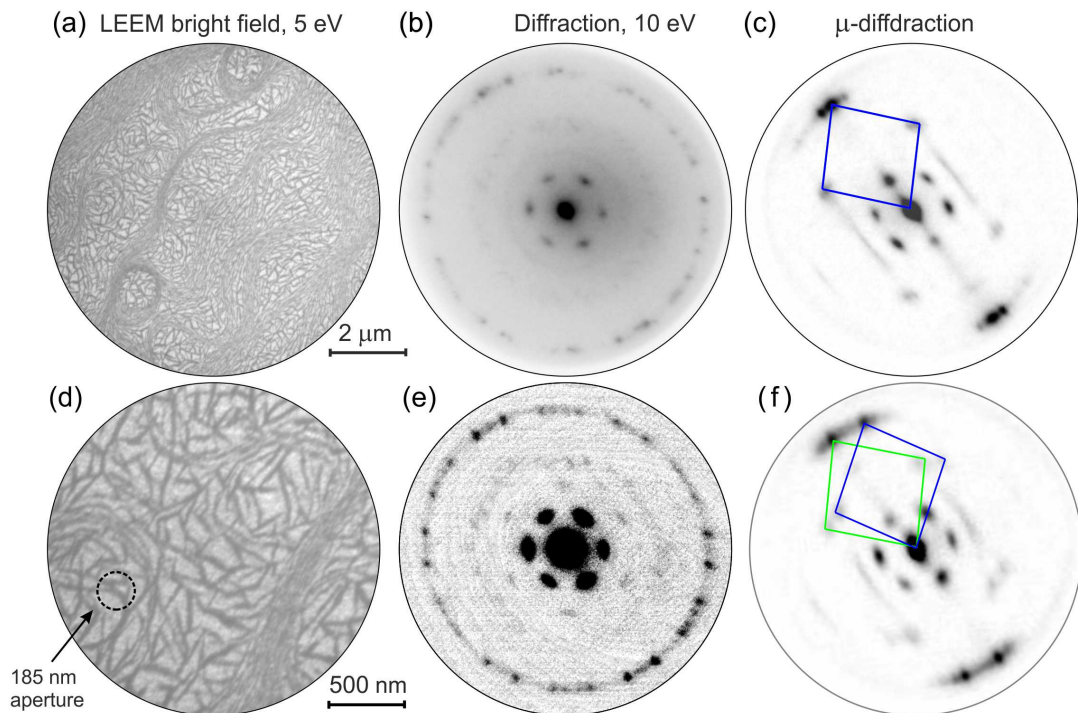


Fig. 6.7: LEEM analysis of BDA on Graphene: (a) and (d) LEEM bright-field images acquired at 5 eV. BDA islands appears as dark needle-like areas. (b) Large area diffraction image showing a ring with 24 more prominent diffraction spots that can be observed in the same contrast enhanced image (e) below. (c) μ -diffraction image acquired with smallest 185 nm aperture. (f) another μ -diffraction image showing the distinct pair of spots. BDA unit cell are drawn in with blue and green rhombus.

The STM measurement revealed a possible explanation of the blurry diffraction patterns observed in LEEM. The BDA self-assembly on graphene appears to be very flexible, and molecules were observed to seamlessly change their direction, as shown in Fig. 6.8(a). Additionally, the self-assembly can traverse the step-edges as the graphene also grows over the It step-edges. On the other hand, the islands were often observed to grow along the step-edges suggesting they have a minor role in BDA islands orientations. The BDA molecule on graphene observed in STM appears to have more features compared to the BDA on Ag(100). Faint rings can be distinguished inside the molecule, as shown in Fig. 6.8(d) that can be assigned to the phenyl rings of the

BDA. An apparent increase in STM resolution is because graphene effectively decouples BDA from underlying metallic substrate [11].

XPS measurement confirmed that BDA molecule is chemically intact, and the self-assembled structure on graphene is similar to the α -phase observed on the Ag(100). Graphene does not appear to be modifying the self-assembly; a similar result was observed in the case of TPA [260]. Intermolecular distance of BDA in chains was measured as $13.2 \pm 0.2 \text{ \AA}$. Molecular distances were measured at multiple positions from the STM FFT data. Hydrogen bond length (O–O in OH–O bond) of $1.6 - 2.0 \text{ \AA}$ was estimated from theoretical BDA length of 11.4 \AA (length from O to O along the molecule) subtracted from measured molecule-molecule distances. This hydrogen bond length is smaller than the typically observed length and is not corresponding to expected values in calculations (on metallic surfaces) [173]. In order to eliminate the possible errors that are inherent to the STM, the graphene moiré pattern on Ir was used as a substrate calibration tool. Initially, the pattern could not be observed by the eye. However, a distinct hexagonal pattern was found around the BDA (1,1) spot in FFT images (shown in Fig. 6.8(c)). By careful examination of filtered STM images, the hexagonal pattern was identified and found to be slightly smaller by approx. 4% compared to the expected reference value of 25.4 \AA . A correction factor was applied to the BDA-BDA distance, and new hydrogen bond length was calculated as $0.21 - 0.25 \text{ \AA}$, which is in accordance with a typical length of a strong hydrogen bond.

Observation of moiré structure can initially suggest some modulation of the BDA self-assembly on graphene. However, the moiré was found to be incommensurate with the BDA, which is the reason why its not clearly observable inside of self-assembly. The moiré is also not visible in the LEEM diffraction suggesting that it is the result of small height modulations of molecules (or possibly electronic structure). Observed changes of island directions, optimal hydrogen bond length as well as the fact that BDA is not commensurate with graphene, confirmed the expectation that graphene is only weakly interacting with BDA molecules.

6.4 Graphene Fe-BDA network

In order to examine the possibility of organo-metallic system growth on graphene, Fe and Ni atoms were utilized together with the BDA molecules. The carboxylic functionalised molecules were previously observed to form metal-carboxylate coordination structures, e.g. benzoic acid with Ni and Fe [133]. The BDA molecules were previously also found to bind with Fe to form various metal-coordination networks on Cu(100) [261]. Coordination complexes are attractive for their possible functionalities, which may be applied in the fields of catalysis, magnetism, and optical applications [20]. Specifically, the magnetic character of Fe and Ni metal centres may induce cooperative magnetic coupling mediated by the spacer molecules or the substrate, making them potential molecular 2D magnetic systems [262]. For example, control of magnetic coupling between neighbouring spins of Co atoms was achieved by employing

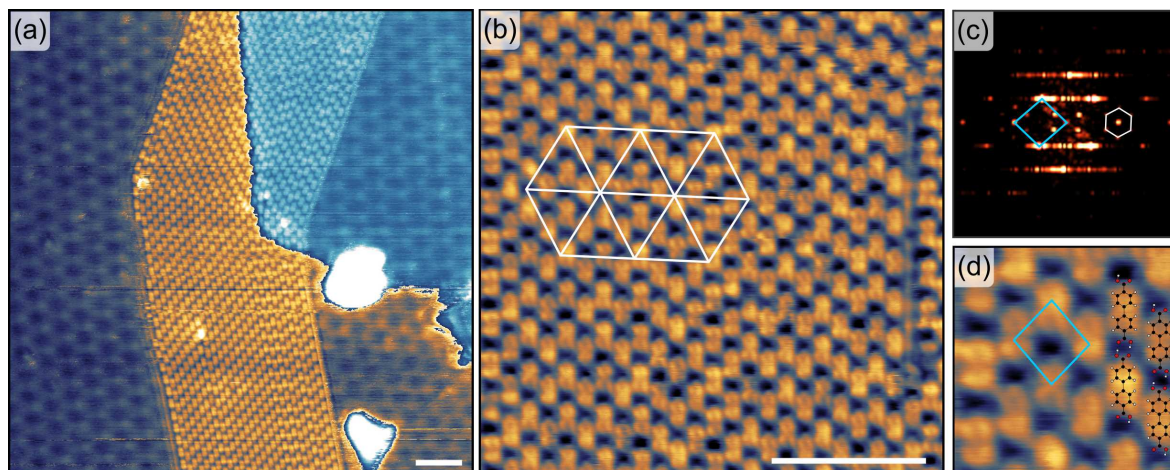


Fig. 6.8: STM topography of BDA on graphene/Ir: (a) self-assembly was observed to change the directions along the island and grow over the step edges; (b)-(d) detail of BDA self-assembled structure exhibiting slight corrugations due to the underlying moiré structure, however, it is not commensurate with the graphene. (c) FFT spectrum calculated from the image in (b). Here, moiré of BDA/Gr appears as satellite spots around the (1,1) spot of BDA in the FFT image. The graphene/Ir moiré unit cell is marked in white and BDA with blue. Scale bars are 5 nm.

organic ligands [263]. Additionally, magnetic properties of individual atoms are dominated by interaction with the metallic substrates which often results in a decrease of their local magnetic moment due to screening of the spin by the substrates conduction electrons [263, 264]. In this respect use of graphene as a decoupling layer may preserve the intrinsic properties of the adsorbed species, both molecules and metal atoms.

6.4.1 Preparation of Fe-BDA network

To achieve the Fe-BDA metal coordinated network, the Fe was deposited after or during the BDA deposition (intermittent deposition). Deposition rate of Fe was ~ 0.03 ML/min at a flux of 5 nA from e-beam type evaporator. Deposition of Fe did not induce any observable changes in the BDA layer as can be seen in Fig. 6.9(a). As mentioned in the previous section, BDA on graphene stays chemically intact compared to the Cu substrate. Therefore, initially, there are no carboxylates that can bind to the Fe atoms. In order to initiate the deprotonation of the BDA and promote the diffusion of atoms and molecules, the sample was annealed to approx. 100 – 110 °C for 10 min. The temperature was chosen to be smaller, than the desorption temperature of BDA from graphene (130 °C).

It was previously reported, that various concentrations of Fe and different annealing temperatures result in different structural configurations of TPA-Fe network on Cu(100) surface [145]. Therefore, various BDA/Fe concentrations were tested for BDA on graphene. Various amounts of Fe 0.1 – 0.4 ML were deposited on submonolayer BDA coverage (approx. 0.5 – 0.6 ML). The amount of Fe was estimated from the Fe-BDA network on Cu, and even the smallest tested coverage should be sufficient to

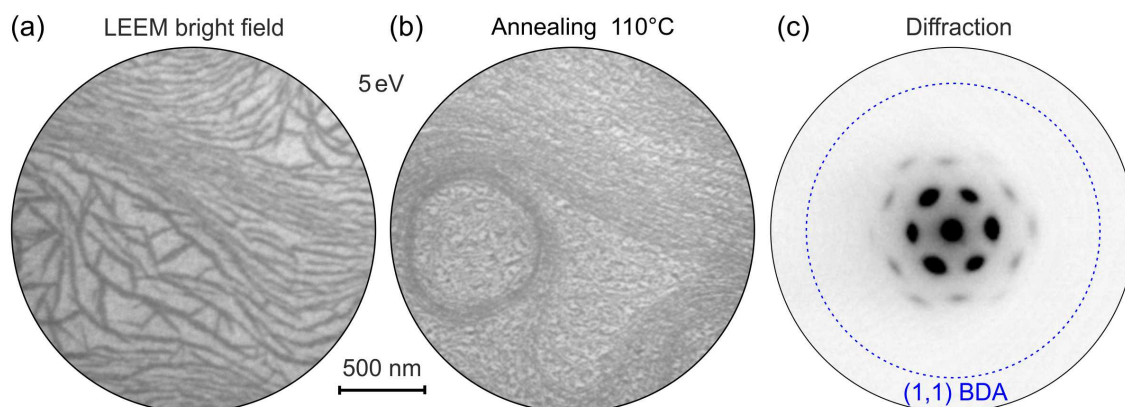


Fig. 6.9: (a) Unchanged appearance of BDA islands on graphene after the deposition of 0.1 ML of Fe. (b) Formation of small evenly distributed spots after annealing to approx. 110 °C. (c) Diffraction image taken after the annealing showing no observable spots of original BDA structure nor any other. Approximate position of original self-assembled BDA structure (1,1) spot is marked by blue circle.

form more than one ML of Fe-BDA network. The expectation was that any excess Fe would form a separate clusters.

After the annealing, the needle-like BDA islands disappear and the graphene surface was covered in evenly distributed spots, as shown in Fig. 6.9(b). Diffraction pattern of BDA phase disappears and no additional spots can be found in large scale nor in μ -diffraction images, as shown in Fig. 6.9(c). Surface coverage suggests the BDA molecules are still present at the surface. However, the absence of diffraction spots means limited order inside the layer. Stronger coordination bonds, compared to the hydrogen-bonded BDA self-assembly, may suppress the long-range order.

6.4.2 XPS analysis of Fe-BDA network

XPS was utilised to test the formation of Fe-BDA bond. In order to achieve a reasonable intensity of Fe signal, the sample with high coverage of the molecules and the Fe atoms was prepared. Approximately 1.7 ML of BDA and 0.4 ML of Fe were co-deposited to ensure sufficient mixture of the components. Temperature-dependent XPS measurements were performed, and the results are shown in Fig. 6.10. The O 1s peak and the Fe 2p doublet were used to demonstrate the chemical changes during annealing. Carbon peak was not suitable for analysis due to the high carbon signal from the graphene layer and proximity of Ir 4d peak.

Oxygen analysis was performed similarly to the study of BDA on Ag in Chapter 5. The O 1s peak was fitted by two components at binding energy of 532.0 eV (O1, blue) and 530.1 eV (O2, red). The peak positions were fixed at these positions for fitting at higher temperatures as shown in Fig. 6.10(a). The 532 eV component of O 1s represents both protonated and partially deprotonated BDA (532 eV energy corresponds to the carbonyl oxygen of partially deprotonated BDA on Ag). Second 530.1 eV component was assign to oxygen bonded to the Fe. This value is slightly lower than the one

measured for fully deprotonated BDA on Cu or Ag (Fig. 5.4 and Fig. 5.9 respectively) and correspond to observed energies of oxygen in various iron compounds [265]. This observation confirmed that BDA is binding to Fe atoms already at 95 °C.

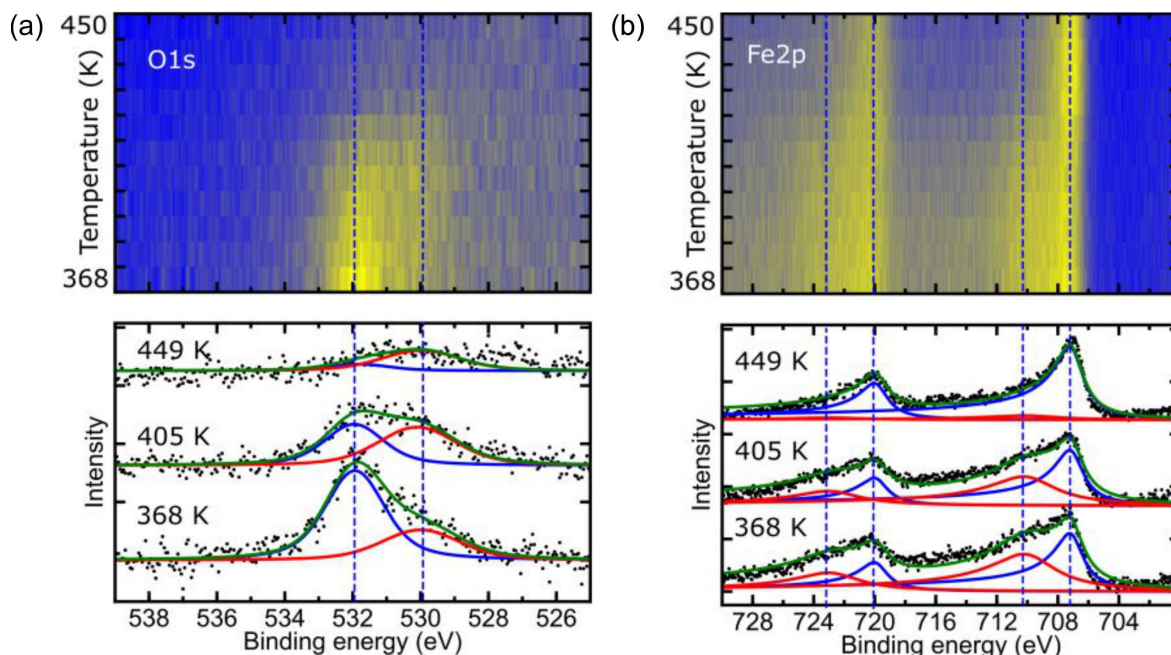


Fig. 6.10: Temperature dependent XPS study of Fe-BDA: (a) the O 1s peak fitted by two components at binding energy of 532 eV (O1, blue) and 530.1 eV (O2, red); (b) the Fe 2p doublet fitted at energies 707 eV and 719.8 eV for metallic Fe (blue) and 709.9 eV and 722.7 eV energies (red) corresponding to higher oxidation states of Fe. Figure adapted from [224].

The Fe 2p doublet of metallic state Fe was fitted by peaks centred at the binding energies 707.0 eV and 719.8 eV in agreement with typically observed energies for Fe [265]. The fitting procedure utilised asymmetric Doniach-Sunjic line profiles and a Tougaard background. The second doublet, observable in the data shown in Fig. 6.10(b), was assigned to represent the multiplet splitting observed for higher oxidation states of Fe with the assumption, that the Fe is bonded to the O in the BDA molecule [265, 266]. The peak positions of the second pair of peaks are 709.9 eV and 722.7 eV. However, there may be more than one oxidation state of Fe present in the multi-layer network. Finally, the Ir 4f doublet position was used as a reference, and no observable changes were found during annealing.

In the temperature-dependent data, two distinct regions can be distinguished for both O 1s and Fe 2p peaks. Initially, the amplitude of the O2 (red) component starts to increase relative to the O1 (blue) one, suggesting an increase in the amount of Fe-BDA bonds. Correspondingly to O 1s changes, the Fe peaks are losing the asymmetry with increasing temperature suggesting the modification of the Fe atoms binding environment. However, exact quantitative analysis was not performed, since the proper Fe fitting would require significantly better data quality. The second change is observable in the region above the 130 °C (400 K). Here, both oxygen components start to

decrease in intensity as the temperature approaches the BDA evaporation temperature from graphene. Correspondingly, the higher oxidation component of Fe peak starts to decrease in amplitude and disappear. After the annealing, only the metallic Fe peak is observed. In summary, this behaviour can be explained as the initial increase in the number of Fe-BDA bonds, followed by the desorption of BDA and eventually also Fe-BDA from the surface (or break up of Fe-BDA bond and BDA desorption).

Multiple samples of Fe-BDA were also analysed in STM. Typical appearance of low and higher Fe concentration is shown in Fig. 6.11(a) and (b) respectively. After the annealing, ordered BDA islands disappear and small clusters are formed. Clusters are randomly distributed over the graphene surface. Unfortunately, no two dimensional ordered structures were observed. Complementary to the Fe-BDA experiment, the BDA-Ni system was attempted. Approximately 0.05 ML of Ni was deposited on the BDA on graphene and annealed. Resulting structure appeared to be similar to the Fe-BDA with same small clusters, as shown in Fig. 6.11(c). In both cases, clusters appeared to be mobile on the surface, as parts of the clusters disappeared or moved during the scanning. In conclusion, it appears that BDA molecules deprotonate and bind to the Fe atoms during the annealing. However, due to the low molecule-substrate interactions, 2D ordering is inhibited, and BDA molecules form 3D clusters of Fe-BDA.

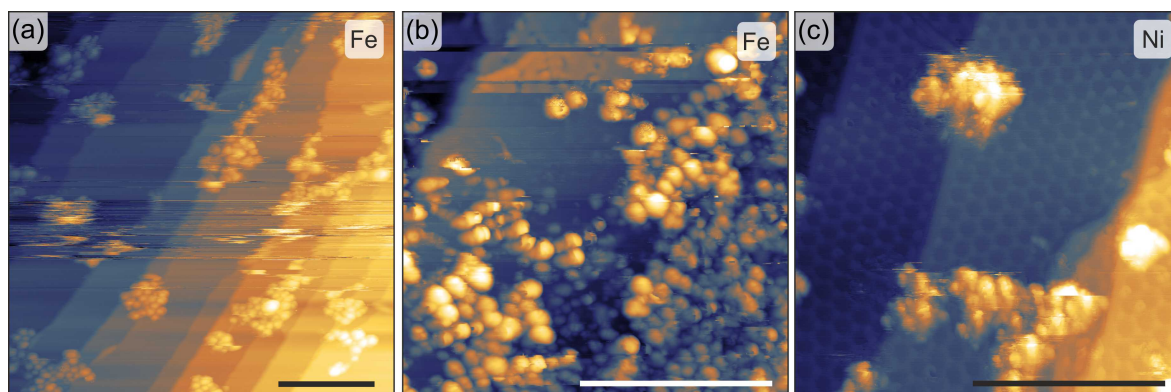


Fig. 6.11: STM images of Fe-BDA structures after the annealing. Both lower (a) and higher (b) concentration of Fe in Fe-BDA result in the randomly distributed clusters on graphene. (c) BDA-Ni structures with similar appearance to the Fe-BDA. Scale bars are 25 nm.

6.5 TCNQ self-assembly on graphene

An initial step towards the preparation of metal-organic Ni-TCNQ network was the study of TCNQ self-assembly on graphene. TCNQ molecule, schematically shown in Fig. 6.12(a), was one of the first molecules to be studied on the graphene in 2010 [11, 267]. The motivation for original TCNQ experiments on graphene was a strong electron acceptor property of TCNQ, leading to a p-doping of graphene. According to theoretical calculations, four cyano groups of TCNQ interact with graphene acceptor electrons and in-plane molecular ordering is mediated by attractive electrostatic

interactions between the negatively charged cyano groups and the positively charged hydrogen atoms of the central ring [268]. Each molecule forms four bonds resulting in a closed packed self-assembled layer on the graphene/Ir (1 1 1) surface. Similar behaviour has been observed for TCNQ self-assembled on Au(1 1 1) [57].

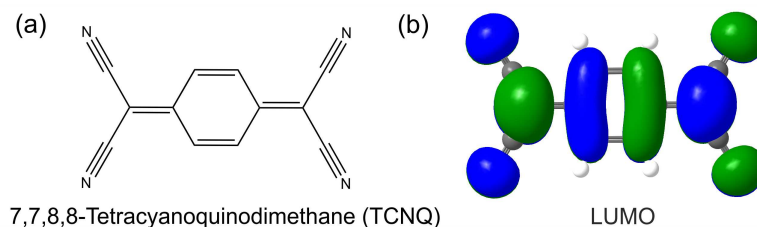


Fig. 6.12: (a) Schematic of 7,7,8,8-tetracyanoquinodimethane (TCNQ) molecule. (b) Visualization of the lowest unoccupied molecular orbital (LUMO) of TCNQ molecule in gas phase.

Several samples were prepared with various TCNQ coverages 0.5–1 ML. No molecular islands were observed in real-space images in LEEM, as shown in the Fig. 6.13(a). This is contrary to the experiments on metal surfaces, e.g. on Ag (1 1 1) [269]. However, it was possible to obtain diffraction images shown in Fig. 6.13(b). Observed patterns quickly disappeared after several seconds of measurement, and sample position had to be moved for each new image. Due to the strong electron affinity of TCNQ, it is possible, that electron beam will charge the TCNQ molecules. The increased negative charge accumulated on the cyano groups will then cause repulsion between the molecules followed by the dissolution of the ordered phase resulting in the eventual disappearance of diffraction spots.

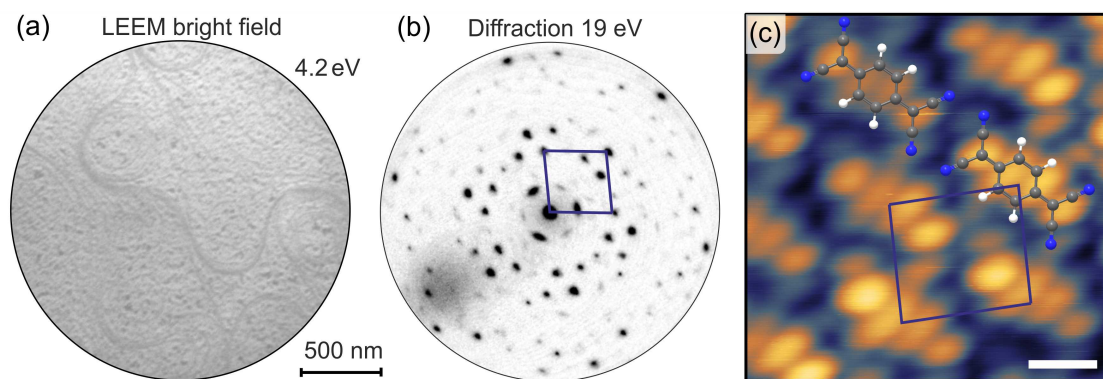


Fig. 6.13: (a) LEEM image of approx. 1 ML of TCNQ on graphene/Ir (1 1 1) substrate. No molecular islands are observed. (b) Large area diffraction taken at 19 eV, TCNQ unit cell is marked by blue rhombus. Diffraction pattern can be reproduced by 3 rotationally equivalent phases of TCNQ (each rotated 60°) and additional 3 mirrored ones. (c) STM image of TCNQ on graphene. TCNQ appearance is similar to LUMO state of TCNQ. Scale bar is 0.5 nm.

Self-assembled TCNQ on graphene was reliably imaged in STM Fig. 6.14. The tightly packed structure was identified in agreement with previous experiments on graphene [11]. Similarly to the BDA on graphene, TCNQ self-assembly can cross over

the step-edges as shown in Fig. 6.14(a). Here, the image contrast was enhanced by local contrast equalisation to observe all three atomic planes simultaneously. The appearance of TCNQ molecule on graphene was observed to change with applied bias voltage. It appears, that due to the weak molecule-graphene interaction and decoupling from the Ir substrate it is possible to distinguish molecular orbitals at room temperature STM measurements. The most stable measurement conditions, where TCNQ structure appearance was similar to its LUMO (shown in Fig. 6.12(b)), were obtained with scanning parameters: -100 to +200 mV of bias voltage with $I_t \sim 200$ pA. Distance between the molecules in row was measured 12.1 ± 0.6 Å and inter-row distance 6.5 ± 0.3 Å. Additionally, multiple brighter spots were observed in the STM images at both lower and higher bias voltages. This can be ascribed to electronic modulations in TCNQ induced by underlying graphene moiré structure.

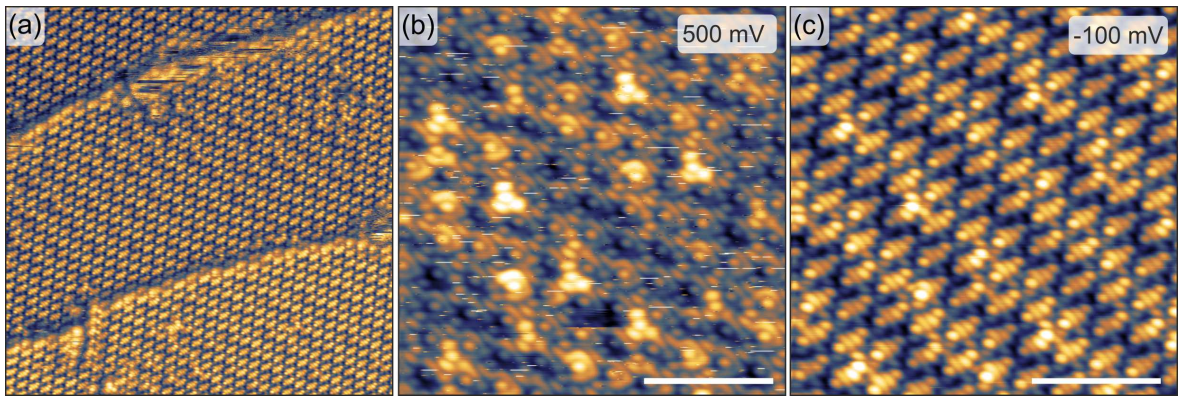


Fig. 6.14: STM images of TCNQ self-assembled on graphene/Ir (111): (a) 30×30 nm² image of extended self-assembly order over multiple step edges. (local contrast function was used to visualize all 3 atomic terraces simultaneously); (b) and (c) images of the same area measured at different voltages. Scale bars are 3 nm.

6.6 Ni-TCNQ network on graphene

Various metal-TCNQ structures were previously prepared in solution chemistry. The magnetic ordering was observed for synthesized X-TCNQ (X= Mn, Fe, Co, Ni) molecule-based magnets [270]. Additionally, several surface-confined metal-organic structures were prepared, e.g.: Sn-TCNQ on Au(111) [271], K-TCNQ on Ag(111), [272] and also Ni-TCNQ on Au(111) and Ag(100) [219]. Research of X-TCNQ 2D systems is driven by a broad range of applications such as doping of TCNQ layer [272], possible use as a single-atom catalyst for oxygen reduction [273] or the aforementioned magnetic properties.

Previous experiments had shown, that metal centre incorporated in metal-organic systems recover their magnetic moments [262]. In the Ni-TCNQ network on Au(111) the ferromagnetic coupling was observed. Theoretical calculation identified the appearance of ferromagnetism in Ni-TCNQ as Heisenberg exchange coupling between spins

localised at Ni sites and the itinerant spin density [221]. The itinerant electrons² appear due to the spin polarisation of the LUMO band, hybridised with Ni 3d states. An alternative explanation of Ni-TCNQ ferromagnetic behaviour was given in terms of indirect coupling mediated by the conduction electrons, i.e., Ruderman-Kittel-Kasuya-Yosida (RKKY) interaction [220].

Compared to the metal substrate, the use of graphene has the potential to further improve the recovery of magnetic moments in metallic centres. Additional motivation to grow Ni-TCNQ metal-organic system on graphene was the possibility to tune magnetic interaction strength. Theoretical work suggested that the indirect interaction strength can be effectively controlled by adjusting the Fermi level position in graphene with an external gate voltage [222]. Similarly, electronic density on molecular states was shown to be controllable by gate voltage [223] applied on the graphene substrate. This could allow control over the superexchange interaction strength as the spin-orbit coupling can be controlled by the subtle change of molecular structure [275].

6.6.1 Preparation of Ni-TCNQ network

In order to prepare the Ni-TCNQ coordination network on graphene, TCNQ molecules were deposited, followed by deposition of the Ni atoms with subsequent annealing (20–30 min). The annealing temperature was estimated from the previous experiments to be approx. 130 °C. Exact temperature calibration in XPS later determined that initial reaction takes place already at 110 °C and the structure is chemically stable up to 140 °C. In contrast, the evaporation temperature of pure TCNQ from graphene was tested and was found to be approx. 70 °C. Observation in LEEM did not reveal any surface changes or diffraction spots, apart decreased intensity of the graphene moiré spots. Absence of both real-space and diffraction pattern initially implied that the structure is forming in disordered clusters instead of the ordered 2D layer (similarly to Fe-BDA). However, the STM measurement revealed the presence of small 2D islands ($5 \times 5 \text{ nm}^2$), scattered across graphene.

STM topography of Ni-TCNQ network is shown in Fig. 6.15. TCNQ molecules are assembled next to each other, and the additional bright feature can be observed in between. This bright spot was attributed to the Ni atom. Similar coordination network, where four N from cyano groups of TCNQ molecule are binding to Ni atom, was observed on Au(111) [219]. Presented images show two appearances of TCNQ molecules acquired at similar scanning parameters. In Fig. 6.15(a), the TCNQ resembles its chemical structure. This appearance was attributed the enhanced resolution of STM due to random functionalisation of STM tip. In the image in Fig. 6.15(b) TCNQ resembles its LUMO-like state, similarly to previously observed structure in pure TCNQ self-assembled layer on graphene. Distance between the molecules in a row decreased to 10.0 – 10.4 Å, from approx. 12 Å in pure TCNQ phase on graphene, sug-

² “Ferromagnets, such as those made of iron or nickel, are called itinerant because the electrons whose spins aligned to create the magnetic state are extended and are the same as the ones responsible for conduction.” [274]

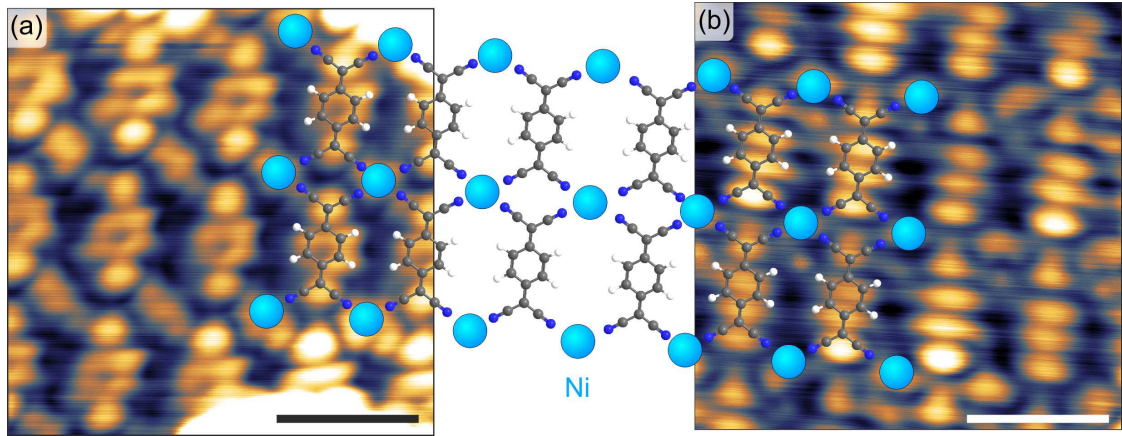


Fig. 6.15: STM images of Ni-TCNQ network on graphene/Ir(111) at different positions. In the image (a) the TCNQ resembles its chemical structure and in the image (b) the LUMO-like state. Scans were taken at similar conditions $U_B = -110$ mV, $I_t = -600$ pA for (a) and $U_B = -90$ mV, $I_t = -450$ pA for (b). Contrast change was attributed to random tip functionalization. Illustration of Ni-TCNQ network is overlaid over the images. Scale bars are 1 nm. Ni atoms are not in scale.

gesting a significant change in the bonding environment. From the proposed geometry, the N-Ni bond length was roughly estimated to be 1.5 \AA , corresponding to previously measured N-Co coordination bond length on graphene $1.5 \pm 0.2 \text{ \AA}$ [105].

In order to improve the Ni-TCNQ island size, multiple experimental strategies including depositions on the hot substrate, co-deposition of Ni or intermittent Ni depositions with post-annealing were tested. However, in all experiments, both the real-space structure and diffraction pattern in LEEM were absent. This complicated the possibilities of tuning of the deposition parameters in-situ, and only qualitative control was the STM measurements. In a limited capacity, the XPS was also utilised to verify the presence of TCNQ (full XPS analysis is presented below). After multiple experiments, it became apparent, that any excess Ni atoms were significantly degrading STM measurement. Only reasonably measurable Ni-TCNQ layers were prepared with the Ni amount of approx. 0.02 ML, that roughly corresponds to the 1 ML of Ni-TCNQ network (1:1 TCNQ:Ni ratio) presented above. STM topography from various experiments prepared with a low amount of Ni is shown in Fig. 6.16. Overall, each of these samples provided qualitatively the same STM images. The problem was that STM tip quality was degrading, most likely catching Ni or Ni-TCNQ clusters. The Ni-TCNQ layer often formed as multi-layer most clearly observed in Fig. 6.16(b). Subjectively it appeared as the STM tip was sometimes removing the top layer. One of the best images is presented in Fig. 6.16(c), corresponding to separate depositions of Ni and TCNQ followed by annealing. However, this is more a result of momentary tip enhancement, than the overall Ni-TCNQ layer quality.

In summary, the Ni-TCNQ was reliably prepared with reaction performed with an excess amount of TCNQ to Ni ratio. However, the layer quality, e.i. long-range order

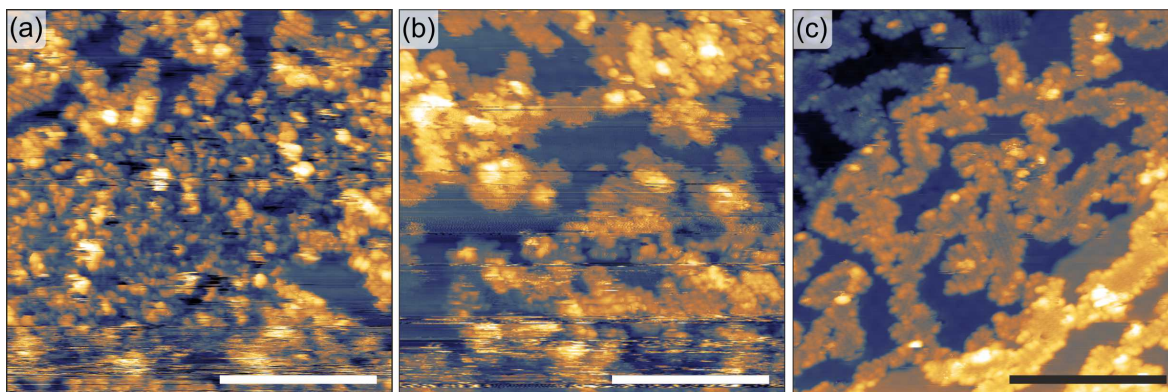


Fig. 6.16: Large scale STM images of Ni-TCNQ network prepared at different conditions: (a) co-deposition of Ni and TCNQ on a hot substrate; (b) co-deposition on RT substrate and additional annealing; (c) separated deposition and post annealing. Scale bars are 20 nm.

was limited, and the resulting structure often appeared as a multi-layer. This was unexpected as at the reaction temperature ($> 110^\circ\text{C}$) excess TCNQ molecules should desorb from the surface. In the 3D chemistry, the Ni-TCNQ coordination polymers were formed with each Ni ion binding to six different TCNQ molecules. Resulting bonding geometry was significantly different from one observed on surfaces and resulted in a 2D honeycomb-like motif that is further interconnecting to 3D networks [276]. This suggests that there may be a potential for Ni-TCNQ network to extend into the second layer.

6.6.2 XPS analysis of Ni-TCNQ network

XPS analysis was performed to verify the formation of Ni-TCNQ bonds. TCNQ chemical state was analysed through the N 1s peak of the cyano groups. The spectrum of full mono-layer of TCNQ on graphene is shown Fig. 6.17(a)-top. The N 1s peak can be fitted by one component at a binding energy of 399.1 eV and a satellite peak at 402 eV with the assumption of the linear background. The second peak is the shake-up satellite formed as a result of an intermolecular excitation process from the HOMO to the LUMO level during the emission of 1s electron. Position of both components is in agreement with the N 1s values reported for neutral TCNQ, i.e. 399.5 eV (and 402.1 eV for its satellite) [277]. The shake-up energy position, 2.9 eV from the main peak, is slightly larger than the one observed in the literature (2.6 eV) for powder or crystalline TCNQ [277] and for TCNQ on metallic substrates [271]. The slight shift of the N 1s peak is most likely caused by the charge accumulation on the TCNQ from graphene layer, reported in a recent theoretical study [268].

Fitting procedure of Ni 2p peak utilised asymmetric Doniach-Sunjic line profile and a Tougaard background. XPS spectra of Ni 2p peak from a Ni layer deposited on clean graphene/Ir(111) is shown in Fig. 6.17(b). Ni peak was fitted by three components, that correspond to main Ni $2_{3/2}$ peak and two satellite peaks. However, the minor satellite peak has only a fraction of the main component intensity, and its presence or

absence in the fit does not change the position of the main peak. Position of the main peak was identified as 852.55 eV, close to the value for bulk Ni crystal (852.6 eV) with the typical asymmetric shape [278, 279].

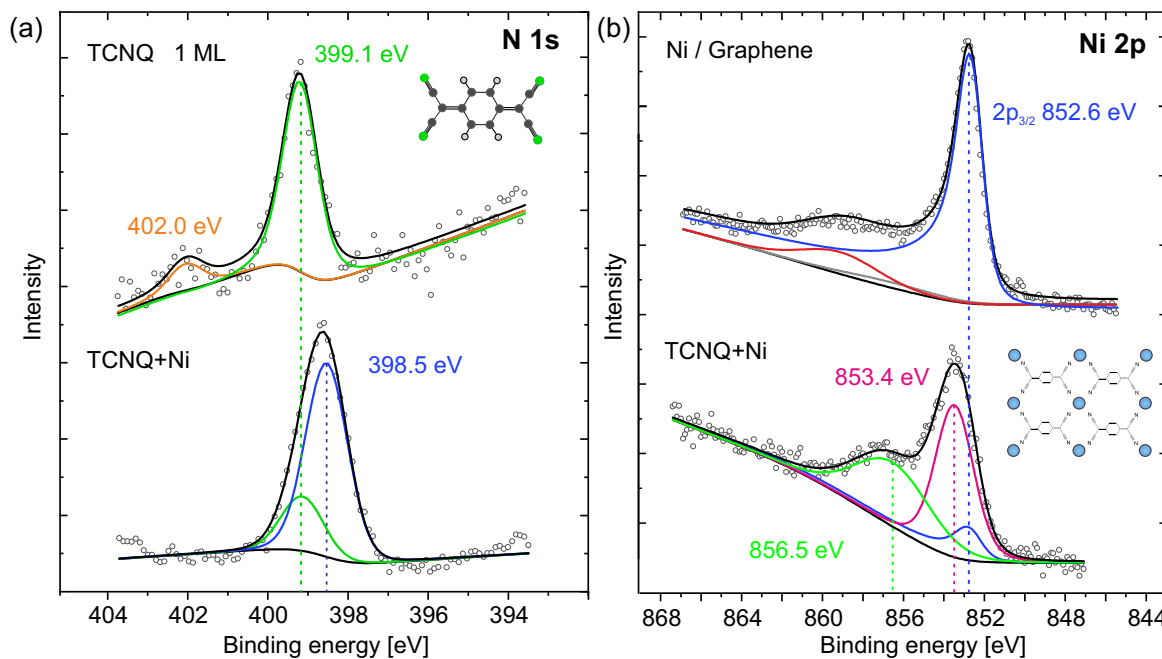


Fig. 6.17: The XPS spectra of N 1s and Ni 2p lines acquired from pure TCNQ and Ni on graphene (top) and from Ni-TCNQ layer after annealing to 110 °C (bottom). XPS spectra were acquired from different samples.

Sample with a larger amount of TCNQ molecules (approx. 2 ML) was prepared in order to achieve sufficient signal to noise ratio. Ni was co-deposited with TCNQ on the hot substrate with the aim to deposit more Ni than required for potential Ni+TCNQ network (approx. 0.1 ML). Changes were observed in the XPS spectra of both N 1s and Ni 3p as shown in the bottom part of Fig. 6.17.

The N 1s peak could be fitted by one component at an energy position 398.6 eV, that was approx. 0.4 eV wider (FWHM) compared to the pure TCNQ N 1s peak. However, with the assumption, that part of the TCNQ molecule did not bind to Ni, the fit was extended to include one component at the position of 399.1 eV and then the second component of modified N could be fitted at binding energy 398.5 eV. Second fit is shown in Fig. 6.17. In both cases, the energy the N 1s peak position is shifted toward the lower binding energies by 0.5–0.6 eV. Change towards the lower binding energies by approx. 1 eV was observed in previous studies of TCNQ-metal complexes [280], TCNQ on metallic surfaces [281] or recently Sn-TCNQ coordination structures on metal surfaces [271].

The change of the Ni 2p peak after the annealing is even more apparent. Two possible fits were tested with and without the component corresponding to the main metallic Ni peak position on graphene. In the first case, the two components were fitted with the main peak positioned at 853.1 eV and second much wider peak shifted

by 4 eV. The second fit (the one shown in Fig. 6.17) included the peak at the position of metallic Ni. In this case, positions of new peaks were shifted slightly to 853.4 eV and secondary peak by another 3.1 eV to 856.5 eV. Both fits provide qualitatively the same information with the relative peak positions changed by approx. 0.3 eV and a slight change of the peak FWHM width. Satellite peaks used for metallic Ni 3p fit were excluded from the fit in the Ni-TCNQ system.

The appearance of the Ni spectra is consistent with a higher oxidation state of Ni, i.e. broad maxima, extended satellite structure and loss of asymmetry. It is necessary to say that the presented analysis of Ni 2p, is highly simplified. The XPS spectra of higher oxidation states of Ni are not easily identified due to the complex mainline splitting. The simplest Ni²⁺ spectra are typically fitted by complex multiplet envelope (seven components in case of Ni²⁺ Gupta-Sen multiplet) [279, 278]. More precise analysis in our case was not possible due to the weak signal and possible multiple oxidation states in a thicker layer of Ni-TCNQ.

On the other hand, in the samples where the 2D structures were successfully observed, the apparent coverage of Ni-TCNQ was ~ 0.5 ML. The amount of Ni in these structures corresponds to around 0.01 ML of Ni. This coverage is well below the reasonable signal to noise ratio for the available XPS apparatus. Nevertheless, observations of shifts in both N 1s and Ni 3p peak towards lower and higher binding energies, respectively, is a strong indication for the formation of the metal-organic bonds on the graphene/Ir(111).

6.7 Conclusion

This chapter provided the extended description of combined TPG/CVD graphene growth on Ir(111) in UHV conditions. High quality single crystalline mono-layer graphene was reliably prepared from ethylene precursor. This graphene was initially utilised for the study of self-assembled BDA and TCNQ molecules. In both cases, the graphene had minimal influence on the resulting self-assembled structure. The BDA assembled in a structure similar to the α -phase on Ag(100). TCNQ formed tightly packed layer similar to ones previously observed in the literature. From the diffraction pattern, it was possible to identify multiple rotationally equivalent structures of BDA and TCNQ self-assembly.

Last sections of the chapter described attempts to prepare Fe-BDA and Ni-TCNQ 2D metal-organic coordination networks. For both cases it was observed that weak substrate-molecule interaction hinders the formation of long-range order. In the case of Fe-BDA, only a limited number of synthesis attempts were performed, without observation of any 2D structures. On the contrary, the Ni-TCNQ synthesis was extensively explored due to the initial successful observations of 2D ordered structures. Ni-TCNQ coordination network formed by four nitrogen atoms from TCNQ cyano groups binding to one Ni atom. However, only a small 2D islands were synthesised. In comparison, previously published metal-organic networks on graphene [104, 105] had two possible

advantages. First, the authors utilized a smaller number of functionalized groups per molecule that restrict possible bonding arrangements. Second, use of larger molecular species, e.g. dicyanobiphenyl, hexaphenyl, that have two and six phenyl rings compared to only one in TCNQ. Large molecules will have more robust interaction with the substrate restricting the formations of multi-layer structures.

7. GRAPHENE NANORIBBONS (GNR)

One-dimensional graphene structures, termed graphene nanoribbons (GNRs), give rise to electronic properties that differ strongly from the graphene layer. Most importantly, the reduced lateral size of the ribbons confines the electrons and creates a sizeable band-gap [16]. Size of the band-gap can be tailored simply by controlling the width of the GNR to values necessary for their specific application.

Electronic transport in GNRs is further dominated by the edge geometry or edge defects [282, 283]. It is therefore required to have the highest precision in GNRs fabrication in order to characterize and utilize their properties. The standard lithography approaches were aiming to cut the graphene monolayers to smaller ribbons by various etching processes. However, the etching of graphene generally fails to provide sufficiently precise edge geometry and chemistry. An alternative approach is the molecular bottom-up synthesis, where the GNR are stitched together from individual precursor molecules. Final shape and properties of GNR will be dictated only by the used molecules. A breakthrough in on-surface synthesis in recent years provided the tools to grow various types of GNRs including ones with armchair, chevron and zigzag edges [284]. It is now possible to tailor the GNRs properties and prepare semiconducting GNRs with variable width and band-gap sizes [285, 286]. Additionally, utilization of more exotic precursor molecules for synthesis yields GNRs with substitutional dopant heteroatoms [287–289] or functional groups [290].

In order to study the electronic properties of GNRs by angle-resolved photoemission spectroscopy (ARPES), large scale ordering of ribbons have to be achieved on the surface. For this purpose, miscut single crystal surfaces with step reconstruction proved to be ideal, e.g. experiment performed by Ruffieux et al. [291] on Au(788). Atomic steps confine the polymerization reaction into the step direction, therefore allowing the area-averaging ARPES technique to achieve sufficient signal. In this chapter, the dibromo-bianthracene (DBBA) molecules were used to synthesize the graphene nanoribbons with a width of seven carbon atoms (7-AGNR) on kinked Au(161415) substrate.

Following chapter is based on the author's publication in Ref. [292]. The author performed part of the sample preparations, STM, XPS and ARPES measurements, under the close supervision of Martina Corso, Jorge Lobo-Checa and Afaf El-Sayed. The research was part of the Erasmus internship at the Materials Physics Centre in San Sebastian, Spain, within the group of prof. Enrique Ortega.

7.1 Au (16 14 15)

Typical kinked surface reconstruction of Au (16 14 15) surface is shown in STM image in Fig. 7.1(a). The Au (16 14 15) has a vicinal angle of 3.1° from (1 1 1) plane. Its surface is formed by monoatomic steps along the $[11\bar{2}]$ direction and by (1 1 1) terraces. Additionally, the steps are ridged or kinked due to reconstruction of atoms into periodic triangular out-protrusions, likely formed by alternating $\{111\}$ and $\{100\}$ mini-facets as shown in the Fig. 7.1(b). The average step size was measured from STM to be 4.2 ± 0.6 nm. Surface reconstruction of Au (16 14 15) is rather delicate as any contamination an improper cleaning parameters lead to formation of the step bunches as shown in Fig. 7.1(c).

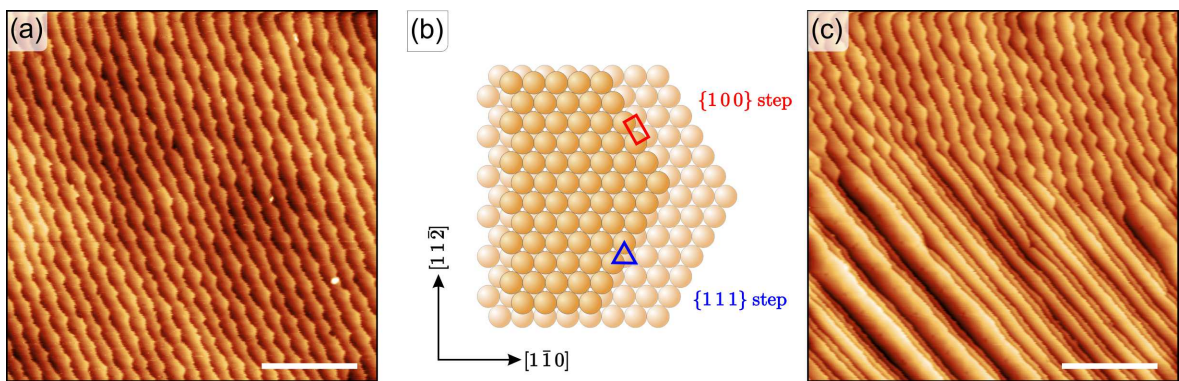


Fig. 7.1: (a) STM image of the Au (16 14 15) surface reconstruction into kinked steps. (b) Model of the reconstructed steps on the kinked Au (16 14 15). (c) Occasionally observed transition of kinked steps into step bunches. Scale bars are 30 nm.

7.2 On-surface synthesis of GNRs

The bottom-up synthesis of GNR's starts with the evaporation of molecular precursor from crucible onto the crystalline surface of a noble metal under UHV conditions. Molecules then undergo a multi-step chemical reaction, including thermally activated polymerization and cyclodehydrogenation as illustrated in Fig. 7.2. Typically, the surface-confined Ullmann coupling reaction that involves halogen functionalized molecules is utilized [293][294]. In the first step of the reaction, halogen atoms are removed from the precursor molecule (bromine in case of DBBA). The metal surfaces significantly reduces the reaction energy barrier for dissociation of halogens [295].

Dehalogenation of DBBA on Au (16 14 15) was observed to occur at $T_1 \sim 200^\circ\text{C}$, similarly to previously reported temperatures on Au (1 1 1). For the comparison on Cu (1 1 1) surface, the reaction can happen already at room temperature. After dehalogenation, the biradical species are stabilized by the surface or adatoms, diffuse and bond to another radical molecule to form the polymer chain. Molecular chains continue to grow in length as more molecules polymerize together.

Growth of the chain is terminated most likely by deactivation (passivation) of the

radical active site (original bromine position) by hydrogen created from sporadic dehydrogenation of DBBA [296]. Different pathways and organometallic intermediates have been proposed for the surface Ullmann coupling reaction. Recent work identified the complete pathway of the reaction on Cu (111) surface, by low-temperature AFM and STM and shown coordination of the two triphenylene radical binding by a Cu adatom, which confirmed a formation of C–Cu–C intermediate after dehalogenation [297].

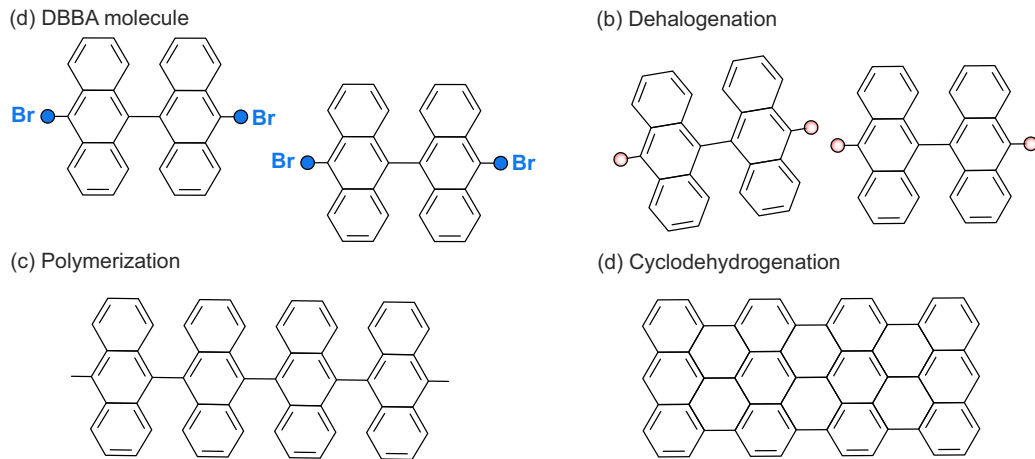


Fig. 7.2: On-surface synthesis of 7 armchair graphene nanoribbons (7-AGNRs). (a) Intact DBBA molecules. (b) Surface-assisted dehalogenation of DBBA monomers. (c) Polymerization of radicals via Ullmann coupling at elevated temperature T_1 (dependant on the surface element). (d) Surface-assisted cyclodehydrogenation at $T_2 > T_1$ creating the GNRs.

The final step in the GNR growth is cyclodehydrogenation at temperature $T_2 > T_1$. The theoretical study shown that the reaction occurs as two hydrogen transfer to the metal surface and new C–C bond is created. The reaction of hydrogen positioned between two anthracenes is more favourable than the removal of hydrogen from the edge site [298]. Cyclodehydrogenation of DBBA on Au (16 14 15) was observed to occur at $T_2 \sim 380^\circ\text{C}$.

7.2.1 GNR growth on Au (16 14 15)

Growth of GNRs on the surface of Au (16 14 15) was initially studied by STM. In all the experiments, the surface reconstruction changed significantly from the original kinked surface. During the initial polymerization reaction, the short polymer chains are very mobile, and their measurement with RT-STM is complicated. Therefore, sample with the low DBBA coverage (approx. 0.2 ML of DBBA) was prepared by annealing to temperature $T_1 \sim 200^\circ\text{C}$. Most of the molecules were found to be attached to the most reactive sites, the step edges, as shown in Fig. 7.3(a). Further, it was possible to observe the partial degradation of original kinked reconstruction and the changing arrangement of Au atoms on the terraces.

After the annealing to $T_2 = 380^\circ\text{C}$ the Au surface is covered in an almost full layer of 7-AGNRs and features larger steps and triangular protrusions as shown in Fig. 7.3(b).

The 7-AGNRs are growing preferentially along the two equivalent $[1\bar{1}0]$ direction. The length of the nanoribbons varies, with up to 35 nm for preferentially oriented GNR and typically below 10 nm for other directions. Preferential orientation of GNRs was also observed in LEED images.

Increasing the temperature above the $\sim 400^\circ\text{C}$ will cause further dehydrogenation on the GNRs at their edges, and the 7-AGNRs will fuse and create wider structures, e.g., 14-AGNR, as shown in Fig. 7.3(c).

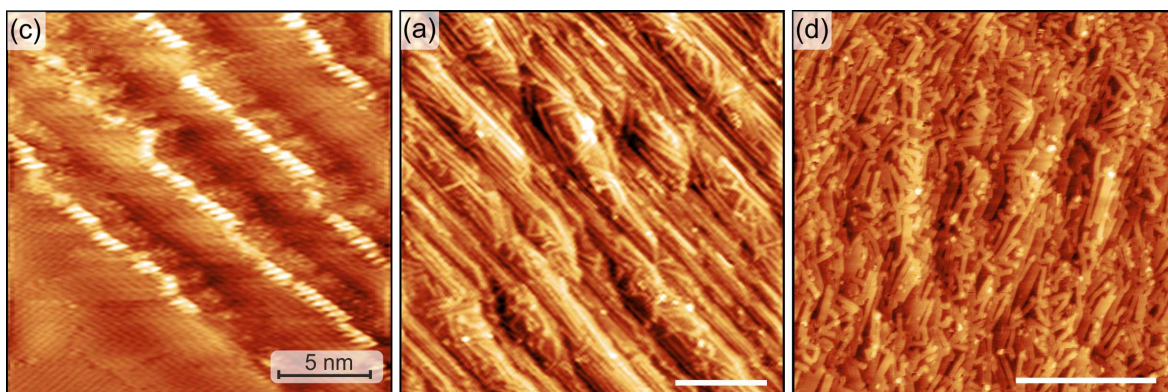


Fig. 7.3: STM images of GNR synthesis on Au(16 14 15): (a) Low coverage ($\sim 0.2\text{ML}$) of polymerized DBBA molecules. All the molecules are attached to the step edges. (b) Large area image of GNRs after the annealing to 380°C . Characteristic kinked reconstruction disappeared. (c) Fused GNRs created by additional annealing to 500°C . Scale bars in (b) and (c) are 30 nm.

7.2.2 XPS analysis

Temperature-dependent XPS measurement was performed in order to observe each step of the chemical reaction of DBBA (up to 500°C) during GNR synthesis on Au (16 14 15). The XPS spectra of C 1s and Br 3p peaks from multiple temperature points are shown in Fig. 7.4. Binding energy position of Br 3p doublet at RT corresponds to the intact DBBA molecule as observed on Au (1 1 1) [299]. Second spectra at 80°C show split of the Br 3p peak into two components. New peak component appears at approx. 2 eV higher binding energy and can be assigned to the metal bonded Br, which suggest partial debromination of DBBA.

The Br peak associated with Br bonded in DBBA decreases in intensity with increasing temperature, and at 180°C only the Br peak corresponding to Br bonded to metal remains. At this stage, all the DBBA molecules were debrominated and polymerized. This behaviour is confirmed by C 1s peak that initially shifts toward lower binding energies by few tenths of an electronvolt due to the formation of poly-anthryl intermediate as was observed for reaction on Au (1 1 1) [300]. The peak shifts back after the start of the cyclodehydrogenation. Above the 250°C , all of the Br atoms desorb from the surface as no signal was observed in the XPS in agreement with previous experiments [301].

The XPS measurement more precisely identified the dehalogenation temperature as 180 °C, which is lower than the reported value ~ 207 °C for Au (111). However this temperature is similar to ~ 177 °C observed on more reactive Au (110) [300]. Lower dehalogenation temperature compared to the flat Au (111) indicates that the kinked Au (16 14 15) have enhanced catalytic properties of Au. Kink defects on Au were previously identified as the catalytically active sites for the dissociation of Br atoms from the monomers [302].

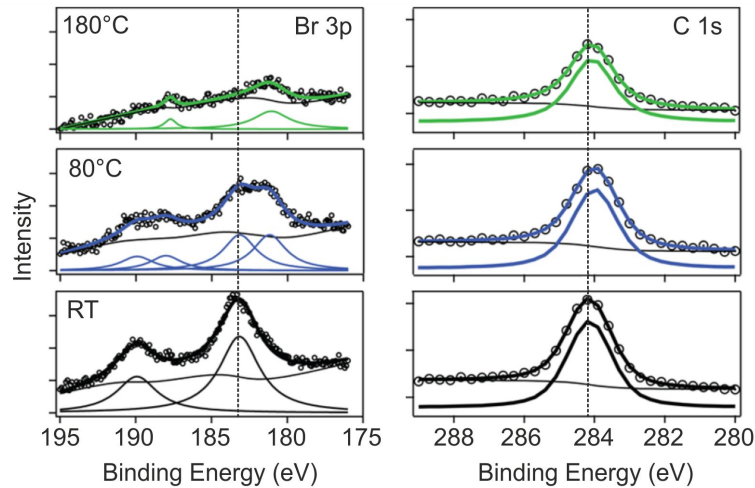


Fig. 7.4: (Temperature dependant XPS spectra of Br 3p and C 1s of 1 ML of DBBA annealed on the Au(16 14 15). The data show partial and full dehalogrnation of DBBA at 80 °C an 180 °C, respectively. Adapted from [292]

7.2.3 New surface reconstruction

STM measurement of samples with reduced molecular surface coverage (approx. 0.5 ML) revealed the formation of new atomic chains observable in between the GNRs. Detailed STM image in Fig. 7.5(a) shows that the chains are following $[1\bar{1}0]$ in-plane direction similarly to the majority of the GNRs. The inter-chain distance was measured as ~ 0.48 nm as shown in the profile plot in Fig. 7.5(b). The chains were identified as Au as the only other possibility could be residual Br atoms. However as mention above, the Br desorbs from the surface at temperatures well below the GNR synthesis temperature of 380 °C. Therefore, the observed structures were identified as Au (2×1) terrace reconstruction as modelled in Fig. 7.5(c). Significant mass transport was already observed during the initial polymerization reaction, as was shown above in Fig. 7.3(a). At the higher temperature used for cyclodehydrogenation, it is likely that the Au atoms diffuse away from the kinks and form the (2×1) missing row reconstruction.

7.2.4 7-AGNR band structure

The preferential alignment and sufficient length of the 7-AGNR allowed the measurement of the GNRs band structure by ARPES. The sample was irradiated by a high-

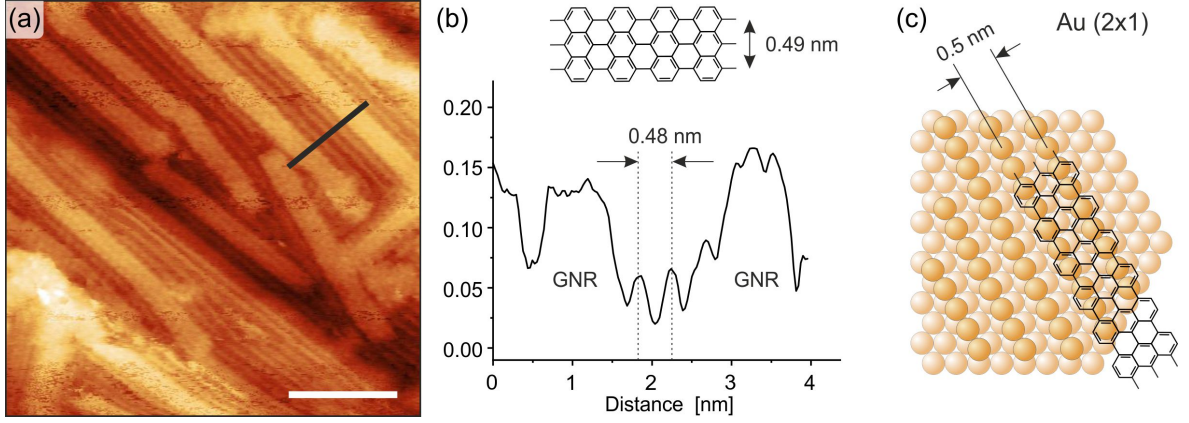


Fig. 7.5: (a) STM image on approx. 0.5 ML of 7-AGNRs. New atomic chains are observable between the GNR. (b) Topography profile of black line in (a), showing the distance between chains is approx. 0.48 nm. (c) Model of (2×1) Au surface reconstruction overlaid with schematic model of 7-AGNR.

intensity monochromatic light (21.2 eV photon energy) formed by He plasma source. A wide band dispersion was measured by the rotation of the sample parallel to the GNR preferential direction (set-up geometry is shown in Fig. 7.6(f)). Measurements were performed with a sample held at 150 K, achieved by He cooled manipulator.

The electronic band structure of 7-AGNRs consists of 1D sub-bands with parabolic energy-momentum relation $E(\mathbf{k})$ at the valence band maximum. They are characterized by the effective mass $m_{VB}^* = \hbar^2(\partial^2 E/\partial \mathbf{k}^2)^{-1}$, which is an important parameter characterizing a semiconductor materials. The GNRs valence bands are then typically identified and labelled from the Fermi level onwards with the highest occupied valence orbital (frontier orbital) labelled as VB_1 [303].

In previous work on on the vicinal Au (788) the bands acquired along the ribbon axis (k_y) that appeared as downward dispersing band [291] were incorrectly identified as the apparent frontier valence band (VB_1) at the Γ point in the first BZ of 7-AGNR, with band maximum at $E_{VB_1} = -0.7$ eV and $k_y = 1.47 \text{ \AA}^{-1}$ ($k_y = 2\pi/d$ with $d = 4.26 \text{ \AA}$). However, the measured effective mass ($m_{VB_1}^* \approx 0.2 m_e$) is in contrast with the scanning tunnelling spectroscopy (STS) data which identified $m_{VB_1}^* \approx 0.4 m_e$ [303]. This discrepancy was explained recently by revealing that first and second valence band are very close to each other (60 meV). Additionally, strong anisotropy in the photoemission intensity of aligned 7-AGNRs, makes it impossible to identify sub-bands in a single ARPES geometry [304]. The authors then assigned the previously observed band at $E = -0.7$ eV to the VB_2 . Further, they were able to measure The VB_1 band at a properly chosen transverse momentum ($k_y = 0$, $k_x = 1.5 \text{ \AA}^{-1}$) and identified the $m_{VB_1}^* \approx 0.4 m_e$ in agreement with STS data.

ARPES data from the measurement of 7-AGNR on Au(161415) are shown in Fig. 7.6(a) and (b) for $k_y = 0$ and $k_x = 0$, for $k_y = 0$ and $k_x = 0$, respectively. The first observable feature in the top area correspond to Au surface state that appears as a parabola closest to the Fermi level. The second features below the surface state

appeared to be the VB_1 band, in contrast with above mentioned determination about the possibility to measure VB_1 at $k_x = 0$. The VB_1 band was fitted as shown in the Fig. 7.6(c) and with the extracted values $E_{VB_1} = -0.89\text{eV}$ and $m_{VB_1}^* \approx 0.4m_e$, that are close to the expected ones for VB_1 [304].

The band structure of individual GNRs and its corresponding ARPES intensity were theoretically simulated with the electron plane wave expansion (EPWE) method. This method has comparable accuracy to results obtained from DFT calculations and was previously successfully applied to GNR [305]. Data from the EPWE calculations shown in Fig. 7.6(d)-(f), collaborated the assignment of the observed band to the VB_1 of 7-AGNR¹. ARPES k_y -dispersion maps were additionally measured for 7-AGNRs grown on Au(111) and Au(788) with the same experimental conditions at $k_y = 0$. Similar downward dispersing band was observed in all cases. Therefore, the ability to reliably detect the VB_1 was demonstrated with the laboratory light source, contrary to the expectations. It is possible that smaller photon energy compared to the previously used synchrotron sources (32-50 eV) and light polarization of 88% p-polarized light favours the observation of the inherently weak band at Γ point in the presented experiment.

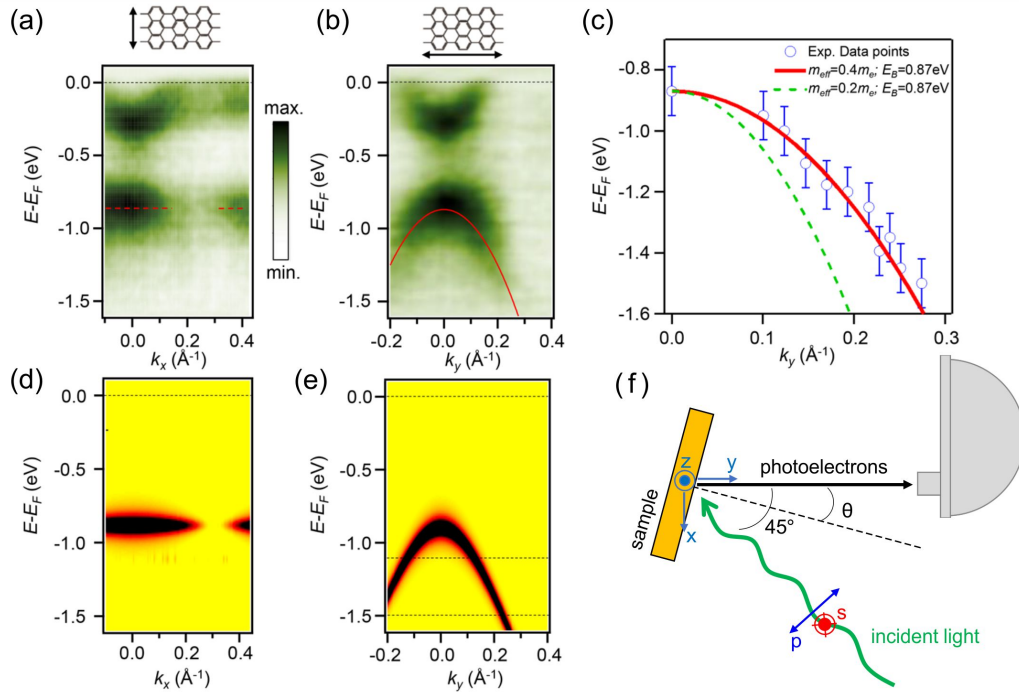


Fig. 7.6: ARPES data acquired at $k_y = 0$ and $k_x = 0$ in (a) and (b), respectively. Typical Au surface state that appears as a parabola below the Fermi energy and additional downward dispersing band appears below. The band was identified as frontier valance band and fitted with expected values as shown the (c). The spectral intensities in (a) and (b) coincide with the simulated VB_1 electronic bands of the 7-AGNRs plotted in (d) and (e). (f) ARPES experimental set-up geometry. Adapted from [292].

¹ For more details about the theoretical calculations please see original article [292], as this information is beyond the scope of this work.

8. CONCLUSIONS

This thesis presented the first experimental results obtained from a newly installed ultra-high vacuum system dedicated to the study of molecular systems on surfaces. Results from multiple self-assembled molecular structures are presented i.e.: (i) BDA on Cu(100); (ii) BDA on Ag(100); (i) BDA on graphene/Ir(111); (iv) TCNQ on graphene/Ir(111). The first experimental chapter (Chapter 5) is dedicated to the BDA on metallic substrates systems (i-ii), which represents a model system of molecular self-assembly on surfaces. Anomalous growth of BDA on Cu(100) was observed, where a molecular island grew without typical preferential nucleation sites at step edges. It was discovered that step edges of atomic planes are decorated by BDA molecules, and due to specific bonding geometry, this prevents the attachment of self-assembled islands. Therefore, the step edges are effectively passivated and present a diffusion barrier for molecular growth. Additionally, the presented molecular model was able to explain observed defects in the BDA self-assembled structure.

The BDA on Ag(100) presented a significantly more complex system, compared to the BDA on Cu(100), and includes multiple unique phases and phase transitions. The transformations of BDA are driven by thermally induced deprotonation, creating chemically different molecules and changing bonding environment of their self-assembly. Each molecular phase was comprehensively analyzed by STM, AFM, LEEM and XPS, resulting in atomic models for each phase. Additionally, several main phase transformations were described based on real-time observations in LEEM. The phase transformation shows a wide range of phenomena including the Ostwald ripening of the α -phase before the transformation, remote dissolution of the α -phase islands in the vicinity of the β -phase islands, burst nucleation of the γ_3 phase and internal directional transformation of γ_3 to γ_2 -phase. Observations of these phenomena could be later employed for modelling of the nucleation and growth in molecular systems featuring weak interactions and specifically applied for molecules functionalized by carboxylic groups.

The BDA self-assembled phases on Ag named here as the δ - , γ_2 - and γ_3 - phases, also represent k-uniform tessellations with 1, 2, and 3 distinct vertex types. A unique feature in the BDA structure compared to other molecular systems is a partially deprotonated BDA molecule that mediates connection of two distinct binding motifs in a single self-assembled molecular phase. This determination can help to provide selection rules for designing new molecular networks with novel physical or chemical properties.

Next chapter (Chapter 6) describes the recipe for the growth of high quality single crystalline mono-layer graphene on Ir(111). Self-assembly of BDA was tested on the graphene on Ir, and the resulting self-assembled structure was similar to the BDA

α -phase on Ag. However, the molecular islands were growing in multiple directions, seamlessly changing orientation and traversing the step edges due to the inert nature of graphene. Additionally, graphene effectively screens the metallic substrate preserving some of the molecular electronic structure as was observed in STM for TCNQ molecules on graphene. From the diffraction pattern, it was possible to identify multiple rotationally equivalent structures of BDA and TCNQ self-assembly on graphene.

The next sections described attempts to prepare Fe-BDA in most part as a test in preparation for the growth of Ni-TCNQ 2D metal-organic coordination networks. In both cases, the XPS data confirmed a chemical reaction between the molecular species and metal atoms; however, the 2D structure was only observed for TCNQ. The Ni-TCNQ coordination network was formed by four nitrogen atoms from TCNQ cyano groups binding to one Ni atom in a fashion similar to networks prepared on metallic substrates. However, on graphene, only small islands were observed due to a weak substrate-molecule interaction that most likely hinders the formation of an extended network. In view of this fact, more robust molecules will be tested in the future. Additionally, the presence of the ferromagnetic coupling between the Ni atoms will be tested by transferring the sample into the state of the art EPR spectroscope. The possibility to tune the Fermi level position of graphene and consequently the electronic states in Ni-TCNQ system in its vicinity could enable externally control the magnetic coupling in the metal-organic systems.

The last chapter (Chapter 7) of this thesis described the on-surface synthesis of graphene nanoribbons (7-AGNR) on the kinked Au(161415) substrate from DBBA precursor molecules. Specific kinked reconstruction of the Au substrate was transformed after the growth of GNRs. The new (2×1) missing row surface reconstruction was formed most likely due to mass transformed from the step edges. Additionally, a sufficient amount of preferentially oriented 7-AGNRs allowed to utilize band mapping in ARPES and determine the position of the 7-AGNR frontier valance band.

In conclusion, this thesis presents several molecular systems on various surfaces. One of the most important results is the observation of structure and phase transformations of BDA on Cu and Ag that may lead to improved applications and theoretical growth models for molecular layers. Another significant result is the growth of the 2D Ni-TCNQ metal coordinated network on graphene. Lessons learned here will provide a roadmap for future experimental realizations of structures on non-interacting substrates.

9. SUPPLEMENTARY

Description of supplementary files:

- (I) *1-SiC-IV.avi*
Video shows sequence of LEEM bright field images of graphene on SiC between energy 1.5 – 8.8 eV. Here, electron reflectivity of graphene changes differently depending on the number of graphene layers. Images from this experiment were used in the main text in Fig. 4.5.
- (II) *2-BDA-Cu.avi*
Movement of BDA molecules on Cu(100) measured in STM. Video shows consecutive $10 \times 10 \text{ nm}^2$ STM images measured every 25 s. BDA molecules attach or detach from the edge of the self-assembled island.
- (III) *3-AlphaToBeta.avi*
Phase transformation of α to β -phase on Ag(100) observed in LEEM. Video shows initial Ostwald ripening of α -phase followed by growth of large β -phase islands. Images from this experiment were used in the main text in Fig. 5.18 and Fig. 5.19.
- (IV) *4-BetaToGamma.avi*
Phase transformation of β to γ -phase on Ag(100) observed in LEEM. Video shows initial formation of small islands of γ_3 form inside of the β -phase. In the second part, inner conversion of γ phases takes place. Please note that the time flow is slowed down by factor of 1/8 in the second part as can be seen in time stamp. Images from this experiment were used in the main text in Fig. 5.24.
- (V) *5-GammaToDelta.avi*
Phase transformation of the γ to δ -phase on Ag(100) observed in LEEM at 1.1 eV. Majority of the new phase formation takes place internally, similarly to the γ_3 to γ_2 and growth is partially propagated through bright spot (presumable cavities in the self-assembly). Images from this experiment were used in the main text in Fig. 5.28.

10. AUTHORS PUBLICATIONS

Thesis related articles:

- 1) PROCHAZKA, P.; GOSALVEZ, M. A.; **KORMOS, L.**; DE LA TORRE, B.; GALLARDO, A.; ALBERDI-RODRIGUEZ, J.; CHUTORA, T.; MAKOVEEV, A.O.; SHAHSAVAR, A.; ARNAU, A.; JELINEK, P.; CECHAL, J.: Multiscale Analysis of Phase Transformations in Self-Assembled Layers of 4,4-Biphenyl Dicarboxylic on the Ag(001) Surface. *ACS Nano*, 2020, 14 (6), p. 7269-7279, ISSN: 1936-0851. <https://doi.org/10.1021/acsnano.0c02491>.
- 2) **KORMOS, L.**; PROCHAZKA, P.; MAKOVEEV, A.O.; CECHAL, J.: Complex k-uniform tilings by a simple bitopic precursor self-assembled on Ag(001). *Nature Comm.*, 2020, 11, p. 1856, ISSN: 2041-1723. <https://doi.org/10.1038/s41467-020-15727-6>.
- 3) **KORMOS, L.**; PROCHAZKA, P.; SIKOLA, T.; CECHAL, J.: Molecular Passivation of Substrate Step Edges as Origin of Unusual Growth Behavior of 4,4-Biphenyl Dicarboxylic Acid on Cu(001). *Journal of Physical Chemistry C*, 2018, 122, p. 2815-2820, ISSN: 1932-7447. <https://doi.org/10.1021/acs.jpcc.7b11436>.
- 4) EL-SAYED, A.; PIQUERO-ZULAICA, I.; ABD EL-FATTAH, Z. M.; **KORMOS, L.**; ALI, K.; WEBER, A.; BREDE, J.; DE OTEYZA, D. G.; LOBO-CHECA, J.; ORTEGA, E. AND MARTINA, C.: Synthesis of Graphene Nanoribbons on a Kinked Au Surface: Revealing the Frontier Valence Band at the Brillouin Zone Center. *Journal of Physical Chemistry C*, 2020, 124, p. 15474-15480, ISSN: 1932-7447. <https://doi.org/10.1021/acs.jpcc.0c02801>.

Other publications:

- 5) FIKACEK, J.; PROCHAZKA, P.; STETSOVYCH, V.; PRUSA, S.; VONDRACEK, M.; **KORMOS, L.**; SKALA, T.; VLAIC, P.; CAHA, O.; CARVA, K.; CECHAL, J.; SPRINGHOLZ, G.; HONOLKA, J.: Step-edge assisted large scale FeSe monolayer growth on epitaxial Bi₂Se₃ thin films. *New Journal of Physics*, 2020, 22, ISSN: 1367-2630. <https://iopscience.iop.org/article/10.1088/1367-2630/ab9b59>.
- 6) REDONDO, J.; LAZAR, P.; PROCHAZKA, P.; PRUSA, S.; MALLADA, B.; CAHLIK, A.; LACHNITT, J.; BERGER, J.; SMID, B.; **KORMOS, L.**; JELINEK, A.; CECHAL, J.; SVEC, M.: Identification of Two-Dimensional FeO₂ Termination of Bulk Hematite α - Fe₂O₃ (0001) Surface. *Journal of Physical Chemistry C*, 2019, 123 (23), 14312-14318, ISSN: 1932-7447. <https://doi.org/10.1021/acs.jpcc.9b00244>.
- 7) **KORMOS, L.**; KRATZER, M.; KOSTECKI, K.; OEME, M.; SIKOLA, T.; KASPER, E.; SCHULZE, J.; TEICHERT, C.: Surface analysis of epitaxially grown GeSn alloys with Sn contents between 15% and 18%. *Surface and Interface Analysis*, 2017, 49 (4), 297-302, ISSN: 1096-9918. <http://dx.doi.org/10.1002/sia.6134>.
- 8) BARTOSIK, M.; **KORMOS, L.**; FLAJSMAN, L.; KALOUSEK, R.; MACH, J.; LISKOVA, Z.; NEZVAL, D.; SVARC, V.; SAMORIL, T.; SIKOLA, T.: Nanometer-Sized Water Bridge and Pull-Off Force in AFM at Different Relative Humidities: Reproducibility Measurement and Model Based on Surface Tension Change. *Journal of Physical Chemistry B*, 2017, 121 (3), 610-619, ISSN: 1520-6106. <http://dx.doi.org/10.1021/acs.jpcc.6b11108>.
- 9) MACH, J.; PROCHAZKA, P.; BARTOSIK, M.; NEZVAL, D.; PIASTEK, J.; HULVA, J.; SVARC, V.; KONECNY, M.; **KORMOS, L.**; SIKOLA, T.: Electronic transport properties of graphene doped by gallium. *Nanotechnology*, 2017, 28 (41), 1-10, ISSN: 0957-4484. <http://dx.doi.org/10.1088/1361-6528/aa86a4>.

BIBLIOGRAPHY

- [1] MOORE, G. E. Cramming more components onto integrated circuits, reprinted from electronics, volume 38, number 8, april 19, 1965, pp.114 ff. *IEEE Solid-State Circuits Society Newsletter* 11, 3 (2006), 33–35.
- [2] MITCHELL, W. The chips are down for moore’s law. *NATURE NEWS* 530 (Feb 2016). <https://www.nature.com/news/the-chips-are-down-for-moore-s-law-1.19338>.
- [3] TOPALOGLU R. O., WONG, P. *Beyond-CMOS Technologies for Next Generation Computer Design*. Springer, 2019. ISBN 978-3-319-90384-2. doi: doi.org/10.1007/978-3-319-90385-9.
- [4] COLLIER, C. P., WONG, E. W., BELOHRADSKÝ, M., RAYMO, F. M., STODDART, J. F., KUEKES, P. J., WILLIAMS, R. S., AND HEATH, J. R. Electronically configurable molecular-based logic gates. *Science* 285, 5426 (Jul 1999), 391. doi: [10.1126/science.285.5426.391](https://doi.org/10.1126/science.285.5426.391).
- [5] METZGER, R. M., AND CAVA, M. P. Rectification by a single molecule of hexadecylquinolinium tricyanoquinodimethanide. *Annals of the New York Academy of Sciences* 852, 1 (Jun 1998), 95–115. doi: [10.1111/j.1749-6632.1998.tb09866.x](https://doi.org/10.1111/j.1749-6632.1998.tb09866.x).
- [6] CHEN, J., REED, M. A., RAWLETT, A. M., AND TOUR, J. M. Large on-off ratios and negative differential resistance in a molecular electronic device. *Science* 286, 5444 (Nov 1999), 1550. doi: [10.1126/science.286.5444.1550](https://doi.org/10.1126/science.286.5444.1550).
- [7] GRAHAM, M. J., ZADROZNY, J. M., FATAFTAH, M. S., AND FREEDMAN, D. E. Forging solid-state qubit design principles in a molecular furnace. *Chemistry of Materials* 29, 5 (Mar 2017), 1885–1897. doi: [10.1021/acs.chemmater.6b05433](https://doi.org/10.1021/acs.chemmater.6b05433).
- [8] BADER, K., DENGLER, D., LENZ, S., ENDEWARD, B., JIANG, S.-D., NEUGEBAUER, P., AND VAN SLAGEREN, J. Room temperature quantum coherence in a potential molecular qubit. *Nature Communications* 5, 1 (Oct 2014), 5304. doi: [10.1038/ncomms6304](https://doi.org/10.1038/ncomms6304).
- [9] FERRANDO-SORIA, J., MORENO PINEDA, E., CHIESA, A., FERNANDEZ, A., MAGEE, S. A., CARRETTA, S., SANTINI, P., VITORICA-YREZABAL, I. J., TUNA, F., TIMCO, G. A., MCINNES, E. J., AND WINPENNY, R. E. A modular design of molecular qubits to implement universal quantum gates. *Nature Communications* 7, 1 (Apr 2016), 11377. doi: [10.1038/ncomms11377](https://doi.org/10.1038/ncomms11377).
- [10] GEIM, A. K. Graphene: Status and prospects. *Science* 324, 5934 (2009), 1530–1534. doi: [10.1126/science.1158877](https://doi.org/10.1126/science.1158877).
- [11] BARJA, S., GARNICA, M., HINAREJOS, J. J., VÁZQUEZ DE PARGA, A. L., MARTÍN, N., AND MIRANDA, R. Self-organization of electron acceptor molecules on graphene. *Chemical Communications* 46, 43 (2010), 8198–8200. doi: [10.1039/C0CC02675A](https://doi.org/10.1039/C0CC02675A).

- [12] HAUGEN, H., HUERTAS-HERNANDO, D., AND BRATAAS, A. Spin transport in proximity-induced ferromagnetic graphene. *Physical Review B* 77 (Mar 2008), 115406. doi: [10.1103/PhysRevB.77.115406](https://doi.org/10.1103/PhysRevB.77.115406).
- [13] ZHOU, B., CHEN, X., WANG, H., DING, K.-H., AND ZHOU, G. Magnetotransport and current-induced spin transfer torque in a ferromagnetically contacted graphene. *Journal of Physics: Condensed Matter* 22, 44 (Oct 2010), 445302. doi: [10.1088/0953-8984/22/44/445302](https://doi.org/10.1088/0953-8984/22/44/445302).
- [14] RISS, A., WICKENBURG, S., TAN, L. Z., TSAI, H.-Z., KIM, Y., LU, J., BRADLEY, A. J., UGEDA, M. M., MEAKER, K. L., WATANABE, K., TANIGUCHI, T., ZETTL, A., FISCHER, F. R., LOUIE, S. G., AND CROMMIE, M. F. Imaging and tuning molecular levels at the surface of a gated graphene device. *ACS Nano* 8, 6 (Jun 2014), 5395–5401. doi: [10.1021/nm501459v](https://doi.org/10.1021/nm501459v).
- [15] DIMAS G. DE OTEYZA, C. R. *On-Surface Synthesis II: Proceedings of the International Workshop On-Surface Synthesis*. Springer, 2016. ISBN 978-3-319-75810-7. doi: [/doi.org/10.1007/978-3-319-75810-7](https://doi.org/10.1007/978-3-319-75810-7).
- [16] SON, Y.-W., COHEN, M. L., AND LOUIE, S. G. Energy gaps in graphene nanoribbons. *Physical Review Letter* 97 (2006), 216803. doi: [10.1103/PhysRevLett.97.216803](https://doi.org/10.1103/PhysRevLett.97.216803).
- [17] ULMAN, A. Formation and structure of self-assembled monolayers. *Chemical Reviews* 96, 4 (Jan 1996), 1533–1554. doi: [10.1021/cr9502357](https://doi.org/10.1021/cr9502357).
- [18] BARTH, J. V., COSTANTINI, G., AND KERN, K. Engineering atomic and molecular nanostructures at surfaces. *Nature* 437, 7059 (Sep 2005), 671–679. doi: [10.1038/nature04166](https://doi.org/10.1038/nature04166).
- [19] BARTH, J. V. Molecular architectonic on metal surfaces. *Annual Review of Physical Chemistry* 58, 1 (May 2007), 375–407. doi: [10.1146/annurev.physchem.56.092503.141259](https://doi.org/10.1146/annurev.physchem.56.092503.141259).
- [20] DONG, L., GAO, Z., AND LIN, N. Self-assembly of metal–organic coordination structures on surfaces. *Progress in Surface Science* 91, 3 (Aug 2016), 101–135. doi: [10.1016/j.progsurf.2016.08.001](https://doi.org/10.1016/j.progsurf.2016.08.001).
- [21] JELÍNEK, P. High resolution spm imaging of organic molecules with functionalized tips. *Journal of Physics: Condensed Matter* 29, 34 (Jul 2017), 343002. doi: [10.1088/1361-648x/aa76c7](https://doi.org/10.1088/1361-648x/aa76c7).
- [22] STONE, A. *The Theory of Intermolecular Forces*. OUP Oxford, 2013. 2nd edition, ISBN: 9780199672394.
- [23] VAN VLEET, M. J., MISQUITTA, A. J., STONE, A. J., AND SCHMIDT, J. R. Beyond born–mayer: Improved models for short-range repulsion in ab initio force fields. *Journal of Chemical Theory and Computation* 12, 8 (Aug 2016), 3851–3870. doi: [10.1021/acs.jctc.6b00209](https://doi.org/10.1021/acs.jctc.6b00209).
- [24] ISRAELACHVILI, J. N. *Intermolecular and Surface Forces*, 3rd revised ed. Academic Press, 2011. ISBN: 0123919274, 9780123919274.

- [25] ZAMBELLI, T., GOUDEAU, S., LAGOUE, J., GOURDON, A., BOUJU, X., AND GAUTHIER, S. Molecular self-assembly of jointed molecules on a metallic substrate: From single molecule to monolayer. *ChemPhysChem* 7, 9 (Sep 2006), 1917–1920. doi: [10.1002/cphc.200600349](https://doi.org/10.1002/cphc.200600349).
- [26] ASCOLANI, H., VAN DER MEIJDEN, M. W., CRISTINA, L. J., GAYONE, J. E., KELLOGG, R. M., FUHR, J. D., AND LINGENFELDER, M. Van der waals interactions in the self-assembly of 5-amino[6]helicene on cu(100) and au(111). *Chemical Communications* 50, 90 (2014), 13907–13909. doi: [10.1039/C4CC04338C](https://doi.org/10.1039/C4CC04338C).
- [27] TAHARA, K., FURUKAWA, S., UJI-I, H., UCHINO, T., ICHIKAWA, T., ZHANG, J., MAMDOUH, W., SONODA, M., DE SCHRYVER, F. C., DE FEYTER, S., AND TOBE, Y. Two-dimensional porous molecular networks of dehydrobenzo[12]annulene derivatives via alkyl chain interdigitation. *Journal of the American Chemical Society* 128, 51 (Dec 2006), 16613–16625. doi: [10.1021/ja0655441](https://doi.org/10.1021/ja0655441).
- [28] CHEN, Q., CHEN, T., PAN, G.-B., YAN, H.-J., SONG, W.-G., WAN, L.-J., LI, Z.-T., WANG, Z.-H., SHANG, B., YUAN, L.-F., AND YANG, J.-L. Structural selection of graphene supramolecular assembly oriented by molecular conformation and alkyl chain. *Proceedings of the National Academy of Sciences* 105, 44 (Nov 2008), 16849. doi: [10.1073/pnas.0809427105](https://doi.org/10.1073/pnas.0809427105).
- [29] LIAO, L.-Y., LI, Y.-B., XU, J., GENG, Y.-F., ZHANG, J.-Y., XIE, J.-L., ZENG, Q.-D., AND WANG, C. Competitive influence of hydrogen bonding and van der waals interactions on self-assembled monolayers of stilbene-based carboxylic acid derivatives. *The Journal of Physical Chemistry C* 118, 49 (Dec 2014), 28625–28630. doi: [10.1021/jp509041b](https://doi.org/10.1021/jp509041b).
- [30] GRAVIL, P. A., DEVEL, M., LAMBIN, P., BOUJU, X., GIRARD, C., AND LUCAS, A. A. Adsorption of c_{60} molecules. *Physical Review B* 53 (Jan 1996), 1622–1629. doi: [10.1103/PhysRevB.53.1622](https://doi.org/10.1103/PhysRevB.53.1622).
- [31] GRIMME, S., ANTONY, J., EHRLICH, S., AND KRIEG, H. A consistent and accurate ab initio parametrization of density functional dispersion correction (dft-d) for the 94 elements h-pu. *The Journal of Chemical Physics* 132, 15 (Apr 2010), 154104. doi: [10.1063/1.3382344](https://doi.org/10.1063/1.3382344).
- [32] STEINER, T. The hydrogen bond in the solid state. *Angewandte Chemie International Edition* 41, 1 (Jan 2002), 48–76. doi: [10.1002/1521-3773\(20020104\)41:1<48::AID-ANIE48>3.0.CO;2-U](https://doi.org/10.1002/1521-3773(20020104)41:1<48::AID-ANIE48>3.0.CO;2-U).
- [33] MO, Y. Probing the nature of hydrogen bonds in dna base pairs. *Journal of Molecular Modeling* 12, 5 (Jul 2006), 665–672. doi: [10.1007/s00894-005-0021-y](https://doi.org/10.1007/s00894-005-0021-y).
- [34] TAYLOR, R., AND KENNARD, O. Crystallographic evidence for the existence of ch.cntdot..cntdot..cntdot.o, ch.cntdot..cntdot..cntdot.n and ch.cntdot..cntdot..cntdot.cl hydrogen bonds. *Journal of the American Chemical Society* 104, 19 (Sep 1982), 5063–5070. doi: [10.1021/ja00383a012](https://doi.org/10.1021/ja00383a012).
- [35] ARUNAN, E., DESIRAJU, G. R., KLEIN, R. A., SADLEJ, J., SCHEINER, S., ALKORTA, I., CLARY, D. C., CRABTREE, R. H., DANNENBERG, J. J., HOBZA, P., KJAERGAARD, H. G., LEGON, A. C., MENNUCCI, B., AND NESBITT, D. J. Definition of

- the hydrogen bond (iupac recommendations 2011). *Pure and Applied Chemistry* 83, 8 (2011), 1637–1641. doi: [10.1351/PAC-REC-10-01-02](https://doi.org/10.1351/PAC-REC-10-01-02).
- [36] WENDLER, K., THAR, J., ZAHN, S., AND KIRCHNER, B. Estimating the hydrogen bond energy. *The Journal of Physical Chemistry A* 114, 35 (Sep 2010), 9529–9536. doi: [10.1021/jp103470e](https://doi.org/10.1021/jp103470e).
- [37] GRIESSL, S. J. H., LACKINGER, M., JAMITZKY, F., MARKERT, T., HIETSCHOLD, M., AND HECKL, W. M. Incorporation and manipulation of coronene in an organic template structure. *Langmuir* 20, 21 (Oct 2004), 9403–9407. doi: [10.1021/la049441c](https://doi.org/10.1021/la049441c).
- [38] DMITRIEV, A., LIN, N., WECKESSER, J., BARTH, J. V., AND KERN, K. Supramolecular assemblies of trimesic acid on a cu(100) surface. *The Journal of Physical Chemistry B* 106, 27 (Jul 2002), 6907–6912. doi: [10.1021/jp014214u](https://doi.org/10.1021/jp014214u).
- [39] PLEVIN, M. J., BRYCE, D. L., AND BOISBOUVIER, J. Direct detection of ch/ π interactions in proteins. *Nature Chemistry* 2, 6 (Jun 2010), 466–471. doi: [10.1038/nchem.650](https://doi.org/10.1038/nchem.650).
- [40] NISHIO, M. The ch/ π hydrogen bond in chemistry. conformation, supramolecules, optical resolution and interactions involving carbohydrates. *Physical Chemistry Chemical Physics* 13, 31 (2011), 13873–13900. doi: [10.1039/C1CP20404A](https://doi.org/10.1039/C1CP20404A).
- [41] CAVALLO, G., METRANGOLO, P., MILANI, R., PILATI, T., PRIMAGI, A., RESNATI, G., AND TERRANEO, G. The halogen bond. *Chemical Reviews* 116, 4 (Feb 2016), 2478–2601. doi: [10.1021/acs.chemrev.5b00484](https://doi.org/10.1021/acs.chemrev.5b00484).
- [42] PAVAN, M. S., DURGA PRASAD, K., AND GURU ROW, T. N. Halogen bonding in fluorine: experimental charge density study on intermolecular $\text{F}\cdots\text{F}$ and $\text{F}\cdots\text{Z}$ donor–acceptor contacts. *Chemical Communications* 49, 68 (2013), 7558–7560. doi: [10.1039/C3CC43513J](https://doi.org/10.1039/C3CC43513J).
- [43] CHUNG, K.-H., PARK, J., KIM, K. Y., YOON, J. K., KIM, H., HAN, S., AND KAHNG, S.-J. Polymorphic porous supramolecular networks mediated by halogen bonds on ag(111). *Chemical Communications* 47, 41 (2011), 11492–11494. doi: [10.1039/C1CC14679C](https://doi.org/10.1039/C1CC14679C).
- [44] JANG, W. J., CHUNG, K.-H., LEE, M. W., KIM, H., LEE, S., AND KAHNG, S.-J. Tetragonal porous networks made by rod-like molecules on au(111) with halogen bonds. *Applied Surface Science* 309 (Aug 2014), 74–78. doi: [10.1016/j.apsusc.2014.04.174](https://doi.org/10.1016/j.apsusc.2014.04.174).
- [45] DALLOCCHIO, R., DESSÌ, A., SOLINAS, M., ARRAS, A., COSSU, S., AUBERT, E., MAMANE, V., AND PELUSO, P. Halogen bond in high-performance liquid chromatography enantioseparations: Description, features and modelling. *Journal of Chromatography A* 1563 (Aug 2018), 71–81. doi: [10.1016/j.chroma.2018.05.061](https://doi.org/10.1016/j.chroma.2018.05.061).
- [46] TSUZUKI, S., HONDA, K., UCHIMARU, T., MIKAMI, M., AND TANABE, K. Origin of attraction and directionality of the π/π interaction: model chemistry calculations of benzene dimer interaction. *Journal of the American Chemical Society* 124, 1 (Jan 2002), 104–112. doi: [10.1021/ja0105212](https://doi.org/10.1021/ja0105212).
- [47] HUNTER, C. A., AND SANDERS, J. K. The nature of π - π interactions. *Journal of the American Chemical Society* 112, 14 (1990), 5525–5534. doi: doi.org/10.1021/ja00170a016.

- [48] MEYER, E. A., CASTELLANO, R. K., AND DIEDERICH, F. Interactions with aromatic rings in chemical and biological recognition. *Angewandte Chemie International Edition* **42**, 11 (Mar 2003), 1210–1250. doi: [10.1002/anie.200390319](https://doi.org/10.1002/anie.200390319).
- [49] MAIER, S., FENDT, L.-A., ZIMMERLI, L., GLATZEL, T., PFEIFFER, O., DIEDERICH, F., AND MEYER, E. Nanoscale engineering of molecular porphyrin wires on insulating surfaces. *Small* **4**, 8 (Aug 2008), 1115–1118. doi: [10.1002/sml.200701259](https://doi.org/10.1002/sml.200701259).
- [50] SCHIFFRIN, A., RIEMANN, A., AUWÄRTER, W., PENNEC, Y., WEBER-BARGIONI, A., CVETKO, D., COSSARO, A., MORGANTE, A., AND BARTH, J. V. Zwitterionic self-assembly of l-methionine nanogratings on the ag(111) surface. *Proceedings of the National Academy of Sciences* **104**, 13 (2007), 5279–5284. doi: [10.1073/pnas.0607867104](https://doi.org/10.1073/pnas.0607867104).
- [51] WON, S.-Y., KIM, J.-H., KIM, H., YOON, J. K., KAHNG, S.-J., KWON, Y.-K., AND PARK, Y. Linear and Hexagonal Porous Structures of an Organic Charge Acceptor Hexaaza-triphenylene-hexacarbonitrile on Au(111) with $CN\dot{A}\cdot\dot{A}\cdot\dot{A}\cdot CN$ Dipolar Interactions. *The Journal of Physical Chemistry C* **117**, 41 (Oct. 2013), 21371–21375. doi: [10.1021/jp407173w](https://doi.org/10.1021/jp407173w).
- [52] CABELLOS, J. L., MOWBRAY, D. J., GOIRI, E., EL-SAYED, A., FLOREANO, L., DE OTEYZA, D. G., ROGERO, C., ORTEGA, J. E., AND RUBIO, A. Understanding Charge Transfer in Donor-Acceptor/Metal Systems: A Combined Theoretical and Experimental Study. *The Journal of Physical Chemistry C* **116**, 34 (Aug. 2012), 17991–18001. doi: [10.1021/jp3004213](https://doi.org/10.1021/jp3004213).
- [53] SEDONA, F., DI MARINO, M., BASAGNI, A., COLAZZO, L., AND SAMBI, M. Structurally Tunable Self-Assembled 2D Cocystals of C_{60} and Porphyrins on the Ag (110) Surface. *The Journal of Physical Chemistry C* **118**, 3 (Jan. 2014), 1587–1593. doi: [10.1021/jp409367x](https://doi.org/10.1021/jp409367x).
- [54] WAGNER, M., HOFINGER, J., SETVÍN, M., BOATNER, L. A., SCHMID, M., AND DIEBOLD, U. Prototypical organic–oxide interface: Intramolecular resolution of sexiphenyl on in2o3(111). *ACS Applied Materials & Interfaces* **10**, 16 (Apr 2018), 14175–14182. doi: [10.1021/acsami.8b02177](https://doi.org/10.1021/acsami.8b02177).
- [55] HURTADO SALINAS, D., COMETTO, F., STEL, B., KERN, K., AND LINGENFELDER, M. 2-d assembly of supramolecular nanoarchitectures on mg(0001). *Chemical Communications* **55**, 12 (2019), 1793–1796. doi: [10.1039/C8CC08565J](https://doi.org/10.1039/C8CC08565J).
- [56] ISHII, H., OJI, H., ITO, E., HAYASHI, N., YOSHIMURA, D., AND SEKI, K. Energy level alignment and band bending at model interfaces of organic electroluminescent devices. *Journal of Luminescence* **87-89** (May 2000), 61–65. doi: [10.1016/S0022-2313\(99\)00230-6](https://doi.org/10.1016/S0022-2313(99)00230-6).
- [57] UMBACH, T. R., FERNANDEZ-TORRENTE, I., LADENTHIN, J. N., PASCUAL, J. I., AND FRANKE, K. J. Enhanced charge transfer in a monolayer of the organic charge transfer complex ttf–tnap on au(111). *Journal of Physics: Condensed Matter* **24**, 35 (Aug 2012), 354003. doi: [10.1088/0953-8984/24/35/354003](https://doi.org/10.1088/0953-8984/24/35/354003).
- [58] FERNÁNDEZ-TORRENTE, I., KREIKEMEYER-LORENZO, D., STRÓŻECKA, A., FRANKE, K. J., AND PASCUAL, J. I. Gating the charge state of single molecules by local electric fields. *Physical Review Letters* **108**, 3 (Jan 2012), 036801. doi: [10.1103/PhysRevLett.108.036801](https://doi.org/10.1103/PhysRevLett.108.036801).

- [59] WITTE, G., LUKAS, S., BAGUS, P. S., AND WÖLL, C. Vacuum level alignment at organic/metal junctions: “cushion” effect and the interface dipole. *Applied Physics Letters* 87, 26 (Dec 2005), 263502. doi: [10.1063/1.2151253](https://doi.org/10.1063/1.2151253).
- [60] HAMMER, B., AND NORSKOV, J. K. Why gold is the noblest of all the metals. *Nature* 376, 6537 (Jul 1995), 238–240. doi: [10.1038/376238a0](https://doi.org/10.1038/376238a0).
- [61] BÜRKER, C., FERRI, N., TKATCHENKO, A., GERLACH, A., NIEDERHAUSEN, J., HOSOKAI, T., DUHM, S., ZEGENHAGEN, J., KOCH, N., AND SCHREIBER, F. Exploring the bonding of large hydrocarbons on noble metals: Diindoperylene on cu(111), ag(111), and au(111). *Physical Review B* 87 (Apr 2013), 165443. doi: [10.1103/PhysRevB.87.165443](https://doi.org/10.1103/PhysRevB.87.165443).
- [62] KRÖGER, I., STADTMÜLLER, B., KLEIMANN, C., RAJPUT, P., AND KUMPF, C. Normal-incidence x-ray standing-wave study of copper phthalocyanine submonolayers on cu(111) and au(111). *Physical Review B* 83, 19 (May 2011), 195414. doi: [10.1103/PhysRevB.83.195414](https://doi.org/10.1103/PhysRevB.83.195414).
- [63] MÜLLER, K., MORENO-LÓPEZ, J. C., GOTTARDI, S., MEINHARDT, U., YILDIRIM, H., KARA, A., KIVALA, M., AND STÖHR, M. Cyano-functionalized triarylamines on coinage metal surfaces: Interplay of intermolecular and molecule–substrate interactions. *Chemistry – A European Journal* 22, 2 (Jan 2016), 581–589. doi: [10.1002/chem.201503205](https://doi.org/10.1002/chem.201503205).
- [64] ROSEI, F., SCHUNACK, M., NAITOH, Y., JIANG, P., GOURDON, A., LAEGSGAARD, E., STENSGAARD, I., JOACHIM, C., AND BESENBACHER, F. Properties of large organic molecules on metal surfaces. *Progress in Surface Science* 71, 5 (Jun 2003), 95–146. doi: [10.1016/S0079-6816\(03\)00004-2](https://doi.org/10.1016/S0079-6816(03)00004-2).
- [65] BARTH, J. V. Transport of adsorbates at metal surfaces: from thermal migration to hot precursors. *Surface Science Reports* 40, 3 (Oct 2000), 75–149. doi: [10.1016/S0167-5729\(00\)00002-9](https://doi.org/10.1016/S0167-5729(00)00002-9).
- [66] WECKESSER, J., BARTH, J. V., AND KERN, K. Mobility and bonding transition of c₆₀ on pd(110). *Physical Review B* 64 (Sep 2001), 161403. doi: [10.1103/PhysRevB.64.161403](https://doi.org/10.1103/PhysRevB.64.161403).
- [67] SCHUNACK, M., PETERSEN, L., KÜHNLE, A., LÆGSGAARD, E., STENSGAARD, I., JOHANNSEN, I., AND BESENBACHER, F. Anchoring of organic molecules to a metal surface: Htbdc on cu(110). *Physical Review Letter* 86 (Jan 2001), 456–459. doi: [10.1103/PhysRevLett.86.456](https://doi.org/10.1103/PhysRevLett.86.456).
- [68] STEPANOW, S., OHMANN, R., LEROY, F., LIN, N., STRUNSKUS, T., WÖLL, C., AND KERN, K. Rational design of two-dimensional nanoscale networks by electrostatic interactions at surfaces. *ACS Nano* 4, 4 (Apr 2010), 1813–1820. doi: [10.1021/nm100303z](https://doi.org/10.1021/nm100303z).
- [69] YU, M., XU, W., KALASHNYK, N., BENJALAL, Y., NAGARAJAN, S., MASINI, F., LÆGSGAARD, E., HLIWA, M., BOUJU, X., GOURDON, A., JOACHIM, C., BESENBACHER, F., AND LINDEROTH, T. R. From zero to two dimensions: supramolecular nanostructures formed from perylene-3,4,9,10-tetracarboxylic diimide (ptcdi) and ni on the au(111) surface through the interplay between hydrogen-bonding and electrostatic metal-organic interactions. *Nano Research* 5, 12 (Dec 2012), 903–916. doi: [10.1007/s12274-012-0274-6](https://doi.org/10.1007/s12274-012-0274-6).

- [70] SCHLICKUM, U., DECKER, R., KLAPPENBERGER, F., ZOPPELLARO, G., KLY-ATSKAYA, S., RUBEN, M., SILANES, I., ARNAU, A., KERN, K., BRUNE, H., AND BARTH, J. V. Metal-organic honeycomb nanomeshes with tunable cavity size. *Nano Letters* 7, 12 (Dec 2007), 3813–3817. doi: [10.1021/nl072466m](https://doi.org/10.1021/nl072466m).
- [71] BARTELS, L. Tailoring molecular layers at metal surfaces. *Nature Chemistry* 2, 2 (Feb 2010), 87–95. doi: [10.1038/nchem.517](https://doi.org/10.1038/nchem.517).
- [72] KRULL, C., CASTELLI, M., HAPALA, P., KUMAR, D., TADICH, A., CAPSONI, M., EDMONDS, M. T., HELLERSTEDT, J., BURKE, S. A., JELINEK, P., AND SCHIFFRIN, A. Iron-based trinuclear metal-organic nanostructures on a surface with local charge accumulation. *Nature Communications* 9, 1 (Aug 2018), 3211. doi: [10.1038/s41467-018-05543-4](https://doi.org/10.1038/s41467-018-05543-4).
- [73] LI, Y., XIAO, J., SHUBINA, T. E., CHEN, M., SHI, Z., SCHMID, M., STEINRÜCK, H.-P., GOTTFRIED, J. M., AND LIN, N. Coordination and metalation bifunctionality of cu with 5,10,15,20-tetra(4-pyridyl)porphyrin: Toward a mixed-valence two-dimensional coordination network. *Journal of the American Chemical Society* 134, 14 (Apr 2012), 6401–6408. doi: [10.1021/ja300593w](https://doi.org/10.1021/ja300593w).
- [74] QUECK, F., KREJČÍ, O., SCHEUERER, P., BOLLAND, F., OTYEPKA, M., JELÍNEK, P., AND REPP, J. Bonding motifs in metal–organic compounds on surfaces. *Journal of the American Chemical Society* 140, 40 (Oct 2018), 12884–12889. doi: [10.1021/jacs.8b06765](https://doi.org/10.1021/jacs.8b06765).
- [75] BOUJU, X., MATTIOLI, C., FRANC, G., PUJOL, A., AND GOURDON, A. Bicomponent supramolecular architectures at the vacuum-solid interface. *Chemical Reviews* 117, 3 (Feb 2017), 1407–1444. doi: [10.1021/acs.chemrev.6b00389](https://doi.org/10.1021/acs.chemrev.6b00389).
- [76] MACLEOD, J. M., BEN CHAOUCH, Z., PEREPICHKA, D. F., AND ROSEI, F. Two-dimensional self-assembly of a symmetry-reduced tricarboxylic acid. *Langmuir* 29, 24 (Jun 2013), 7318–7324. doi: [10.1021/la3047593](https://doi.org/10.1021/la3047593).
- [77] HIPPS, K. W., AND MAZUR, U. Kinetic and thermodynamic control in porphyrin and phthalocyanine self-assembled monolayers. *Langmuir* 34, 1 (Jan 2018), 3–17. doi: [10.1021/acs.langmuir.7b02672](https://doi.org/10.1021/acs.langmuir.7b02672).
- [78] DAPPE, Y. J., ANDERSEN, M., BALOG, R., HORNEKÆR, L., AND BOUJU, X. Adsorption and stm imaging of polycyclic aromatic hydrocarbons on graphene. *Physical Review B* 91 (Jan 2015), 045427. doi: [10.1103/PhysRevB.91.045427](https://doi.org/10.1103/PhysRevB.91.045427).
- [79] AVVISATI, G., CARDOSO, C., VARSANO, D., FERRETTI, A., GARGIANI, P., AND BETTI, M. G. Ferromagnetic and antiferromagnetic coupling of spin molecular interfaces with high thermal stability. *Nano Letters* 18, 4 (Apr 2018), 2268–2273. doi: [10.1021/acs.nanolett.7b04836](https://doi.org/10.1021/acs.nanolett.7b04836).
- [80] OTERO, R., VÁZQUEZ DE PARGA, A. L., AND GALLEGÓ, J. M. Electronic, structural and chemical effects of charge-transfer at organic/inorganic interfaces. *Surface Science Reports* 72, 3 (2017), 105–145. doi: [10.1016/j.surfrep.2017.03.001](https://doi.org/10.1016/j.surfrep.2017.03.001).
- [81] MAK, K. F., SFEIR, M. Y., WU, Y., LUI, C. H., MISEWICH, J. A., AND HEINZ, T. F. Measurement of the optical conductivity of graphene. *Physical Review Letter* 101 (2008), 196405. doi: [10.1103/PhysRevLett.101.196405](https://doi.org/10.1103/PhysRevLett.101.196405).

- [82] KUZMENKO, A. B., VAN HEUMEN, E., CARBONE, F., AND VAN DER MAREL, D. Universal optical conductance of graphite. *Physical Review Letter* 100 (2008), 117401. doi: [10.1103/PhysRevLett.100.117401](https://doi.org/10.1103/PhysRevLett.100.117401).
- [83] BAE, S., KIM, H., LEE, Y., XU, X., PARK, J.-S., ZHENG, Y., BALAKRISHNAN, J., LEI, T., KIM, H. R., SONG, Y. I., KIM, Y.-J., KIM, K. S., OZYILMAZ, B., AHN, J.-H., HONG, B. H., AND IJIMA, S. Roll-to-roll production of 30-inch graphene films for transparent electrodes. *Nature nanotechnology* 5, 8 (2010), 574–578. doi: [10.1038/nnano.2010.132](https://doi.org/10.1038/nnano.2010.132).
- [84] WU, J., AGRAWAL, M., BECERRIL, H. A., BAO, Z., LIU, Z., CHEN, Y., AND PEUMANS, P. Organic light-emitting diodes on solution-processed graphene transparent electrodes. *ACS Nano* 4, 1 (2010), 43–48. doi: [10.1021/nm900728d](https://doi.org/10.1021/nm900728d).
- [85] WANG, X., ZHI, L., AND MULLEN, K. Transparent, conductive graphene electrodes for dye-sensitized solar cells. *Nano Letters* 8, 1 (2008), 323–327. doi: [10.1021/nl072838r](https://doi.org/10.1021/nl072838r).
- [86] VOLOSHINA, E., BERDUNOV, N., AND DEDKOV, Y. Restoring a nearly free-standing character of graphene on ru(0001) by oxygen intercalation. *Scientific Reports* 6 (2016), 20285. doi: [10.1038/srep20285](https://doi.org/10.1038/srep20285).
- [87] MORITZ, W., WANG, B., BOCQUET, M. L., BRUGGER, T., GREBER, T., WINTERLIN, J., AND GÜNTHER, S. Structure determination of the coincidence phase of graphene on ru(0001). *Physical Review Letter* 104 (2010), 136102. doi: [10.1103/PhysRevLett.104.136102](https://doi.org/10.1103/PhysRevLett.104.136102).
- [88] SUTTER, P., HYBERTSEN, M. S., SADOWSKI, J. T., AND SUTTER, E. Electronic structure of few-layer epitaxial graphene on ru(0001). *Nano Letters* 9, 7 (2009), 2654–2660. doi: [10.1021/nl901040v](https://doi.org/10.1021/nl901040v).
- [89] MAO, J., ZHANG, H., JIANG, Y., PAN, Y., GAO, M., XIAO, W., AND GAO, H.-J. Tunability of supramolecular kagome lattices of magnetic phthalocyanines using graphene-based moire patterns as templates. *Journal of the American Chemical Society* 131, 40 (2009), 14136–14137. doi: [10.1021/ja904907z](https://doi.org/10.1021/ja904907z).
- [90] ZHANG, H. G., SUN, J. T., LOW, T., ZHANG, L. Z., PAN, Y., LIU, Q., MAO, J. H., ZHOU, H. T., GUO, H. M., DU, S. X., GUINEA, F., AND GAO, H. Assembly of iron phthalocyanine and pentacene molecules on a graphene monolayer grown on ru(0001). *Physical Review B* 84 (2011), 245436. doi: [10.1103/PhysRevB.84.245436](https://doi.org/10.1103/PhysRevB.84.245436).
- [91] HAMALAINEN, S. K., STEPANOVA, M., DROST, R., LILJEROTH, P., LAHTINEN, J., AND SAINIO, J. Self-assembly of cobalt-phthalocyanine molecules on epitaxial graphene on ir(111). *The Journal of Physical Chemistry C* 116, 38 (2012), 20433–20437. doi: [10.1021/jp306439h](https://doi.org/10.1021/jp306439h).
- [92] JARVINEN, P., HAMALAINEN, S. K., IJAS, M., HARJU, A., AND LILJEROTH, P. Self-assembly and orbital imaging of metal phthalocyanines on a graphene model surface. *The Journal of Physical Chemistry C* 118, 24 (2014), 13320–13325. doi: [10.1021/jp504813v](https://doi.org/10.1021/jp504813v).
- [93] KUMAR, A., BANERJEE, K., AND LILJEROTH, P. Molecular assembly on two-dimensional materials. *Nanotechnology* 28, 8 (Jan 2017), 082001. doi: [10.1088/1361-6528/aa564f](https://doi.org/10.1088/1361-6528/aa564f).

- [94] MACLEOD, J. M., AND ROSEI, F. Molecular self-assembly on graphene. *Small* 10, 6 (2014), 1038–1049. doi: [10.1002/smll.201301982](https://doi.org/10.1002/smll.201301982).
- [95] SHIROTA, Y., AND KAGEYAMA, H. Charge carrier transporting molecular materials and their applications in devices. *Chemical Reviews* 107, 4 (2007), 953–1010. doi: [10.1021/cr050143+](https://doi.org/10.1021/cr050143+).
- [96] FU, Y.-S., JI, S.-H., CHEN, X., MA, X.-C., WU, R., WANG, C.-C., DUAN, W.-H., QIU, X.-H., SUN, B., ZHANG, P., JIA, J.-F., AND XUE, Q.-K. Manipulating the kondo resonance through quantum size effects. *Physical Review Letter* 99 (Dec 2007), 256601. doi: [10.1103/PhysRevLett.99.256601](https://doi.org/10.1103/PhysRevLett.99.256601).
- [97] ZHAO, A., LI, Q., CHEN, L., XIANG, H., WANG, W., PAN, S., WANG, B., XIAO, X., YANG, J., HOU, J. G., AND ZHU, Q. Controlling the kondo effect of an adsorbed magnetic ion through its chemical bonding. *Science* 309, 5740 (2005), 1542–1544. doi: [10.1126/science.1113449](https://doi.org/10.1126/science.1113449).
- [98] MURDEY, R., SATO, N., AND BOUVET, M. Frontier electronic structures in fluorinated copper phthalocyanine thin films studied using ultraviolet and inverse photoemission spectroscopies. *Molecular Crystals and Liquid Crystals* 455, 1 (2006), 211–218. doi: [10.1080/15421400600698469](https://doi.org/10.1080/15421400600698469).
- [99] WANG, Y.-L., REN, J., SONG, C.-L., JIANG, Y.-P., WANG, L.-L., HE, K., CHEN, X., JIA, J.-F., MENG, S., KAXIRAS, E., XUE, Q.-K., AND MA, X.-C. Selective adsorption and electronic interaction of $f_{16}\text{CuPc}$ on epitaxial graphene. *Physical Review B* 82 (Dec 2010), 245420. doi: [10.1103/PhysRevB.82.245420](https://doi.org/10.1103/PhysRevB.82.245420).
- [100] ZHAO, Y., YUAN, B., LI, C., ZHANG, P., MAI, Y., GUAN, D., LI, Y., ZHENG, H., LIU, C., WANG, S., AND JIA, J. On-surface synthesis of iron phthalocyanine using metal-organic coordination templates. *ChemPhysChem* 20, 18 (Sep 2019), 2394–2397. doi: [10.1002/cphc.201900238](https://doi.org/10.1002/cphc.201900238).
- [101] JARVINEN, P., HAMALAINEN, S. K., BANERJEE, K., HAKKINEN, P., IJAS, M., HARJU, A., AND LILJEROTH, P. Molecular self-assembly on graphene on SiO_2 and hBN substrates. *Nano Letters* 13, 7 (2013), 3199–3204. doi: [10.1021/nl401265f](https://doi.org/10.1021/nl401265f).
- [102] WANG, Z. F., LIU, Z., AND LIU, F. Quantum anomalous hall effect in 2d organic topological insulators. *Physical Review Letter* 110 (May 2013), 196801. doi: [10.1103/PhysRevLett.110.196801](https://doi.org/10.1103/PhysRevLett.110.196801).
- [103] ZHOU, J. Stacking interactions of nickel bis(dithiolene) with graphene and beyond. *RSC Advances* 4, 26 (2014), 13361–13366.
- [104] LI, J., SOLIANYK, L., SCHMIDT, N., BAKER, B., GOTTARDI, S., MORENO LOPEZ, J. C., ENACHE, M., MONJAS, L., VAN DER VLAG, R., HAVENITH, R. W. A., HIRSCH, A. K. H., AND STÖHR, M. Low-dimensional metal-organic coordination structures on graphene. *The Journal of Physical Chemistry C* 123, 20 (May 2019), 12730–12735. doi: [10.1021/acs.jpcc.9b00326](https://doi.org/10.1021/acs.jpcc.9b00326).
- [105] KUMAR, A., BANERJEE, K., FOSTER, A. S., AND LILJEROTH, P. Two-dimensional band structure in honeycomb metal-organic frameworks. *Nano Letters* 18, 9 (Sep 2018), 5596–5602. doi: [10.1021/acs.nanolett.8b02062](https://doi.org/10.1021/acs.nanolett.8b02062).

- [106] HUTTMANN, F., SCHLEHECK, N., ATODIRESEI, N., AND MICHELY, T. On-surface synthesis of sandwich molecular nanowires on graphene. *Journal of the American Chemical Society* 139, 29 (Jul 2017), 9895–9900. doi: [10.1021/jacs.7b03381](https://doi.org/10.1021/jacs.7b03381).
- [107] HOSOYA, N., TAKEGAMI, R., SUZUMURA, J.-I., YADA, K., MIYAJIMA, K., MITSUI, M., KNICKELBEIN, M. B., YABUSHITA, S., AND NAKAJIMA, A. Formation and electronic structures of organoeuropium sandwich nanowires. *The Journal of Physical Chemistry A* 118, 37 (Sep 2014), 8298–8308. doi: [10.1021/jp5011007](https://doi.org/10.1021/jp5011007).
- [108] HUTTMANN, F., ROTHENBACH, N., KRAUS, S., OLLEFS, K., ARRUDA, L. M., BERNIEN, M., THONIG, D., DELIN, A., FRANSSON, J., KUMMER, K., BROOKES, N. B., ERIKSSON, O., KUCH, W., MICHELY, T., AND WENDE, H. Europium cyclooctatetraene nanowire carpets: A low-dimensional, organometallic, and ferromagnetic insulator. *The Journal of Physical Chemistry Letters* 10, 5 (Mar 2019), 911–917. doi: [10.1021/acs.jpcelett.8b03711](https://doi.org/10.1021/acs.jpcelett.8b03711).
- [109] CEITEC Nano research infrastructure. *Brno University of Technology, Purkynova 123, 612 00 Brno, Czech Republic* (<http://nano.ceitec.cz/>).
- [110] RAHE, P., BECHSTEIN, R., AND KÜHNLE, A. Vertical and lateral drift corrections of scanning probe microscopy images. *Journal of Vacuum Science & Technology B* 28, 3 (May 2010), C4E31–C4E38. doi: [10.1116/1.3360909](https://doi.org/10.1116/1.3360909).
- [111] NECAS, D., AND KLAPETEK, P. Gwyddion: an open-source software for SPM data analysis. *Central European Journal of Physics* 10 (2012), 181–188. doi: [10.2478/s11534-011-0096-2](https://doi.org/10.2478/s11534-011-0096-2).
- [112] TROMP, R. M., MANKOS, M., REUTER, M. C., ELLIS, A. W., AND COPEL, M. A new low energy electron microscope. *Surface Review and Letters* 05, 06 (Dec 1998), 1189–1197. doi: [10.1142/S0218625X98001523](https://doi.org/10.1142/S0218625X98001523).
- [113] TELIEPS, W., AND BAUER, E. An analytical reflection and emission uhv surface electron microscope. *Ultramicroscopy* 17, 1 (1985), 57–65. doi: [10.1016/0304-3991\(85\)90177-9](https://doi.org/10.1016/0304-3991(85)90177-9).
- [114] SPECS. User manual: Fe-leem p90 low energy electron microscope, version 2.1. *SPECS Surface Nano Analysis GmbH* (2015).
- [115] TROMP, R. M., FUJIKAWA, Y., HANNON, J. B., ELLIS, A. W., BERGHAUS, A., AND SCHAFF, O. A simple energy filter for low energy electron microscopy/photoelectron emission microscopy instruments. *Journal of Physics: Condensed Matter* 21, 31 (jul 2009), 314007. doi: [10.1088/0953-8984/21/31/314007](https://doi.org/10.1088/0953-8984/21/31/314007).
- [116] TROMP, R., HANNON, J., WAN, W., BERGHAUS, A., AND SCHAFF, O. A new aberration-corrected, energy-filtered leem/peem instrument ii. operation and results. *Ultramicroscopy* 127 (2013), 25 – 39. *Frontiers of Electron Microscopy in Materials Science*. doi: <https://doi.org/10.1016/j.ultramic.2012.07.016>.
- [117] KENNEDY, S., ZHENG, C., TANG, W., PAGANIN, D., AND JESSON, D. Caustic imaging of gallium droplets using mirror electron microscopy. *Ultramicroscopy* 111, 5 (2011), 356 – 363. doi: [10.1016/j.ultramic.2011.01.019](https://doi.org/10.1016/j.ultramic.2011.01.019).

- [118] ALTMAN, M. S., CHUNG, W. F., AND LIU, C. H. Leem phase contrast. *Surface Review and Letters* 05, 06 (1998), 1129–1141. doi: [10.1142/S0218625X98001468](https://doi.org/10.1142/S0218625X98001468).
- [119] CHUNG, W. F., FENG, Y. J., POON, H. C., CHAN, C. T., TONG, S. Y., AND ALTMAN, M. S. Layer spacings in coherently strained epitaxial metal films. *Physical Review Letter* 90 (May 2003), 216105. doi: [10.1103/PhysRevLett.90.216105](https://doi.org/10.1103/PhysRevLett.90.216105).
- [120] ALTMAN, M. S. Low energy electron microscopy of quantum well resonances in ag films on w(110). *Journal of Physics: Condensed Matter* 17, 16 (apr 2005), S1305–S1310. doi: [10.1088/0953-8984/17/16/001](https://doi.org/10.1088/0953-8984/17/16/001).
- [121] SRIVASTAVA, N., GAO, Q., WIDOM, M., FEENSTRA, R. M., NIE, S., MCCARTY, K. F., AND VLASSIOUK, I. V. Low-energy electron reflectivity of graphene on copper and other substrates. *Physical Review B* 87 (Jun 2013), 245414. doi: [10.1103/PhysRevB.87.245414](https://doi.org/10.1103/PhysRevB.87.245414).
- [122] FORTUNA, S., AND TROISI, A. Agent-based modeling for the 2d molecular self-organization of realistic molecules. *The Journal of Physical Chemistry B* 114, 31 (2010), 10151–10159. doi: [10.1021/jp103950m](https://doi.org/10.1021/jp103950m).
- [123] SCHWARZ, D., VAN GASTEL, R., ZANDVLIET, H. J. W., AND POELSEMA, B. Formation and decay of a compressed phase of 4,4-biphenyldicarboxylic acid on cu(001). *Physical Chemistry Chemical Physics* 15 (2013), 5007–5016. doi: [10.1039/C3CP00049D](https://doi.org/10.1039/C3CP00049D).
- [124] STEPANOW, S., STRUNSKUS, T., LINGENFELDER, M., DMITRIEV, A., SPILLMANN, H., LIN, N., BARTH, J. V., WÖLL, C., AND KERN, K. Deprotonation driven phase transformations in terephthalic acid self assembly on cu(100). *The Journal of Physical Chemistry B* 108, 50 (2004), 19392–19397. doi: [10.1021/jp046766t](https://doi.org/10.1021/jp046766t).
- [125] SCHMITT, T., HAMMER, L., AND SCHNEIDER, M. A. Evidence for on-site carboxylation in the self-assembly of 4,4-biphenyl dicarboxylic acid on cu(111). *The Journal of Physical Chemistry C* 120, 2 (Jan 2016), 1043–1048. doi: [10.1021/acs.jpcc.5b10394](https://doi.org/10.1021/acs.jpcc.5b10394).
- [126] WHITE, T. W., MARTSINOVICH, N., TROISI, A., AND COSTANTINI, G. Quantifying the "subtle interplay" between intermolecular and molecule-substrate interactions in molecular assembly on surfaces. *The Journal of Physical Chemistry C* 122, 31 (Aug 2018), 17954–17962. doi: [10.1021/acs.jpcc.8b06797](https://doi.org/10.1021/acs.jpcc.8b06797).
- [127] CAO, N., DING, J., YANG, B., ZHANG, J., PENG, C., LIN, H., ZHANG, H., LI, Q., AND CHI, L. Deprotonation-induced phase evolutions in co-assembled molecular structures. *Langmuir* 34, 26 (Jul 2018), 7852–7858. doi: [10.1021/acs.langmuir.8b00228](https://doi.org/10.1021/acs.langmuir.8b00228).
- [128] LI, J., GOTTARDI, S., SOLIANYK, L., MORENO-LÓPEZ, J. C., AND STÖHR, M. 1,3,5-benzenetribenzoic acid on cu(111) and graphene/cu(111): A comparative stm study. *The Journal of Physical Chemistry C* 120, 32 (Aug 2016), 18093–18098. doi: [10.1021/acs.jpcc.6b05541](https://doi.org/10.1021/acs.jpcc.6b05541).
- [129] FUHR, J. D., CARRERA, A., MURILLO-QUIRÓS, N., CRISTINA, L. J., COSSARO, A., VERDINI, A., FLOREANO, L., GAYONE, J. E., AND ASCOLANI, H. Interplay between hydrogen bonding and molecule-substrate interactions in the case of terephthalic acid molecules on cu(001) surfaces. *The Journal of Physical Chemistry C* 117, 3 (Jan 2013), 1287–1296. doi: [10.1021/jp305455v](https://doi.org/10.1021/jp305455v).

- [130] STEPANOW, S., LIN, N., VIDAL, F., LANDA, A., RUBEN, M., BARTH, J. V., AND KERN, K. Programming supramolecular assembly and chirality in two-dimensional dicarboxylate networks on a cu(100) surface. *Nano Letters* 5, 5 (May 2005), 901–904. doi: [10.1021/nl050362a](https://doi.org/10.1021/nl050362a).
- [131] CLASSEN, T., LINGENFELDER, M., WANG, Y., CHOPRA, R., VIROJANADARA, C., STARKE, U., COSTANTINI, G., FRATESI, G., FABRIS, S., DE GIRONCOLI, S., BARONI, S., HAQ, S., RAVAL, R., AND KERN, K. Hydrogen and coordination bonding supramolecular structures of trimesic acid on cu(110). *The Journal of Physical Chemistry A* 111, 49 (Dec 2007), 12589–12603. doi: [10.1021/jp076037o](https://doi.org/10.1021/jp076037o).
- [132] SCHNADT, J., XU, W., VANG, R. T., KNUDSEN, J., LI, Z., LÆGSGAARD, E., AND BESENBACHER, F. Interplay of adsorbate-adsorbate and adsorbate-substrate interactions in self-assembled molecular surface nanostructures. *Nano Research* 3, 7 (2010), 459–471. doi: [10.1007/s12274-010-0005-9](https://doi.org/10.1007/s12274-010-0005-9).
- [133] CECHAL, J., KLEY, C. S., KUMAGAI, T., SCHRAMM, F., RUBEN, M., STEPANOW, S., AND KERN, K. Convergent and divergent two-dimensional coordination networks formed through substrate-activated or quenched alkynyl ligation. *Chemical Communications* 50, 69 (2014), 9973–9976. doi: [10.1039/C4CC03723E](https://doi.org/10.1039/C4CC03723E).
- [134] QUIROGA ARGANARAZ, B., CRISTINA, L. J., RODRÍGUEZ, L. M., COSSARO, A., VERDINI, A., FLOREANO, L., FUHR, J. D., GAYONE, J. E., AND ASCOLANI, H. Ubiquitous deprotonation of terephthalic acid in the self-assembled phases on cu(100). *Physical Chemistry Chemical Physics* 20, 6 (2018), 4329–4339. doi: [10.1039/C7CP06612K](https://doi.org/10.1039/C7CP06612K).
- [135] KLEY, C. S., CECHAL, J., KUMAGAI, T., SCHRAMM, F., RUBEN, M., STEPANOW, S., AND KERN, K. Highly adaptable two-dimensional metal-organic coordination networks on metal surfaces. *Journal of the American Chemical Society* 134, 14 (Apr 2012), 6072–6075. doi: [10.1021/ja211749b](https://doi.org/10.1021/ja211749b).
- [136] PAYER, D., COMISSO, A., DMITRIEV, A., STRUNSKUS, T., LIN, N., WÖLL, C., DEVITA, A., BARTH, J. V., AND KERN, K. Ionic hydrogen bonds controlling two-dimensional supramolecular systems at a metal surface. *Chemistry - A European Journal* 13, 14 (May 2007), 3900–3906. doi: [10.1002/chem.200601325](https://doi.org/10.1002/chem.200601325).
- [137] LIPTON-DUFFIN, J., ABYAZISANI, M., AND MACLEOD, J. Periodic and nonperiodic chiral self-assembled networks from 1,3,5-benzenetricarboxylic acid on ag(111). *Chemical Communications* 54, 60 (2018), 8316–8319. doi: [10.1039/C8CC04380A](https://doi.org/10.1039/C8CC04380A).
- [138] RUBEN, M., PAYER, D., LANDA, A., COMISSO, A., GATTINONI, C., LIN, N., COLLIN, J.-P., SAUVAGE, J.-P., DE VITA, A., AND KERN, K. 2d supramolecular assemblies of benzene-1,3,5-triyl-tribenzoic acid: Temperature-induced phase transformations and hierarchical organization with macrocyclic molecules. *Journal of the American Chemical Society* 128, 49 (Dec 2006), 15644–15651. doi: [10.1021/ja063601k](https://doi.org/10.1021/ja063601k).
- [139] ZHOU, X., WANG, C., ZHANG, Y., CHENG, F., HE, Y., SHEN, Q., SHANG, J., SHAO, X., JI, W., CHEN, W., XU, G., AND WU, K. Steering surface reaction dynamics with a self-assembly strategy: Ullmann coupling on metal surfaces. *Angewandte Chemie International Edition* 56, 42 (Oct 2017), 12852–12856. doi: [10.1002/anie.201705018](https://doi.org/10.1002/anie.201705018).

- [140] CAÑAS-VENTURA, M. E., KLAPPENBERGER, F., CLAIR, S., PONS, S., KERN, K., BRUNE, H., STRUNSKUS, T., WÖLL, C., FASEL, R., AND BARTH, J. V. Coexistence of one- and two-dimensional supramolecular assemblies of terephthalic acid on pd(111) due to self-limiting deprotonation. *The Journal of Chemical Physics* 125, 18 (Nov 2006), 184710. doi: [10.1063/1.2364478](https://doi.org/10.1063/1.2364478).
- [141] ZHU, N., OSADA, T., AND KOMEDA, T. Supramolecular assembly of biphenyl dicarboxylic acid on au(1 1 1). *Surface Science* 601, 8 (2007), 1789 – 1794. doi: [10.1016/j.susc.2007.02.003](https://doi.org/10.1016/j.susc.2007.02.003).
- [142] ZHANG, W., NEFEDOV, A., NABOKA, M., CAO, L., AND WÖLL, C. Molecular orientation of terephthalic acid assembly on epitaxial graphene: Nexafs and xps study. *Physical Chemistry Chemical Physics* 14, 29 (2012), 10125–10131. doi: [10.1039/C2CP23748B](https://doi.org/10.1039/C2CP23748B).
- [143] SVANE, K. L., AND HAMMER, B. Thermodynamic aspects of dehydrogenation reactions on noble metal surfaces. *The Journal of Chemical Physics* 141, 17 (Nov 2014), 174705. doi: [10.1063/1.4900628](https://doi.org/10.1063/1.4900628).
- [144] KORMOS, L., PROCHÁZKA, P., SIKOLA, T., AND CECHAL, J. Molecular passivation of substrate step edges as origin of unusual growth behavior of 4,4'-biphenyl dicarboxylic acid on cu(001). *The Journal of Physical Chemistry C* 122, 5 (Feb 2018), 2815–2820. doi: [10.1021/acs.jpcc.7b11436](https://doi.org/10.1021/acs.jpcc.7b11436).
- [145] LINGENFELDER, M. A., SPILLMANN, H., DMITRIEV, A., STEPANOW, S., LIN, N., BARTH, J. V., AND KERN, K. Towards surface-supported supramolecular architectures: Tailored coordination assembly of 1,4-benzenedicarboxylate and fe on cu(100). *Chemistry - A European Journal* 10, 8 (Apr 2004), 1913–1919. doi: [10.1002/chem.200305589](https://doi.org/10.1002/chem.200305589).
- [146] ANGER, G., WINKLER, A., AND RENDULIC, K. D. Adsorption and desorption kinetics in the systems h₂/cu(111), h₂/cu(110) and h₂/cu(100). *Surface Science* 220, 1 (Oct 1989), 1–17.
- [147] MUDIYANSELAGE, K., YANG, Y., HOFFMANN, F. M., FURLONG, O. J., HRBEK, J., WHITE, M. G., LIU, P., AND STACCHIOLA, D. J. Adsorption of hydrogen on the surface and sub-surface of cu(111). *The Journal of Chemical Physics* 139, 4 (Jul 2013), 044712. doi: [10.1063/1.4816515](https://doi.org/10.1063/1.4816515).
- [148] WAGNER, S. R., LUNT, R. R., AND ZHANG, P. Anisotropic crystalline organic step-flow growth on deactivated si surfaces. *Physical Review Letter* 110 (Feb 2013), 086107. doi: [10.1103/PhysRevLett.110.086107](https://doi.org/10.1103/PhysRevLett.110.086107).
- [149] FRANKE, M., MARCHINI, F., ZHANG, L., TARIQ, Q., TSUD, N., VOROKHTA, M., VONDRÁČEK, M., PRINCE, K., RÖCKERT, M., WILLIAMS, F. J., STEINRUCK, H.-P., AND LYTKEN, O. Temperature-dependent reactions of phthalic acid on ag(100). *The Journal of Physical Chemistry C* 119, 41 (Oct 2015), 23580–23585. doi: [10.1021/acs.jpcc.5b07858](https://doi.org/10.1021/acs.jpcc.5b07858).
- [150] KHOKHAR, F. S., VAN GASTEL, R., SCHWARZ, D., ZANDVLIET, H. J. W., AND POELSEMA, B. A low energy electron microscopy study of the initial growth, structure and thermal stability of bda-domains on cu(001). *Journal of chemical physics* 135, 12 (2011). Article. doi: [10.1063/1.3641893](https://doi.org/10.1063/1.3641893).

- [151] TAIT, S. L., LIM, H., THEERTHAM, A., AND SEIDEL, P. First layer compression and transition to standing second layer of terephthalic acid on cu(100). *Physical Chemistry Chemical Physics* 14, 22 (2012), 8217–8223. doi: [10.1039/C2CP41256J](https://doi.org/10.1039/C2CP41256J).
- [152] SCHWARZ, D., VAN GASTEL, R., ZANDVLIET, H. J. W., AND POELSEMA, B. Growth anomalies in supramolecular networks: 4,4'-biphenyldicarboxylic acid on cu(001). *Physical Review Letter* 110 (Feb 2013), 076101. doi: [10.1103/PhysRevLett.110.076101](https://doi.org/10.1103/PhysRevLett.110.076101).
- [153] TSENG, T.-C., URBAN, C., WANG, Y., OTERO, R., TAIT, S. L., ALCAMÍ, M., ÉCIJA, D., TRELKA, M., GALLEGRO, J. M., LIN, N., KONUMA, M., STARKE, U., NEFEDOV, A., LANGNER, A., WÖLL, C., HERRANZ, M. Á., MARTÍN, F., MARTÍN, N., KERN, K., AND MIRANDA, R. Charge-transfer-induced structural rearrangements at both sides of organic/metal interfaces. *Nature Chemistry* 2, 5 (2010), 374–379. doi: [10.1038/nchem.591](https://doi.org/10.1038/nchem.591).
- [154] BEDWANI, S., WEGNER, D., CROMMIE, M. F., AND ROCHEFORT, A. Strongly re-shaped organic-metal interfaces: Tetracyanoethylene on cu(100). *Physical Review Letter* 101 (Nov 2008), 216105. doi: [10.1103/PhysRevLett.101.216105](https://doi.org/10.1103/PhysRevLett.101.216105).
- [155] FARAGGI, M. N., ROGERO, C., ARNAU, A., TRELKA, M., ÉCIJA, D., ISVORANU, C., SCHNADT, J., MARTI-GASTALDO, C., CORONADO, E., GALLEGRO, J. M., OTERO, R., AND MIRANDA, R. Role of deprotonation and cu adatom migration in determining the reaction pathways of oxalic acid adsorption on cu(111). *The Journal of Physical Chemistry C* 115, 43 (Nov 2011), 21177–21182. doi: [10.1021/jp205779g](https://doi.org/10.1021/jp205779g).
- [156] EVANS, J. W., THIEL, P. A., AND BARTELT, M. C. Morphological evolution during epitaxial thin film growth: Formation of 2d islands and 3d mounds. *Surface Science Reports* 61, 1 (2006), 1–128. doi: [10.1016/j.surfrep.2005.08.004](https://doi.org/10.1016/j.surfrep.2005.08.004).
- [157] RATSCH, C., AND VENABLES, J. A. Nucleation theory and the early stages of thin film growth. *Journal of Vacuum Science & Technology A* 21, 5 (Sep 2003), S96–S109. doi: [10.1116/1.1600454](https://doi.org/10.1116/1.1600454).
- [158] WHITELAM, S., TAMBLYN, I., HAXTON, T. K., WIELAND, M. B., CHAMPNESS, N. R., GARRAHAN, J. P., AND BETON, P. H. Common physical framework explains phase behavior and dynamics of atomic, molecular, and polymeric network formers. *Physical Review X* 4, 1 (Mar 2014), 011044. doi: [10.1103/PhysRevX.4.011044](https://doi.org/10.1103/PhysRevX.4.011044).
- [159] MORALES-CIFUENTES, J. R., EINSTEIN, T. L., AND PIMPINELLI, A. How “hot precursors” modify island nucleation: A rate-equation model. *Physical Review Letter* 113 (Dec 2014), 246101. doi: [10.1103/PhysRevLett.113.246101](https://doi.org/10.1103/PhysRevLett.113.246101).
- [160] PIMPINELLI, A., TUMBEEK, L., AND WINKLER, A. Scaling and exponent equalities in island nucleation: Novel results and application to organic films. *The Journal of Physical Chemistry Letters* 5, 6 (Mar 2014), 995–998. doi: [10.1021/jz500282t](https://doi.org/10.1021/jz500282t).
- [161] KLEPPMANN, N., AND KLAPP, S. H. L. Nonequilibrium surface growth in a hybrid inorganic-organic system. *Physical Review B* 94 (Dec 2016), 241404. doi: [10.1103/PhysRevB.94.241404](https://doi.org/10.1103/PhysRevB.94.241404).
- [162] YATES, J. T. Surface chemistry at metallic step defect sites. *Journal of Vacuum Science & Technology A* 13, 3 (May 1995), 1359–1367. doi: [10.1116/1.579564](https://doi.org/10.1116/1.579564).

- [163] WANG, H., BULLER, O., WANG, W., HEUER, A., ZHANG, D., FUCHS, H., AND CHI, L. Area confined position control of molecular aggregates. *New Journal of Physics* 18, 5 (2016), 053006. doi: [10.1088/1367-2630/18/5/053006](https://doi.org/10.1088/1367-2630/18/5/053006).
- [164] GABERLE, J., GAO, D. Z., SHLUGER, A. L., AMROUS, A., BOCQUET, F., NONY, L., PARA, F., LOPPACHER, C., LAMARE, S., AND CHERIOUX, F. Morphology and growth mechanisms of self-assembled films on insulating substrates: Role of molecular flexibility and entropy. *The Journal of Physical Chemistry C* 121, 8 (Mar 2017), 4393–4403. doi: [10.1021/acs.jpcc.6b12738](https://doi.org/10.1021/acs.jpcc.6b12738).
- [165] WINKLER, A. On the nucleation and initial film growth of rod-like organic molecules. *Surface Science* 652 (2016), 367–377. doi: [10.1016/j.susc.2016.02.015](https://doi.org/10.1016/j.susc.2016.02.015).
- [166] SCHWOEBEL, R. L., AND SHIPSEY, E. J. Step motion on crystal surfaces. *Journal of Applied Physics* 37, 10 (Sep 1966), 3682–3686. doi: [10.1063/1.1707904](https://doi.org/10.1063/1.1707904).
- [167] HLAWACEK, G., AND TEICHERT, C. Nucleation and growth of thin films of rod-like conjugated molecules. *Journal of Physics: Condensed Matter* 25, 14 (2013), 143202. doi: [10.1088/0953-8984/25/14/143202](https://doi.org/10.1088/0953-8984/25/14/143202).
- [168] KORMOŠ, L., PROCHÁZKA, P., MAKOVEEV, A. O., AND ČECHAL, J. Complex k-uniform tilings by a simple bitopic precursor self-assembled on ag(001) surface. *Nature Communications* 11, 1 (Apr 2020), 1856. doi: [10.1038/s41467-020-15727-6](https://doi.org/10.1038/s41467-020-15727-6).
- [169] PROCHÁZKA, P., GOSALVEZ, M. A., KORMOŠ, L., DE LA TORRE, B., GALLARDO, A., ALBERDI-RODRIGUEZ, J., CHUTORA, T., MAKOVEEV, A. O., SHAHSAVAR, A., ARNAU, A., JELÍNEK, P., AND ČECHAL, J. Multiscale analysis of phase transformations in self-assembled layers of 4,4-biphenyl dicarboxylic acid on the ag(001) surface. *ACS Nano* (May 2020). doi: [10.1021/acs.nano.0c02491](https://doi.org/10.1021/acs.nano.0c02491).
- [170] SEAH, M. P., GILMORE, I. S., AND BEAMSON, G. Xps: binding energy calibration of electron spectrometers 5—re-evaluation of the reference energies. *Surface and Interface Analysis* 26, 9 (Aug 1998), 642–649. doi: [10.1002/\(SICI\)1096-9918\(199808\)26:9<642::AID-SIA408>3.0.CO;2-3](https://doi.org/10.1002/(SICI)1096-9918(199808)26:9<642::AID-SIA408>3.0.CO;2-3).
- [171] MENZEL, D. The development of core electron spectroscopies of adsorbates. *Surface Science* 299-300 (1994), 170–182. doi: [10.1016/0039-6028\(94\)90653-X](https://doi.org/10.1016/0039-6028(94)90653-X).
- [172] KULESHOVA, L. N., AND ZORKII, P. M. Hydrogen bond length in homomolecular organic crystals. *Acta Crystallographica Section B* 37, 7 (Jul 1981), 1363–1366. doi: [10.1107/S0567740881005943](https://doi.org/10.1107/S0567740881005943).
- [173] IRRERA, S., ROLDAN, A., PORTALONE, G., AND DE LEEUW, N. H. The role of hydrogen bonding and proton transfer in the formation of uracil networks on the gold (100) surface: A density functional theory approach. *The Journal of Physical Chemistry C* 117, 8 (Feb 2013), 3949–3957. doi: [10.1021/jp3094353](https://doi.org/10.1021/jp3094353).
- [174] VAN DER LIT, J., DI CICCIO, F., HAPALA, P., JELINEK, P., AND SWART, I. Submolecular resolution imaging of molecules by atomic force microscopy: The influence of the electrostatic force. *Physical Review Letter* 116 (Mar 2016), 096102. doi: [10.1103/PhysRevLett.116.096102](https://doi.org/10.1103/PhysRevLett.116.096102).

- [175] HERMANN, K., AND VAN HOVE, M. Leedpat utility, version 4.2. LEED pattern analyzer software available from: <http://www.fhi-berlin.mpg.de/KHsoftware/LEEDpat/index.html>.
- [176] ANTCZAK, G., BOOM, K., AND MORGENSTERN, K. Revealing the presence of mobile molecules on the surface. *The Journal of Physical Chemistry C* 121, 1 (Jan 2017), 542–549. doi: [10.1021/acs.jpcc.6b11246](https://doi.org/10.1021/acs.jpcc.6b11246).
- [177] MATVIJA, P., ROZBORIL, F., SOBOTÍK, P., OST’ÁDAL, I., AND KOCÁN, P. Pair correlation function of a 2d molecular gas directly visualized by scanning tunneling microscopy. *The Journal of Physical Chemistry Letters* 8, 17 (Sep 2017), 4268–4272. doi: [10.1021/acs.jpcllett.7b01965](https://doi.org/10.1021/acs.jpcllett.7b01965).
- [178] UPHOFF, M., MICHELITSCH, G. S., HELLWIG, R., REUTER, K., BRUNE, H., KLAPPENBERGER, F., AND BARTH, J. V. Assembly of robust holmium-directed 2d metal-organic coordination complexes and networks on the ag(100) surface. *ACS Nano* 12, 11 (Nov 2018), 11552–11560. doi: [10.1021/acsnano.8b06704](https://doi.org/10.1021/acsnano.8b06704).
- [179] GAO, H.-Y., HELD, P. A., KNOR, M., MÜCK-LICHTENFELD, C., NEUGEBAUER, J., STUDER, A., AND FUCHS, H. Decarboxylative polymerization of 2,6-naphthalenedicarboxylic acid at surfaces. *Journal of the American Chemical Society* 136, 27 (Jul 2014), 9658–9663. doi: [10.1021/ja5033875](https://doi.org/10.1021/ja5033875).
- [180] BÖHLER, E., WARNEKE, J., AND SWIDEREK, P. Control of chemical reactions and synthesis by low-energy electrons. *Chemical Society Reviews* 42, 24 (2013), 9219–9231. doi: [10.1039/C3CS60180C](https://doi.org/10.1039/C3CS60180C).
- [181] GRUNBAUM, B., AND SHEPHARD, G. *Tilings and Patterns*, second ed. Dover Publications Inc., 2016. ISBN: 9780486469812.
- [182] KEPLER, J. *Harmonices Mundi*. Linz - Johann Planck, 1619. Reprint: The Harmony of the World, E. J. Aiton, Alistair M. Duncan, Judith V. Field, American Philosophical Society, 1997.
- [183] TÓTH, L. F. Isoperimetric problems concerning tessellations. *Acta Mathematica Hungarica* 14, 3-4 (Sep 1963), 343–351. doi: [10.1007/BF01895720](https://doi.org/10.1007/BF01895720).
- [184] BURKOV, S. E. Structure model of the al-cu-co decagonal quasicrystal. *Physical Review Letters* 67, 5 (Jul 1991), 614–617. doi: [10.1103/PhysRevLett.67.614](https://doi.org/10.1103/PhysRevLett.67.614).
- [185] ZHOU, H., DANG, H., YI, J.-H., NANJI, A., ROCHEFORT, A., AND WUEST, J. D. Frustrated 2d molecular crystallization. *Journal of the American Chemical Society* 129, 45 (Nov 2007), 13774–13775. doi: [10.1021/ja0742535](https://doi.org/10.1021/ja0742535).
- [186] UEDA, K., DOTERA, T., AND GEMMA, T. Photonic band structure calculations of two-dimensional archimedean tiling patterns. *Physical Review B* 75, 19 (May 2007), 195122. doi: [10.1103/PhysRevB.75.195122](https://doi.org/10.1103/PhysRevB.75.195122).
- [187] STELSON, A. C., BRITTON, W. A., AND LIDDELL WATSON, C. M. Photonic crystal properties of self-assembled archimedean tilings. *Journal of Applied Physics* 121, 2 (Jan 2017), 023101. doi: [10.1063/1.4973472](https://doi.org/10.1063/1.4973472).

- [188] UEDA, K., DOTERA, T., AND GEMMA, T. Photonic band structure calculations of two-dimensional archimedean tiling patterns. *Physical Review B* 75 (May 2007), 195122. doi: [10.1103/PhysRevB.75.195122](https://doi.org/10.1103/PhysRevB.75.195122).
- [189] OLSON, A. J., HU, Y. H. E., AND KEINAN, E. Chemical mimicry of viral capsid self-assembly. *Proceedings of the National Academy of Sciences* 104, 52 (Dec 2007), 20731. doi: [10.1073/pnas.0709489104](https://doi.org/10.1073/pnas.0709489104).
- [190] GRANER, F., JIANG, Y., JANIAUD, E., AND FLAMENT, C. Equilibrium states and ground state of two-dimensional fluid foams. *Phys. Rev. E* 63 (Dec 2000), 011402. doi: [10.1103/PhysRevE.63.011402](https://doi.org/10.1103/PhysRevE.63.011402).
- [191] BASNARKOV, L., AND URUMOV, V. Diffusion on archimedean lattices. *Phys. Rev. E* 73 (Apr 2006), 046116. doi: [10.1103/PhysRevE.73.046116](https://doi.org/10.1103/PhysRevE.73.046116).
- [192] STAVANS, J. The evolution of cellular structures. *Reports on Progress in Physics* 56, 6 (Jun 1993), 733–789. doi: [10.1088/0034-4885/56/6/002](https://doi.org/10.1088/0034-4885/56/6/002).
- [193] KEMPKE, S. N., SLOT, M. R., FREENEY, S. E., ZEVENHUIZEN, S. J. M., VAN-MAEKELBERGH, D., SWART, I., AND SMITH, C. M. Design and characterization of electrons in a fractal geometry. *Nature Physics* 15, 2 (Feb 2019), 127–131. doi: [10.1038/s41567-018-0328-0](https://doi.org/10.1038/s41567-018-0328-0).
- [194] HARRISON, A. First catch your hare: the design and synthesis of frustrated magnets. *Journal of Physics: Condensed Matter* 16, 11 (Mar 2004), S553–S572. doi: [10.1088/0953-8984/16/11/001](https://doi.org/10.1088/0953-8984/16/11/001).
- [195] BLUNT, M. O., RUSSELL, J. C., GIMÉNEZ-LÓPEZ, M. D. C., GARRAHAN, J. P., LIN, X., SCHRÖDER, M., CHAMPNESS, N. R., AND BETON, P. H. Random tiling and topological defects in a two-dimensional molecular network. *Science* 322, 5904 (Nov 2008), 1077. doi: [10.1126/science.1163338](https://doi.org/10.1126/science.1163338).
- [196] STANNARD, A., RUSSELL, J. C., BLUNT, M. O., SALESIOTIS, C., GIMÉNEZ-LÓPEZ, M. D. C., TALEB, N., SCHRÖDER, M., CHAMPNESS, N. R., GARRAHAN, J. P., AND BETON, P. H. Broken symmetry and the variation of critical properties in the phase behaviour of supramolecular rhombus tilings. *Nature Chemistry* 4, 2 (Feb 2012), 112–117. doi: [10.1038/nchem.1199](https://doi.org/10.1038/nchem.1199).
- [197] STEPANOW, S., LIN, N., PAYER, D., SCHLICKUM, U., KLAPPENBERGER, F., ZOPPELLARO, G., RUBEN, M., BRUNE, H., BARTH, J., AND KERN, K. Surface-assisted assembly of 2d metal–organic networks that exhibit unusual threefold coordination symmetry. *Angewandte Chemie International Edition* 46, 5 (Jan 2007), 710–713. doi: [10.1002/anie.200603644](https://doi.org/10.1002/anie.200603644).
- [198] TAO, Z., WANG, T., WU, D., FENG, L., HUANG, J., WU, X., AND ZHU, J. Construction of molecular regular tessellations on a cu(111) surface. *Chemical Communications* 54, 51 (2018), 7010–7013. doi: [10.1039/C8CC01719K](https://doi.org/10.1039/C8CC01719K).
- [199] LIU, J., CHEN, Q., CAI, K., LI, J., LI, Y., YANG, X., ZHANG, Y., WANG, Y., TANG, H., ZHAO, D., AND WU, K. Stepwise on-surface dissymmetric reaction to construct binodal organometallic network. *Nature Communications* 10, 1 (Jun 2019), 2545. doi: [10.1038/s41467-019-10522-4](https://doi.org/10.1038/s41467-019-10522-4).

- [200] ÉCIJA, D., URGEL, J. I., PAPAGEORGIOU, A. C., JOSHI, S., AUWÄRTER, W., SEITSONEN, A. P., KLYATSKAYA, S., RUBEN, M., FISCHER, S., VIJAYARAGHAVAN, S., REICHERT, J., AND BARTH, J. V. Five-vertex archimedean surface tessellation by lanthanide-directed molecular self-assembly. *Proceedings of the National Academy of Sciences* 110, 17 (Apr 2013), 6678. doi: [10.1073/pnas.1222713110](https://doi.org/10.1073/pnas.1222713110).
- [201] ZHANG, Y.-Q., PASZKIEWICZ, M., DU, P., ZHANG, L., LIN, T., CHEN, Z., KLYATSKAYA, S., RUBEN, M., SEITSONEN, A. P., BARTH, J. V., AND KLAPPENBERGER, F. Complex supramolecular interfacial tessellation through convergent multi-step reaction of a dissymmetric simple organic precursor. *Nature Chemistry* 10, 3 (Mar 2018), 296–304. doi: [10.1038/nchem.2924](https://doi.org/10.1038/nchem.2924).
- [202] CHENG, F., WU, X.-J., HU, Z., LU, X., DING, Z., SHAO, Y., XU, H., JI, W., WU, J., AND LOH, K. P. Two-dimensional tessellation by molecular tiles constructed from halogen–halogen and halogen–metal networks. *Nature Communications* 9, 1 (Nov 2018), 4871. doi: [10.1038/s41467-018-07323-6](https://doi.org/10.1038/s41467-018-07323-6).
- [203] FENG, L., WANG, T., TAO, Z., HUANG, J., LI, G., XU, Q., TAIT, S. L., AND ZHU, J. Supramolecular tessellations at surfaces by vertex design. *ACS Nano* 13, 9 (Sep 2019), 10603–10611. doi: [10.1021/acsnano.9b04801](https://doi.org/10.1021/acsnano.9b04801).
- [204] SHI, Z., AND LIN, N. Porphyrin-based two-dimensional coordination kagome lattice self-assembled on a au(111) surface. *Journal of the American Chemical Society* 131, 15 (Apr 2009), 5376–5377. doi: [10.1021/ja900499b](https://doi.org/10.1021/ja900499b).
- [205] SCHLICKUM, U., DECKER, R., KLAPPENBERGER, F., ZOPPELLARO, G., KLYATSKAYA, S., AUWÄRTER, W., NEPLL, S., KERN, K., BRUNE, H., RUBEN, M., AND BARTH, J. V. Chiral kagomé lattice from simple ditopic molecular bricks. *Journal of the American Chemical Society* 130, 35 (Sep 2008), 11778–11782. doi: [10.1021/ja8028119](https://doi.org/10.1021/ja8028119).
- [206] SHANG, J., WANG, Y., CHEN, M., DAI, J., ZHOU, X., KUTTNER, J., HILT, G., SHAO, X., GOTTFRIED, J. M., AND WU, K. Assembling molecular sierpiński triangle fractals. *Nature Chemistry* 7, 5 (May 2015), 389–393. doi: [10.1038/nchem.2211](https://doi.org/10.1038/nchem.2211).
- [207] SARKAR, R., GUO, K., MOOREFIELD, C. N., SAUNDERS, M. J., WESDEMIOTIS, C., AND NEWKOME, G. R. One-step multicomponent self-assembly of a first-generation sierpiński triangle: From fractal design to chemical reality. *Angewandte Chemie International Edition* 53, 45 (Nov 2014), 12182–12185. doi: [10.1002/anie.201407285](https://doi.org/10.1002/anie.201407285).
- [208] LI, C., ZHANG, X., LI, N., WANG, Y., YANG, J., GU, G., ZHANG, Y., HOU, S., PENG, L., WU, K., NIECKARZ, D., SZABELSKI, P., TANG, H., AND WANG, Y. Construction of sierpiński triangles up to the fifth order. *Journal of the American Chemical Society* 139, 39 (Oct 2017), 13749–13753. doi: [10.1021/jacs.7b05720](https://doi.org/10.1021/jacs.7b05720).
- [209] ZHANG, X., LI, N., GU, G.-C., WANG, H., NIECKARZ, D., SZABELSKI, P., HE, Y., WANG, Y., XIE, C., SHEN, Z.-Y., LÜ, J.-T., TANG, H., PENG, L.-M., HOU, S.-M., WU, K., AND WANG, Y.-F. Controlling molecular growth between fractals and crystals on surfaces. *ACS Nano* 9, 12 (Dec 2015), 11909–11915. doi: [10.1021/acsnano.5b04427](https://doi.org/10.1021/acsnano.5b04427).
- [210] URGEL, J. I., ÉCIJA, D., LYU, G., ZHANG, R., PALMA, C.-A., AUWÄRTER, W., LIN, N., AND BARTH, J. V. Quasicrystallinity expressed in two-dimensional coordination networks. *Nature Chemistry* 8, 7 (Jul 2016), 657–662. doi: [10.1038/nchem.2507](https://doi.org/10.1038/nchem.2507).

- [211] ZENG, X., UNGAR, G., LIU, Y., PERCEC, V., DULCEY, A. E., AND HOBBS, J. K. Supramolecular dendritic liquid quasicrystals. *Nature* *428*, 6979 (Mar 2004), 157–160. doi: [10.1038/nature02368](https://doi.org/10.1038/nature02368).
- [212] WASIO, N. A., QUARDOKUS, R. C., FORREST, R. P., LENT, C. S., CORCELLI, S. A., CHRISTIE, J. A., HENDERSON, K. W., AND KANDEL, S. A. Self-assembly of hydrogen-bonded two-dimensional quasicrystals. *Nature* *507*, 7490 (Mar 2014), 86–89. doi: [10.1038/nature12993](https://doi.org/10.1038/nature12993).
- [213] COATES, S., SMERDON, J. A., MCGRATH, R., AND SHARMA, H. R. A molecular overlayer with the fibonacci square grid structure. *Nature Communications* *9*, 1 (Aug 2018), 3435. doi: [10.1038/s41467-018-05950-7](https://doi.org/10.1038/s41467-018-05950-7).
- [214] DOLINŠEK, J. Electrical and thermal transport properties of icosahedral and decagonal quasicrystals. *Chemical Society Reviews* *41*, 20 (2012), 6730–6744. doi: [10.1039/C2CS35036J](https://doi.org/10.1039/C2CS35036J).
- [215] WHITELAM, S., TAMBLYN, I., BETON, P. H., AND GARRAHAN, J. P. Random and ordered phases of off-lattice rhombus tiles. *Physical Review Letter* *108* (Jan 2012), 035702. doi: [10.1103/PhysRevLett.108.035702](https://doi.org/10.1103/PhysRevLett.108.035702).
- [216] ZHANG, F., LIU, Y., AND YAN, H. Complex archimedean tiling self-assembled from dna nanostructures. *Journal of the American Chemical Society* *135*, 20 (May 2013), 7458–7461. doi: [10.1021/ja4035957](https://doi.org/10.1021/ja4035957).
- [217] ASARI, T., ARAI, S., TAKANO, A., AND MATSUSHITA, Y. Archimedean tiling structures from aba/cd block copolymer blends having intermolecular association with hydrogen bonding. *Macromolecules* *39*, 6 (Mar 2006), 2232–2237. doi: [10.1021/ma0524880](https://doi.org/10.1021/ma0524880).
- [218] MIKHAEL, J., ROTH, J., HELDEN, L., AND BECHINGER, C. Archimedean-like tiling on decagonal quasicrystalline surfaces. *Nature* *454*, 7203 (Jul 2008), 501–504. doi: [10.1038/nature07074](https://doi.org/10.1038/nature07074).
- [219] ABDURAKHMANOVA, N., TSENG, T.-C., LANGNER, A., KLEY, C. S., SESSI, V., STEPANOW, S., AND KERN, K. Superexchange-mediated ferromagnetic coupling in two-dimensional ni-tenq networks on metal surfaces. *Physical Review Letter* *110* (Jan 2013), 027202. doi: [10.1103/PhysRevLett.110.027202](https://doi.org/10.1103/PhysRevLett.110.027202).
- [220] GIOVANELLI, L., SAVOYANT, A., ABEL, M., MACCHEROZZI, F., KSARI, Y., KOUDIA, M., HAYN, R., CHOUEIKANI, F., OTERO, E., OHRESSER, P., THEMLIN, J.-M., DHESI, S. S., AND CLAIR, S. Magnetic coupling and single-ion anisotropy in surface-supported mn-based metal–organic networks. *The Journal of Physical Chemistry C* *118*, 22 (Jun 2014), 11738–11744. doi: [10.1021/jp502209q](https://doi.org/10.1021/jp502209q).
- [221] FARAGGI, M. N., GOLOVACH, V. N., STEPANOW, S., TSENG, T.-C., ABDURAKHMANOVA, N., KLEY, C. S., LANGNER, A., SESSI, V., KERN, K., AND ARNAU, A. Modeling ferro- and antiferromagnetic interactions in metal–organic coordination networks. *The Journal of Physical Chemistry C* *119*, 1 (Jan 2015), 547–555. doi: [10.1021/jp512019w](https://doi.org/10.1021/jp512019w).

- [222] KRAINOV, I. V., ROZHANSKY, I. V., AVERKIEV, N. S., AND LÄHDERANTA, E. Indirect exchange interaction between magnetic adatoms in graphene. *Physical Review B* *92* (Oct 2015), 155432. doi: [10.1103/PhysRevB.92.155432](https://doi.org/10.1103/PhysRevB.92.155432).
- [223] WICKENBURG, S., LU, J., LISCHNER, J., TSAI, H.-Z., OMRANI, A. A., RISS, A., KARRASCH, C., BRADLEY, A., JUNG, H. S., KHAJEH, R., WONG, D., WATANABE, K., TANIGUCHI, T., ZETTL, A., NETO, A. C., LOUIE, S. G., AND CROMMIE, M. F. Tuning charge and correlation effects for a single molecule on a graphene device. *Nature Communications* *7*, 1 (Nov 2016), 13553. doi: [10.1038/ncomms13553](https://doi.org/10.1038/ncomms13553).
- [224] KOVAŘÍK, S. Self-assembled molecular layers on epitaxial graphene. Master's thesis, Brno University of Technology, Faculty of Mechanical Engineering, 54p, 2018.
- [225] NOVOSELOV, K. S., GEIM, A. K., MOROZOV, S. V., JIANG, D., KATSNELSON, M. I., GRIGORIEVA, I. V., DUBONOS, S. V., AND FIRSOV, A. Two-dimensional gas of massless Dirac fermions in graphene. *Nature* *438*, 7065 (2005), 197–200. doi: [10.1038/nature04233](https://doi.org/10.1038/nature04233).
- [226] BEENAKKER, C. W. J. Colloquium: Andreev reflection and Klein tunneling in graphene. *Reviews of Modern Physics* *80*, 4 (2008), 1337–1354. doi: [10.1103/RevModPhys.80.1337](https://doi.org/10.1103/RevModPhys.80.1337).
- [227] NOVOSELOV, K. S., GEIM, A. K., MOROZOV, S. V., JIANG, D., ZHANG, Y., DUBONOS, S. V., GRIGORIEVA, I. V., AND FIRSOV, A. Electric field effect in atomically thin carbon films. *Science (New York, N.Y.)* *306*, 5696 (2004), 666–669. doi: [10.1126/science.1102896](https://doi.org/10.1126/science.1102896).
- [228] BERGER, C., SONG, Z., LI, T., LI, X., OGBAZGHI, A. Y., FENG, R., DAI, Z., MARCHENKOV, A. N., CONRAD, E. H., FIRST, P. N., AND DE HEER, W. A. Ultra-thin epitaxial graphite 2d electron gas properties and a route toward graphene based nanoelectronics. *The Journal of Physical Chemistry B* *108*, 52 (2004), 19912–19916. doi: [10.1021/jp040650f](https://doi.org/10.1021/jp040650f).
- [229] HERNANDEZ, Y., NICOLSI, V., LOTYA, M., BLIGHE, F. M., SUN, Z., DE, S., T., M., HOLLAND, B., BYRNE, M., GUN'KO, Y. K., BOLAND, J. J., NIRAJ, P., DUESBERG, G., KRISHNAMURTHY, S., GOODHUE, R., HUTCHISON, J., SCARDACI, V., FERRARI, A. C., AND COLEMAN, J. N. High yield production of graphene by liquid phase exfoliation of graphite. *Nat Nano* *3*, 9 (2008), 563–568. doi: [10.1038/nnano.2008.215](https://doi.org/10.1038/nnano.2008.215).
- [230] MOREAU, E., GODEY, S., FERRER, F. J., VIGNAUD, D., WALLART, X., AVILA, J., ASENSIO, M. C., BOURNEL, F., AND GALLET, J.-J. Graphene growth by molecular beam epitaxy on the carbon-face of sic. *Applied Physics Letters* *97*, 24 (2010), 241907. doi: [10.1063/1.3526720](https://doi.org/10.1063/1.3526720).
- [231] MARCHINI, S., GÜNTHER, S., AND WINTERLIN, J. Scanning tunneling microscopy of graphene on ru(0001). *Physical Review B* *76* (2007), 075429. doi: [10.1103/PhysRevB.76.075429](https://doi.org/10.1103/PhysRevB.76.075429).
- [232] SUTTER, P., SADOWSKI, J. T., AND SUTTER, E. Graphene on pt(111): Growth and substrate interaction. *Physical Review B* *80* (2009), 245411. doi: [10.1103/PhysRevB.80.245411](https://doi.org/10.1103/PhysRevB.80.245411).

- [233] N-DIAYE, A., CORAUX, J., PLASA, T. N., BUSSE, C., AND MICHELY, T. Structure of epitaxial graphene on ir(111). *New Journal of Physics* 10, 4 (2008), 043033. doi: [10.1088/1367-2630/10/4/043033](https://doi.org/10.1088/1367-2630/10/4/043033).
- [234] SUN, Z., YAN, Z., YAO, J., BEITLER, E., ZHU, Y., AND TOUR, J. M. Growth of graphene from solid carbon sources. *Nature* 468, 7323 (2010), 549–552. doi: [10.1038/nature09579](https://doi.org/10.1038/nature09579).
- [235] SRIVASTAVA, A., GALANDE, C., CI, L., SONG, L., RAI, C., JARIWALA, D., KELLY, K. F., AND AJAYAN, P. M. Novel liquid precursor-based facile synthesis of large-area continuous, single, and few-layer graphene films. *Chemistry of Materials* 22, 11 (2010), 3457–3461. doi: [10.1021/cm101027c](https://doi.org/10.1021/cm101027c).
- [236] LI, X., CAI, W., AN, J., KIM, S., NAH, J., YANG, D., PINER, R., VELAMAKANNI, A., JUNG, I., TUTUC, E., BANERJEE, S. K., COLOMBO, L., AND RUOFF, R. S. Large-area synthesis of high-quality and uniform graphene films on copper foils. *Science (New York, N.Y.)* 324, 5932 (2009), 1312–1314. doi: [10.1126/science.1171245](https://doi.org/10.1126/science.1171245).
- [237] PROCHAZKA, P., MACH, J., BISCHOFF, D., LSKOVA, Z., DVORAK, P., VANATKA, M., SIMONET, P., VARLET, A., HEMZAL, D., PETRENEC, M., KALINA, L., BARTOSIK, M., ENSSLIN, K., VARGA, P., CECHAL, J., AND SIKOLA, T. Ultrasmooth metallic foils for growth of high quality graphene by chemical vapor deposition. *Nanotechnology* 25, 18 (2014), 185601. doi: [10.1088/0957-4484/25/18/185601](https://doi.org/10.1088/0957-4484/25/18/185601).
- [238] YAN, Z., LIN, J., PENG, Z., SUN, Z., ZHU, Y., LI, L., XIANG, C., SAMUEL, E. L., KITTRELL, C., AND TOUR, J. M. Toward the synthesis of wafer-scale single-crystal graphene on copper foils. *ACS Nano* 6, 10 (2012), 9110–9117. doi: [10.1021/nm303352k](https://doi.org/10.1021/nm303352k).
- [239] HAO, Y., BHARATHI, M. S., WANG, L., LIU, Y., CHEN, H., NIE, S., WANG, X., CHOU, H., TAN, C., FALLAHAZAD, B., RAMANARAYAN, H., MAGNUSON, C. W., TUTUC, E., YAKOBSON, B. I., MCCARTY, K. F., ZHANG, Y.-W., KIM, P., HONE, J., COLOMBO, L., AND RUOFF, R. S. The role of surface oxygen in the growth of large single-crystal graphene on copper. *Science* 342, 6159 (2013), 720–723. doi: [10.1126/science.1243879](https://doi.org/10.1126/science.1243879).
- [240] HAO, Y., WANG, L., LIU, Y., CHEN, H., WANG, X., TAN, C., NIE, S., SUK, J. W., JIANG, T., LIANG, T., XIAO, J., YE, W., DEAN, C. R., YAKOBSON, B. I., MCCARTY, K. F., KIM, P., HONE, J., COLOMBO, L., AND RUOFF, R. S. Oxygen-activated growth and bandgap tunability of large single-crystal bilayer graphene. *Nat Nano* 11, 5 (2016), 426–431. Letter. doi: [10.1038/nnano.2015.322](https://doi.org/10.1038/nnano.2015.322).
- [241] GAO, M., PAN, Y., HUANG, L., HU, H., ZHANG, L. Z., GUO, H. M., DU, S. X., AND GAO, H.-J. Epitaxial growth and structural property of graphene on pt(111). *Applied Physics Letters* 98, 3 (2011), 033101. doi: [10.1063/1.3543624](https://doi.org/10.1063/1.3543624).
- [242] ZHANG, Y., GOMEZ, L., ISHIKAWA, F. N., MADARIA, A., RYU, K., WANG, C., BADMAEV, A., AND ZHOU, C. Comparison of graphene growth on single-crystalline and polycrystalline ni by chemical vapor deposition. *The Journal of Physical Chemistry Letters* 1, 20 (2010), 3101–3107. doi: [10.1021/jz1011466](https://doi.org/10.1021/jz1011466).
- [243] GAO, L., GUEST, J. R., AND GUISENGER, N. P. Epitaxial graphene on cu(111). *Nano Letters* 10, 9 (2010), 3512–3516. doi: [10.1021/nl1016706](https://doi.org/10.1021/nl1016706).

- [244] BATZILL, M. The surface science of graphene: Metal interfaces, {CVD} synthesis, nanoribbons, chemical modifications, and defects. *Surface Science Reports* 67 (2012), 83–115. doi: [10.1016/j.surfrep.2011.12.001](https://doi.org/10.1016/j.surfrep.2011.12.001).
- [245] MARTINEZ-GALERA, A. J., BRIHUEGA, I., AND GOMEZ-RODRIGUEZ, J. M. Ethylene irradiation: A new route to grow graphene on low reactivity metals. *Nano Letters* 11, 9 (2011), 3576–3580. doi: [10.1021/nl201281m](https://doi.org/10.1021/nl201281m).
- [246] GONZALEZ-HERRERO, H., POU, P., LOBO-CHECA, J., FERNANDEZ-TORRE, D., CRAES, F., MARTINEZ-GALERA, A. J., UGEDA, M. M., CORSO, M., ORTEGA, J. E., GOMEZ-RODRIGUEZ, J. M., PEREZ, R., AND BRIHUEGA, I. Graphene tunable transparency to tunneling electrons: A direct tool to measure the local coupling. *ACS Nano* 10, 5 (2016), 5131–5144. doi: [10.1021/acsnano.6b00322](https://doi.org/10.1021/acsnano.6b00322).
- [247] CORAUX, J., N DIAYE, A. T., BUSSE, C., AND MICHELY, T. Structural coherency of graphene on ir(111). *Nano Letters* 8, 2 (2008), 565–570. doi: [10.1021/nl0728874](https://doi.org/10.1021/nl0728874).
- [248] ARNOULT, W. J., AND MCLELLAN, R. B. The solubility of carbon in rhodium ruthenium, iridium and rhenium. *Scripta Metallurgica* 6, 10 (Oct 1972), 1013–1018. doi: [10.1016/0036-9748\(72\)90163-9](https://doi.org/10.1016/0036-9748(72)90163-9).
- [249] STARODUB, E., BOSTWICK, A., MORESCHINI, L., NIE, S., GABALY, F. E., MCCARTY, K. F., AND ROTENBERG, E. In-plane orientation effects on the electronic structure, stability, and raman scattering of monolayer graphene on ir(111). *Physical Review B* 83 (2011), 125428. doi: [10.1103/PhysRevB.83.125428](https://doi.org/10.1103/PhysRevB.83.125428).
- [250] NIEUWENHUYS, B. E., HAGEN, D. I., ROVIDA, G., AND SOMORJAI, G. A. Leed, aes and thermal desorption studies of chemisorbed hydrogen and hydrocarbons (c2h2, c2h4, c6h6, c6h12) on the (111) and stepped [6(111) × (100)] iridium crystal surfaces; comparison with platinum. *Surface Science* 59, 1 (Sep 1976), 155–176. doi: [10.1016/0039-6028\(76\)90298-3](https://doi.org/10.1016/0039-6028(76)90298-3).
- [251] LOGINOVA, E., NIE, S., THÜRMER, K., BARTELT, N. C., AND MCCARTY, K. F. Defects of graphene on ir(111): Rotational domains and ridges. *Physical Review B* 80 (2009), 085430. doi: [10.1103/PhysRevB.80.085430](https://doi.org/10.1103/PhysRevB.80.085430).
- [252] VAN GASTEL, R., N'DIAYE, A. T., WALL, D., CORAUX, J., BUSSE, C., BUCKANIE, N. M., MEYER ZU HERINGDORF, F.-J., HORN VON HOEGEN, M., MICHELY, T., AND POELSEMA, B. Selecting a single orientation for millimeter sized graphene sheets. *Applied Physics Letters* 95, 12 (Sep 2009), 121901. doi: [10.1063/1.3225554](https://doi.org/10.1063/1.3225554).
- [253] MENG, L., WU, R., ZHANG, L., LI, L., DU, S., WANG, Y., AND GAO, H.-J. Multi-oriented moiré superstructures of graphene on ir(111): experimental observations and theoretical models. *Journal of Physics: Condensed Matter* 24, 31 (Jul 2012), 314214. doi: [10.1088/0953-8984/24/31/314214](https://doi.org/10.1088/0953-8984/24/31/314214).
- [254] HATTAB, H., N'DIAYE, A. T., WALL, D., JNAWALI, G., CORAUX, J., BUSSE, C., VAN GASTEL, R., POELSEMA, B., MICHELY, T., MEYER ZU HERINGDORF, F.-J., AND HORN-VON HOEGEN, M. Growth temperature dependent graphene alignment on ir(111). *Applied Physics Letters* 98, 14 (Apr 2011), 141903. doi: [10.1063/1.3548546](https://doi.org/10.1063/1.3548546).

- [255] OMAMBAC, K. M., HATTAB, H., BRAND, C., JNAWALI, G., N'DIAYE, A. T., CORAUX, J., VAN GASTEL, R., POELSEMA, B., MICHELY, T., MEYER ZU HERINGDORF, F.-J., AND HOEGEN, M. H.-V. Temperature-controlled rotational epitaxy of graphene. *Nano Letters* 19, 7 (Jul 2019), 4594–4600. doi: [10.1021/acs.nanolett.9b01565](https://doi.org/10.1021/acs.nanolett.9b01565).
- [256] SÜLE, P., SZENDRŐ, M., HWANG, C., AND TAPASZTÓ, L. Rotation misorientated graphene moiré superlattices on cu (111): Classical molecular dynamics simulations and scanning tunneling microscopy studies. *Carbon* 77 (Oct 2014), 1082–1089. doi: [10.1016/j.carbon.2014.06.024](https://doi.org/10.1016/j.carbon.2014.06.024).
- [257] HATTAB, H., N'DIAYE, A. T., WALL, D., KLEIN, C., JNAWALI, G., CORAUX, J., BUSSE, C., VAN GASTEL, R., POELSEMA, B., MICHELY, T., MEYER ZU HERINGDORF, F.-J., AND HORN-VON HOEGEN, M. Interplay of wrinkles, strain, and lattice parameter in graphene on iridium. *Nano Letters* 12, 2 (Feb 2012), 678–682. doi: [10.1021/nl203530t](https://doi.org/10.1021/nl203530t).
- [258] MAN, K. L., AND ALTMAN, M. S. Small-angle lattice rotations in graphene on ru(0001). *Physical Review B* 84 (Dec 2011), 235415. doi: [10.1103/PhysRevB.84.235415](https://doi.org/10.1103/PhysRevB.84.235415).
- [259] BATTILOMO, R., SCOPIGNO, N., AND ORTIX, C. Berry curvature dipole in strained graphene: A fermi surface warping effect. *Physical Review Letter* 123 (Nov 2019), 196403. doi: [10.1103/PhysRevLett.123.196403](https://doi.org/10.1103/PhysRevLett.123.196403).
- [260] ADDOU, R., AND BATZILL, M. Defects and domain boundaries in self-assembled terephthalic acid (tpa) monolayers on cvd-grown graphene on pt(111). *Langmuir* 29, 21 (May 2013), 6354–6360. doi: [10.1021/la400972k](https://doi.org/10.1021/la400972k).
- [261] STEPANOW, S., LIN, N., BARTH, J. V., AND KERN, K. Surface template assembly of two dimensional metal organic coordination networks. *The Journal of Physical Chemistry B* 110, 46 (Nov 2006), 23472–23477. doi: [10.1021/jp065066g](https://doi.org/10.1021/jp065066g).
- [262] GAMBARDILLA, P., STEPANOW, S., DMITRIEV, A., HONOLKA, J., DE GROOT, F. M. F., LINGENFELDER, M., GUPTA, S. S., SARMA, D. D., BENCOK, P., STANESCU, S., CLAIR, S., PONS, S., LIN, N., SEITSONEN, A. P., BRUNE, H., BARTH, J. V., AND KERN, K. Supramolecular control of the magnetic anisotropy in two-dimensional high-spin fe arrays at a metal interface. *Nature Materials* 8, 3 (Mar 2009), 189–193. doi: [10.1038/nmat2376](https://doi.org/10.1038/nmat2376).
- [263] WAHL, P., DIEKHÖNER, L., WITTICH, G., VITALI, L., SCHNEIDER, M. A., AND KERN, K. Kondo effect of molecular complexes at surfaces: Ligand control of the local spin coupling. *Physical Review Letters* 95, 16 (Oct 2005), 166601. doi: [10.1103/PhysRevLett.95.166601](https://doi.org/10.1103/PhysRevLett.95.166601).
- [264] NAGAOKA, K., JAMNEALA, T., GROBIS, M., AND CROMMIE, M. F. Temperature dependence of a single kondo impurity. *Physical Review Letter* 88 (Feb 2002), 077205. doi: [10.1103/PhysRevLett.88.077205](https://doi.org/10.1103/PhysRevLett.88.077205).
- [265] BIESINGER, M. C., PAYNE, B. P., GROSVENOR, A. P., LAU, L. W., GERSON, A. R., AND SMART, R. S. Resolving surface chemical states in xps analysis of first row transition metals, oxides and hydroxides: Cr, mn, fe, co and ni. *Applied Surface Science* 257, 7 (Jan 2011), 2717–2730. doi: [10.1016/j.apsusc.2010.10.051](https://doi.org/10.1016/j.apsusc.2010.10.051).

- [266] GROSVENOR, A. P., KOBE, B. A., BIESINGER, M. C., AND MCINTYRE, N. S. Investigation of multiplet splitting of fe 2p xps spectra and bonding in iron compounds. *Surface and Interface Analysis* 36, 12 (Dec 2004), 1564–1574. doi: [10.1002/sia.1984](https://doi.org/10.1002/sia.1984).
- [267] SUN, J. T., LU, Y. H., CHEN, W., FENG, Y. P., AND WEE, A. T. S. Linear tuning of charge carriers in graphene by organic molecules and charge-transfer complexes. *Physical Review B* 81 (Apr 2010), 155403. doi: [10.1103/PhysRevB.81.155403](https://doi.org/10.1103/PhysRevB.81.155403).
- [268] DE OLIVEIRA, I. S. S., AND MIWA, R. H. Organic molecules deposited on graphene: A computational investigation of self-assembly and electronic structure. *The Journal of Chemical Physics* 142, 4 (Jan 2015), 044301. doi: [10.1063/1.4906435](https://doi.org/10.1063/1.4906435).
- [269] BLOWEY, P. J., HAAGS, A., ROCHFORD, L. A., FELTER, J., WARR, D. A., DUNCAN, D. A., LEE, T.-L., COSTANTINI, G., KUMPF, C., AND WOODRUFF, D. P. Characterization of growth and structure of tcnq phases on ag(111). *Phys. Rev. Materials* 3 (Nov 2019), 116001. doi: [10.1103/PhysRevMaterials.3.116001](https://doi.org/10.1103/PhysRevMaterials.3.116001).
- [270] VICKERS, E. B., GILES, I. D., AND MILLER, J. S. M[tcnq]y-based magnets (m = mn, fe, co, ni; tcnq = 7,7,8,8-tetracyano-p-quinodimethane). *Chemistry of Materials* 17, 7 (Apr 2005), 1667–1672. doi: [10.1021/cm047869r](https://doi.org/10.1021/cm047869r).
- [271] RODRÍGUEZ, L. M., FUHR, J. D., MACHAÍN, P., ASCOLANI, H., LINGENFELDER, M., AND GAYONE, J. E. Building two-dimensional metal–organic networks with tin. *Chemical Communications* 55, 3 (2019), 345–348. doi: [10.1039/C8CC08280D](https://doi.org/10.1039/C8CC08280D).
- [272] HAAGS, A., ROCHFORD, L. A., FELTER, J., BLOWEY, P. J., DUNCAN, D. A., WOODRUFF, D. P., AND KUMPF, C. Growth and evolution of tetracyanoquinodimethane and potassium coadsorption phases on ag(111). *New Journal of Physics* 22, 6 (Jun 2020), 063028. doi: [10.1088/1367-2630/ab825f](https://doi.org/10.1088/1367-2630/ab825f).
- [273] DENG, Q., ZHAO, J., WU, T., CHEN, G., HANSEN, H. A., AND VEGGE, T. 2d transition metal–tcnq sheets as bifunctional single-atom catalysts for oxygen reduction and evolution reaction. *Journal of Catalysis* 370 (Feb 2019), 378–384. doi: [10.1016/j.jcat.2018.12.012](https://doi.org/10.1016/j.jcat.2018.12.012).
- [274] ZWERGER, W. Itinerant ferromagnetism with ultracold atoms. *Science* 325, 5947 (Sep 2009), 1507. doi: [10.1126/science.1179767](https://doi.org/10.1126/science.1179767).
- [275] SCHOTT, S., MCNELLIS, E. R., NIELSEN, C. B., CHEN, H.-Y., WATANABE, S., TANAKA, H., MCCULLOCH, I., TAKIMIYA, K., SINOVA, J., AND SIRRINGHAUS, H. Tuning the effective spin-orbit coupling in molecular semiconductors. *Nature Communications* 8, 1 (May 2017), 15200. doi: [10.1038/ncomms15200](https://doi.org/10.1038/ncomms15200).
- [276] SABER, M. R., PROSVIRIN, A. V., ABRAHAMS, B. F., ELLIOTT, R. W., ROBSON, R., AND DUNBAR, K. R. Magnetic coupling between metal spins through the 7,7,8,8-tetracyanoquinodimethane (tcnq) dianion. *Chemistry – A European Journal* 20, 25 (Jun 2014), 7593–7597. doi: [10.1002/chem.201402227](https://doi.org/10.1002/chem.201402227).
- [277] LINDQUIST, J. M., AND HEMMINGER, J. C. High-resolution core level photoelectron spectra of solid tcnq: determination of molecular orbital spatial distribution from localized shake-up features. *The Journal of Physical Chemistry* 92, 6 (Mar 1988), 1394–1396. doi: [10.1021/j100317a005](https://doi.org/10.1021/j100317a005).

- [278] GROSVENOR, A. P., BIESINGER, M. C., SMART, R. S., AND MCINTYRE, N. S. New interpretations of xps spectra of nickel metal and oxides. *Surface Science* 600, 9 (May 2006), 1771–1779. doi: [10.1016/j.susc.2006.01.041](https://doi.org/10.1016/j.susc.2006.01.041).
- [279] BIESINGER, M. C., PAYNE, B. P., LAU, L. W. M., GERSON, A., AND SMART, R. S. C. X-ray photoelectron spectroscopic chemical state quantification of mixed nickel metal, oxide and hydroxide systems. *Surface and Interface Analysis* 41, 4 (Apr 2009), 324–332. doi: [10.1002/sia.3026](https://doi.org/10.1002/sia.3026).
- [280] LINDQUIST, J. M., AND HEMMINGER, J. C. High energy resolution x-ray photoelectron spectroscopy studies of tetracyanoquinodimethane charge transfer complexes with copper, nickel, and lithium. *Chemistry of Materials* 1, 1 (Jan 1989), 72–78. doi: [10.1021/cm00001a017](https://doi.org/10.1021/cm00001a017).
- [281] GIERGIEL, J., WELLS, S., LAND, T. A., AND HEMMINGER, J. C. Growth and chemistry of tcnq films on nickel (111). *Surface Science* 255, 1 (Sep 1991), 31–40. doi: [10.1016/0039-6028\(91\)90009-H](https://doi.org/10.1016/0039-6028(91)90009-H).
- [282] GUNLYCKE, D., ARESHKIN, D. A., AND WHITE, C. T. Semiconducting graphene nanostrips with edge disorder. *Applied Physics Letters* 90, 14 (2007), 142104. doi: [10.1063/1.2718515](https://doi.org/10.1063/1.2718515).
- [283] WAKABAYASHI, K., SASAKI, K.-I., NAKANISHI, T., AND ENOKI, T. Electronic states of graphene nanoribbons and analytical solutions. *Science and Technology of Advanced Materials* 11, 5 (Oct 2010), 054504. doi: [10.1088/1468-6996/11/5/054504](https://doi.org/10.1088/1468-6996/11/5/054504).
- [284] TALIRZ, L., RUFFIEUX, P., AND FASEL, R. On-surface synthesis of atomically precise graphene nanoribbons. *Advanced Materials* 28, 29 (2016), 6222–6231. doi: [10.1002/adma.201505738](https://doi.org/10.1002/adma.201505738).
- [285] TALIRZ, L., SÖDE, H., DUMSLAFF, T., WANG, S., SANCHEZ-VALENCIA, J. R., LIU, J., SHINDE, P., PIGNEDOLI, C. A., LIANG, L., MEUNIER, V., PLUMB, N. C., SHI, M., FENG, X., NARITA, A., MÜLLEN, K., FASEL, R., AND RUFFIEUX, P. On-surface synthesis and characterization of 9-atom wide armchair graphene nanoribbons. *ACS Nano* 11, 2 (Feb 2017), 1380–1388. doi: [10.1021/acsnano.6b06405](https://doi.org/10.1021/acsnano.6b06405).
- [286] MERINO-DÍEZ, N., GARCIA-LEKUE, A., CARBONELL-SANROMÀ, E., LI, J., CORSO, M., COLAZZO, L., SEDONA, F., SÁNCHEZ-PORTAL, D., PASCUAL, J. I., AND DE OTEYZA, D. G. Width-dependent band gap in armchair graphene nanoribbons reveals fermi level pinning on au(111). *ACS Nano* 11, 11 (Nov 2017), 11661–11668. doi: [10.1021/acsnano.7b06765](https://doi.org/10.1021/acsnano.7b06765).
- [287] NGUYEN, G. D., TOMA, F. M., CAO, T., PEDRAMRAZI, Z., CHEN, C., RIZZO, D. J., JOSHI, T., BRONNER, C., CHEN, Y.-C., FAVARO, M., LOUIE, S. G., FISCHER, F. R., AND CROMMIE, M. F. Bottom-up synthesis of $n = 13$ sulfur-doped graphene nanoribbons. *The Journal of Physical Chemistry C* 120, 5 (Feb 2016), 2684–2687. doi: [10.1021/acs.jpcc.5b09986](https://doi.org/10.1021/acs.jpcc.5b09986).
- [288] KAWAI, S., NAKATSUKA, S., HATAKEYAMA, T., PAWLAK, R., MEIER, T., TRACEY, J., MEYER, E., AND FOSTER, A. S. Multiple heteroatom substitution to graphene nanoribbon. *Science Advances* 4, 4 (Apr 2018), eaar7181. doi: [10.1126/sciadv.aar7181](https://doi.org/10.1126/sciadv.aar7181).

- [289] KAWAI, S., SAITO, S., OSUMI, S., YAMAGUCHI, S., FOSTER, A. S., SPIJKER, P., AND MEYER, E. Atomically controlled substitutional boron-doping of graphene nanoribbons. *Nature Communications* 6, 1 (Aug 2015), 8098. doi: [10.1038/ncomms9098](https://doi.org/10.1038/ncomms9098).
- [290] CARBONELL-SANROMÀ, E., HIEULLE, J., VILAS-VARELA, M., BRANDIMARTE, P., IRAOLA, M., BARRAGÁN, A., LI, J., ABADIA, M., CORSO, M., SÁNCHEZ-PORTAL, D., PEÑA, D., AND PASCUAL, J. I. Doping of graphene nanoribbons via functional group edge modification. *ACS Nano* 11, 7 (Jul 2017), 7355–7361. doi: [10.1021/acsnano.7b03522](https://doi.org/10.1021/acsnano.7b03522).
- [291] RUFFIEUX, P., CAI, J., PLUMB, N. C., PATTHEY, L., PREZZI, D., FERRETTI, A., MOLINARI, E., FENG, X., MULLEN, K., PIGNEDOLI, C. A., AND FASEL, R. Electronic structure of atomically precise graphene nanoribbons. *ACS Nano* 6, 8 (2012), 6930–6935. doi: [10.1021/nm3021376](https://doi.org/10.1021/nm3021376).
- [292] EL-SAYED, A., PIQUERO-ZULAICA, I., ABD EL-FATTAH, Z. M., KORMOŠ, L., ALI, K., WEBER, A., BREDE, J., DE OTEYZA, D. G., LOBO-CHECA, J., ORTEGA, J. E., AND CORSO, M. Synthesis of graphene nanoribbons on a kinked au surface: Revealing the frontier valence band at the brillouin zone center. *The Journal of Physical Chemistry C* 124, 28 (Jul 2020), 15474–15480. doi: [10.1021/acs.jpcc.0c02801](https://doi.org/10.1021/acs.jpcc.0c02801).
- [293] CAI, J., RUFFIEUX, P., JAAFAR, R., BIERI, M., BRAUN, T., BLANKENBURG, S., MUOTH, M., SEITSONEN, A. P., SALEH, M., FENG, X., MULLEN, K., AND FASEL, R. Atomically precise bottom-up fabrication of graphene nanoribbons. *Nature* 466, 7305 (2010), 470–473. doi: [10.1038/nature09211](https://doi.org/10.1038/nature09211).
- [294] DONG, L., LIU, P. N., AND LIN, N. Surface-activated coupling reactions confined on a surface. *Accounts of Chemical Research* 48, 10 (2015), 2765–2774. doi: [10.1021/acs.accounts.5b00160](https://doi.org/10.1021/acs.accounts.5b00160).
- [295] BJORK, J., HANKE, F., AND STAFSTROM, S. Mechanisms of halogen-based covalent self-assembly on metal surfaces. *Journal of the American Chemical Society* 135, 15 (2013), 5768–5775. doi: [10.1021/ja400304b](https://doi.org/10.1021/ja400304b).
- [296] TALIRZ, L., SODE, H., CAI, J., RUFFIEUX, P., BLANKENBURG, S., JAAFAR, R., BERGER, R., FENG, X., MULLEN, K., PASSERONE, D., FASEL, R., AND PIGNEDOLI, C. A. Termini of bottom-up fabricated graphene nanoribbons. *Journal of the American Chemical Society* 135, 6 (2013), 2060–2063. doi: [10.1021/ja311099k](https://doi.org/10.1021/ja311099k).
- [297] ZINT, S., EBELING, D., SCHLODER, T., AHLES, S., MOLLENHAUER, D., WEGNER, H. A., AND SCHIRMEISEN, A. Imaging successive intermediate states of the on-surface ullmann reaction on cu(111): Role of the metal coordination. *ACS Nano* 0, 0 (2017), null. doi: [10.1021/acsnano.7b01109](https://doi.org/10.1021/acsnano.7b01109).
- [298] BJORK, J., STAFSTROM, S., AND HANKE, F. Zipping up: Cooperativity drives the synthesis of graphene nanoribbons. *Journal of the American Chemical Society* 133, 38 (2011), 14884–14887. doi: [10.1021/ja205857a](https://doi.org/10.1021/ja205857a).
- [299] SIMONOV, K. A., VINOGRADOV, N. A., VINOGRADOV, A. S., GENERALOV, A. V., ZAGREBINA, E. M., MÅRTENSSON, N., CAFOLLA, A. A., CARPY, T., CUNNIFFE, J. P., AND PREOBRAJENSKI, A. B. Effect of substrate chemistry on the bottom-up fabrication of graphene nanoribbons: Combined core-level spectroscopy and stm

- study. *The Journal of Physical Chemistry C* 118, 23 (Jun 2014), 12532–12540. doi: [10.1021/jp502215m](https://doi.org/10.1021/jp502215m).
- [300] MASSIMI, L., OURDJINI, O., LAFFERENTZ, L., KOCH, M., GRILL, L., CAVALIERE, E., GAVIOLI, L., CARDOSO, C., PREZZI, D., MOLINARI, E., FERRETTI, A., MARIANI, C., AND BETTI, M. G. Surface-assisted reactions toward formation of graphene nanoribbons on au(110) surface. *The Journal of Physical Chemistry C* 119, 5 (Feb 2015), 2427–2437. doi: [10.1021/jp509415r](https://doi.org/10.1021/jp509415r).
- [301] DE OTEYZA, D. G., GARCIA-LEKUE, A., VILAS-VARELA, M., MERINO-DIEZ, N., CARBONELL-SANROMA, E., CORSO, M., VASSEUR, G., ROGERO, C., GUITIAN, E., PASCUAL, J. I., ORTEGA, J. E., WAKAYAMA, Y., AND PENA, D. Substrate-independent growth of atomically precise chiral graphene nanoribbons. *ACS Nano* 10, 9 (2016), 9000–9008. doi: [10.1021/acsnano.6b05269](https://doi.org/10.1021/acsnano.6b05269).
- [302] SAYWELL, A., SCHWARZ, J., HECHT, S., AND GRILL, L. Polymerization on stepped surfaces: Alignment of polymers and identification of catalytic sites. *Angewandte Chemie International Edition* 51, 21 (May 2012), 5096–5100. doi: [10.1002/anie.201200543](https://doi.org/10.1002/anie.201200543).
- [303] SÖDE, H., TALIRZ, L., GRÖNING, O., PIGNEDOLI, C. A., BERGER, R., FENG, X., MÜLLEN, K., FASEL, R., AND RUFFIEUX, P. Electronic band dispersion of graphene nanoribbons via fourier-transformed scanning tunneling spectroscopy. *Physical Review B* 91 (Jan 2015), 045429. doi: [10.1103/PhysRevB.91.045429](https://doi.org/10.1103/PhysRevB.91.045429).
- [304] SENKOVSKIY, B. V., USACHOV, D. Y., FEDOROV, A. V., HABERER, D., EHLEN, N., FISCHER, F. R., AND GRÜNEIS, A. Finding the hidden valence band of $n = 7$ armchair graphene nanoribbons with angle-resolved photoemission spectroscopy. *2D Materials* 5, 3 (Apr 2018), 035007. doi: [10.1088/2053-1583/aabb70](https://doi.org/10.1088/2053-1583/aabb70).
- [305] ABD EL-FATTAH, Z. M., KHER-ELDEN, M. A., PIQUERO-ZULAICA, I., DE ABAJO, F. J. G., AND ORTEGA, J. E. Graphene: Free electron scattering within an inverted honeycomb lattice. *Physical Review B* 99 (Mar 2019), 115443. doi: [10.1103/PhysRevB.99.115443](https://doi.org/10.1103/PhysRevB.99.115443).